Alkali-Halide Thin Films : Growth, Structure and Reactivity upon Electron Irradiation

Ala Husseen

université PARIS-SACLAY

NNT : 2018SACLS081

Thèse de doctorat

UNIVERSITÉ PARIS SUD
Comprendre le monde, construire l'avenir

Alkali-Halide Thin Films: Growth, Structure and Reactivity upon Electron Irradiation

Thèse de doctorat de l'Université Paris-Saclay
Préparée à l'Université Paris-Sud

École Doctorale n° 572 : Ondes et Matière (EDOM)
Spécialité de doctorat : Physique et Chimie de la Matière et des Matériaux

Thèse présentée et soutenue à Orsay, le 29 Mars 2018, par

Ala HUSSEEN

Composition du Jury :

Anne LAFOSSE Professeur Institut des Sciences Moléculaires d'Orsay (-UPS)	Présidente
Clemens BARTH Chargé de Recherche, HDR Centre Interdisciplinaire de Nanoscience de Marseille (-AMU)	Rapporteur
Régis STEPHAN Maître de Conférences, HDR Institut de Science des Matériaux de Mulhouse (-UHA)	Rapporteur
Jean-Marc THEMLIN Professeur Inst. Matériaux Microélectronique Nanosciences de Provence (-AMU)	Examinateur
Andrew MAYNE Directeur de Recherche Institut des Sciences Moléculaires d'Orsay (-UPS)	Directeur de thèse
Eric LE MOAL Chargé de Recherche Institut des Sciences Moléculaires d'Orsay (-UPS)	Invité

Acknowledgments

First of all, I would like to express my sincere gratitude to my supervisors, Dr. Andrew Mayne, Dr. Séverine Le Moal and Dr. Eric Le Moal. Thank you very much for giving me the opportunity to conduct my research project in your group and for all the advice and the guidance that you gave to me. You offered me a lot of help both on scientific subjects and daily life. I really enjoyed the free atmosphere that you gave to me which helped me a lot to continue my work easily. Studying with you has not only broadened my knowledge but also has helped me to know how to do research because each of you gave me a different experience. Especial thanks to Dr. Eric with whom I did most of the experiments, it was a great opportunity for me to work with him because of his serious attitude on research and his extensive knowledge in science. Besides, I will never forget the surprise birthday that he organized for me with our group.

I would like to thank Prof. Hamid Oughaddou and Dr. Hanna Enriquez for the help with our experiment. When I had the problem with the RT-STM setup, they offered me their help and gave me the LT-STM setup in between their experiments, and this helped me a lot and allowed me to finish my thesis and publish my article. In addition, Prof. Hamid sometimes was following my experiments and provide me a lot of advice to improve my STM images, I highly appreciate his help.

My sincerest thanks also to Dr. Philippe Roncin, Dr. Hocine Khemliche, Dr. Anouchah Momeni, and Dr. Magda Staicu-Casagrande for the GIFAD experiment. I am happy that I had an opportunity to do the GIFAD experiment, even though it was done in only a short time, but I learned a lot. Thanks to all the members of the group for their kindness and their help, especially Dr. Hocine with whom I did most of the experiment. He was very kind to me and he always shared ideas with openness and enthusiasm.

I want to express my gratitude to all the jury members present at my PhD defense: Prof. Anne Lafosse, Dr. Clemens Barth, Dr. Régis Stephan, and Dr. Jean-Marc Themlin. The discussion with them really inspired me a lot and broadened my knowledge. Thanks all the insightful comments from them.

Special thanks go to Dr. Eric Charron for his support and his kindness, and for giving me the opportunity to work in the Nanoscience group. I also would like to thank the other members of Nanoscience Group Dr. Gérald Dujardin, Dr. Elizabeth Boer- Duchemin, Dr. Georges Raseev, and Dr. Damien Riedel for the free atmosphere and for their kindness. Especially Dr. Mali Zhao who helped me a lot when I started working on the RT-STM setup and taught me many things about the experimental set-up during my training. In addition, the financial support of the Campus France at the Ministry of Foreign Affairs is also grateful acknowledged.

Moreover, I would like to extend my sincerest thanks to my fellow office-mates Moustafa Achlan, Khalid Quertite, Shuiyan Cao, Wei Zhang, Delphine Pommier, and Laury Martins, for all the fun we had together, I really enjoyed being with you, and you gave me the family atmosphere. Especially Moustafa Achlan was a constant source of inspiration and support.

My gratitude to my friends Leo-Albert Sala and Ivan Alata for their support and help, as well as my very kind and nice friends Mahda Garamaki and Somaye Rostampour, who arrived with me in France, and who they supported me a lot and helped me always, thanks for the great time that I spent with you.

Last but not the least, I want to take this opportunity to thank all my family for their great support, constant understanding, and care. I am deeply indebted to my uncle Salam Nouman and my great mother Asia Nouman for their unconditional love and support throughout the period of this study. Finally, special thanks to my fiance Ahmad Mejwal for being in my life.

Abstract

NaCl and KCl are wide band gap materials that are increasingly used as thin films in surface science and single-molecule spectroscopy studies to electronically decouple organic molecules from a metal substrate. In addition, the reactivity of bulk NaCl and KCl crystals under electron irradiation has been widley studied since the year 1970 s.

In this dissertation, we report a detailed investigation on the structures of two different thin films of NaCl and KCl grown on the Ag(001) substrate by scanning tunneling microscopy (STM), scanning tunneling spectroscopy (STS), low energy electron diffraction (LEED), and Auger electron spectroscopy (AES) in ultrathin vacuum condition. In order to obtain high-quality thin films and to control the properties of these films on the metal surface (film thickness, domain size, domain orientation, etc), we study in detail the film growth, especially as a function of the growth parameters. In addition, the apparent height measurements by STM show that the apparent thickness and the STM contrast of these two insulating films are bias dependent.

We report on an electron-induced modification of alkali halides in the ultrathin film regime. The reaction kinetics and products of the modifications are investigated in the case of NaCl films grown on Ag(001). Their structural and chemical modification upon irradiation with electrons of energy 52–60 eV and 3 keV is studied using LEED and AES, respectively. The irradiation effects on the film geometry and thickness (ranging from between two and five atomic layers) are examined using STM. We observe that Cl depletion follows different reaction kinetics, as compared to previous studies on thick NaCl films and bulk crystals. Na atoms produced from NaCl dissociation diffuse to bare areas of the Ag(001) surface, where they form Na-Ag superstructures that are known for the Na/Ag(001) system. The modification of the film is shown to proceed through two processes, which are interpreted as a fast disordering of the film with removal of NaCl from the island edges and a slow decrease of the structural order in the NaCl with formation of holes due to Cl depletion. The kinetics of the Na-Ag superstructure growth is explained by the limited diffusion on the irradiated surface, due to aggregation of disordered NaCl molecules at the substrate step edges.

We have also investigated the deposition of PTCDA molecules on the metallic substrate Ag(001) and on the KCl/Ag(001) system using STM. We obtain a monolayer of PTCDA molecules on Ag(001) that is arranged in a square unit cell. On KCl films, both individual PTCDA molecules and a densely packed structure are found.

Contents

Introduction

Insulating thin films on metals are key ingredients in numerous applications, e.g., microelectronics, catalysis, energy generation, and plasmonic sensors. As well, they are central in many fundamental research fields, notably in surface science [1], where they serve as model templates and atomically controlled spacers, for the manipulation molecules [2]–[10] or single atoms [11]. The structural quality of the molecular film is dependent on the presence of defects in the insulating layers and at the interfaces. Therefore, highly controlled preparation conditions of the thin insulating films are required to keep defect density extermely low, especially if a non-local method such as electron diffraction or photoemission spectroscopy is used [12].

Alkali halides materials have been successfully investigated in detail on numerous crystalline metal surfaces such as silver [13]–[16], aluminum [17], gold [18], [19], and copper [20]. Controlling the growth conditions such as the sample temperature, the deposition time, and the cell temperature, etc. are most straightforward to study various epitaxial relationships to the substrate.

The growth of NaCl and KCl layers has already been the subject of several experiment studies on various metal substrates [10], [12]–[16], [18]–[25] and characterized using different surface-sensitive techniques including non-contact atomic force microscopy (nc-AFM) [13], Kelvin probe force microscopy (KPFM) [20], [21], scanning tunneling microscopy (STM) [10], [12], [14], [16], [18], [22], scanning tunneling spectroscopy (STS) [13], [14], [22], and spot-analysis low energy electron diffraction (SPA-LEED) [12], [15], [20], [23].

Most of the time, chemical stability of insulating thin films upon charged particle irradiation is required, e.g., for characterization using electron spectroscopy and microscopy. In some specific

cases, their reactivity may even be turned into a unique opportunity to control matter on a sub-nanometer scale [26], [27]. In this context, understanding the reaction kinetics is central to the control of the reaction products.

Sodium chloride (NaCl) exposed to electron irradiation has been observed within different energy ranges, in low energy electron diffraction (LEED) and Auger electron spectroscopy (AES), reflected electron energy loss microscopy (REELM) and reflection high-energy electron diffraction (RHEED) experiments [28]–[30]. When exposed to the low-energy electron beam of a LEED, thin NaCl films on an Ag(110) crystal have been shown to transform within a few minutes into 2D periodic arrays of sodium atoms adsorbed on silver [31]. These periodic arrays exhibit the same atomic arrangements as observed when sodium is evaporated directly onto Ag(110) [32], [33]. To our knowledge, no studies other than Ref. [31] deal with the electron-induced modification of alkali-halide thin films on fcc metals. It has also been reported that a number of surface reconstructions and 2D alloys can be produced through alkali-metal (Li, Na, K, Rb) deposition on fcc metals (Al, Ni, Cu, Ag, Au), by finely controlling the surface coverage [34]–[47]. However, it is not known whether these superstructures may be obtained through dissociation of alkali-halide thin films.

The electron-induced dissociation of alkali halides has been attributed to the substitution of halide ions with incident electrons, a process that is also at the origin of color centers (i.e., light absorbing defects) in NaCl crystals [28]. This effect, which is known to occur over a broad energy range, could be used to engineer areas within insulating layers. However, the kinetics of the electron-induced dissociation of alkali halides in the form of ultrathin films, i.e., a few atomic layers in thickness, have rarely been addressed [48], [49]; most often, bulk crystals and thick films (tens to hundreds of nanometers) were considered [28], [50]. In the ultrathin film case, the limited amount of reactants and the interactions with the substrate may play a crucial part, thus leading to different reaction kinetics, compared to the bulk crystal and thick film cases. The products of alkali-halide dissociation may be different too, since they may adsorb or even react with the substrate, which can be of a different material, e.g., of a metal, whereas on bulk crystals and thick films the dissociation products inevitably adsorb on the same alkali-halide material.

Perylene-3,4,9,10-tetracarboxylic di-anhydride (PTCDA) is one of the organic molecules with promising applications in optical and semiconductor devices [8]. These molecules were studied on several alkali halide surfaces, KCl [51], [52], NaCl [5], [8], [10], [53], and KBr [54],

[55]. The conductivity of PTCDA films is reported to be anisotropic. Understanding the growth of PTCDA films on insulating substrates is therefore key to control these direction-dependent properties so that the use of PTCDA in organic devices can be enhanced [10]. On different metal and salt surfaces, for example, different epitaxial adsorbate structures of PTCDA have been identified such as the so-called quadratic (Q), herringbone (HB) and brick wall (BW) structures. These structures are formed from different combinations of the non-equivalent sites of adjacent PTCDA molecules [52].

This thesis focuses on the study of the quality of the NaCl and KCl ultrathin films grown on Ag(001) by STM, LEED, and AES in ultrahigh vacuum conditions. In addition, to the study of the reaction kinetics of ultrathin NaCl films on Ag(001) upon irradiation with the electron beams of a LEED (50-60 eV) and an AES (3 keV). Moreover, the formation of PTCDA molecules on Ag(001) substrate and on Ag(001) covered with KCl thin film also are reported in this work.

In chapter 1, the prior studies on alkali halides materials are reviewed, in particular, NaCl and KCl. We focus on the growth of these films on a metal substrate that has a low index. We discuss the most important applications based on these films. Finally, we review the previous dissociation studies of thick films and bulk crystals of alkali halides under electron irradiation and photon irradiation by several techniques.

In chapter 2, we describe the experimental setup and the preparation procedure of thin films. We also discuss the basic principle of the techniques that are used in our experiments.

In chapter 3, the NaCl and KCl thin films on Ag(001) are investigated. In order to obtain high-quality thin films and to control the properties of these films on the metal surface (film thickness, domain size, domain orientation, etc.), we study in detail the film growth, especially as a function of the growth parameters. We also investigate the local information at the nanometer scale using STM, STS, LEED, and AES. We show that the NaCl film is composed of large crystalline islands (Wolmer-Weber growth mode), whereas the growth of KCl film is layer-plus-island (Stranski-Krastanov mode). The apparent height measurements show that the apparent thickness and the STM contrast of these two insulating films are bias dependent.

In chapter 4, we report on the reaction kinetics of ultrathin NaCl films grown on Ag(001) upon irradiation with the electron beams of a LEED and an AES. Here, LEED and AES are used both to induce NaCl dissociation and to monitor the structural and chemical modifications of the sample

surface. In addition, scanning tunneling microscopy (STM) is used to compare the topography of the as-grown and irradiated NaCl films. We observe that Cl depletion follows different reaction kinetics, as compared to previous studies on NaCl thick films and bulk crystals. Thus, we analyze the reaction kinetics and retrieve the rate constant of Cl depletion, and we propose models for the morphological evolution of the irradiated film and the formation of Na-Ag superstructures.

In chapter 5, we present experiments involving the adsorption of PTCDA molecules on the silver substrate Ag(001) and on KCl/Ag(001) using STM. In the STM images, we observe a monolayer of PTCDA molecules on Ag(001) that is arranged in a quadratic unit cell. On KCl/Ag(001), a different arrangement for these molecules was found, where on bare silver, the molecules form islands with random shapes, while on KCl films, both individual PTCDA molecules, and a dense packed structure are found.

Bibliography

[1] R. Bennewitz, "Structured surfaces of wide band gap insulators as templates for overgrowth of adsorbates," *J. Phys. Condens. Matter*, vol. 18, no. 26, p. R417, 2006.

[2] J. Repp, M. Gerhard, S. M, A. Gourdon, and C. Joachim, "Molecules on Insulating Films: Scanning-Tunneling Microscopy Imaging of Individual Molecular Orbitals," *Phys. Rev. Lett.*, vol. 94, no. 2, p. 26803, Jan. 2005.

[3] P. Merino, C. Große, A. Rosławska, K. Kuhnke, and K. Kern, "Exciton dynamics of C60-based single-photon emitters explored by Hanbury Brown–Twiss scanning tunnelling microscopy," *Nat. Commun.*, vol. 6, p. 8461, Sep. 2015.

[4] T. Leoni, O. Guillermet, H. Walch, V. Langlais, A. Scheuermann, J. Bonvoisin, and S. Gauthier, "Controlling the Charge State of a Single Redox Molecular Switch," *Phys. Rev. Lett.*, vol. 106, no. 21, p. 216103, 2011.

[5] M. Müller, E. Le Moal, R. Scholz, and M. Sokolowski, "Exciton and polarization contributions to optical transition energies in an epitaxial organic monolayer on a dielectric substrate," *Phys. Rev. B*, vol. 83, no. 24, p. 241203, 2011.

[6] H. Imada, K. Miwa, M. Imai-Imada, S. Kawahara, K. Kimura, and Y. Kim, "Real-space investigation of energy transfer in heterogeneous molecular dimers," *Nature*, vol. 538, no. 7625, pp. 364–367, Oct. 2016.

[7] Y. Zhang, Y. Luo, Y. Zhang, Y.-J. Yu, Y.-M. Kuang, L. Zhang, Q.-S. Meng, Y. Luo, J.-L. Yang, Z.-C. Dong, and J. G. Hou, "Visualizing coherent intermolecular dipole–dipole coupling in real space," *Nature*, vol. 531, no. 7596, pp. 623–627, Mar. 2016.

[8] E. Le Moal, M. Müller, O. Bauer, and M. Sokolowski, "Stable and metastable phases of PTCDA on epitaxial NaCl films on Ag(100)," *Phys. Rev. B*, vol. 82, no. 4, p. 45301, 2010.

[9] K. A. Cochrane, A. Schiffrin, T. S. Roussy, M. Capsoni, and S. A. Burke, "Pronounced polarization-induced energy level shifts at boundaries of organic semiconductor nanostructures," *Nat. Commun.*, vol. 6, p. 8312, Oct. 2015.

[10] X. Sun and F. Silly, "NaCl islands decorated with 2D or 3D 3,4,9,10-perylene-tetracarboxylic-dianhydride nanostructures," *Appl. Surf. Sci.*, vol. 256, no. 7, pp. 2228–2231, 2010.

[11] W. Steurer, J. Repp, L. Gross, I. Scivetti, M. Persson, and G. Meyer, "Manipulation of the Charge State of Single Au Atoms on Insulating Multilayer Films," *Phys. Rev. Lett.*, vol. 114, no. 3, p. 36801, Jan. 2015.

[12] M. Müller, J. Ikonomov, and M. Sokolowski, "Structure of Epitaxial Layers of KCl on Ag(100)," *Surf. Sci.*, vol. 605, no. 11, pp. 1090–1094, 2011.

[13] H.-C. Ploigt, C. Brun, M. Pivetta, F. Patthey, and W.-D. Schneider, "Local work function changes determined by field emission resonances: NaCl/Ag(100)," *Phys. Rev. B*, vol. 76, no. 19, p. 195404, Nov. 2007.

[14] M. Pivetta, F. Patthey, M. Stengel, A. Baldereschi, and W.-D. Schneider, "Local work function Moiré pattern on ultrathin ionic films: NaCl on Ag(100)," *Phys. Rev. B*, vol. 72, no. 11, p. 115404, Sep. 2005.

[15] E. Le Moal, M. Müller, O. Bauer, and M. Sokolowski, "Misfit driven azimuthal orientation of NaCl domains on Ag(100)," *Surf. Sci.*, vol. 603, no. 16, pp. 2434–2444, 2009.

[16] W. Hebenstreit, J. Redinger, Z. Horozova, M. Schmid, R. Podloucky, and P. Varga, "Atomic resolution by STM on ultra-thin films of alkali halides: experiment and local density calculations," *Surf. Sci.*, vol. 424, no. 2, pp. L321–L328, 1999.

[17] W. Hebenstreit, M. Schmid, J. Redinger, R. Podloucky, and P. Varga, "Bulk Terminated NaCl(111) on Aluminum: A Polar Surface of an Ionic Crystal?," *Phys. Rev. Lett.*, vol. 85, no. 25, pp. 5376–5379, 2000.

[18] X. Sun, M. P. Felicissimo, P. Rudolf, and F. Silly, "NaCl multi-layer islands grown on Au(111)-(22× √3) probed by scanning tunneling microscopy," *Nanotechnology*, vol. 19, no. 49, p. 495307, 2008.

[19] C. Loppacher, U. Zerweck, and L. M. Eng, "Kelvin probe force microscopy of alkali chloride thin films on Au(111)," *Nanotechnology*, vol. 15, no. 2, p. S9, 2004.

[20] A. Riemann, S. Fölsch, and K. H. Rieder, "Epitaxial growth of alkali halides on stepped metal surfaces," *Phys. Rev. B*, vol. 72, no. 12, p. 125423, Sep. 2005.

[21] G. Cabailh, C. R. Henry, and C. Barth, "Thin NaCl films on silver (001): island growth and work function," *New J. Phys.*, vol. 14, no. 10, p. 103037, 2012.

[22] Q. Guo, Z. Qin, C. Liu, K. Zang, Y. Yu, and G. Cao, "Bias dependence of apparent layer thickness and Moiré pattern on NaCl/Cu(001)," *Surf. Sci.*, vol. 604, no. 19, pp. 1820–1824, 2010.

[23] J. Kramer, C. Tegenkamp, and H. Pfnür, "The growth of NaCl on flat and stepped silver surfaces," *J. Phys. Condens. Matter*, vol. 15, no. 38, p. 6473, 2003.

[24] F. Gao, G. Wu, D. Stacchiola, M. Kaltchev, P. V Kotvis, and W. T. Tysoe, "The Tribological Properties of Monolayer KCl Films on Iron in Ultrahigh Vacuum: Modeling the Extreme-Pressure Lubricating Interface," *Tribol. Lett.*, vol. 14, no. 2, pp. 99–104, 2003.

[25] M. Kiguchi, G. Yoshikawa, S. Ikeda, and K. Saiki, "Electronic properties of metal-induced gap states formed at alkali-halide/metal interfaces," *Phys. Rev. B*, vol. 71, no. 15, p. 153401, Apr. 2005.

[26] S. Günther, S. Böcklein, R. Reichelt, J. Wintterlin, A. Barinov, T. O. Menteş, M. Á. Niño, and A. Locatelli, "Surface Patterning of Silver using an Electron- or Photon-Assisted Oxidation Reaction," *ChemPhysChem*, vol. 11, no. 7, pp. 1525–1532, 2010.

[27] S. Günther, R. Reichelt, J. Wintterlin, A. Barinov, T. O. Menteş, M. Á. Niño, and A. Locatelli, "Chemical patterning of Ag(111): Spatially confined oxide formation induced by electron beam irradiation," *Appl. Phys. Lett.*, vol. 93, no. 23, p. 233117, Dec. 2008.

[28] H. Tokutaka, M. Prutton, I. G. Higginbotham, and T. E. Gallon, "The (100) surfaces of alkali halides," *Surf. Sci.*, vol. 21, no. 2, pp. 233–240, 1970.

[29] E. Paparazzo and N. Zema, "Reflected electron energy loss microscopy and scanning Auger microscopy studies of electron irradiated alkali halide surfaces," *Surf. Sci.*, vol. 372, no. 1, pp. L301–L308, 1997.

[30] A. Friedenberg and Y. Shapira, "Electron induced dissociation of the NaCl(111) surface,"

Surf. Sci., vol. 87, no. 2, pp. 581–594, 1979.

[31] K. Aït-Mansour, M. Bielmann, O. Gröning, P. Ruffieux, R. Fasel, and P. Gröning, "(2×1)-Na surface reconstruction induced by NaCl dissociation on Ag(110) during LEED analysis," *Appl. Surf. Sci.*, vol. 252, no. 18, pp. 6368–6374, 2006.

[32] R. A. Marbrow and R. M. Lambert, "Adsorption and surface structural chemistry of Na and Na + O2 on Ag(110)," *Surf. Sci.*, vol. 61, no. 2, pp. 329–342, 1976.

[33] R. A. Marbrow and R. M. Lambert, "Chemisorption and surface reactivity of nitric oxide on clean and sodium-dosed Ag(110)," *Surf. Sci.*, vol. 61, no. 2, pp. 317–328, 1976.

[34] A. Schmalz, S. Aminpirooz, L. Becker, J. Haase, J. Neugebauer, M. Scheffler, D. R. Batchelor, D. L. Adams, and E. B\ogh, "Unusual chemisorption geometry of Na on Al(111)," *Phys. Rev. Lett.*, vol. 67, no. 16, pp. 2163–2166, Oct. 1991.

[35] C. Stampfl, M. Scheffler, H. Over, J. Burchhardt, M. Nielsen, D. L. Adams, and W. Moritz, "Identification of stable and metastable adsorption sites of K adsorbed on Al(111)," *Phys. Rev. Lett.*, vol. 69, no. 10, pp. 1532–1535, Sep. 1992.

[36] J. V Barth, H. Brune, R. Schuster, G. Ertl, and R. J. Behm, "Intermixing and two-dimensional alloy formation in the Na/Au(111) system," *Surf. Sci.*, vol. 292, no. 1, pp. L769–L774, 1993.

[37] Seigi Mizuno, Hiroshi Tochihara, and Takaaki Kawamura, "Missing-row-type restructuring of the Cu(001) surface induced by Li adsorption: a low-energy electron diffraction analysis," *Surf. Sci.*, vol. 292, no. 3, pp. L811–L816, 1993.

[38] R. Fasel, P. Aebi, J. Osterwalder, L. Schlapbach, R. G. Agostino, and G. Chiarello, "Local structure of c(2 X2)-Na on Al(001): Experimental evidence for the coexistence of intermixing and on-surface adsorption," *Phys. Rev. B*, vol. 50, no. 19, pp. 14516–14524, Nov. 1994.

[39] S. Mizuno, H. Tochihara, A. Barbieri, and M. A. Van Hove, "Completion of the structural determination of and rationalization of the surface-structure sequence (2X1)→(3X3)→(4X4) formed on Cu(001) with increasing Li coverage," *Phys. Rev. B*, vol.

52, no. 16, pp. R11658--R11661, Oct. 1995.

[40] J. V Barth, R. J. Behm, and G. Ertl, "Adsorption, surface restructuring and alloy formation in the Na/Au(111) system," *Surf. Sci.*, vol. 341, no. 1, pp. 62–91, 1995.

[41] W. Berndt, D. Weick, C. Stampfl, A. M. Bradshaw, and M. Scheffler, "Structural analysis of the two c(2 × 2) phases of Na adsorbed on Al(100)," *Surf. Sci.*, vol. 330, no. 2, pp. 182–192, 1995.

[42] M. Imaki, S. Mizuno, and H. Tochihara, "Surface structure sequences formed on Ag(001) with increasing alkali-metal coverages at room temperature," *Surf. Sci.*, vol. 357, pp. 145–149, 1996.

[43] H. Jiang, S. Mizuno, and H. Tochihara, "Adsorption mode change from adlayer- to restructuring-type with increasing coverage, evidenced by structural determination of c(2 × 2)→(4 × 4)→(5 × 5) sequence formed on Ni(001) by Li deposition," *Surf. Sci.*, vol. 380, no. 2, pp. L506–L512, 1997.

[44] H. L. Meyerheim, I. K. Robinson, and R. Schuster, "Temperature-dependent surface X-ray diffraction on K/Ag(001)-(2 × 1)," *Surf. Sci.*, vol. 370, no. 2, pp. 268–276, 1997.

[45] S. Mizuno, H. Tochihara, Y. Matsumoto, and K. Tanaka, "STM observation of restructured Cu(001) surfaces induced by Li deposition," *Surf. Sci.*, vol. 393, no. 1, pp. L69–L76, 1997.

[46] H. Tochihara and S. Mizuno, "Composite surface structures formed by restructuring-type adsorption of alkali-metals on fcc metals," *Prog. Surf. Sci.*, vol. 58, no. 1, pp. 1–74, 1998.

[47] A. Mikkelsen and D. L. Adams, "Surface structure of Cu(100)-c(2 X 2)-Na: A LEED analysis," *Phys. Rev. B*, vol. 60, no. 3, pp. 2040–2045, 1999.

[48] M. Szymonski, J. Kolodziej, P. Czuba, P. Piatkowski, P. Korecki, Z. Postawa, and N. Itoh, "Thickness dependent electron stimulated desorption of thin epitaxial films of alkali halides," *Appl. Surf. Sci.*, vol. 100, pp. 102–106, 1996.

[49] J. Kolodziej, P. Piatkowski, and M. Szymonski, "Electron-stimulated desorption of thin epitaxial films of KBr grown on (100)InSb," *Surf. Sci.*, vol. 390, no. 1, pp. 152–157, 1997.

[50] M. Szymonski, J. Kolodziej, B. Such, P. Piatkowski, P. Struski, P. Czuba, and F. Krok, "Nano-scale modification of ionic surfaces induced by electronic transitions," *Prog. Surf. Sci.*, vol. 67, no. 1, pp. 123–138, 2001.

[51] H. Proehl, T. Dienel, R. Nitsche, and T. Fritz, "Formation of Solid-State Excitons in Ultrathin Crystalline Films of PTCDA: From Single Molecules to Molecular Stacks," *Phys. Rev. Lett.*, vol. 93, no. 9, p. 97403, 2004.

[52] H. Aldahhak, W. G. Schmidt, and E. Rauls, "Adsorption of PTCDA on NaCl(100) and KCl(100)," *Surf. Sci.*, vol. 617, no. Supplement C, pp. 242–248, 2013.

[53] H. Karacuban, S. Koch, M. Fendrich, T. Wagner, and R. Möller, "PTCDA on Cu(111) partially covered with NaCl," *Nanotechnology*, vol. 22, no. 29, p. 295305, 2011.

[54] T. Kunstmann, A. Schlarb, M. Fendrich, T. Wagner, R. Möller, and R. Hoffmann, "Dynamic force microscopy study of 3,4,9,10-perylenetetracarboxylic dianhydride on KBr(001)," *Phys. Rev. B*, vol. 71, no. 12, p. 121403, Mar. 2005.

[55] J. M. Mativetsky, S. A. Burke, S. Fostner, and P. Grutter, "Templated growth of 3,4,9,10-perylenetetracarboxylic dianhydride molecules on a nanostructured insulator," *Nanotechnology*, vol. 18, no. 10, p. 105303, 2007.

Chapter 1

State of the Art: Alkali Halides Films

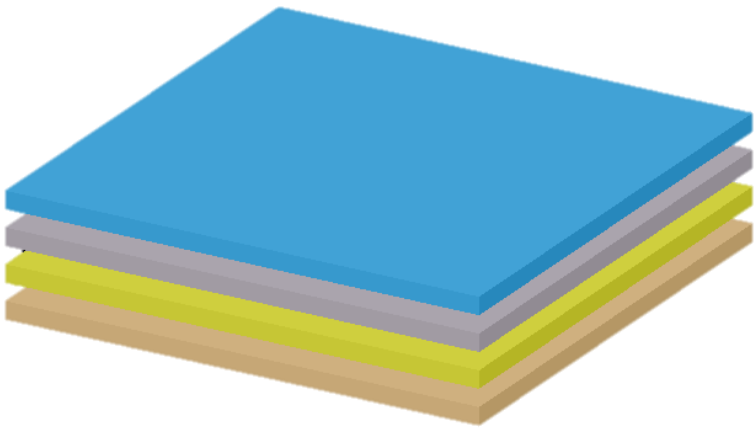

Table of Contents

1.1 Introduction

In this chapter, we review the literature on alkali halides, in particular, NaCl and KCl. At the beginning, it is important to know the electronic and structure properties of the bulk NaCl and KCl crystals before using these materials. Then we focus on the growth of these materials on low-index metal crystal surfaces, highlighting the growth conditions, the growth modes, and several techniques that are used to characterize the NaCl and KCl films in detail. In addition, we discuss the usefulness of the preparation of these films, and we mention the most important applications based on these films. Finally, the dissociation studies of thick films and bulk crystals of alkali halides under electron irradiation and photon irradiation by several techniques are reported also in this chapter.

1.2 Electronic and Structural Properties of Bulk NaCl and KCl Crystals

Sodium chloride and potassium chloride are alkali halides, which have been used in many studies because they were found to exhibit a large electronic bandgap even for thin films with thicknesses as low as two monolayers [1]. The energy gaps of NaCl and KCl bulk crystals at 77K are 8.97eV [2] and 8.7 eV [3] respectively.

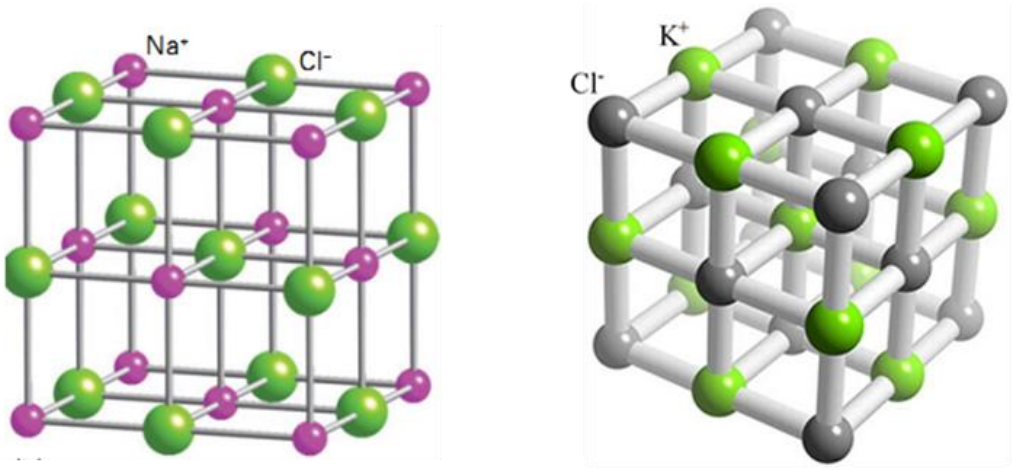

Figure 1.1: (Left image) Bulk NaCl structure, where the green balls are chlorine atoms and the small pink balls are sodium atoms. (Right image) Bulk KCl structure, where the gray balls are chlorine atoms and the green balls are sodium atoms [4], [5].

A characteristic common to all alkali halides is that they are ionic crystals with cubic symmetry, sodium and potassium have a positive charge (Na^+, K^+) and chlorine has a negative charge (Cl^-). Each ion in both structures is surrounded by six ions of the opposite charge in a cubic close packed (ccp) structure. The bulk unit cell of NaCl and KCl are presented in Fig. 1.1(a-b). The lattice parameters of the NaCl and KCl unit cells are 5.64 Å and 6.29 Å respectively.

The ionic crystals have only a few facets, such as the (100) surface, which are electrically neutral and stable, whereas others, such as (111) surface, have a charged surface (polar surface) because they contain only one type of ion, either Na^+/K^+ or Cl^- resulting in an unstable surface, one of the reasons being that the surface energy is infinite [6].

1.3 Growth of Thin Insulating Film on fcc Metals

1.3.1 Growth of thin NaCl layers

The growth of NaCl layers has been investigated in ultra-high vacuum on several metal substrates (Ag, Al, Cu, and Au) [7]–[16], and characterized using different surface-sensitive techniques including non-contact atomic force microscopy (nc-AFM) [9], Kelvin probe force microscopy (KPFM) [9], scanning tunneling microscopy (STM) [7], [10], [12]–[14], scanning tunneling spectroscopy (STS) [8], [10], [12], and spot-analysis low energy electron diffraction (SPA-LEED) [11], [15].

In these studies, it has been reported that ultrathin films of NaCl form crystalline islands [7]–[14] and the size of these islands depends on the substrate temperature during the growth of the NaCl film [9]; by increasing the temperature, the sizes of the islands increase and their density decreases, whereas the thickness of the island remains constant (see Fig. 1.2(a-e)) [9].

Figure 1.2(a-j) shows nc-AFM and KPFM images of NaCl islands grown on Ag(001) taken from the investigations by Cabailh et al [9]. The varying morphology of the islands shows the influence of the growth temperature on the NaCl island growth. The initial growth process of NaCl (1 or 2 ML) is a subject of controversy. For example, it has been reported that NaCl molecules formed an initial double-layer directly on Cu(001) implying the absence of a monatomic layer (see Fig. 1.3) [12]. However, in the case of the NaCl on Ag(001) two different formations have been

reported, a monolayer in [9] (see Fig. 1.2), and a monatomic layer and double-layer simultaneously in [8]. This difference is probably due to the different preparation conditions such as the substrate temperature or the technique used to measure the thickness (e.g. the STM height does not give the real height). In addition, the interaction of the NaCl with the metal may differ from one metal to another [8], [9], [12].

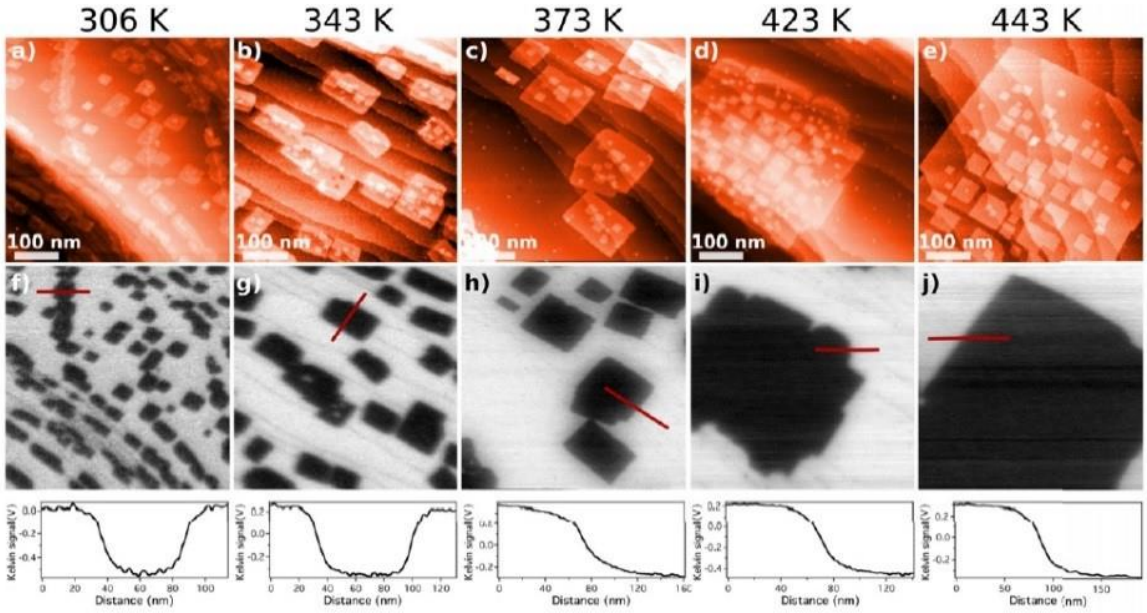

Figure 1.2: (a-e) nc-AFM and (f-j) KPFM images of 0.75 MLE thin NaCl films grown on Ag(001) at various substrate temperatures, the line profiles of the Kelvin images were taken over the edges of the islands and represent the work function change between Ag(001) and NaCl/Ag(001) [9].

Figure 1.3(a-d) shows a series of STM images of NaCl islands grown on Cu(001) which has been investigated by Guo et al and shows the initial double-layer of NaCl molecules on the Cu (001) substrate [10]. Scanning tunnelling microscopy (STM) and spot-analysis low energy electron diffraction (SPA-LEED) show that the NaCl domains have two possible orientations; one at 0˚ and the other at 45˚ with respect to the substrate. The domains have different azimuthal orientations and non-polar edges, composed of Cl^- and Na^+ ions, (see Figs. 1.2, 1.3, and 1.4) [10]–[12]. In addition, the growth orientation is independent of the direction of the substrate step [10].

A Moiré pattern was also observed in the NaCl film growth on different substrates due to the mismatch in the lattice constants between the NaCl adlayer and the substrate [9], [10], [12], (see Fig. 1.3(c-d)).

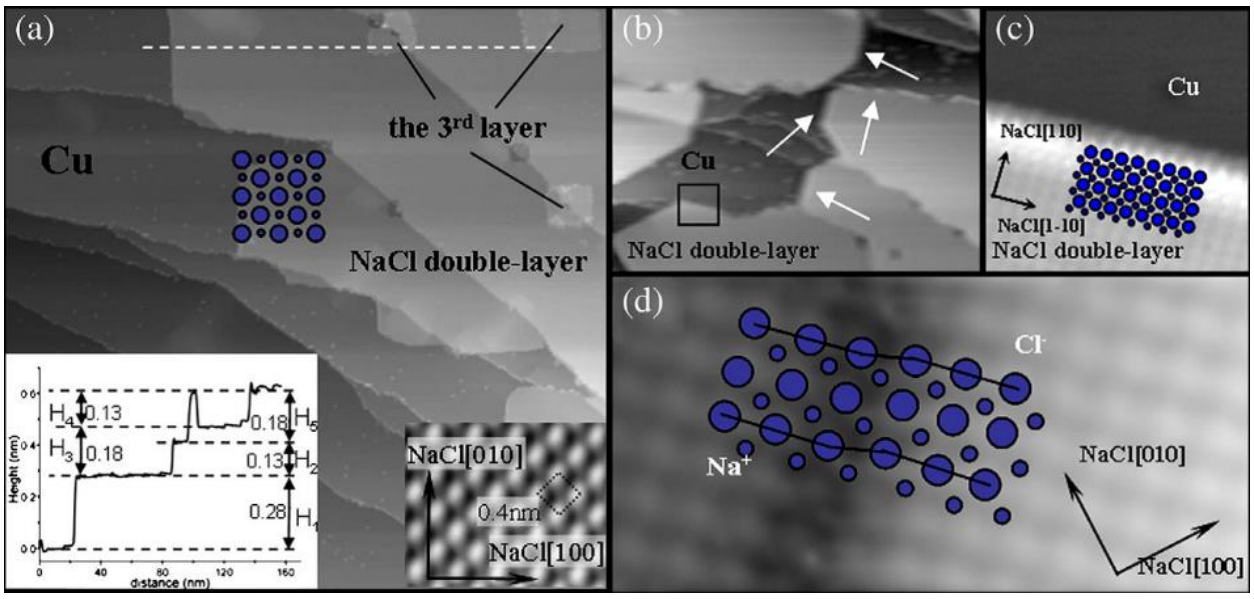

Figure 1.3: (a) STM image of the NaCl layer on Cu(001) with a coverage of 0.9 monolayers (ML). The left inset: height profile is along the dashed line, calibrated by the copper step height. The right inset: atomic resolution image is obtained on the initial double-layer in which the protrusions are Cl−ions. (b) STM image of the NaCl double layer with both non-polar and polar edges. (c) The atomic resolution image of a polar edge. (d) The atomically resolved STM image at step region showing that the layer covers the steps like a carpet [12].

Figure 1.4(top) shows STM images of the ultrathin film of NaCl grown on Ag(001) that has been studied by Pivetta et al. This study reveals that the islands with a 0° orientation have a strong lattice mismatch with the Ag substrate which will results in a weak Moiré pattern with a periodicity of 1.2 nm and a corrugation below 10 pm, in contrast with the islands with a 45° orientation which have a comparatively larger periodicity of 7.8 nm and a corrugation of up to 200 pm [10]. In the bottom panel of figure 1.4, the LEED image of the ultrathin film of NaCl grown on Ag(001) is shown. This has been studied by Le Moal et al, and shows that most of the NaCl domains are oriented with their unit cell aligned with that of Ag(001), with a rotational spread of less than

14˚ at RT. The azimuthal mosaicity of the NaCl domains varies as a function of the growth temperature and for different film thicknesses [11]. They found that the width of the azimuthal distribution becomes sharper when the growth temperature increases or the deposition rate decreases, and they assign this to the thermal expansion and higher diffusion rates of NaCl on Ag(001) [11].

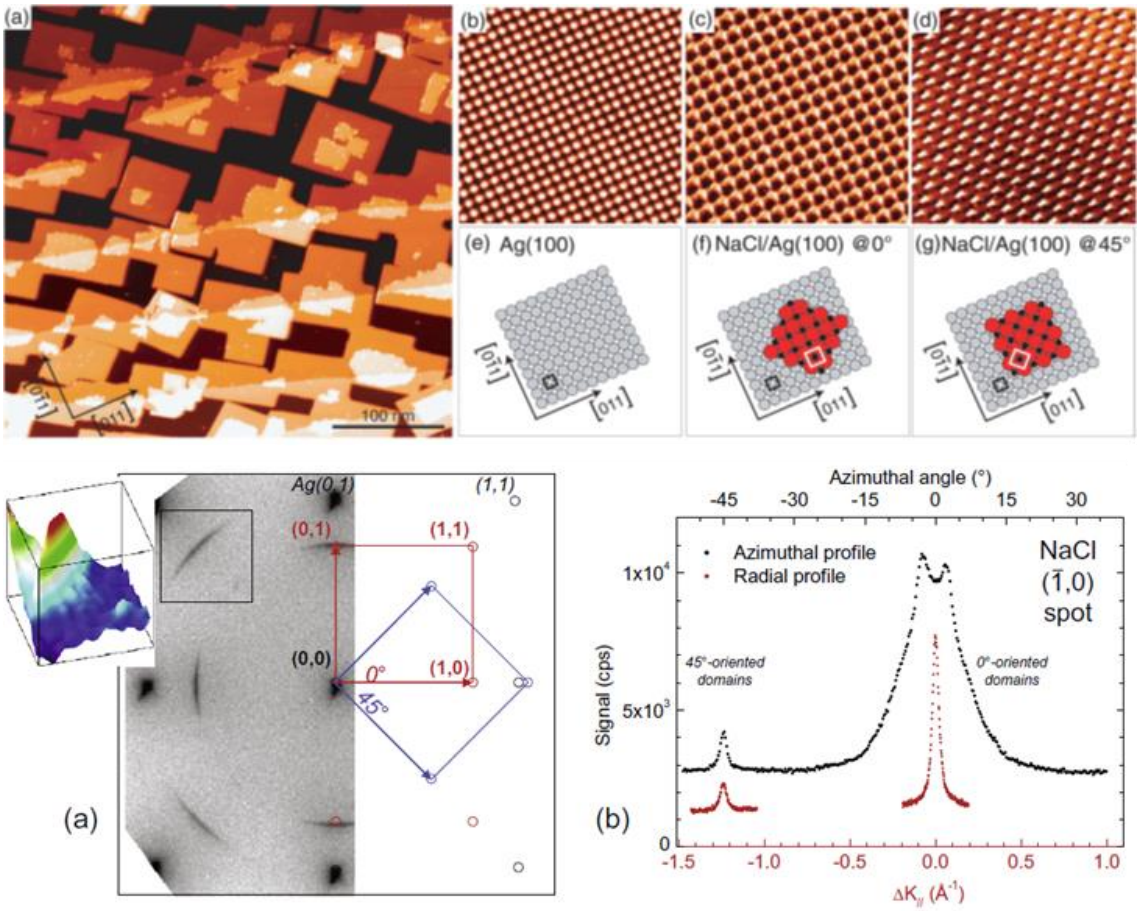

Figure 1.4: Top images: (a) STM image of NaCl islands grown on Ag(001). STM images showing atomic resolution on (b) Ag(100), (c) 1 ML NaCl/Ag(001) @ 0°, (d) 1 ML NaCl/Ag(001) @ 45°[10]. Bottom images**:** (a) LEED pattern and LEED pattern simulation of a (100)-terminated NaCl layer on Ag(001) of a 1 ML thick NaCl film grown at RT, with two different azimuthal orientations, namely NaCl [0 1 0] //Ag [0 1 0] (red) and NaCl [0 1 0]//Ag [0 1 1] (blue). (b) Azimuthal (black line) and radial (red line) spot profiles, measured on the ($\bar{1}$, 0) spots of 0˚ and 45˚-oriented domains [11].

In the STM studies, the atomic resolution on 1ML and 2ML NaCl and KCl on different substrates was always observed at low bias voltage, e.g., -110 mV for the NaCl/Ag(001) system [10], 0.5 V for NaCl/Cu(001) [12], (-0.5 V to -3 V) for NaCl on $Al_{99}Cu_1$(111) [13], 0.5 V for NaCl/Au(111), 0.6 V for NaCl/Au(111)-(22× √3) [14], and -1.57 V for KCl /Ag(001) [1]. These voltages are lower than the conduction and valence band edges for an undoped insulator, which would be of about ± 4 eV. On the other hand, obtaining atomic resolution on the metal substrate is only possible with a lower bias voltage in the millivolt regime (as usual for metals) [12], [13]. The ability to image at low voltage can be explained by the fact that the deposition of alkali halide on a metal creates an interface between the metal and the insulating layer. The interaction with the metal induces interface electronic states in the band gap of alkali halide which are called metal-induced gap states (MIGS) [12], [17]. MIGS are electronic states formed at the semiconductor (or insulator)/metal interface when a free electron-like metal wave function penetrates into the semiconductor (or insulator) side. The intensity of the MIGS at the interface depends on the metal substrate, in particular, the density of states of the metal substrate near the Fermi energy [17]. This enables the atomic structure of NaCl and KCl to be observed at a lower bias voltage.

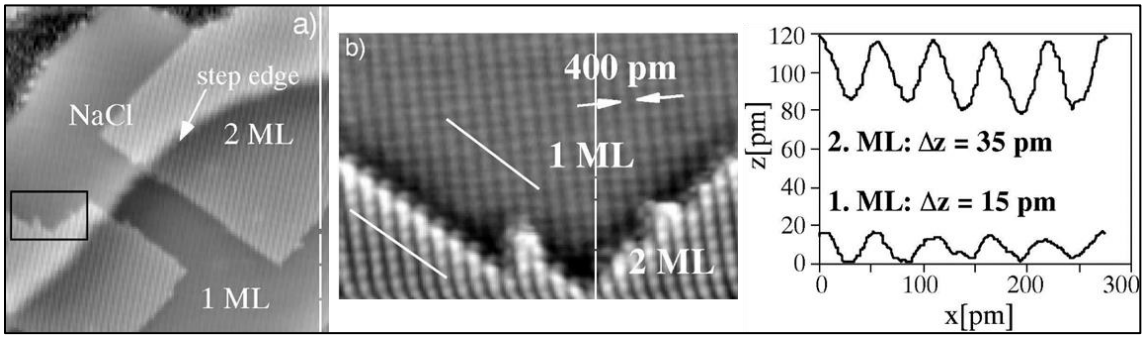

Figure 1.5: (a) STM single and double layer NaCl island (marked 1ML and 2 ML, respectively) lying over an $Al_{99}Cu_1$(111) substrate step edge; (b) atomically resolved of a single and a double layer [13].

The atomically resolved images on the NaCl film showed that only one type of ion was imaged (see Figs. 1.3, 1.4 top, and 1.5), which could be attributed to the anion Cl^-, with the Na^+ being completely invisible [9], [10], [12], [13]. The clear evidence was given by Kiguchi et al [17]. They studied the NEXAFS (near-edge-x-ray absorption fine structure) of MIGS for the KCl/Cu(001) system. The unoccupied Cl-p and K-p electronic densities of states can be identified

from the Cl-K-edge and K-K-edge NEXAFS. From their NEXAFS spectra, they observed the unoccupied electronic densities of states at the Cl edge originating from the MIGS but not at the K edge, indicating that the MIGS are formed only at the anion site [17]. Figure 1.5(a-b) shows two STM images of NaCl islands grown on the $Al_{99}Cu_1(111)$ substrate from the investigation by Hebenstreit et al. The atomic structure of the single and double layer of NaCl island is clearly visible [11].

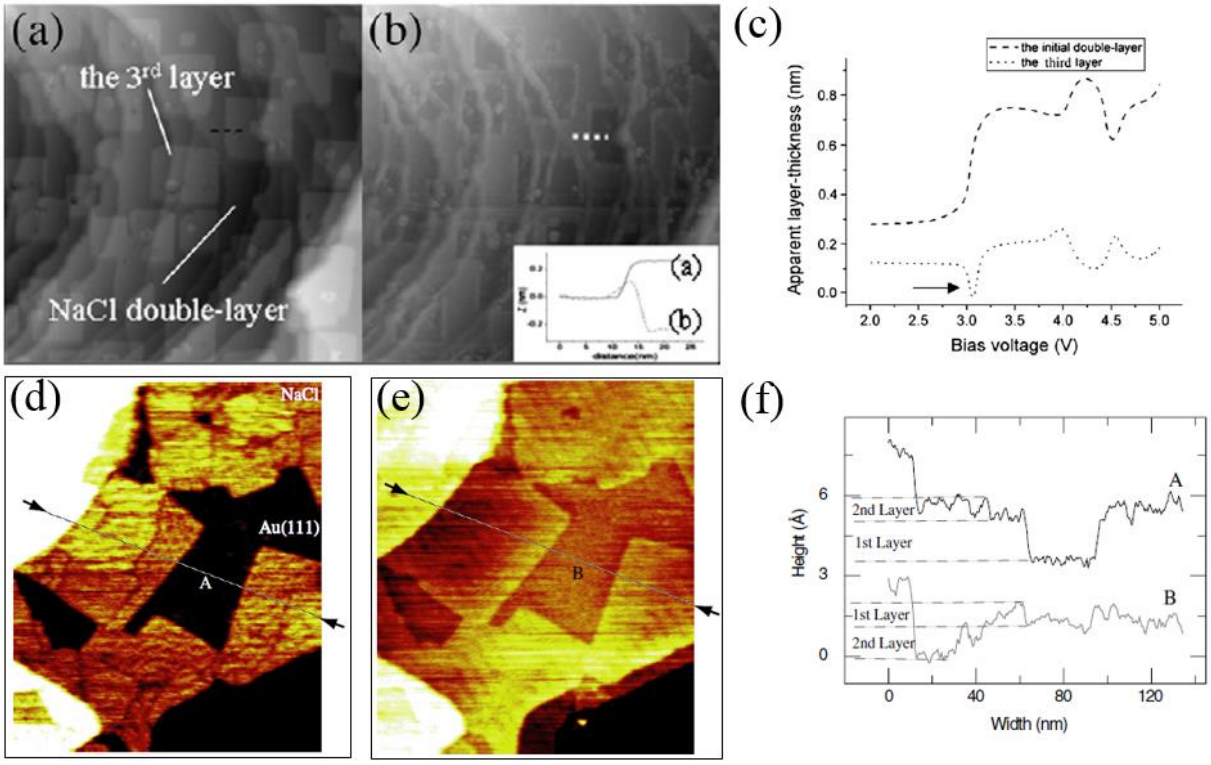

Figure 1.6: Upper images: (a) STM image (Vs=3.5 V, I=80 pA) of NaCl layers on Cu(001), (b) STM image of the same area at 3.1 V, (c) the characteristics of the apparent layer thickness with bias voltages on the initial double-layer and the third layer of NaCl [12]. Bottom images: (d) STM image (Vs =-0.3V, I_t=0.15 nA) of NaCl layers on Au(111) surface,(e) STM image of the same area at (Vs = −1.0 V, I_t = 0.7 nA), (f) the characteristics of the apparent layer thickness with bias voltages on the initial double-layer and the third layer of NaCl [14].

One important aspect is the determination of the local thickness of the NaCl domains, i.e., the number of atomic monolayers (ML). This can be obtained from the apparent height measured by AFM [9] and by STM at different bias voltages [12], [14]. Figure 1.6 shows STM images of

NaCl islands on Cu(001) in (a-c) [12], and on Au(111) in (d-f) [14], measured at different bias voltages. These images show that the apparent height of the NaCl layer and the contrast of the islands depend on the tunneling conditions as opposed to the metal substrate where it is independent of the tunneling conditions (see c and f curves in the Fig. 1.6) [12]–[14].

Guo et al found that the thickness of the NaCl layers gave different values at different bias voltages ranging from 2.8 to 3.2 V and 4 to 4.5 V as shown in Fig. 1.6(c). They observed that below 2.8 V the thickness for the initial double layer of NaCl island was 0.28 Å and at 3.2 V the apparent thickness for this layer had increased to 0.7 Å [12]. This difference has been explained by image potential states (IPSs) measured on the insulating film and the metal substrate [8], [10], [12]. The measurements showed that at lower bias voltage, electrons tunnel through the NaCl to the metal surface states, which gives an apparent height lower than the expected value, whereas at higher bias voltage electrons tunnel to an image potential state above the metal surface, which is accessible at U_b = 4 V because the first field emission resonance is shifted in energy from about 4.5 eV to 3.3 eV upon NaCl adsorption [8]. For this reason, the measured thickness increases with increasing bias voltage and becomes closer to the real value. In addition, measurements have shown that the apparent height of the top NaCl layer decreases when the number of NaCl layers on the surface increases for height measurements on one to three layers [13].

Finally, the work function was measured after deposition of NaCl on several substrates using different measurements (KPFM) [9], STS [12], and DFT calculations [10]. The measurements showed that the work function of Ag(001) is reduced after deposition of NaCl on Ag(001) (see Fig. 1.2(f-j)), with no dependence on the film thickness [9], [10].

1.3.2 Growth of thin KCl layers

The growth of KCl layers has been investigated in ultra-high vacuum on several metal substrates (Ag, Cu, Au, and Fe) [1], [16]–[19], and characterized using different surface-sensitive techniques including non-contact atomic force microscopy (no-AFM), Kelvin probe force microscopy (KPFM), scanning tunneling microscopy (STM), and spot-analysis low energy electron diffraction (SPA-LEED), [1], [17], [18].

The measurements showed that KCl forms a uniform first layer on different substrates [1], [16], [19] and has a carpet-like growth mode (see Fig. 1.7) [1], [16], where it covers the steps of Ag(001) substrate without any discontinuities, in contrast with NaCl which always forms islands on the surface of the metal and not a continous layer [8]–[10], [12]–[14]. However, in the work by Müller et al, they reported that the KCl film becomes non-uniform over a long-range scale but no further details were given [1].

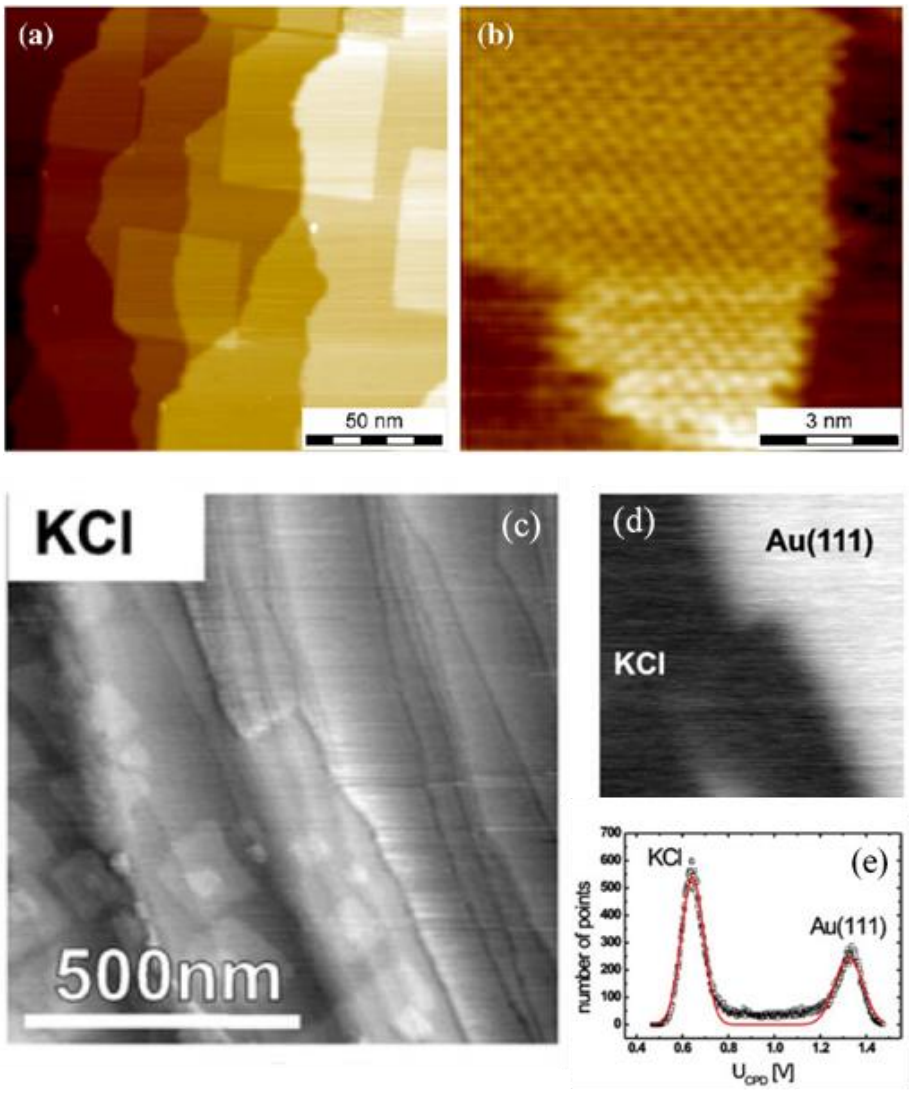

Figure 1.7: (a) STM image of a monolayer of KCl grown on Ag(001) surface. The square KCl islands indicated a second layer of KCl, which nucleate at the step edges, (b) STM image with the atomic resolution on the second KCl layer [1]. (c-e) show the topography, Kelvin probe signal, and the resulting Kelvin histogram respectively of potassium chloride (KCl) thin films on Au(111) [16].

Figure 1.7 (a) and (b) shows the STM topography and atomic structure of the KCl film grown on Ag(001) substrate from the investigation by Müller et al [1]. Figure 1.7(c-d) are the KPFM images of KCl grown on Au(111) substrate [16], showing the topography in (c), Kelvin probe signal in (d), and the resulting Kelvin histogram in (e). The investigation by Loppacher et al [16] revealed that the observed island size is much larger than the tip radius, which limits the resolution in KPFM. Therefore, the measured contact potentials U_{CPD} deduced from the histogram curves (e) can be considered to give quantitative values and stems from a complete ML (continuous over the surface) with no evidence for a further change of the work function for the second and third layer of the alkali halide [16].

The average domain size of the KCl films grown on Ag(001) has been calculated by Müller et al [1] using (SPA-LEED), where the FWHM of the <1,0> spots give a value around L=250 Å for KCl and 400 Å for the Ag substrate (see Fig. 1.8(a-b)). This value shows that the average domain size for the Ag substrate is larger than the one obtained for the KCl. This is because the domain size of the KCl is independent of the structural quality of the metal substrate. Their measurements also showed that the width of the spots depends on the domain size and the surface roughness of the KCl films and is independent of the film thickness [1]. Figure 1.8 shows LEED images of KCl on two different substrates Ag(001) [1], and on Cu (311) [15]. In figure 1.8(a-b) the LEED image of KCl shows an orientation aligned with the Ag substrate (0˚ growth) [1], and no rotational mosaicity was found in the growth of KCl on Ag(001) , contrary to the case of NaCl on Ag(001) [11]. The lattice constant of KCl could be measured from both the atomic resolution in Fig. 1.7(b) and the LEED pattern in Fig. 1.8(a) of KCl grown on Ag(001) [1], where $b_{KCl} = 4.44 \pm 0.02$ Å. This lattice constant does not depend on the thickness of the film (from 1 to 10 ML) [1]. Moreover, from the relation between the unit cell of Ag(001) and KCl, it was concluded that the growth of KCl on Ag(001) is incommensurate growth [1].

Finally, it has been reported that the growth of the alkali halides on a semiconductor or low-index metal always form (100)-terminated layers (see Fig. 1.8(a-d)) [1], [18]. This is due to the fact that the nonpolar (100) plan is the only stable face in the bulk crystal of alkali halides because the surface free energy is minimized with this orientation [18]. A different superstructure symmetry had been found in the growth of 1ML of KCl on Cu (311) shown in Fig. 1.8(c), similar to the case of NaCl monolayer growth on Cu (311).

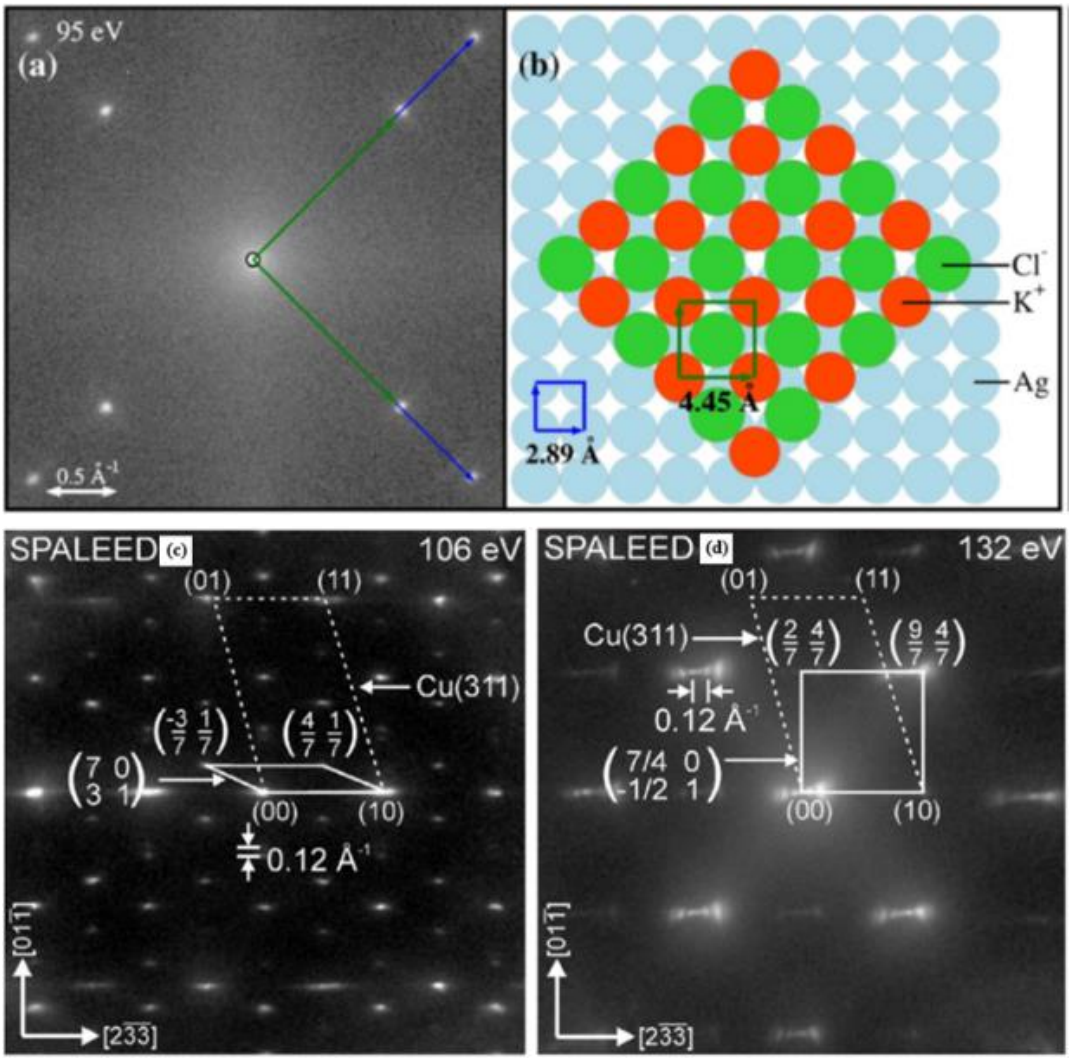

Figure 1.8: (a) LEED pattern of a KCl film grown on Ag(001), the blue arrow indicated unit cells of the Ag(001) surface, and a green arrow indicated unit cells of KCl film, (b) a schematic representation of Ag(001) and KCl(001) surface[1]. LEED pattern of 1 ML KCl/Cu (311) (c) and 6 ML (d), deposited at 520 K. Dashed line indicates diffraction pattern of Cu (311) unit cell and full line indicates $\begin{pmatrix} 7 & 0 \\ 3 & 1 \end{pmatrix}$ superstructure cell induced by the KCl (c) and $\begin{pmatrix} 7/4 & 0 \\ -1/2 & 1 \end{pmatrix}$ superstructure cell(d) [18].

The LEED pattern for this monolayer growth indicates an $\begin{pmatrix} 7 & 0 \\ 3 & 1 \end{pmatrix}$ overlayer superstructure (see Fig. 1.8(c)). In the case of 6 ML growth of KCl on Cu (311), the LEED pattern indicates

an $\begin{pmatrix} 7/4 & 0 \\ -1/2 & 1 \end{pmatrix}$ overlayer superstructure with a unit cell close to that of bulk KCl(100) (see Fig. 1.8(d). The growth of NaCl and KCl at high-coverage on Cu (311) shows the same overall structural features [18].

1.4 Applications of thin insulating layers

Insulating thin films on metals are key ingredients in numerous applications, e.g., microelectronics, catalysis, energy generation, and plasmonic sensors. As well, they are central in many fundamental research fields, notably in surface science [20], where they serve as model templates and atomically controlled spacers, for the manipulation of molecules [7], [21]–[28] or individual atoms [29].

1.4.1 Single molecule manipulation

Thin insulating films play an important role for controlling the charge state of individual adsorbed molecules. These films can be used for their specific adsorption properties or for their electronic decoupling effect between the adsorbed molecules and the metallic substrate [23]. These thin films enable the study of fundamental phenomena at the single molecule level, such as electron transfer between two redox centres, or to develop new charge manipulation schemes, such as triggering the mechanical motion in a molecule by electron injection [23].

Ultrathin films of NaCl have been used to decouple individual molecules of pentacene from the metallic Cu(111) substrate in order to study the electronic properties of individual pentacene molecules as illustrated in Fig. 1.9(a-b) [21], and to study the manipulation of a Single Redox Molecular Switch adsorbed on a NaCl bilayer grown on Cu(111) by using Scanning tunnelling microscopy and dynamic force microscopy in non-contact mode as shown in Fig. 1.9(c-d) [23]. The manipulation of a molecular switch performed on metal surfaces has been studied in detail [23]. When a molecule is adsorbed onto a metal surface, its orbitals are not only influenced and broadened by a direct coupling to the electronic states of the substrate, but there is also a mutual electronic coupling of different molecular states through the surface [21].This effect usually results in such a strong distortion of the molecular states that there is hardly any resemblance to the native orbitals of the free molecule [21]. Therefore, to understand the electronic properties of an individual

molecule in mesoscale devices and for monomolecular electronics, an electronic decoupling of the molecules from the supporting substrate is therefore desirable, if not mandatory [21].

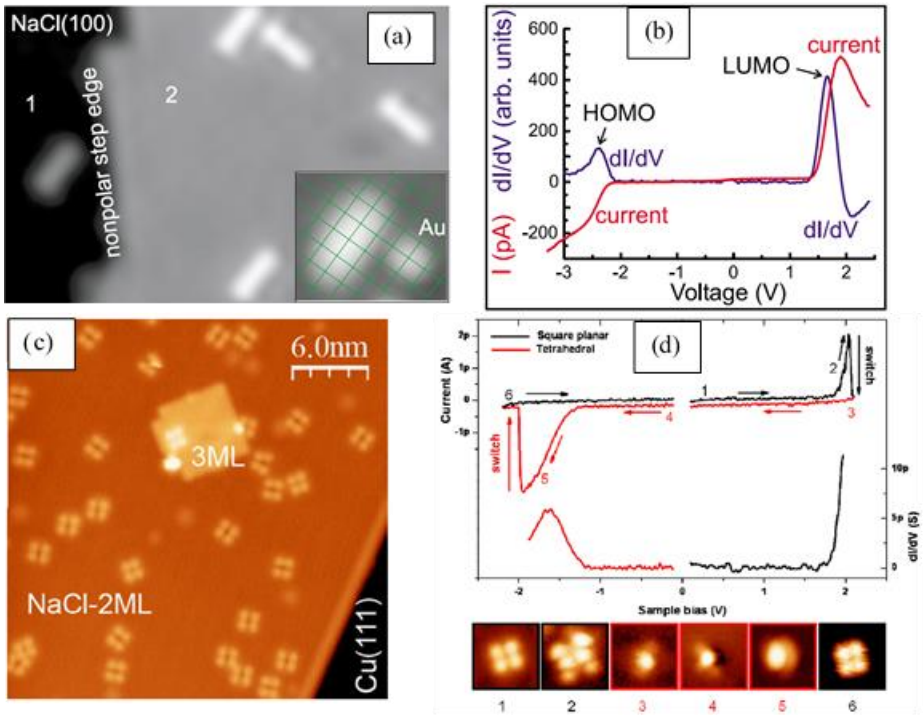

Figure 1.9: Top [reference [21]]: (a) Pentacene molecules on one and two layers of NaCl on Cu(111).(b) dI/dV spectroscopy at the center of a pentacene molecule on NaCl [21]. Bottom [reference [23]] (c) STM images of $Cu(dbm)_2$ on a bilayer of NaCl on Cu(111). (d) I(V) and dI/dV spectroscopy curves obtained on the SP (black lines) and the Td (red line) species [23].

As STM relies on the non-zero conductance of its tunneling junction to produce an image, the majority of the STM studies of individual molecules have so far been limited to molecules on metals or semiconductors. In these cases, the electronic structure of the molecules is strongly perturbed by the presence of the substrate electrons [21]. Therefore to allow the inherent electronic properties of individual molecules to be studied by using STM the insulating films should have a thickness of only a few atomic layers on a metallic substrate, which provides sufficient electronic decoupling of the organic molecules. At the same time, the electrons can still tunnel through the ultrathin insulating films, allowing imaging with the STM at a low tunneling current [21].

Figure 1.9(c-d) shows the manipulation of a single redox molecular switch using STM and STS measurements in order to study the electronic structure of this molecule [23]. By varying the bias voltage, the molecule switches from a square-planar (SP) (black line) to a 3D tetrahedral (Td) geometry (red line). As the voltage is increased, the images in 1.9 (d) show the change in lateral dimensions and the increased height of the molecules. These features are attributed to molecular ion resonances, which dominate the spectrum because the NaCl bilayer partially decouples the molecule electronically from the metallic substrate [23].

1.4.2 Spectroscopy of Molecular layers

Thin insulating films also play an important role in the morphology of epitaxial layers of molecules [7], [27], [28]. The charging effects of electrons can be avoided by using thin epitaxial layers of insulators on semiconductor or metal substrates [27]. For instance, NaCl, KCl, and KBr can be deposited in the form of (100)-terminated layers on a number of metals. These thin epitaxial films exhibit the chemical surface properties of the respective bulk insulators but charging effects can be avoided, since the electrons can tunnel into the underlying conducting substrate. Evidently, the spectroscopy of large organic molecules on insulating surfaces is highly interesting and complementary to that on metal surfaces. One reason is that due to the weaker interactions with the substrate compared to metal substrates, the intrinsic molecular states and intermolecular interactions are dominant and hence can be studied. A second reason is the technological relevance of the organic/insulator interface, e.g., for organic field-effect transistors. So far, mostly thin alkali-halide films on metals have been used for this purpose [27].

NaCl films are promising substrates to tailor molecular nanostructures with the aim of adjusting their shape dependent properties [7]. For example, they have been used as seedlayers to grow 2D molecular domains of PTCDA (3,4,9,10-perylene-tetracarboxylic-dianhydride) on metal surfaces or as a substrate to grow 3D molecular clusters [7], or to study the stable and metastable phases of the PTCDA grown on epitaxial NaCl films on Ag(001) [27], and finally to decouple PTCDA from the metallic substrate of Ag(111) in order to study the electronic structure of PTCDA monolayers using STM and STS measurement [28].

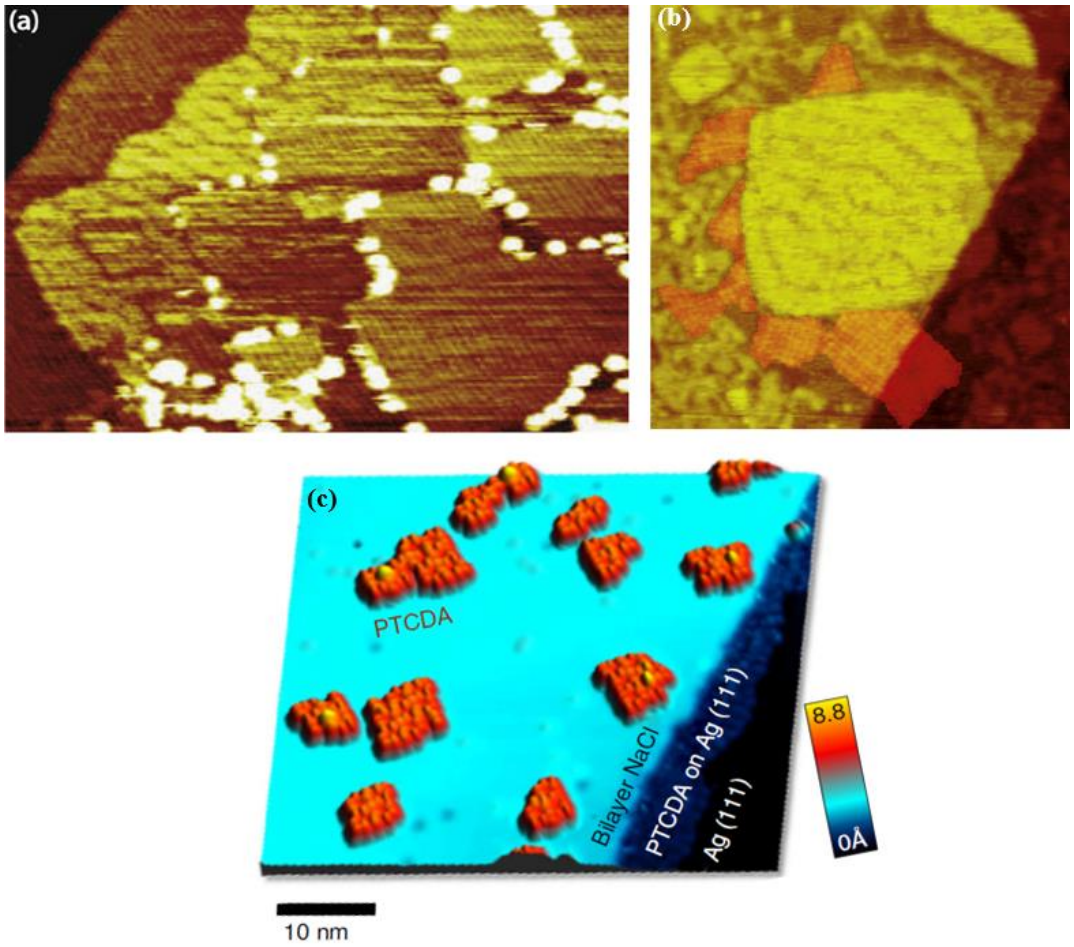

Figure 1.10: (a) PTCDA deposited on an Au(111) surface fully covered with NaCl layers (PTCDA molecules form 3D clusters at the edges of NaCl multilayers). (b) PTCDA and NaCl islands on Au(111) surface (PTCDA grow 2D molecular domains on metal surfaces and nucleate at NaCl island step edges) [7]. (c) STM imaging and structure of PTCDA 2D clusters on NaCl (2 ML)/Ag(111)[28].

In the case of PTCDA nanostructures on Au(111)- $(22\times\sqrt{3})$ covered with NaCl islands [7], the STM images in Fig. 1.10(a-b) show that PTCDA islands grow on Au(111) and preferentially nucleate at the NaCl island step edges. At high NaCl coverage, PTCDA molecules form 3D clusters decorating the step edges of the NaCl(100) islands, as shown in Fig. 1.10(a) [7]. PTCDA molecules prefer to form 3D clusters rather than 2D layers on the NaCl(1 0 0) thin film surface, this is in contrast with what has been reported in reference [28], where PTCDA grows as layers or differently shaped nanocrystals on the (100) surface of a NaCl single crystal, shown in Fig. 1.10(c). This

highlights that the experimental conditions and the NaCl(100) surface preparation are key parameters driving the PTCDA growth on NaCl.

Using a thin film of NaCl allows the energy levels of electronic states to be probed with sub-molecular spatial resolution using STS. This reveals the influence of the abrupt change in the local chemical and electrostatic environment at the edges of the nanoislands [28]. The ability to study large systems via an analytical model, where the electronic polarization plays a dominant role, opens up the possibility of studying realistic interfacial systems, including the effect of disorder, by determining only the position, orientation and anisotropic polarizability of the molecular components [28].

A compact and highly ordered monolayer of PTCDA on thin epitaxial NaCl constitutes an ideal system to study the intermolecular interactions in an extended two-dimensional organic film by surface-sensitive probes involving electrons, since charging effects, present on bulk NaCl(100), are avoided. The presence of differently ordered structures makes this system especially interesting, notably for investigating the correlations between the intermolecular structural order and the electronic and/or optical properties of ultrathin organic films [27].

1.4.3 Single ion manipulation

Stabilizing the charge states of atoms and molecules, as well as controlled charge-state manipulation, is of great interest in the framework of molecular electronics and is a prerequisite for single-electron-transport experiments on insulating films. It seems perfectly natural to employ bulk insulators and bulk-like insulating films for these purposes, whereby charge states can be intrinsically stabilized by the suppression of the charge transfer with the substrate [29]. Controlled manipulation of the charge state of single atoms and molecules is hampered by technical issues on these substrates and has yet to be shown. Perhaps the most severe difficulty is that scanning tunneling microscopy (STM) is ruled out by the insulating nature of the samples. So far, charge-state manipulation has been shown only for single atoms and molecules on bi- and trilayer NaCl films, on which STM operation is enabled by a sufficiently high tunneling probability through the film and the charge states are stabilized by large ionic relaxations of the NaCl film. In contrast to charge stabilization on bulk insulators, the charge-state-stabilization mechanism on thin films with

a non-zero tunneling probability depends strongly on the specific properties of the adsorbate, film, and substrate, and only selected charge states can be stabilized [29].

The charge-state manipulation of single Au adatoms on 2–11 monolayers (ML) thick NaCl films on Cu surfaces (Au/NaCl/Cu) has been studied by attaching or detaching single electrons via the tip of a conducting atomic force microscope (AFM) as shown in Fig. 1.11 [29]. This study provided a direct determination of the ionic relaxation energy of charged, adsorbed single atoms, as well as the relaxation energy of single molecules. On Cu(100) and Cu(111), charge tristability of Au adatoms can be achieved independently of the NaCl layer thickness, where in contrast, on Cu(311), only Au anions are stable on the thinnest NaCl films, but neutral and positive charge states become sufficiently long lived on films thicker than 4 ML to allow conducting AFM-based charge-state-manipulation. However, the lifetime of the metastable neutral and positive states increases by 2 orders of magnitude per NaCl layer due to a reduction of the tunneling probability through the film. On NaCl (5 ML)/ Cu(311), their lifetime is of the order of an hour, long enough to permit AFM-based charge-state manipulation experiments [29].

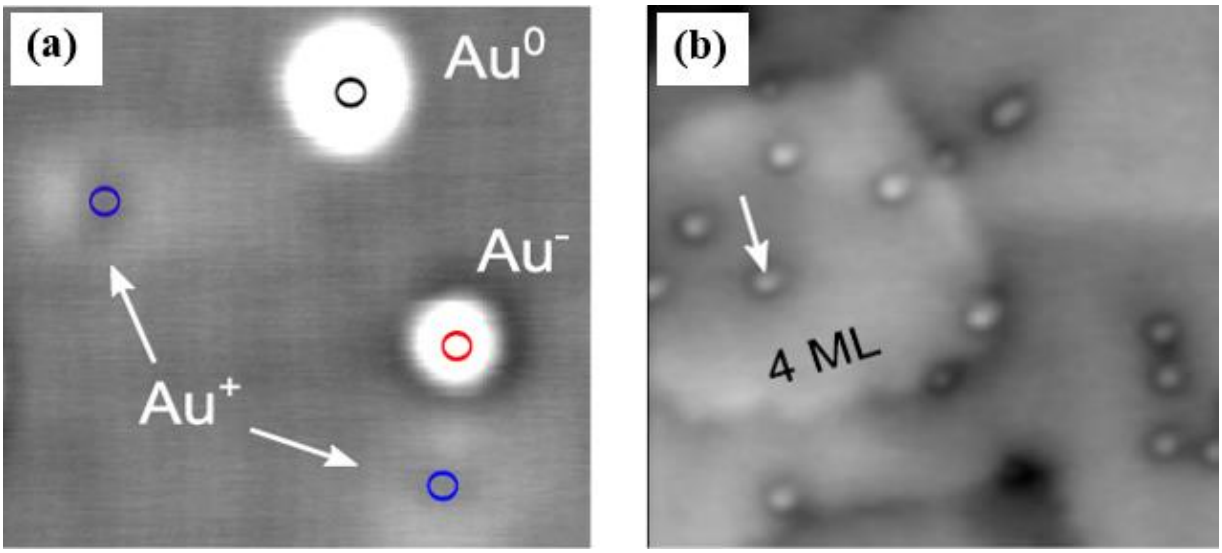

Figure 1.11: (a) STM image of Neutral, positively charged, and negatively charged Au adatoms on a NaCl(2 ML)/Cu(100) film, (b) STM topography image of Au^0 state on NaCl (4 ML)/Cu(311) indicating the position of the tip during data acquisition [29].

1.4.4 STM– induced light

Dipole formation and luminescence quenching close to the metal surface are well-known phenomena, and to a large extend are responsible for the poor performance and efficiency of most organic devices [16]. Due to their ability to form extended homogeneous ultrathin dielectric layers, alkali halides are promising candidates to minimize such phenomena at the metal/organic interface by acting as spacer layers [16].

Concerning-optical excitation, so far this has been less successful for a variety of reasons. On metal surfaces, strong coupling of states to the metal leads to substrate induced-quenching of the molecular fluorescence. On insulators, often unwanted dewetting and clustering of the molecules occurs, and structural control by surface-sensitive techniques using electrons is impossible due to charging effects [24]. A thin insulating film as a spacer to decouple the molecule from the metallic substrate has been used both for manipulation of the molecules and also to enable the optical investigation of these molecules.

Ultrathin films of NaCl have been used to investigate the excitation of molecular fluorescence using the tunnelling current of the scanning tunnelling microscope [25], [26], [30] of individual molecular dimers composed of a magnesium phthalocyanine and a free base phthalocyanine (MgPc and H_2Pc), where MgPc, H_2Pc, and CO molecules are co-deposited on an ultrathin NaCl(100) film grown on Ag(111) [25]. Other examples include the luminescence of zinc phthalocyanine molecules (ZnPc) on NaCl/Ag(001) are shown in Fig. 1.12 [26], and the electroluminescence from C_{60} nanocrystals formed on a NaCl ultrathin film grown on Au(111) [30], Finally, the optical emission and excitation spectra of PTCDA adsorbed on NaCl (100) on Ag(001) were measured on individual monomers and also on two epitaxial monolayer phases (Q and HB*) [24].

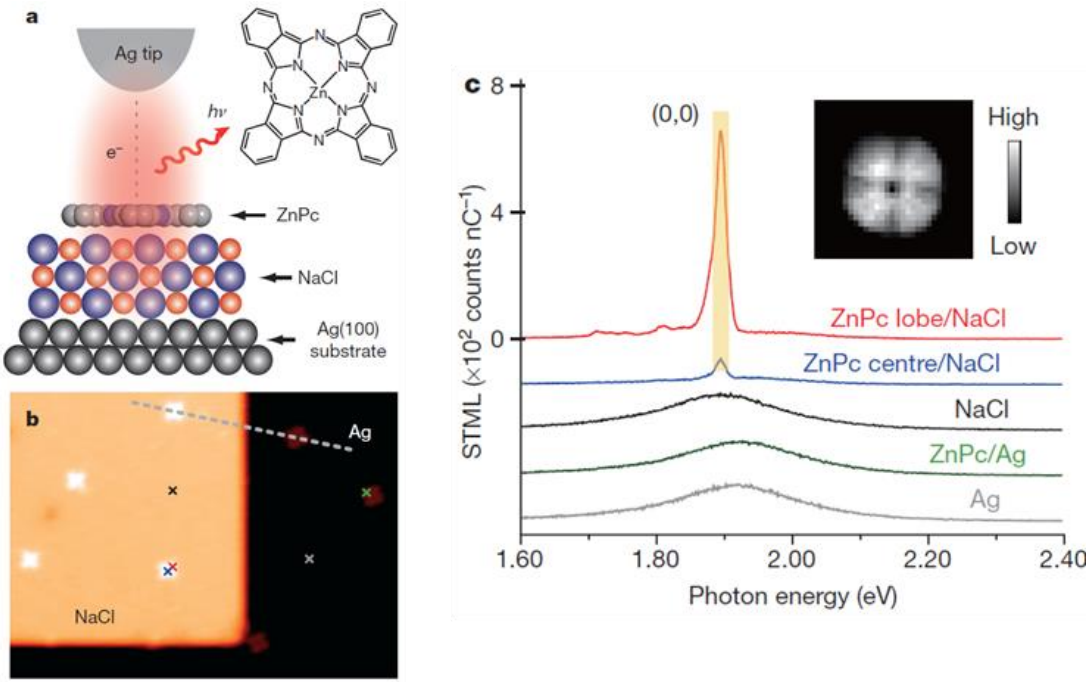

Figure 1.12: Single-molecule electro-luminescence through electronic decoupling and nanocavity-plasmon enhancement. (a) Schematic of STML from a ZnPc molecule on NaCl/Ag(001). Inset, ZnPc molecular structure. (b) STM image showing isolated single ZnPc molecules adsorbed on either a three-monolayer NaCl island or bare Ag(001). (c) STML spectra acquired at the positions marked within b [26].

The realization of molecule-specific exciton emission from single molecules requires the use of an ultrathin NaCl layer to electronically decouple molecules from the metallic substrate. To observe excitation emission involves enhancing the spontaneous emission by resonant nanocavity plasmons [26]. In this context, efficient decoupling of the emitter from the metallic substrate through the thin NaCl spacer layer is crucial to facilitate the observation of the coherent dipole–dipole coupling [26]. Figure 1.12(a-c)) show images of single ZnPc molecules adsorbed on a three-monolayer NaCl island and on the bare Ag(001) surface. The ZnPc molecules appear as four-lobe shapes (see Fig. 1.12(b)). Excitation of the adsorbed molecules through injection of electrons from the STM tip generates detectable single-molecule fluorescence only in the case of the decoupled ZnPc molecules. The spectra provide detailed spatial information on the coherent dipole–dipole

coupling in molecular systems, furthering our understanding and rational engineering of light harvesting structures and quantum light sources [26].

1.5 Reactivity of Alkali Halides upon Electron Irradiation

Electron-induced modification of alkali halides may be envisaged as a way to engineer a surface at the atomic scale. The electron-induced dissociation of alkali halides has been attributed to the substitution of halide ions with incident electrons, a process that is also at the origin of color centers (i.e., light absorbing defects) in NaCl crystals [31]. This effect, which is known to occur over a broad energy range, could be used to engineer areas within insulating layers. Numerous studies on the dissociation of thick and bulk films of alkali halides under electron irradiation and photon irradiation using Auger electron Spectroscopy (AES), low energy electron diffraction (LEED), reflection high energy electron diffraction (RHEED), and reflected electron energy loss microscopy (REELM) have been reported [31]–[40].

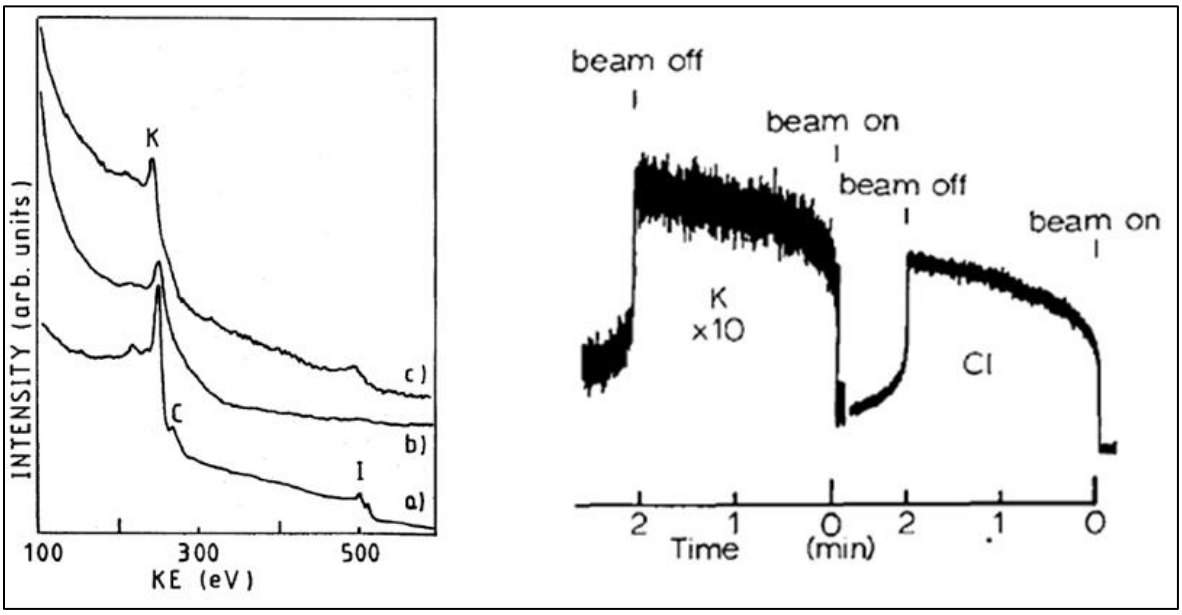

Figure 1.13: (left) Auger spectra of KI analyzed in the following conditions: (a) as-deposited, T=300K; (b) after electron irradiation, T= 300 K; (e) after electron irradiation, T= 460 K [33]. (right) Time-dependent desorption of K and Cl from (100) KCl at room temperature due to 800 eV electron bombardment [31].

The left hand image in figure 1.13 shows an ASS (Auger Survey Spectroscopy) image of the chemical changes produced by electron irradiation of the surface of KI [33], and the right hand image shows observations of the electron stimulated dissociation of the KCl surface as a function of time [31].

The dissociation of sodium chloride (NaCl) upon electron irradiation has been observed within different energy ranges, in low energy electron diffraction (LEED) and Auger electron spectroscopy (AES), reflected electron energy loss microscopy (REELM), and reflection high-energy electron diffraction (RHEED) experiments [31]–[33]. Figure 1.14(a-e) shows the RHEED patterns of the dissociated NaCl (111) surface and Auger electron spectra of the NaCl (111) surface taken during continuous electron bombardment [32].

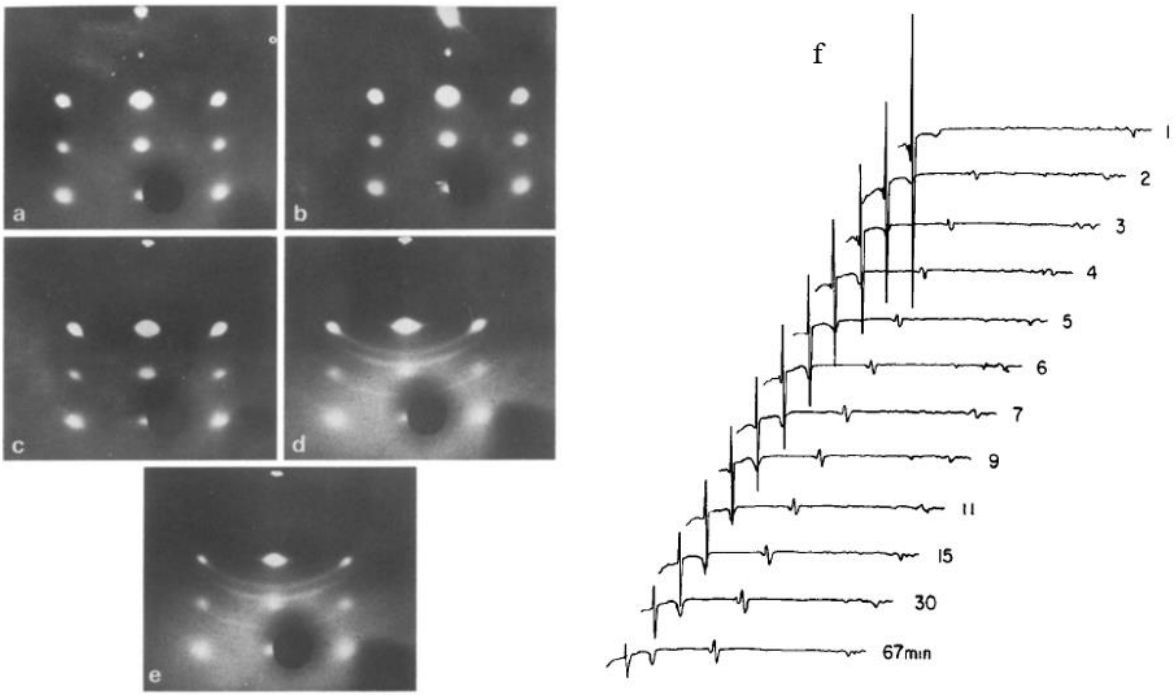

Figure 1.14: RHEED patterns of freshly evaporated NaCl (111) surface (a) and of the same surface after electron bombardment for (b) 10 min (c) 30 min (d) 60 min (e) 90 min [32]. (f) Auger electron spectra of NaCl (111) surface taken during continuous electron bombardment. Scan start times which are equal to the total bombarding time are indicated next to spectra [32].

It has been observed in most of the studies on the dissociation of the thick films and bulk alkali halides that incident electrons induce defects in the bulk (halogen vacancies and interstitial halogen atoms), which may diffuse to the surface where the halogen atoms are ejected out of the plane and the alkali metal atoms diffuse before forming aggregates of metallic clusters [32], [37], [41]. These defects (holes) that are produced on the top layer of the surface reveal an underlying surface that is of the same composition and structure.

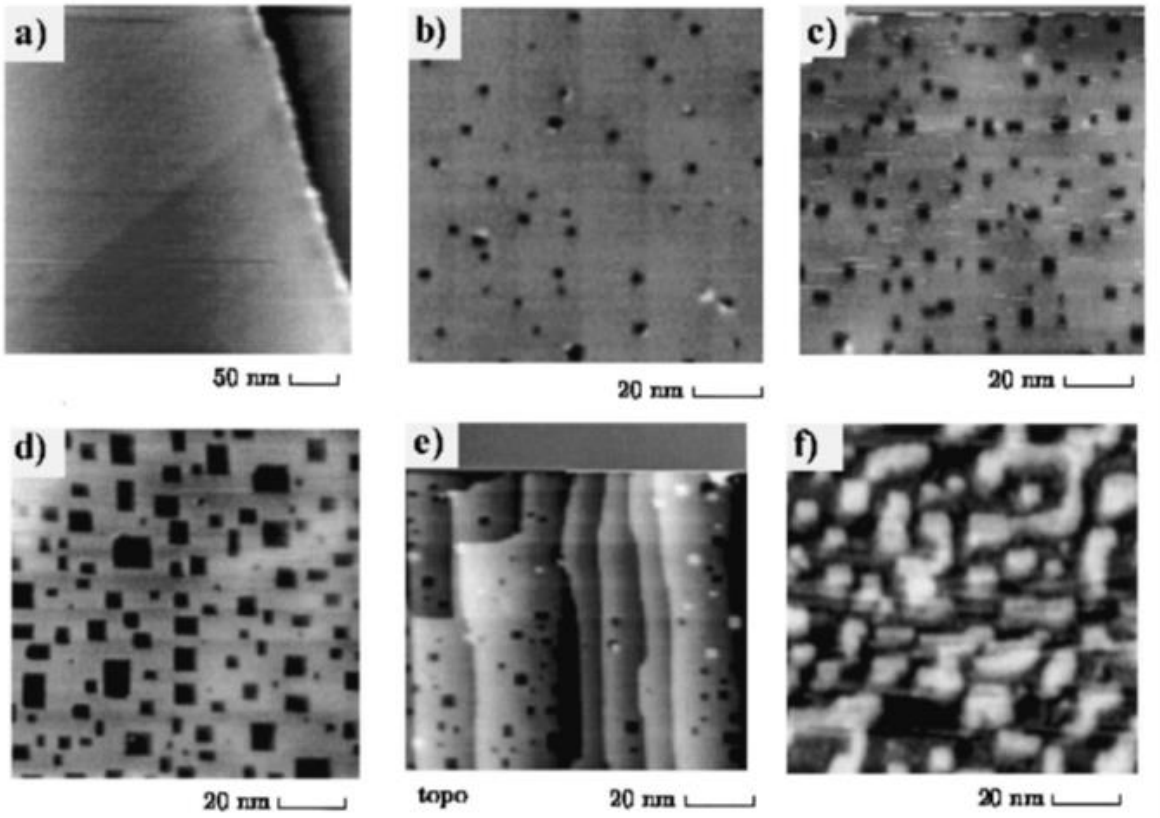

Figure 1.15: NC-AFM images of cleaved KBr surface: (a) as-cleaved (b) irradiated with an electron dose of ~ 4 μC/cm^{2,} (d) irradiated with a dose of ~ 8 μC/cm^2 (e) irradiated surface region with high initial step density, (f) surface irradiated with a dose of 8 μC/cm^2 [37].

The AFM images in Figs. 1.15 and 1.16 show randomly dispersed rectangular holes with a depth of one monolayer, where the edges of these holes are oriented along the main crystallographic directions of the (001) plane, which is always noticeable, in the AFM measurements [34]–[39]. The studies suggest that electron induced desorption of alkali halide surfaces essentially leads to

halogen atom removal, similar kinetics and desorption fluxes have been reported for halogen and alkali metal atom desorption [31], [32], [34], [37].

The left image in figure 1.16 shows a typical mass spectrometry (MS) signal of K and Br atoms desorbed from a KBr crystal irradiated with 1 keV electrons as a function of the irradiation time [34]. It can be seen that both K and Br signals exhibit an oscillatory behavior. The alkali component starts at a low value of the desorption rate and rises quickly, whereas the halogen component starts at a much higher rate, but then decreases rapidly and, after some seconds, follows the alkali rate. Figure 1.16(a-c) demonstrates that the oscillations of the K and Br yields are correlated with periodic changes of the surface morphology [34].

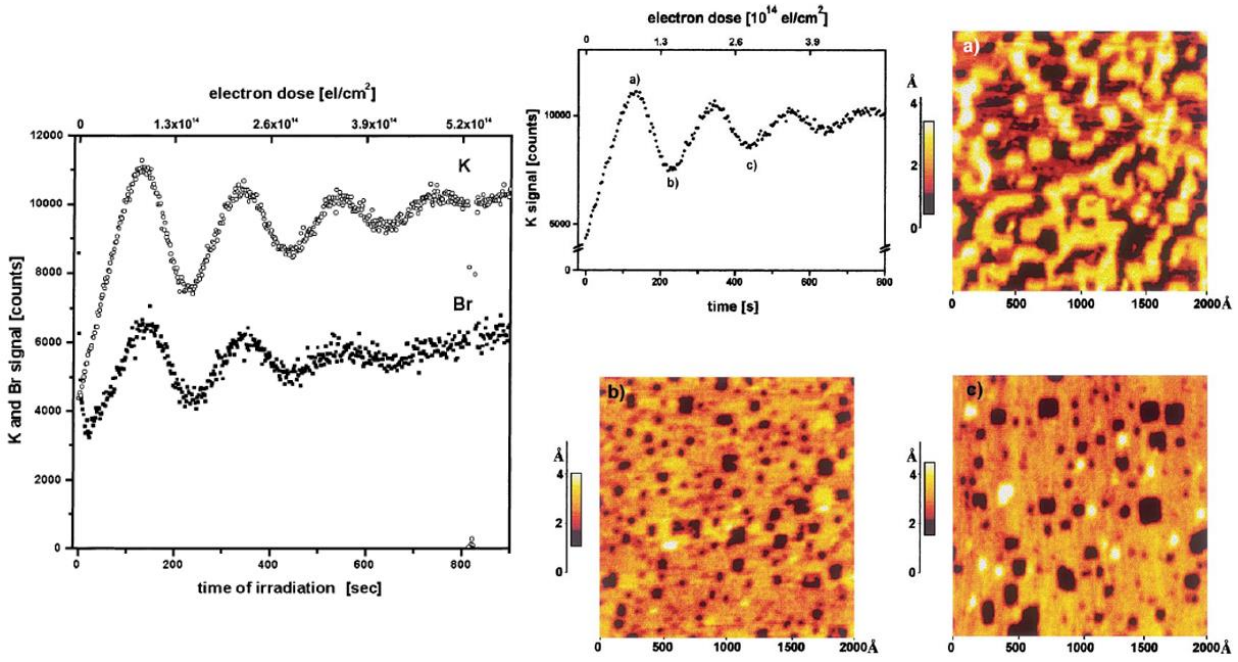

Figure 1.16: (Right): Topography-dependent desorption of KBr. Plot of oscillating mass spectroscopy K signal is shown together with NCAFM images of KBr(001) surface at different stages of irradiation indicated on plot: (a) represents image was taken at first maximum of signal, (b) and (c) are imaged at first and second minimum of signal, respectively [34]. (left): Topography-dependent modulation of desorption yield. MS signal of K and Br atoms desorbed from KBr crystal with 1 keV electrons [34].

This observation has been explained by surface diffusion of alkali metal atoms to the step edges of the alkali-halide surface, where electron-stimulated desorption of alkali metal atoms is more efficient [35]–[37]. As a result, the desorption of alkali-halides occurs in a layer-by-layer mode by the growth and linking of the rectangular holes of monolayer depth in the topmost layer which results in a periodic variation of the step density with a period corresponding the removal of one atomic layer. The periodic change from the lowest value, coincides with the removed of the whole layer, whereas at the highest value, exactly half of the layer has been removed [34], [35], [37]. In this case, the thick film and the bulk crystal of alkali halide can be considered as an infinite reservoir of molecules to dissociate. In addition, in order to model the oscillation that is observed during the desorption of bulk alkali-halide, damped oscillator functions have been used [39].

In other experiments, different kinetics have been reported for thick NaCl (111) films grown on mica [32]. From the AES measurement, it was found that the Cl concentration varies as a logarithmic function of the electron irradiation time. This behaviour was interpreted as an Elovitch-type mechanism (i.e., a standard model for chemisorption), where the activation energy for dissociation is concentration dependent. The argument for this interpretation is that the increasing surface concentration of alkali metal atoms creates disorder, which slows down the dissociation of further alkali-halide molecules.

On the other hand, high desorption yields have been observed in all the studies that have been made on bulk crystals and thick films of alkali-halide as compared to the thin film of this material, e.g. desorption yields of 8 molecules per single 1 keV electron at a sample temperature 423 K and 12 molecules per electron at 573 K were reported for thick (> 150 A˚) NaCl films on GaAs(001) [42]. As well, Cl and Na desorption yields from 1.7 (at 308 K) up to 12.3 atoms (at 480 K) per 1 keV electron were retrieved from combined AFM and mass spectrometry measurements on a cleaved NaCl(001) crystal surface [34]. Similar yields (7.3 atoms per electron) were found for Br desorption from irradiated KBr(001) surfaces [35].

However, few studies have been made to investigate the dissociation of ultrathin films of alkali halides i.e. a few atomic layers in thickness [42]–[44]. It has been observed that exposing the surface of NaCl/Ag(110) to the low energy electron beam (LEED) dissociates NaCl and gives rise to an ordered Na structure (Cl desorption from the surface while Na remains) [43]. Figure 1.17

shows the transformation of thin NaCl films within a few minutes into 2D periodic arrays of sodium atoms adsorbed on silver [43]. These periodic arrays exhibit the same atomic arrangements as observed when sodium is directly evaporated onto Ag(110) [45], [46].

In our work, we studied the reaction kinetics of ultrathin NaCl films grown on Ag(001) upon irradiation with the electron beams of a LEED (50-60 eV) and an AES (3 keV). We observe that Cl depletion follows different reaction kinetics, as compared to previous studies on NaCl thick films and bulk crystals. Na atoms produced from NaCl dissociation diffuse to the bare areas of the Ag(001) surface, where they form Na-Ag superstructures that are known for the Na/Ag(001) system.

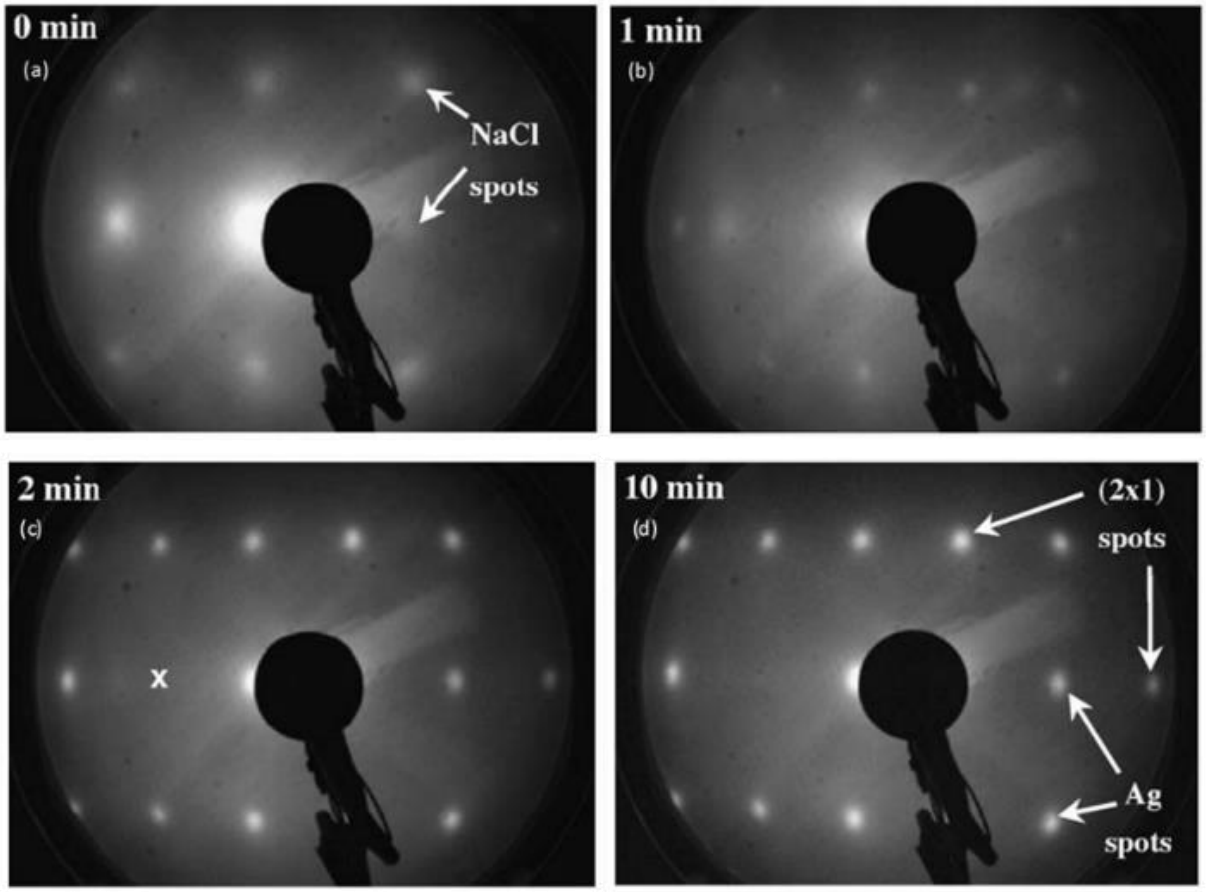

Figure 1.17: LEED pattern of a 10 ML NaCl film deposited on Ag (110) recorded in the very first moments (a) and its evolution as a function of LEED analysis or electron exposure time: (b) 1 min, (c) 2 min and (d) 10 min. All patterns were recorded at 63 eV electron energy [43].

1.6 Conclusion

- **Growth thin insulating film on fcc metals**

Previous studies showed that the growth of NaCl films on several metal substrates follows an island growth mode, whereas in the case of KCl layer-plus-island growth is formed and has a carpet-like growth mode. The initial growth process of these films (1 or 2 ML) is a subject of controversy. This is probably due to the different preparation conditions such as the substrate temperature or the technique used to measure the thickness (e.g. STM height does not give the real height). In addition, the interaction of the NaCl with the metal may differ from one metal to another. The studies also showed that the sizes of the domains formed of insulating films depend on the substrate temperature during deposition, where by increasing the temperature, the sizes of the domains increase and their density decreases, whereas the thickness remains constant.

Furthermore, the NaCl domains have different azimuthal orientations and non-polar edges, which give a variety of orientations for the NaCl island edges with respect to the substrate axes. The growth orientation is independent of the direction of the substrate step. In addition, a Moiré pattern was also observed in the NaCl film growth on different substrates due to the mismatch in the lattice constants between the NaCl adlayer and the substrate. On the other hand, the atomically resolved images on NaCl film showed that only one type of ion was imaged which could be attributed to the anion Cl^-, with the Na^+ being completely invisible.

Finally, the apparent layer thickness of the grown NaCl layer measured by STM at different bias voltage shows that these thicknesses are bias dependent. This has been explained by image potential states (IPSs) measurement on the insulating film and the metal substrate.

- **Application of thin insulating layers**

It has been reported that thin insulating films play an important role for controlling the charge state of single adsorbed molecules. These films can be used for their specific adsorption properties or for their electronic decoupling effect between the adsorbed molecules and the metallic substrate. Thin insulating films also play an important role in the morphology of epitaxial layers of molecules. The charging effects of electrons can be avoided by using thin epitaxial layers of

insulators on semiconductor or metal substrates. Therefore, they serve as model templates and atomically controlled spacers, for the manipulation molecules or single atoms. Moreover, on insulating surfaces, large molecules exhibit luminescence, unlike on metal surfaces since strong coupling of molecular states to the metal lead to a quenching of the excitations occurs.

- **Reactivity of alkali halides upon electron irradiation**

Electron-induced modification of alkali halides may be envisaged as a way to engineer a surface at the atomic scale. The dissociation of sodium chloride (NaCl) upon electron irradiation has been observed within different energy ranges. It has been observed in most of the studies on the dissociation of the thick films and bulk alkali halides that incident electrons induce defects in the bulk (halogen vacancies and interstitial halogen atoms), which may diffuse to the surface where the halogen atoms are ejected out of the plane and the alkali metal atoms diffuse before forming aggregates of metallic clusters. These defects (holes) that occur on the top layer of the surface reveal an underlying surface that is of the same composition and structure.

However, only a few studies have been made to investigate the dissociation of ultrathin films of alkali halides i.e. a few atomic layers in thickness. It has been reported that thin films of alkali halides upon electron irradiation behave differently because of the limited amount of reactants and the interactions with the substrate, thus leading to different reaction kinetics and products, compared to thick films and bulk crystals.

1.7 Bibliography

[1] M. Müller, J. Ikonomov, and M. Sokolowski, "Structure of Epitaxial Layers of KCl on Ag(100)," *Surf. Sci.*, vol. 605, no. 11, pp. 1090–1094, 2011.

[2] D. M. Roessler and W. C. Walker, "Electronic Spectra of Crystalline NaCl and KCl," *Phys. Rev.*, vol. 166, no. 3, pp. 599–606, 1968.

[3] Z. J. Chen, H. Y. Xiao, and X. T. Zu, "First principles study of structural, electronic and optical properties of KCl crystal," *Chem. Phys.*, vol. 330, no. 1, pp. 1–8, 2006.

[4] Available from www.openchemistryhelp.blogspot.fr.

[5] Available from www.chemtube3d.com.

[6] W. Hebenstreit, M. Schmid, J. Redinger, R. Podloucky, and P. Varga, "Bulk Terminated NaCl(111) on Aluminum: A Polar Surface of an Ionic Crystal?," *Phys. Rev. Lett.*, vol. 85, no. 25, pp. 5376–5379, 2000.

[7] X. Sun and F. Silly, "NaCl islands decorated with 2D or 3D 3,4,9,10-perylene-tetracarboxylic-dianhydride nanostructures," *Appl. Surf. Sci.*, vol. 256, no. 7, pp. 2228–2231, 2010.

[8] H.-C. Ploigt, C. Brun, M. Pivetta, F. Patthey, and W.-D. Schneider, "Local work function changes determined by field emission resonances: NaCl/Ag(100)," *Phys. Rev. B*, vol. 76, no. 19, p. 195404, Nov. 2007.

[9] G. Cabailh, C. R. Henry, and C. Barth, "Thin NaCl films on silver (001): island growth and work function," *New J. Phys.*, vol. 14, no. 10, p. 103037, 2012.

[10] M. Pivetta, F. Patthey, M. Stengel, A. Baldereschi, and W.-D. Schneider, "Local work function Moiré pattern on ultrathin ionic films: NaCl on Ag(100)," *Phys. Rev. B*, vol. 72, no. 11, p. 115404, Sep. 2005.

[11] E. Le Moal, M. Müller, O. Bauer, and M. Sokolowski, "Misfit driven azimuthal orientation of NaCl domains on Ag(100)," *Surf. Sci.*, vol. 603, no. 16, pp. 2434–2444, 2009.

[12] Q. Guo, Z. Qin, C. Liu, K. Zang, Y. Yu, and G. Cao, "Bias dependence of apparent layer thickness and Moiré pattern on NaCl/Cu(001)," *Surf. Sci.*, vol. 604, no. 19, pp. 1820–1824, 2010.

[13] W. Hebenstreit, J. Redinger, Z. Horozova, M. Schmid, R. Podloucky, and P. Varga, "Atomic resolution by STM on ultra-thin films of alkali halides: experiment and local density

calculations," *Surf. Sci.*, vol. 424, no. 2, pp. L321–L328, 1999.

[14] X. Sun, M. P. Felicissimo, P. Rudolf, and F. Silly, "NaCl multi-layer islands grown on Au(111)-(22× √3) probed by scanning tunneling microscopy," *Nanotechnology*, vol. 19, no. 49, p. 495307, 2008.

[15] J. Kramer, C. Tegenkamp, and H. Pfnür, "The growth of NaCl on flat and stepped silver surfaces," *J. Phys. Condens. Matter*, vol. 15, no. 38, p. 6473, 2003.

[16] C. Loppacher, U. Zerweck, and L. M. Eng, "Kelvin probe force microscopy of alkali chloride thin films on Au(111)," *Nanotechnology*, vol. 15, no. 2, p. S9, 2004.

[17] M. Kiguchi, G. Yoshikawa, S. Ikeda, and K. Saiki, "Electronic properties of metal-induced gap states formed at alkali-halide/metal interfaces," *Phys. Rev. B*, vol. 71, no. 15, p. 153401, Apr. 2005.

[18] A. Riemann, S. Fölsch, and K. H. Rieder, "Epitaxial growth of alkali halides on stepped metal surfaces," *Phys. Rev. B*, vol. 72, no. 12, p. 125423, Sep. 2005.

[19] F. Gao, G. Wu, D. Stacchiola, M. Kaltchev, P. V Kotvis, and W. T. Tysoe, "The Tribological Properties of Monolayer KCl Films on Iron in Ultrahigh Vacuum: Modeling the Extreme-Pressure Lubricating Interface," *Tribol. Lett.*, vol. 14, no. 2, pp. 99–104, 2003.

[20] R. Bennewitz, "Structured surfaces of wide band gap insulators as templates for overgrowth of adsorbates," *J. Phys. Condens. Matter*, vol. 18, no. 26, p. R417, 2006.

[21] J. Repp, M. Gerhard, S. M, A. Gourdon, and C. Joachim, "Molecules on Insulating Films: Scanning-Tunneling Microscopy Imaging of Individual Molecular Orbitals," *Phys. Rev. Lett.*, vol. 94, no. 2, p. 26803, Jan. 2005.

[22] P. Merino, C. Große, A. Rosławska, K. Kuhnke, and K. Kern, "file:///C:/Users/Ala/Downloads/ncomms9461.ris," vol. 6, p. 8461, Sep. 2015.

[23] T. Leoni, O. Guillermet, H. Walch, V. Langlais, A. Scheuermann, J. Bonvoisin, and S. Gauthier, "Controlling the Charge State of a Single Redox Molecular Switch," *Phys. Rev. Lett.*, vol. 106, no. 21, p. 216103, 2011.

[24] M. Müller, E. Le Moal, R. Scholz, and M. Sokolowski, "Exciton and polarization contributions to optical transition energies in an epitaxial organic monolayer on a dielectric substrate," *Phys. Rev. B*, vol. 83, no. 24, p. 241203, 2011.

[25] H. Imada, K. Miwa, M. Imai-Imada, S. Kawahara, K. Kimura, and Y. Kim, "Real-space investigation of energy transfer in heterogeneous molecular dimers," *Nature*, vol. 538, no.

7625, pp. 364–367, Oct. 2016.

[26] Y. Zhang, Y. Luo, Y. Zhang, Y.-J. Yu, Y.-M. Kuang, L. Zhang, Q.-S. Meng, Y. Luo, J.-L. Yang, Z.-C. Dong, and J. G. Hou, "Visualizing coherent intermolecular dipole–dipole coupling in real space," *Nature*, vol. 531, no. 7596, pp. 623–627, Mar. 2016.

[27] E. Le Moal, M. Müller, O. Bauer, and M. Sokolowski, "Stable and metastable phases of PTCDA on epitaxial NaCl films on Ag(100)," *Phys. Rev. B*, vol. 82, no. 4, p. 45301, 2010.

[28] K. A. Cochrane, A. Schiffrin, T. S. Roussy, M. Capsoni, and S. A. Burke, "Pronounced polarization-induced energy level shifts at boundaries of organic semiconductor nanostructures," *Nat. Commun.*, vol. 6, p. 8312, Oct. 2015.

[29] W. Steurer, J. Repp, L. Gross, I. Scivetti, M. Persson, and G. Meyer, "Manipulation of the Charge State of Single Au Atoms on Insulating Multilayer Films," *Phys. Rev. Lett.*, vol. 114, no. 3, p. 36801, Jan. 2015.

[30] E. Ćavar, M.-C. Blüm, M. Pivetta, F. Patthey, M. Chergui, and W.-D. Schneider, "Fluorescence and Phosphorescence from Individual C60 Molecules Excited by Local Electron Tunneling," *Phys. Rev. Lett.*, vol. 95, no. 19, p. 196102, Nov. 2005.

[31] H. Tokutaka, M. Prutton, I. G. Higginbotham, and T. E. Gallon, "The (100) surfaces of alkali halides," *Surf. Sci.*, vol. 21, no. 2, pp. 233–240, 1970.

[32] A. Friedenberg and Y. Shapira, "Electron induced dissociation of the NaCl(111) surface," *Surf. Sci.*, vol. 87, no. 2, pp. 581–594, 1979.

[33] E. Paparazzo and N. Zema, "Reflected electron energy loss microscopy and scanning Auger microscopy studies of electron irradiated alkali halide surfaces," *Surf. Sci.*, vol. 372, no. 1, pp. L301–L308, 1997.

[34] M. Szymonski, J. Kolodziej, B. Such, P. Piatkowski, P. Struski, P. Czuba, and F. Krok, "Nano-scale modification of ionic surfaces induced by electronic transitions," *Prog. Surf. Sci.*, vol. 67, no. 1, pp. 123–138, 2001.

[35] B. Such, P. Czuba, P. Piatkowski, and M. Szymonski, "AFM studies of electron-stimulated desorption process of KBr(001) surface," *Surf. Sci.*, vol. 451, no. 1, pp. 203–207, 2000.

[36] B. Such, J. Kolodziej, P. Czuba, P. Piatkowski, P. Struski, F. Krok, and M. Szymonski, "Surface Topography Dependent Desorption of Alkali Halides," *Phys. Rev. Lett.*, vol. 85, no. 12, pp. 2621–2624, Sep. 2000.

[37] J. J. Kolodziej, B. Such, P. Czuba, F. Krok, P. Piatkowski, P. Struski, M. Szymonski, R.

Bennewitz, S. Schär, and E. Meyer, “Frenkel defect interactions at surfaces of irradiated alkali halides studied by non-contact atomic-force microscopy,” *Surf. Sci.*, vol. 482, pp. 903–909, 2001.

[38] R. Bennewitz, S. Schär, V. Barwich, O. Pfeiffer, E. Meyer, F. Krok, B. Such, J. Kolodzej, and M. Szymonski, “Atomic-resolution images of radiation damage in KBr,” *Surf. Sci.*, vol. 474, no. 1, pp. L197–L202, 2001.

[39] M. Goryl, B. Such, F. Krok, K. Meisel, J. J. Kolodziej, and M. Szymonski, “Atomic force microscopy studies of alkali halide surfaces nanostructured by DIET,” *Surf. Sci.*, vol. 593, no. 1, pp. 147–154, 2005.

[40] T. R. Pian, N. H. Tolk, M. M. Traum, J. Kraus, and W. E. Collins, “Energy dependence of electron stimulated desorption of excited neutral alkalis from alkali halides,” *Surf. Sci.*, vol. 129, no. 2, pp. 573–580, 1983.

[41] T. R. Pian, M. M. Traum, J. S. Kraus, N. H. Tolk, N. G. Stoffel, and G. Margaritondo, “Electron and photon stimulated desorption of positive ions from alkali halide surfaces,” *Surf. Sci.*, vol. 128, no. 2, pp. 13–21, 1983.

[42] M. Szymonski, J. Kolodziej, P. Czuba, P. Piatkowski, P. Korecki, Z. Postawa, and N. Itoh, “Thickness dependent electron stimulated desorption of thin epitaxial films of alkali halides,” *Appl. Surf. Sci.*, vol. 100, pp. 102–106, 1996.

[43] K. Aït-Mansour, M. Bielmann, O. Gröning, P. Ruffieux, R. Fasel, and P. Gröning, “(2×1)-Na surface reconstruction induced by NaCl dissociation on Ag(110) during LEED analysis,” *Appl. Surf. Sci.*, vol. 252, no. 18, pp. 6368–6374, 2006.

[44] J. Kolodziej, P. Piatkowski, and M. Szymonski, “Electron-stimulated desorption of thin epitaxial films of KBr grown on (100)InSb,” *Surf. Sci.*, vol. 390, no. 1, pp. 152–157, 1997.

[45] R. A. Marbrow and R. M. Lambert, “Chemisorption and surface reactivity of nitric oxide on clean and sodium-dosed Ag(110),” *Surf. Sci.*, vol. 61, no. 2, pp. 317–328, 1976.

[46] R. A. Marbrow and R. M. Lambert, “Adsorption and surface structural chemistry of Na and Na + O2 on Ag(110),” *Surf. Sci.*, vol. 61, no. 2, pp. 329–342, 1976.

Chapter 2

Experimental Apparatus and Methods

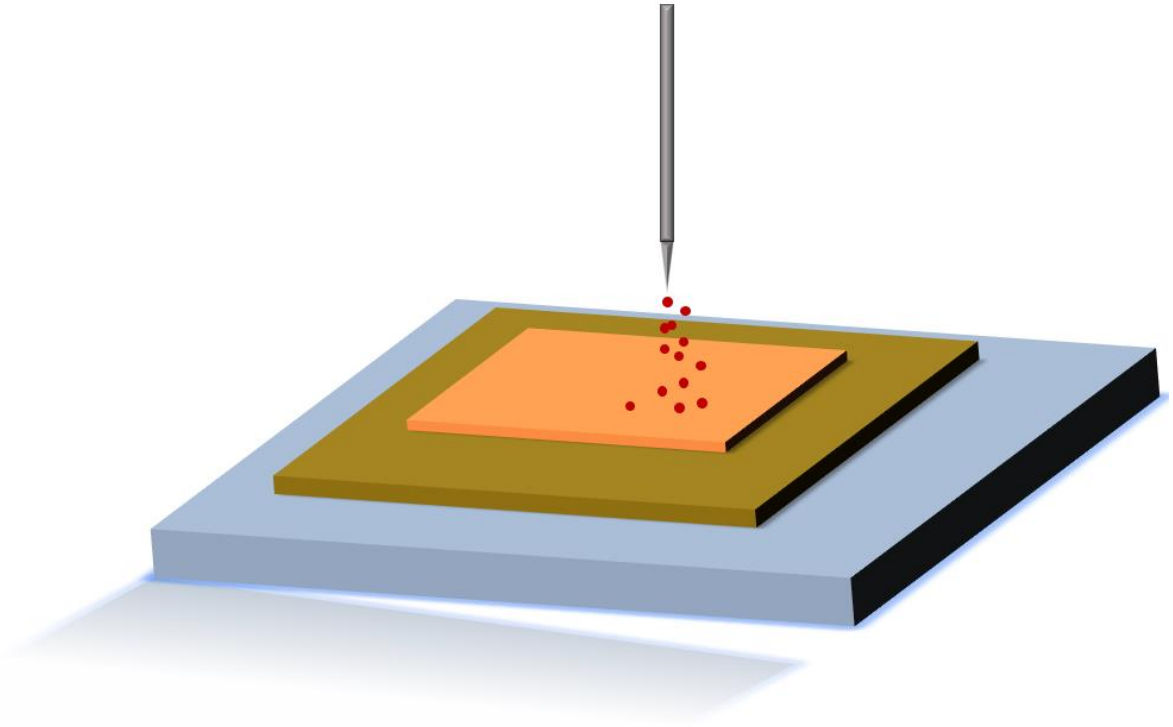

Table of Contents

2.1 Introduction

In this chapter, we describe in detail the two different setups that are used to perform our experiments. As these setups are working in Ultra-High Vacuum (UHV) conditions, we give a short explanation for these conditions. In addition, we mention the materials that are used in our study; the Ag(001) single crystal, NaCl/KCl molecules, and PTCDA molecules. We describe the preparation procedure of the systems studied, which includes the cleaning of the surface, and the evaporation conditions required to obtain thin films of NaCl, KCl, and PTCDA. Finally, we report the basic principles of the techniques that are used for the characterization of the prepared films; low energy electron diffraction (LEED), Auger electron spectroscopy (AES), and scanning tunneling microscopy (STM).

2.2 Experimental setup

The experiments discussed in this thesis were performed under Ultra-High Vacuum (UHV) conditions. Two setups were used: one equipped with a low-temperature scanning tunneling microscope (LT-STM), and the other with a room-temperature scanning tunneling microscope (RT-STM).

2.2.1 Low-temperature scanning tunneling microscope (LT-STM) setup

The LT-STM setup consists of three chambers: (i) a preparation chamber where sputtering and annealing operations were performed. (ii) The analysis chamber where the Auger electron spectroscopy (AES) and low energy electron diffraction (LEED) measurements were made. This chamber also contains a Knudsen effusion cell used for evaporating NaCl and organic molecules in the form of solid powders. (iii) The third chamber contains the Low-Temperature Scanning Tunneling Microscopy (LT-STM). Here, the STM stage is attached to the bottom of the cryostat by a spring which provides a very efficient damping system based on eddy current damping. This system is designed to restrict the vibrations to a minimum and gives the STM stability during scanning. The cryostat is filled with liquid nitrogen to cool the sample down to 77 K. In the LT-STM setup, we investigated the growth of NaCl films on Ag(001) and we studied the dissociation of these films under electron irradiation using the Auger electron spectroscopy (AES) and low

energy electron diffraction (LEED) techniques. The photographs of the LT-STM setup shown in Fig. 2.1.

The back-display LEED spectrometer was purchased from VacGen (Hailsham, UK) and the cylindrical-mirror-analyzer AES from STAIB Instruments (Langenbach, Germany), and the STM from Scienta Omicron.

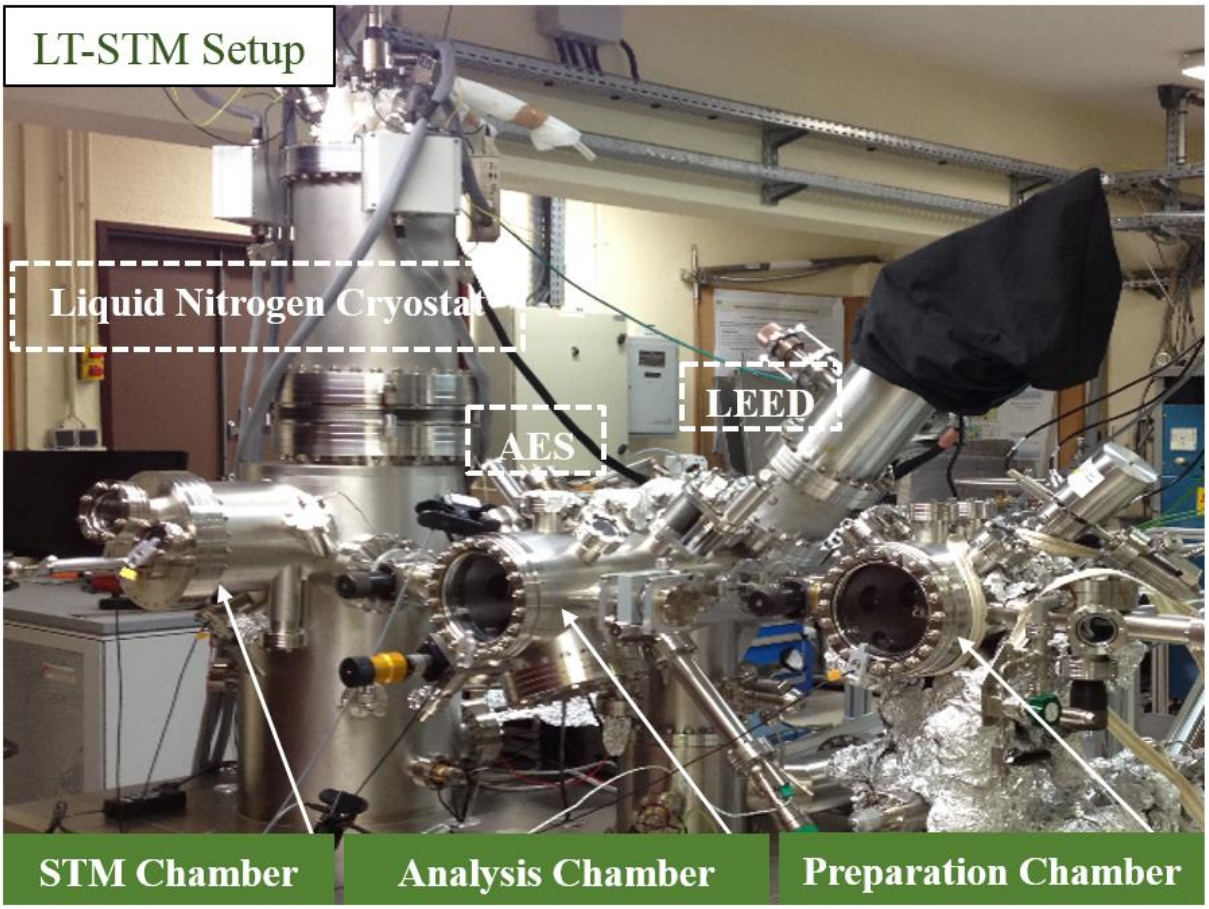

Figure 2.1: LT-STM setup: preparation, analysis, and STM chambers

2.2.2 Room-temperature scanning tunneling microscope (RT-STM)

Figure 2.2 shows the RT-STM setup which consists of two chambers: a preparation chamber with a Knudsen effusion cell used for evaporating NaCl and organic molecules in the

form of solid powders. This chamber is also equipped for sputtering and annealing, and low energy electron diffraction (LEED).

Using the RT-STM setup we investigated the growth of a KCl film on the Ag(001) substrate and the adsorption of perylene-3,4,9,10-tetracarboxylic dianhydride (PTCDA) molecules on the Ag(001) substrate.

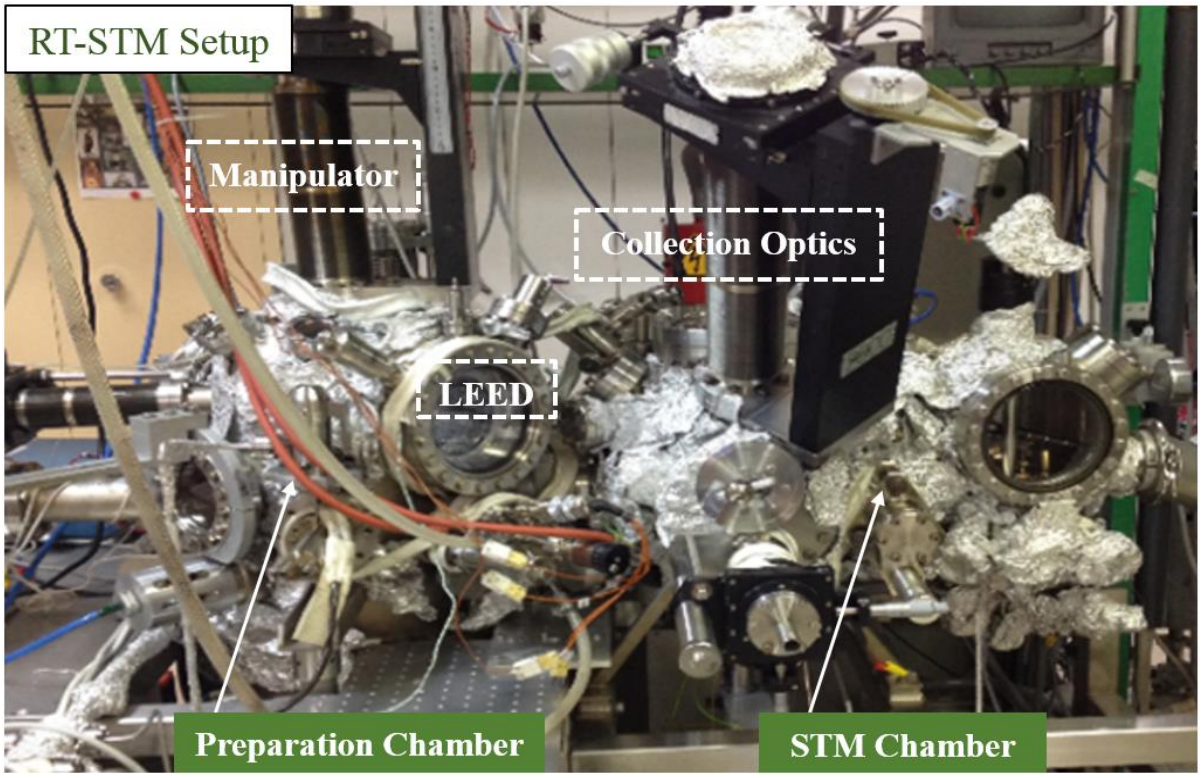

Figure 2.2: RT-STM setup: preparation chamber, STM chamber, and collection optics.

2.3 Ultra-high vacuum (UHV)

Many surface analysis techniques require UHV conditions to maintain the sample in a clean state for study over several days. In such a vacuum, undesirable contamination is negligible which allows a good analysis of the surface in atomically controlled conditions. Working in UHV requires the use of ion pumps, turbo pumps, and bake-out procedures. In our setup, we perform

experiments at pressures 10^{-9} mbar in the preparation chamber, 10^{-10} mbar in the analysis chamber, and between 10^{-10} and 10^{-11} mbar in the STM chamber.

2.4 Preparation procedures

2.4.1 Materials used for study

The Ag(001) single crystals used as substrates are purchased from Surface Preparation Laboratories (Zaandam, The Netherlands). These are hat-shaped cylinders of diameter 8 mm and height 1 mm (where the top of the hat is 6 mm in diameter), (see Fig. 2.3). Their purity grade is 6N. Their surface is aligned to 0.1 degrees and polished (surface roughness is guaranteed at 0.03 microns or better). For the thin film growth, we use sodium chloride (NaCl) and potassium chloride (KCl) powder of 99.999% purity (trace metals basis) purchased from Sigma Aldrich (Saint Louis, MO, USA).

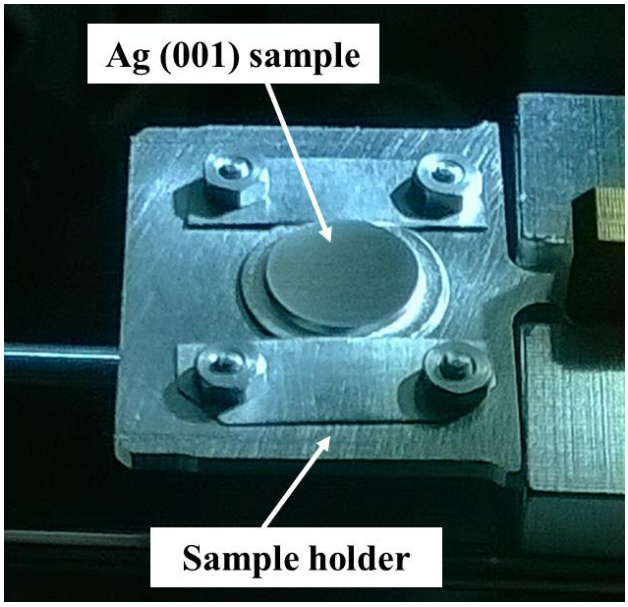

Figure 2.3: shows the Ag(001) single crystals with 6 mm in diameter and the sample holder.

2.4.2 Evaporation of solids

For the deposition of the molecules on the surface, we evaporated the molecules from a Knudsen effusion cell. The Knudsen effusion cell is commonly used in molecular–beam epitaxy to grow molecular layers and thin inorganic films. The Knudsen cell is the ideal method for the deposition of materials and molecules over a temperature range between 150 C˚ and 500 C˚. The deposition rate can be carefully controlled by heating to provide a suitable vapor pressure so that the deposited material gradually cover the surface.

Several cycles of degassing of the molecular source were made to evaporate water and other volatile impurities. The calibration of the deposition temperature for NaCl, KCl, and PTCDA was carried out by monitoring over time, the changes in pressure (with respect to the starting base pressure).

During degassing of the source, the shutter of the evaporation cell was closed, and when the temperature was ramped up to the sublimation temperature, the shutter of the evaporation cell was opened. The parameters to obtain a monolayer of molecules are shown in the table (2.1).

Materials	T_{cell} (K)-start (in LT-STM setup)	P(mbar)-start	Deposition time (min)
NaCl	773	2×10^{-9}	10-40
KCl	778	8.6×10^{-9}	5-11
PTCDA	553	3.4×10^{-10}	30-50

Table 2. 1: Table shows the parameter of deposition of NaCl, KCl and PTCDA in LT-STM setup

It is important to point out that the absolute calibration of the NaCl deposition using a quartz microbalance is hampered by the temperature dependence of molecular sticking factors on surfaces. Indeed, we use STM to assess the local thickness and geometry of the NaCl islands. In addition, the NaCl film thickness gradually decreases when moving away from the center of the silver crystal (because the emission is directional), which provides a supplementary way to explore the thickness effect when conducting the LEED and AES measurements.

2.4.3 Sputtering and thermal annealing

Sputtering

Sputtering is a process which ejects the particles from a solid target material due to the bombardment of the target with energetic ions. This process happens when the kinetic energy of the incoming particles is much higher than conventional thermal energies (>> 1 eV). However, this process can damage the surface if exposures to ion bombardment are prolonged, in which erosion of the materials can lead to the formation of pits and ridges that cannot be fully removed by post annealing. In our case, we used this process for preparing the metallic substrate Ag(100) to remove the contamination and deposited film residues, where we sputtered with Ar^+ ions using the following parameters (Ar^+ ions energy =0.65 eV, the pressure of ions gas ~ 1.5×10^{-5} mbar, sample current ~ 15μA during 30 minutes, while the sample is held at room temperature).

Thermal annealing

We used post-annealed the metal substrate at different temperatures (via indirect heating) for several purposes:

- To remove the contamination on the surface or the residues of the deposited film.
- To recover the atomic order of the surface, which needs a high temperature (annealing the sample up to 775 K during 30 mins).
- To increase the diffusion of the molecules to cover and rearrange themselves on the surface of the silver Ag (100) substrate which increases the quality of the grown film [1], [2].

During the growth of NaCl on Ag(001), two different substrate temperatures (413 K and 500 K) are used, which yielded different film geometries. In the case of the growth of KCl on Ag(001) , the growth temperature are 438 K in the LT-STM setup, and three different substrate temperatures (300-398-473 K) are used for the growth of this film in RT-STM setup. Finally, for the growth of PTCDA on Ag(001) substrate, the sample are annealed after deposition up to 373 K for 20 mins in RT-STM preparation chamber.

2.5 Techniques Used for Characterization

2.5.1 Low Energy Electron Diffraction (LEED)

LEED is a technique used to characterize the surface structure of a single crystal or of a layer adsorbed on a substrate. It provides information on the atomic arrangement and at the unit cell dimensions and orientation. This apparatus consists of an electron gun and a hemispherical fluorescent screen (see Fig. 2.4). The surface structure is probed using an incident beam of low energy electrons (~ 30 - 200 eV) normal to the sample. The electron beam undergoes Bragg diffraction by the surface layers of the crystal which are then projected on a phosphor screen, showing the typical LEED diffraction patterns that correspond to the crystal structure of the sample. The analysis of each spot position on the LEED pattern allows the symmetry and the size of the surface unit cell to be determined, where the spot extinction rules provide information on the symmetry inside the unit cell.

LEED provides Fourier-space information on the surface structure averaged over ~ μm^2 (beam spot), whereas STM provides real-space images and spectra of the atomic scale (local structural and electronic information). The LEED experiment is much easier than STM because STM study needs several conditions such as a good tip, and a good substrate. Hence using LEED before STM helps to check the state or the phase of the surface, to find the right conditions for the coverage of the molecules on the surface, and also to check if the surface of the substrate is clean.

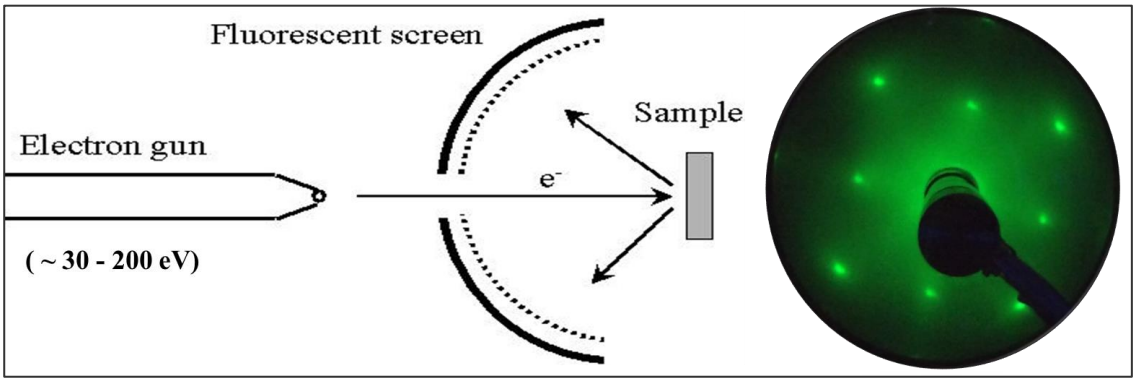

Figure 2.4: Schematic diagram of a LEED

In addition, the electron beams of the LEED and AES can be used to irradiate the sample as in this experiment. In this thesis, the irradiation of the NaCl film with an electron beam of LEED (primary electron energy 52-60 eV) led to several surface reconstructions. This will be presented in detail in chapter 4. Some representative examples of the substrate Ag (100) and NaCl on Ag (100) are shown in Fig. 2.5.

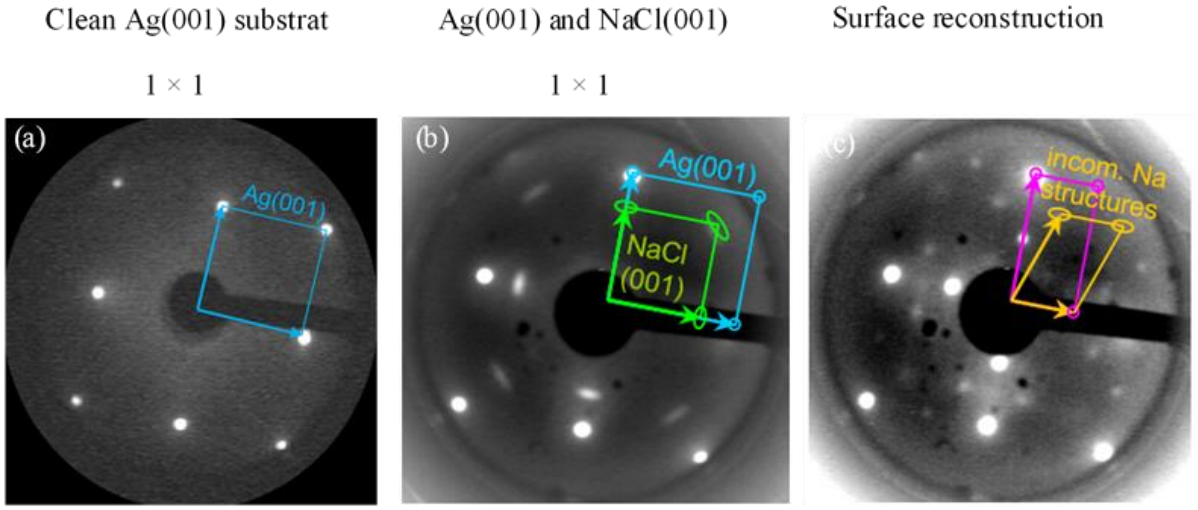

Figure 2.5: (a) LEED pattern of clean Ag(001), (b) and (c) the surface reconstructions after deposition NaCl on Ag(001).

For the thicker film that are grown at 500 K, we subtract the background from the LEED images because the spots were difficult to see. The subtract was done by the liner function taken from the centre to the edges of the LEED image using the ImageJ software.

The LEED images are analyzed using ImageJ (imagej.nih.gov/ij). Graphs are made using the Origin 2016 software (originlab.com/2016). Temporal variations of the LEED spot intensity are retrieved from AVI movies of the LEED back display recorded using a video CCD camera. The AVI files are converted into TIFF image stacks. Areas fitted to the contour of the diffraction spots are selected using the Oval Selection tool of ImageJ and time traces are obtained using the Plot Z-Axis Profile tool.

2.5.2 Auger Electron Spectroscopy (AES)

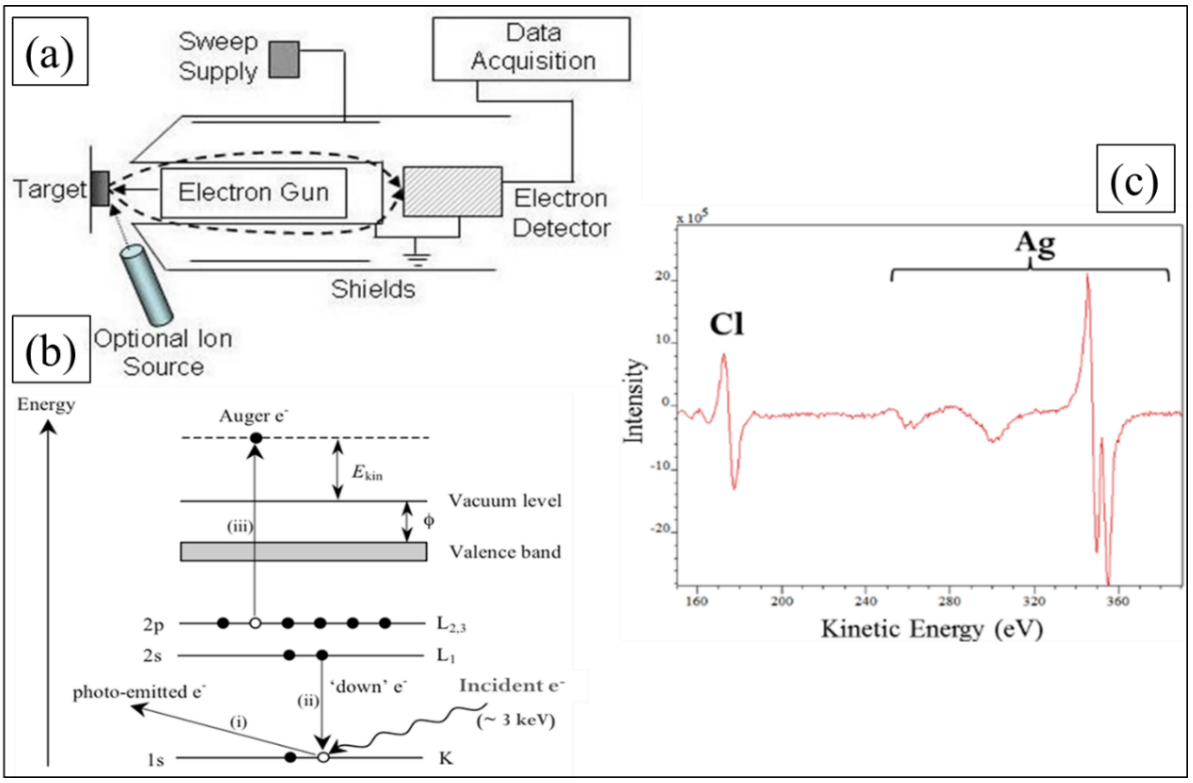

Figure 2.6: (a) Schematic diagram of an AES, (b) Auger process, (c) the spectrum of a thin film of NaCl on Ag(001).

AES is a technique used to determine the chemical composition of the surface of the material. It is based on the Auger process where a high energy electron or photon beam (~3kV) that is incident on a sample causes a series of internal electronic excitation and relaxation events in the excited atoms on the surface. The Auger electrons emitted with different kinetic energies are collected by a detector to generate the spectrum shown in Fig. 2.6. The Auger electron has a specific energy for each element.

In our experiment, we use AES measurement for several purposes, first to check if the surface of the substrate is clean. Second to make semi-quantitative comparisons of the nominal thicknesses of the NaCl films, based on the intensity ratio of the chlorine and silver AES peaks.

To do so, we use the peak-to-peak intensity of the Cl *LV V* and Ag M_4NN Auger lines, which lie at 181 eV and 358 eV, respectively. The Cl/Ag AES peak ratio is taken at time t = 0, i.e. before electron irradiation starts to modify the chemical composition. Finally, AES (3keV) measurement is also used to induce NaCl dissociation and to monitor the structural and chemical modifications of the sample.

2.5.3 Scanning tunneling microscopy (STM)

STM is an atomic scale probe technique used to study the structure and electronic properties of material e.g., imaging the surface of the material with atomic resolution. It was invented by Gerd Binnig and Heinrich Rohrer, and the first images were published in 1982 [2]. STM works in different environments (Air, ultra-high vacuum, water, and diverse liquid or atmospheres) and can be used at different temperatures [3]. The basic components of the STM are a very sharp metallic tip and the surface. Atomic resolution is achieved by a very precise control of the bias voltage, piezoelectric scanner, current amplifier, and the feedback loop (tunneling current) (see Fig. 2.7). This will be presented concisely in the following section.

2.5.3.1 STM principle

The principle of this technique is that the bias voltage is applied between the sample and the tip, so the electrons can tunnel, if the tip is sufficiently close to the surface. The bias determines the direction of the tunneling; a positive voltage applied to the surface induces tunneling from the tip to the surface, while a negative bias induced tunneling from the surface to the tip. This determines whether the local density of occupied or unoccupied electronic states are probed and observed in the STM images. The tip motion is controlled by a piezoelectric scanner which allows access to the sub-Angstrom topography of the surface. The position of the tip is controlled by a feedback loop composed of the *z*-piezo, an amplifier and the tunnel current. The tip height follows a contour of the constant local density of states to keep this tunneling current constant through the feedback loop (constant current mode). For a fixed “tunneling current”, the *z*-piezo position of the tip is measured and converted to produce an image.

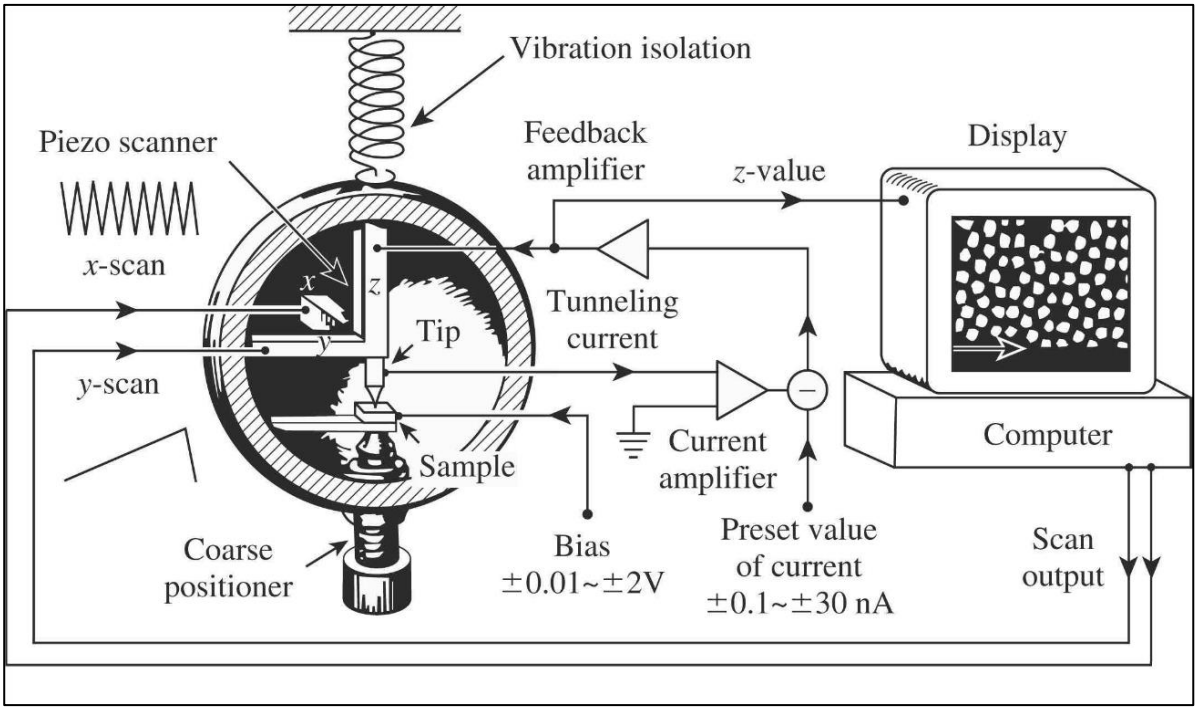

Figure 2.7: Schematic diagram of an STM [3].

The constant current mode is obtained by an electronic feedback loop current amplifier, where it keeps the tunnel current between tip and sample constant while scanning the tip over the surface. If the tunneling current exceeds its set-point value, the distance between tip and sample is increased, while this distance decreases when the tunneling current drops below the set-point value. For constant height mode, the tip position is kept constant with the feedback loop off. Ohm's law below shows that the tunneling current depends exponentially on the distance d and proportional to the voltage V:

$$I(d) = constant * eV \exp\left(-\frac{2\sqrt{2\,m\,\Phi}}{\hbar}\,d\right)$$

The tunneling distance of only 1 Å changes the tunneling current by about an order of magnitude.

Where

Φ: work function (energy barrier)

e: electron charge

m: electron mass

h: Planck's constant

V: applied voltage

d: tip-sample distance

STM has two main operating modes: constant current and constant height. The difference between two modes is that in constant current mode, there is a feedback loop that keeps the tunneling current constant by adjusting the distance of the tip to the sample surface. The screen shows the plotted image with the height versus position. In the constant height mode, the tip trajectory distance is constant during the scan, but because of the sample surface corrugation, the Density of States varies at the atomic scale. In this mode, the variations of the tunneling current is recorded as a function of position. Since the loop is open during the scanning, the constant height mode is only applicable for very flat surfaces. An image is generated with the measured tunneling current versus position. Note that in both cases, the measured signal (either the current or height) is a result of both the topography of the surface and the local density of states [3].

In our experiment scanning tunneling microscopy (STM) is used to characterize the topography of the as-grown thin film of NaCl, KCl, PTCDA on Ag(001) and also to compare the topography of the as-grown and irradiated NaCl films. All STM images are acquired in constant current mode. The geometry of the NaCl films before and after electron irradiation is investigated using a low-temperature STM at 78 K (liquid nitrogen cryostat) and at a base pressure of 2×10^{-11} mbar. Bias voltages U_b refer to the sample voltage with respect to the tip. The KCl and PTCDA on Ag(001) thin films are investigated using a room-temperature STM at 300 K. Here also the bias voltages U_b refer to the sample voltage with respect to the tip.

2.5.3.2 Tunneling current

To obtain an STM image depends on the tunneling conditions between the tip and the sample. Here, a brief description of the tunneling effect will be given. Electrons cannot flow from the

sample to the tip without applying voltage because the sample and the tip have the same electronic potential (Fermi levels line up exactly) and there is a potential barrier between the two electrodes (see Fig. 2.8 (Left image))[4]. By applying a voltage (bias voltage) between the sample and the tip effectively will raise the Fermi level of the sample with respect to the tip, so that electrons in the sample could pass to the empty states of the tip (see Fig. 2.8 (Right image)). However, the potential barrier prevents this electron transfer from occurring in classical physics.

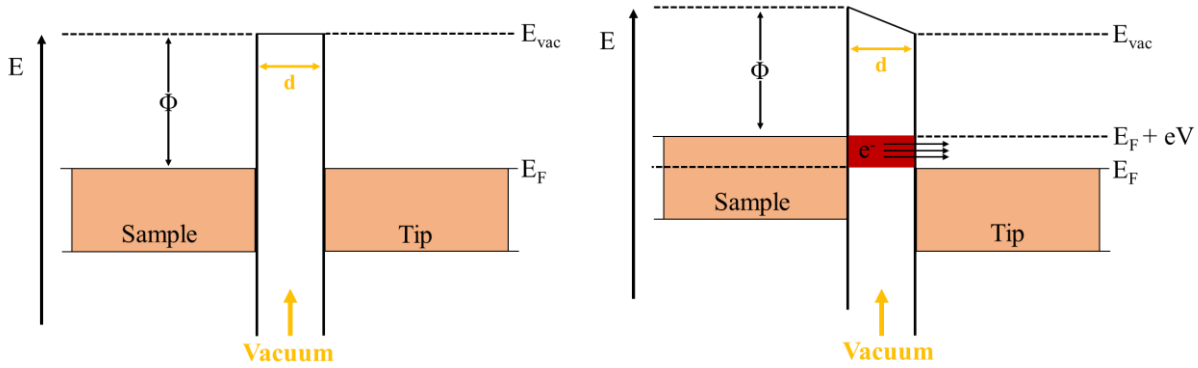

Figure 2.8: Left image: before applying the voltage the Fermi level of the sample and the tip is the same. Right image: after applying voltage the Fermi level of the sample will rise with respect to the tip, this will give the empty states to tunneling into.

To overcome the potential barrier, we would need high energy (of the order of the work function) in order to bring an electron up and over the barrier. The electron movement in a potential U(z) is described by the following equation:

$$\frac{P_z^2}{2\,m} + U(z) = E \qquad (1)$$

Where

E	The electron energy
U(z)	Potential barrier
m	The electron mass
p	The electron momentum

This is an impossible situation in classical physics because the potential barrier is larger than the available energy. The electron cannot penetrate into any region with E < U(z), so no current should flow according to classical physics. However, according to quantum mechanics, the same electron can flow even without applying the voltage by the overlap of the electronic wave functions of the sample and the tip. The state of the same electron is described by a wave function ψ(z), which is expressed by Schrodinger's equation, [3].

$$\frac{-\hbar}{2m}\frac{d^2}{dz^2}\psi(z) + U(z) = E\,\psi(z) \tag{2}$$

As in the classical case, the electron is moving with a constant momentum $p_z = \hbar k = [2m(E-U)]^{1/2}$, or a constant velocity $v_z = p_z/m$, (in either a positive or negative direction). The solution for the Schrodinger's equation (Eq. (3)), in the classically forbidden region, is as follows:

$$\psi(z) = \psi(0)\,e^{-kz} \tag{3}$$

$$k = \sqrt{\frac{2m(U-E)}{\hbar}} \tag{4}$$

Where k describes a state of the electron decaying in the +z direction, which is called the decay constant.

The probability density of observing an electron near a point z has a nonzero value in the barrier region and is proportional to $|\psi(0)|^2 e^{-2kz}$. Hence the electron in the sample can tunnel into the tip and vice versa as shown in Fig. 2.8. However, there is no net tunneling current without a bias voltage.

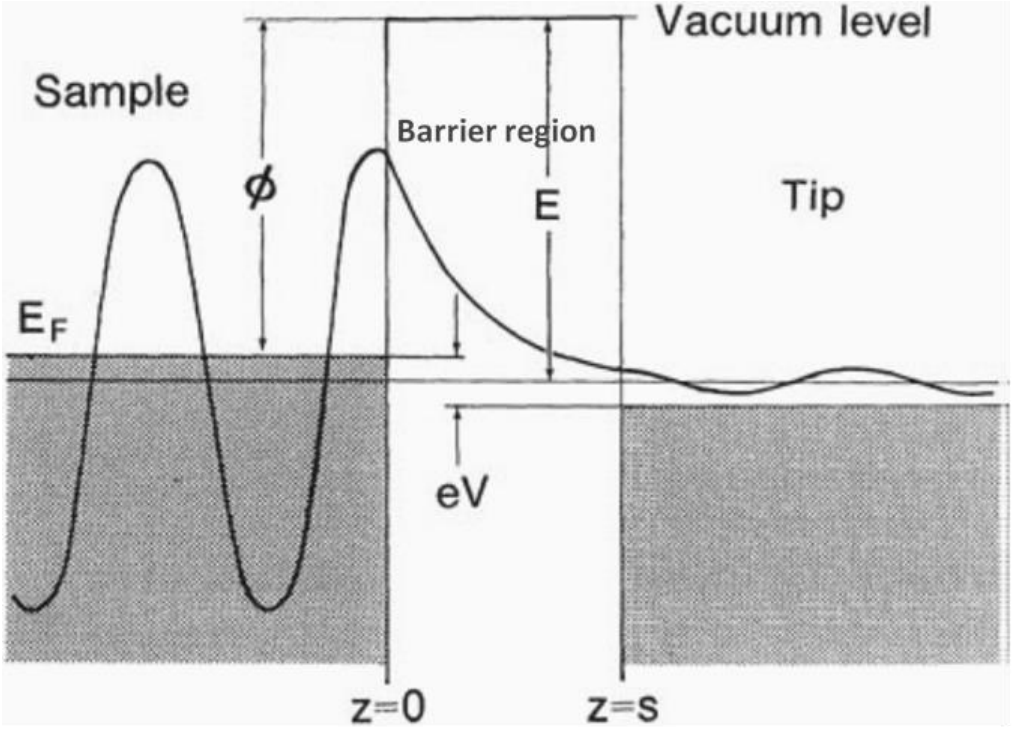

Figure 2.8: A one-dimensional metal-vacuum-metal tunneling junction. Free-electron tunnels from the sample to the tip [3].

Now by applying a small bias voltage eV between the sample and the tip(which is suitable for the metal substrates), and which is much smaller than the value of the work function of the sample ϕ, the probability w for an electron in the occupied sample states to be present at the tip surface, z = w, is:

$$w \propto |\psi_n(0)|^2 e^{-2kW} \qquad (5)$$

Where $\psi_n(0)$ is the value of the occupied sample state at the sample surface.

The decay constant (k) of a sample state near the Fermi level in the barrier region is:

$$k = \sqrt{\frac{2\,m\,\Phi}{\hbar}} \tag{6}$$

Where m is the electron mass, Φ is the work function of the conducting electrode, and ħ is Planck's constant.

The condition of the tip during its scanning of the sample usually does not change, and the electrons which flow from the apex of the tip surface can be considered to have constant velocity. The tunneling current is directly proportional to the number of states on the sample surface within the energy interval eV and depends on the local nature of the sample surface as we mentioned earlier.

By including all the sample states in the energy interval eV, the tunneling current is:

$$I \propto \sum_{E_n=E_F-eV}^{E_F} |\psi_n(0)|^2\, e^{-2\,k\,W} \tag{7}$$

The density of electronic states does not vary significantly if V is small enough, then the equation (7) can be written in terms of the local density of states (LDOS) at the Fermi level.

$$\rho_s(z,E) \equiv \frac{1}{\varepsilon} \sum_{E_n=E-\varepsilon}^{E} |\psi_n(z)|^2 \tag{8}$$

The probability density $|\psi(\mathrm{n})|^2$ of a single state decreases when the volume increases, but the number of states per unit energy increases so that the LDOS remains constant. From the value of the surface LDOS near the Fermi level, we can determine whether the surface is metallic or insulating. The tunneling current can be conveniently written in terms of the LDOS of the sample:

$$I \propto V\,\rho_s(0,E_F)e^{-2\,k\,W} \tag{9}$$

Since Z=W from equation (7), (8)

$$\sum_{E_F - eV}^{E_F} |\psi_n(0)|^2 \, e^{-2\,k\,W} = \rho_s(W, E_F)\, eV \tag{10}$$

Then the tunneling current will be:

$$I \propto \rho_s(W, E_F)\; V \tag{11}$$

2.5.3.3 Metallic tip

The STM tip is an essential part of the STM experiment. In order to obtain an image of the topography of the surface with atomic resolution or to study the electronic properties of the surface using scanning tunneling spectroscopy (STS), a tip of high quality is required, so that ideally there is one atom of the material at the apex of the tip.

The tip can be made from different materials such as Pt/Ir, plasmonic materials such as gold or silver, or Tungsten. Generally, a plasmonic tip is used to study the optical properties of the material. Pt/Ir is known to slowly oxidize, nevertheless, Pt/Ir tips are of limited use because they are unstable mechanically due to the poorly structured tip apex, [5]. Tungsten is very hard and mechanically stable and has a high and smooth DOS [5], [6].

The tips used for our STM experiments were made of a tungsten wire with a diameter of 0.25 mm. About 5mm of wire was cut, and part of the wire then was held in place, by a cylindrical holder. Then the whole wire was submerged in sodium hydroxide (NaOH) solution. Electrochemical etching was done with a direct current (DC) power supply. An initial etch of 20 seconds removed the oxide from the W wire. The wire was retracted partially from the solution so that only 1.7 mm of it remained in the solution. The electrochemical etching started again and as the chemical etching progressed, the current decreased. Afterwards, the current would suddenly drop to 0 A, which means that the etching was complete with at the end, a very sharp tip with perhaps one atom of the material at the apex of the tip (see Fig. 2.10). The tip then was washed with water and ethanol and immediately dried off. Then it was then carefully mounted on a tip holder.

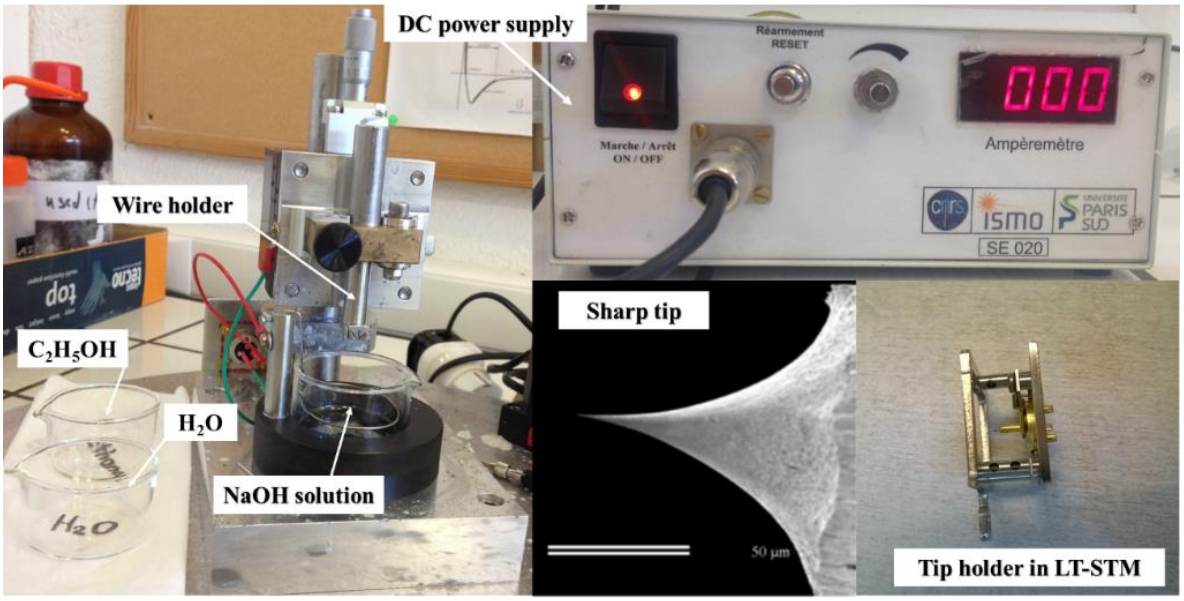

Figure 2.10: Shows tip-etching device, a very sharp tip made by etching process, and tip holder in LT-STM.

Before using the tip to scan the surface, we degassed it in the preparation chamber using indirect heating at temperature 673 K for about one hour in order to remove the contamination such as the water or an oxide layer. In a few times. We used also electron bombardment (in RT-STM setup) for cleaning the tip, to increase the quality of cleaning. The quality of the tip was tested through the STM imaging of a clean silver surface. Further, sharpening and improvement of the tip were done by applying pulses of varying voltage and current during the scan.

2.6 Bibliography

[1] H.-C. Ploigt, C. Brun, M. Pivetta, F. Patthey, and W.-D. Schneider, "Local work function changes determined by field emission resonances: NaCl/Ag (100)," *Phys. Rev. B*, vol. 76, no. 19, p. 195404, Nov. 2007.

[2] G. Cabailh, C. R. Henry, and C. Barth, "Thin NaCl films on silver (001): island growth and work function," *New J. Phys.*, vol. 14, no. 10, p. 103037, 2012.

[3] C. J. Chen, "Introduction to scanning tunneling microscopy," *New York Oxford Univ. Press*, 1993.

[4] G. Binnig and H. Rohrer, "Scanning tunneling microscopy from birth to adolescence," *Rev. Mod. Phys.*, vol. 59, no. 3, pp. 615–625, 1987.

[5] M. Zhao, "Electronic Properties of Graphene Functionalized with 2D Molecular Assemblies," *Paris-sud Univ.*, 2017.

[6] H. Ness and F. Gautier, "The electronic structure and stability of transition metal nanotips. I," *J. Phys. Condens. Matter*, vol. 7, no. 33, p. 6625, 1995.

Chapter 3

Growth of Thin Insulating Layer on Ag(001)

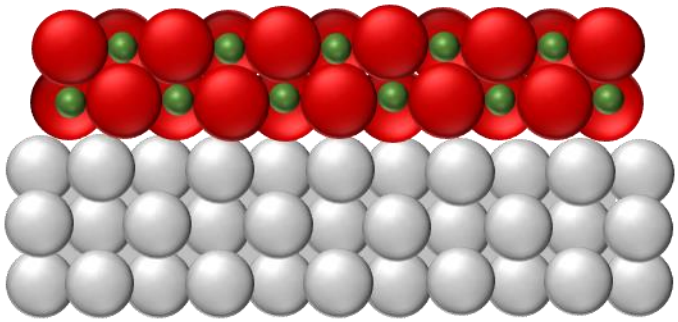

Table of Contents

3.1 Introduction

In this chapter, we report the detailed investigation of the structures of two different thin films grown on the Ag(001) substrate; the NaCl and KCl films by scanning tunneling microscopy (STM), scanning tunneling spectroscopy (STS), low energy electron diffraction (LEED), and Auger electron spectroscopy (AES). For the KCl growth, the experiment was performed in two different setups; RT-STM and LT-STM. Several parameters were varied; the substrate temperature, deposition times, and evaporation cell temperature in order to study the quality of these films and the effects of the film thickness. We also studied the apparent layer thickness of the as-grown NaCl and KCl ultrathin layer by STM measurements at different bias voltages. We found that the apparent thickness and the STM contrast of these two insulating films vary as the bias voltage changes. Finally, the atomic resolution for both films with two particular orientations (0˚ and 45˚ with respect to the Ag substrate) was obtained.

3.2 Thin insulating layer of Sodium Chloride (NaCl)

3.2.1 NaCl deposition

To grow ultrathin NaCl layers, NaCl in the form of a solid powder is evaporated from a Knudsen effusion cell in the analysis chamber. In order to study the quality of the NaCl film and the effect of the film thickness, a number of parameters were varied; different temperatures of the NaCl cell at 756, 773, and 797 K, and the deposition time within the range of 10-40 min. During NaCl deposition, the Ag(001) substrate temperature was held at either 413 or 500 K in order to increase NaCl molecule diffusion on silver during the deposition to obtain larger NaCl domains [1], [2].

3.2.2 NaCl film geometry

The geometry of the as-grown NaCl films is characterized by Scanning Tunneling Microscopy (STM). Their structural and compositional properties are studied using Low Energy Electron Diffraction (LEED) and Auger Electron Spectroscopy (AES), respectively.

3.2.2.1 Scanning Tunneling Microscopy

Scanning tunneling microscopy (STM) was used to study the morphology of the ultrathin NaCl films grown on Ag(001) to determine their thickness as a function of the growth temperature.

- **NaCl films grown at 413 K**

Figures 3.1-3.3 show STM topography images of an ultrathin NaCl film grown on Ag(001) at 413 K after 10 min deposition of NaCl at an evaporation cell temperature of 793 K. The NaCl film consists of islands, which have side lengths in the 100 - 200 nm range and mainly square or rectangular shapes, with rounded corners for the thinnest of them. The island edges exhibit various orientations with respect to the substrate axes, in agreement with previously reported azimuthal mosaicity [1], [3], [4].

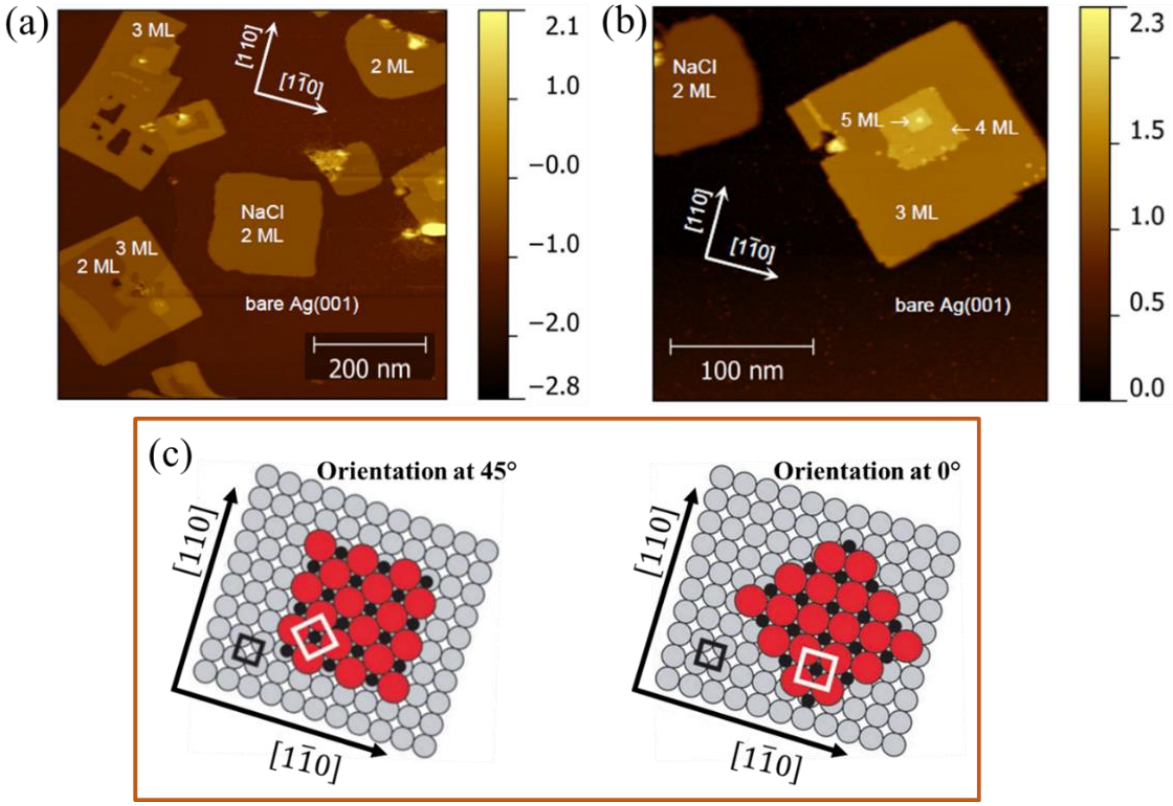

Figure 3.1: STM topography of an ultrathin NaCl film grown on Ag(001) at 413 K (10 min deposition) in different areas of the sample. (a) 680 × 680 nm^2 and (b) 272 × 272 nm^2 (U_b = 4 V, I_t = 0.7 nA). (c) Schematics show NaCl orientation with respect to Ag axes [3]. All STM images are recorded at low temperature (78 K).

In addition, one can observe in Fig. 3.4 that NaCl islands have two particular orientations with respect to the Ag substrate. In the "0° orientation" the unit cells of NaCl and Ag have the same orientation, whereas the NaCl island edges are orientated at ≈ 45° to the $[1\bar{1}0]$ and [110] axes of Ag(001), which is expected for non-polar edges with alternating Cl^- and Na^+ ions. The second type of island is oriented at ≈ 45° (the unit cell of NaCl is rotated by 45° with respect to the unit cell of Ag), where the outer edges of these domains are straight and oriented parallel to the $[1\bar{1}0]$ and [110] axes of Ag(001).

The local thickness of the NaCl domains, i.e., the number of atomic layers (ML), is determined from the apparent height measured by STM at different bias voltages [5], [6]. These measurements were then compared with previous STM [2] and non-contact atomic force microscopy [1] studies. Line profiles, taken along the same lines in Figs. 3.2 (a) and 3.2 (c), are plotted in the graphs shown in Figs. 3.2 (b) and 3.2 (d), respectively. Profile 1 crosses a 2 monolayer (ML)-thick NaCl island, whereas Profile 2 crosses 3-ML, 4-ML and 5-ML NaCl domains of an island. In addition, this island features a defect or aggregate at the top. Cabailh et al [1] have observed that NaCl films grown on Ag(001) at substrate temperatures in the 343-443 K range essentially consist of ≥ 2 ML-thick islands. At low bias voltage (U_b = 1 V), we measure in the area shown in Fig. 3.2(c) STM heights of 0.30, 0.42, 0.53 and 0.65 nm, that we assign to thicknesses of 2, 3, 4 and 5 ML. This is consistent with STM heights of 0.31 and 0.46 nm for 2 and 3-ML NaCl/Ag(001) reported by Ploigt et al [2].

STM spectroscopy and atomic-resolution STM images reveal that, at low bias (U_b = 1 V), electrons tunnel from the tip to metal-induced gap states at the NaCl/Ag(001) interface [5], [7], [8] (see Figs. 3.3 and 3.4). The apparent thickness of the atomic NaCl layers beyond 2 ML in the STM images of 0.12 ± 0.02 nm is lower than the expected value (0.282 nm). At a higher bias voltage U_b = 4 V, in Fig. 3.2(b) the STM height of the 2 ML NaCl/Ag(001) is measured at 0.90 nm and the apparent thickness of the next NaCl layers up to 6 ML is 0.30 ± 0.02 nm, which is close to their

true thickness (0.282 nm). In these conditions, electrons tunnel to an image potential state in front of the Ag(001) surface, which is possible at U_b = 4 V because the first field emission resonance is shifted in energy from about 4.5 eV to 3.3 eV upon NaCl adsorption [2] (see Fig. 3.3). These different values of the thickness confirm that the tunneling parameters strongly affect the apparent thickness of the NaCl layers in STM [9].

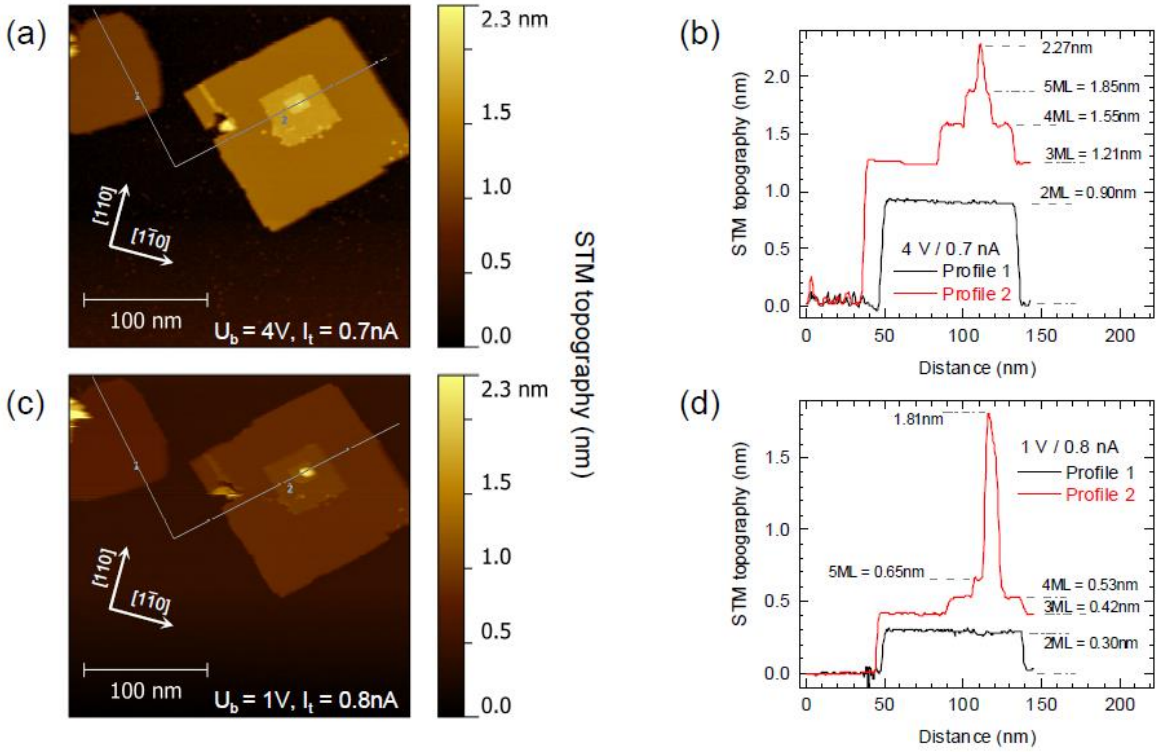

Figure 3.2: 270 × 270 nm^2 STM topography of an ultrathin NaCl film grown on Ag(001) at 413 K in the same area with different bias conditions, (a) (U_b = 4 V, I_t = 0.7 nA),and (c) (U_b = 1 V, I_t = 0.8 nA), where (b) and (d) are apparent height profiles along the lines in the STM images (a) and (c) respectively. The correspondence between STM heights and numbers of NaCl atomic layers (monolayer, ML) is given in inset. All STM images are recorded at low temperature (78 K).

Previous observations of NaCl films grown on Au(111) -(22 ×√3) reported by Sun et al, [9], showed that NaCl layers act as an insulating thin film which perturbs the tunneling between the STM tip and the substrate. This is because the NaCl layer has no electronic states near the Fermi level which lies mid-way within the band gap. Therefore, the insulating NaCl layer plays the role

of a tunneling barrier and forms a double barrier tunnel junction (DBTJ) combining with vacuum gap. However, this may be true in the case of the NaCl/Au(111) system, but not for NaCl/Ag(001). In the film growth of NaCl on Al(001) [5], the apparent height of the NaCl layer decreased when the number of NaCl layers on the surface increased and height measurement was possible only up to three layers with relatively low voltage STM conditions of U_b = -2.2 V, I_t = 0.12 nA. For tunneling through islands composed of a triple layer of NaCl, bias voltages higher than - 2 volts were used [5]. This is in agreement with our observations on NaCl/Ag(001).

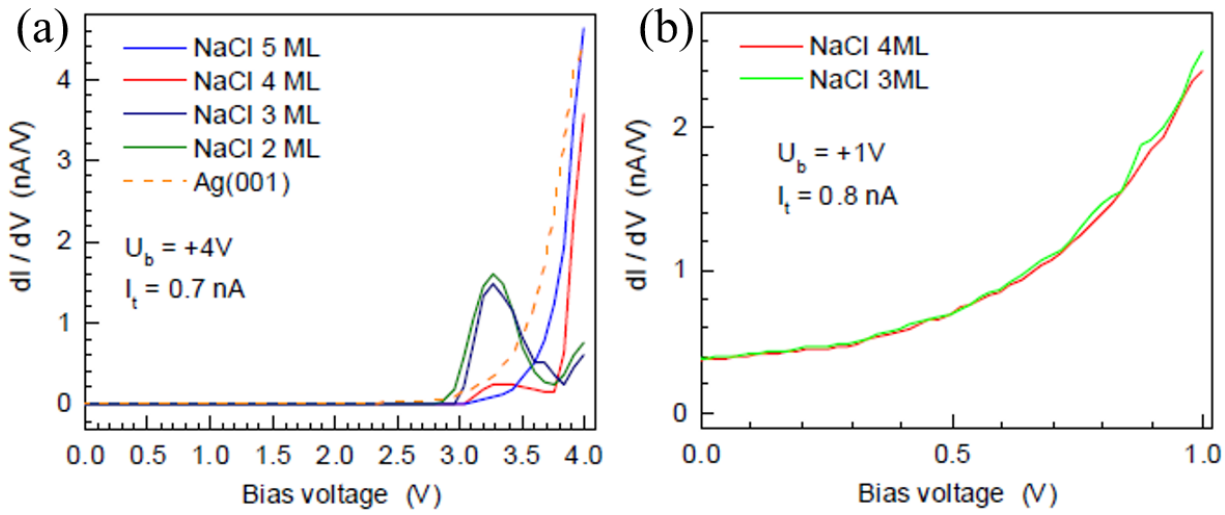

Figure 3.3: Differential conductance (dI/dV) spectra, measured in opened-loop conditions (see initial STM parameters in inset), on an ultrathin NaCl film grown on Ag(001) at 413 K. (a) dI/dV spectra obtained on NaCl domains shown in Fig. 3.2, whose thickness ranges from 2 to 5 NaCl atomic layers (monolayer, ML), and on the bare Ag(001) surface, by varying the bias voltage from 4 V to 0 by steps of 100 mV. (b) dI/dV spectra obtained on 3-ML and 4-ML NaCl domains, by varying the bias voltage from 1 V to 0 by steps of 100 mV.

STM spectroscopy measurements were performed on NaCl domains of different thicknesses. Figure 3.3 shows the differential conductance (dI/dV) spectra, measured in open loop conditions (the initial STM parameters are indicated in each panel). Bias voltages U_b refer to the sample voltage with respect to the tip. At high bias voltage (U_b = 4 V), the dI/dV spectra are

dominated by the field emission resonances of Ag(001), which occur at energies ≥ 4.5 eV on bare Ag(001), but shift to lower energies upon adsorption of NaCl [2]. At NaCl thickness greater than 4 ML, the contribution of the first emission resonance of Ag(001) is totally attenuated in the dI/dV spectrum. At low bias voltage (U_b = 1 V), the electrons tunnel to metal-induced gap states at the NaCl/Ag(001) interface [7]. As shown below, atomic resolution of the NaCl layer can be obtained at a low bias voltage (U_b = 1 V), by using suitable tunnel current setpoint values (e.g., I_t = 1 A). This is possible thanks to the localization of these metal-induced gap states around the Cl sites, which explains the STM contrast between Cl and Na [5], [7].

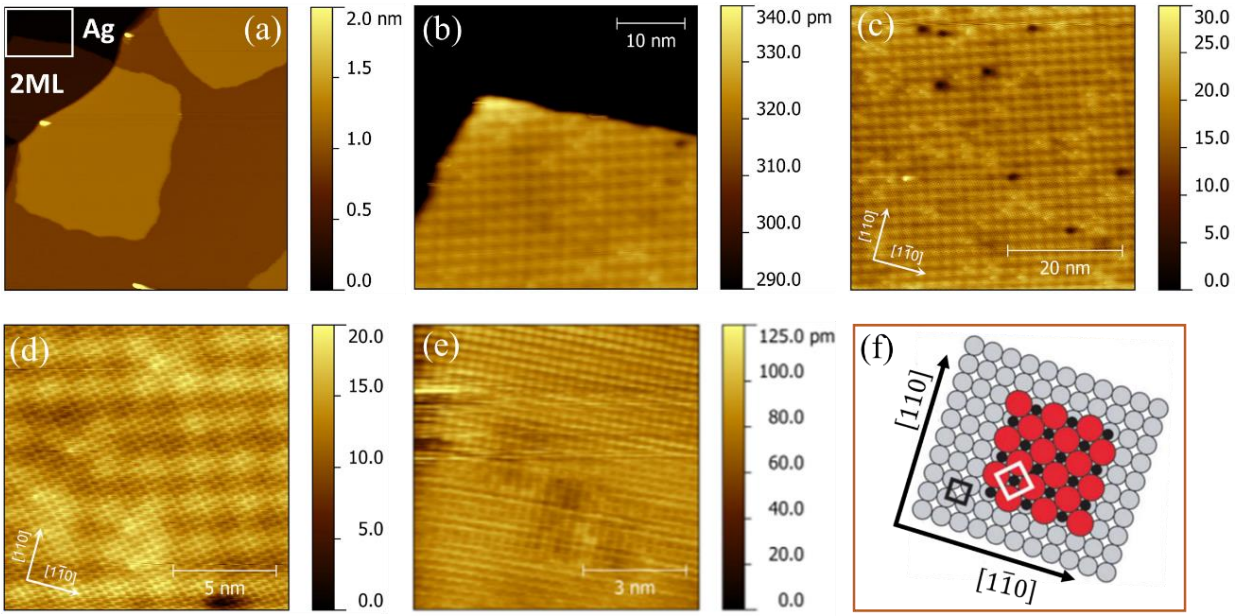

Figure 3.4: STM topography of an ultrathin NaCl film grown on Ag(001) at 413 K (a) 200 × 200 nm^2 (U_b = 4 V, I_t = 0.7 nA), (b) 30 × 30 nm^2 (U_b = 1 V, I_t = 1 nA) of the selected area in the image (a) which shows Moiré pattern on NaCl island, (c) 49×49 nm^2 and (d) 13.6×13.6 nm^2 atomic resolved image and Moiré pattern on NaCl island measured with STM parameters U_b = 1 V and I_t = 1 nA , where NaCl unit cell is oriented at 45° to the unit cell of Ag as represented in schematic image (f) [3], (e) shows the atomic resolution measured on the Ag(001) substrate, 6 × 6 nm^2 (U_b = 1 V, I_t = 1 nA). All the images recorded at low temperature (78 K).

Figure 3.4(a) shows a typical 200 × 200 nm^2 STM image of another area of the same film shown in Fig. 3.2, measured on a 2 ML NaCl/Ag(001) island. Figure 3.4(b) shows the image of the selected area in the image (a) of the Moiré pattern of NaCl with a periodicity of about 2.2 nm. The appearance of this pattern is often due to the mismatch between the ad-layer and substrate [5], [6] or a modulation of the local work function, as previously deduced by tunneling spectroscopy of image-potential states [3], [6]. This Moiré pattern should be observable at any bias voltage even at an ultra-low voltage, and its contrast varies as the bias voltage changes [6].

Figure 3.4 (c) and (d) show two atomic-resolution STM images measured at low bias voltage (U_b =1 V) on the same 2-ML NaCl domain, with two different scan sizes of 49 × 49 nm^2 in Fig. 3.4(c) and 13.6 × 13.6 nm^2 in Fig. 3.4(d). A Moiré pattern is visible in both images, which corresponds to an apparent 2D-periodic corrugation of the surface of 4 pm (peak-to-peak amplitude) with a square lattice of unit cell parameter of 2.23 nm. Atomic resolution in Fig. 3.4(d) reveals a unit cell parameter of the NaCl lattice (assuming that the STM contrast is mainly due to one of the two Na/Cl ions) of 390 pm (in-plane nearest Cl-Cl distance), which indicates a lateral contraction by about 2% compared to (001) plane in a bulk NaCl crystal (expected value 399 pm).

Fig. 3.4(e) shows an atomically resolved image of the Ag(001) substrate, with a measured atomic periodicity a = 0.293 ± 0.005 nm which is consistent with the value expected for the Ag(001) surface, i.e., a = 0.2889 nm. From the island border orientation in Fig. 3.4(a) and the atomic structure for both NaCl and Ag(001), where the NaCl unit cell is oriented 45° with respect to the Ag substrate as represented in Fig. 3.4(e), we can determine the NaCl island orientation along the $[1\bar{1}0]$ and [110] axes of Ag(001), where NaCl [110]//Ag[110].

- **NaCl films grown at 500 K**

In this section, the morphology of NaCl films grown at 500 K is presented and discussed. Figs 3.5-3.7 show two samples of ultrathin NaCl films grown on Ag(001) at 500 K; they differ in nominal thickness by a factor of 4 to 5 according to the AES measurements. On both samples, our STM images show large NaCl domains, exceeding 1 μm^2 in area and the NaCl domains are surrounded by large bare Ag(001) areas.

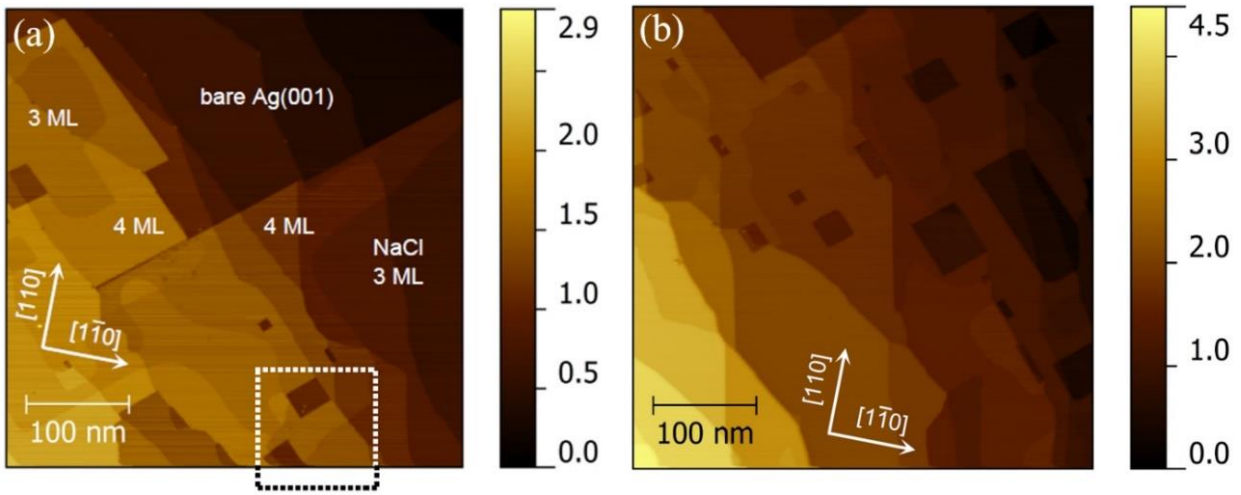

Figure 3.5: STM topography of an ultrathin NaCl film grown on Ag(001) at 500 K. (a) 435 x 435 nm^2 image (U_b = 1 V, I_t =0.8 nA) with indications of the NaCl film thickness (in atomic monolayers, ML), as determined from height variations. (d) 435 x 435 nm^2 image (U_b = 1 V, I_t = 0.8 nA) of another area of the same film, which exhibits rectangular holes, whose sides range from a few nanometers to ≈ 100 nm. All STM images are recorded at low temperature (78 K).

The outer edges of these domains are straight and oriented at ≈ 45° to the [1$\bar{1}$0] and [110] axes of Ag(001). As previously reported, this is consistent with NaCl(001) domains having their crystallographic directions parallel to those of Ag(001) on average; NaCl [011]//Ag[011] and NaCl [1$\bar{1}$0] //Ag[1$\bar{1}$0]. This is in agreement with the low azimuthal mosaicity expected for high-temperature growth [4], and nonpolar edges with alternating Cl^- and Na^+ ions [3].

Figures 3.5 (a and b) show STM data measured on the thinnest of these two samples in a different area. Dark areas within islands, in Fig. 3.5 (a) and (b), are identified as holes since we see the bare Ag(001) surface inside and NaCl molecules (bright dots) pinned at defects of the silver step edges. These holes have a rectangular shape and side length ranging from a few nanometers to ≈ 100 nm, and the enclosed area typically ranges from 10 to 10^4 nm^2. Holes with more regular shapes, almost perfectly rectangular, are seen in the STM images of the NaCl films grown at 500 K, for example, the area inside the dotted line in Fig. 3.5(a) is presented in more detail by the STM images in Fig. 3.6. We assume that the regular shapes are due to lower azimuthal mosaicity

compared to the films grown at 413 K and that hole formation similar to the films grown at 413 K is also driven by the coalescence of azimuthally mismatched islands.

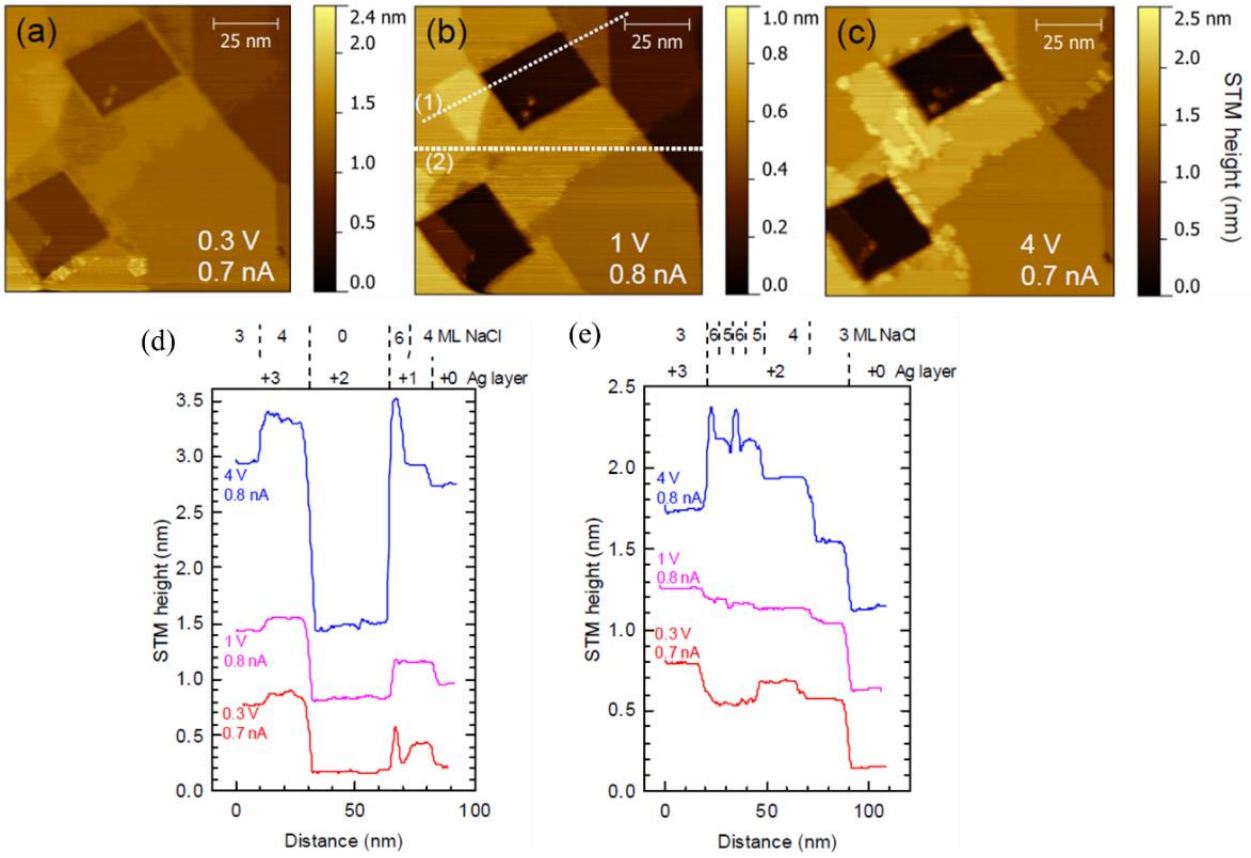

Figure 3.6: STM topography of an ultrathin NaCl film grown on Ag(001) at 500 K. [(a) to (c)] 109 × 109 nm^2 images measured at different tip-sample biases and tunnel current setpoints: (a) U_b = 0.3 V, I_t = 0.7 nA; (b) U_b = 1 V, I_t = 0.8 nA; (c) U_b = 4 V, I_t = 0.8 nA. All STM images are recorded at low temperature (78 K). [(d) and (e)] STM height profiles taken from the three STM images along the two-line segments shown in (b), respectively. Above the graphs, we indicate the step jumps of the underlying Ag(001) surface and the thickness of the NaCl film expressed in atomic monolayer, as determined from the STM height profiles.

The local thickness of the NaCl domains, i.e., the number of atomic monolayers (ML), is determined from the apparent height measured by STM. In these higher temperature growth conditions, the NaCl islands consist of large bases that are 3 to 4-ML thick, on top of which can be

found smaller domains that have higher thicknesses, often 5 to 6 ML. The fifth and sixth NaCl layers are distinguished by their contrast compared to the fourth layer in the STM image, which significantly varies or even reverses when changing the tip-surface bias [9], [10].

The image shown in Fig. 3.5(a) was measured at U_b = 1 V. A selected area scanned at different bias voltage is shown in Fig. 3.6; a lower bias U_b = 0.3 V in Fig. 3.6(a) and at a higher bias U_b = 4 V in Fig. 3.6(c). The 5 ML and 6 ML-thick areas exhibit positive height contrast at U_b = 4 V, whereas this contrast is almost negligible in Fig. 3.6(b) and is negative in Fig. 3.6(a). This electronic contrast is expected for insulating thin films when the STM tunneling voltage corresponds to energies inside the surface band gap. This leads to a decrease in the measured surface local density of states, which can result in a contrast inversion in the STM image [10].

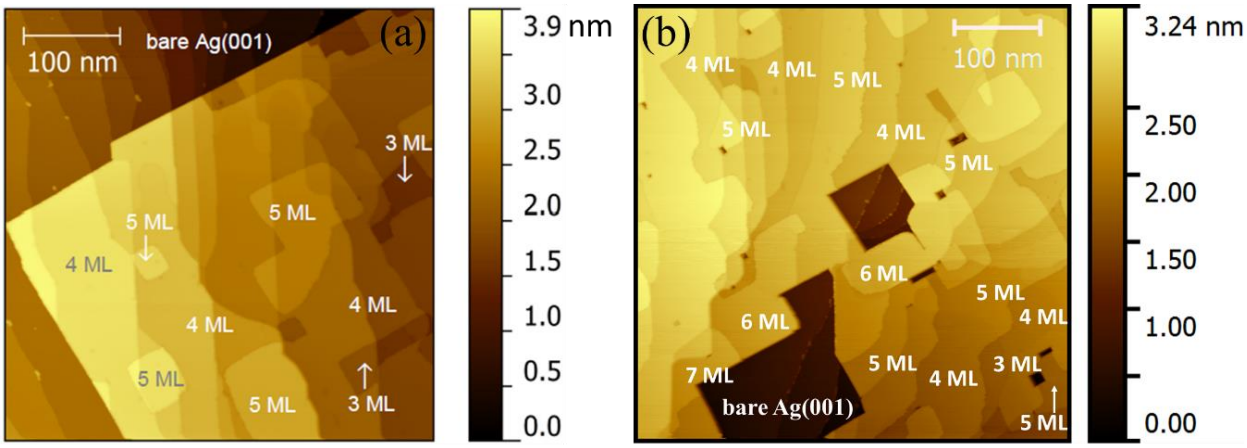

Figure 3.7: STM topography of an ultrathin NaCl film grown on Ag(001) at 500 K, whose nominal thickness is (according to AES measurements) 4 to 5 times as high as that of the film examined in Fig. 1.3, 435 × 435 nm^2 images (U_b = 4 V, I_t = 0.12 nA) showing (a) the outer edges of an NaCl island and (b) holes inside the island. All STM images are recorded at low temperature (78 K).

Fig. 3.7 shows STM images for the second sample, whose nominal thickness according to AES measurements is 4 to 5 times higher than the previous sample shown in Fig. 3.5, even though it was grown at the same sample temperature (500 K). The comparison between Fig. 3.5 and Fig. 3.7 reveals that at high substrate temperature when the amount of NaCl increases, the size and the density of the island and ad-islands also increase, which was previously reported by Cabailh et al

[1]. In both films mentioned above, no Moiré pattern has been observed due to the absence of 45˚ growth in this film as compared to the films grown at 415 K. Also the thicker film reduces the strain between the insulating film and the metal substrate which leads to the absence of the Moiré pattern. The Moiré pattern appears due to the mismatch between the ad-layer and substrate [5], [6].

3.2.2.2 Low Energy Electron Diffraction

LEED reveals the structural properties (diffraction pattern) of the surface. Figure 3.8 shows the initial as-grown NaCl film at 413 K in (a) and at 500 K in (b). In both images, the intense round spots correspond to the LEED pattern of (001) silver substrate in reciprocal space with the square unit cell (blue arrow), giving a lattice parameter of a_{Ag} =0.409 nm in real space.

After deposition of NaCl on the Ag(001) substrate, additional spots appear which correspond to the LEED pattern of NaCl(100)-(1×1) (green arrow in Figs 3.8 (a) and (b)).The latter confirms our STM observations, i.e., the presence of (001)-terminated NaCl domains with parallel orientation with respect to Ag(001) on average (those spots have the same symmetry and same orientation as the Ag (001) substrate, where NaCl [110]//Ag[110] and NaCl [$1\bar{1}0$] //Ag[$1\bar{1}0$]. In addition, the low azimuthal mosaicity (elongated shape) of the NaCl spots shown in Fig. 3.8 is due to the orientation of the NaCl islands around an average orientation which is independent of the film thickness [4]. We mainly observed azimuthally aligned NaCl (001) domains, with the absence of 45°-oriented domains [4]. The azimuthal mosaicity of NaCl on Ag(001) is related to higher-order commensurable NaCl structures, which were fully understood and explained by Le Moal et al [4] .

In contrast with the other references which proposed that the azimuthal mosaicity of NaCl is related to the orientation of the substrate step [11], where (100) terminated NaCl islands start to grow at the substrate steps. Here, the van der Waals interaction is stronger than on the flat terraces. In this case, the angular spread of mosaic orientations must be caused by the angular variation of the step orientation of the original Ag surface [11]. On the other hand, Pivetta et al showed that the nucleation sites of NaCl is not the reason for the formation of the azimuthal mosaicity, where the azimuthal mosaicity was observed on both terraces and the step edges of the silver substrate [3].

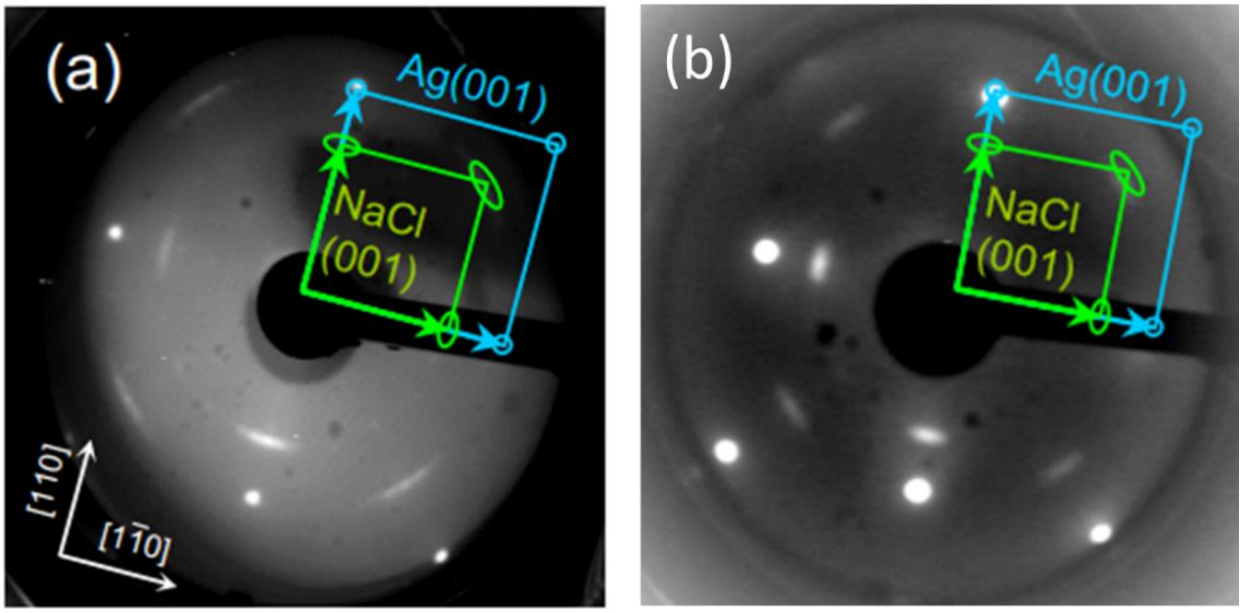

Figure 3.8: Background-subtracted LEED images of NaCl on Ag(001) at (t=0).(a) The film grown at 413K and (b) the film grown at 500K. All the images recorded at 53eV except (a) recorded at 52 eV.

The NaCl growth along the [1 0 0] axis has also been observed on other substrates and has been found to be independent of the metal substrate surface symmetry. This can be explained by the much smaller surface energy of the (100) plane of NaCl compared with that of (110) and (111) by a factor of two and three, respectively. In addition, the (100) surface is neutral in charge as it contains as many Na^+ cations as Cl^- anions whereas, for example, the (111) is a charged surface because it is terminated by only one chemical species due to the alternation of the Na and Cl atomic planes in the NaCl [1 1 1] direction [12].

Furthermore, we found that for the higher thickness of NaCl, the substrate spots are still visible in the LEED images. From this, we infer that the silver surface is not completely covered with the NaCl, bare areas must still be present as we see in the STM images. This is in contrast with the previous work reported for the growth of NaCl on Ag(110), where the Ag spots gradually vanish up to a thickness of ~ 2 ML (and were absent for higher thicknesses) where only NaCl(1 0 0)-(1 × 1) diffraction network could be observed [12].

3.2.2.3 Auger Electron Spectroscopy

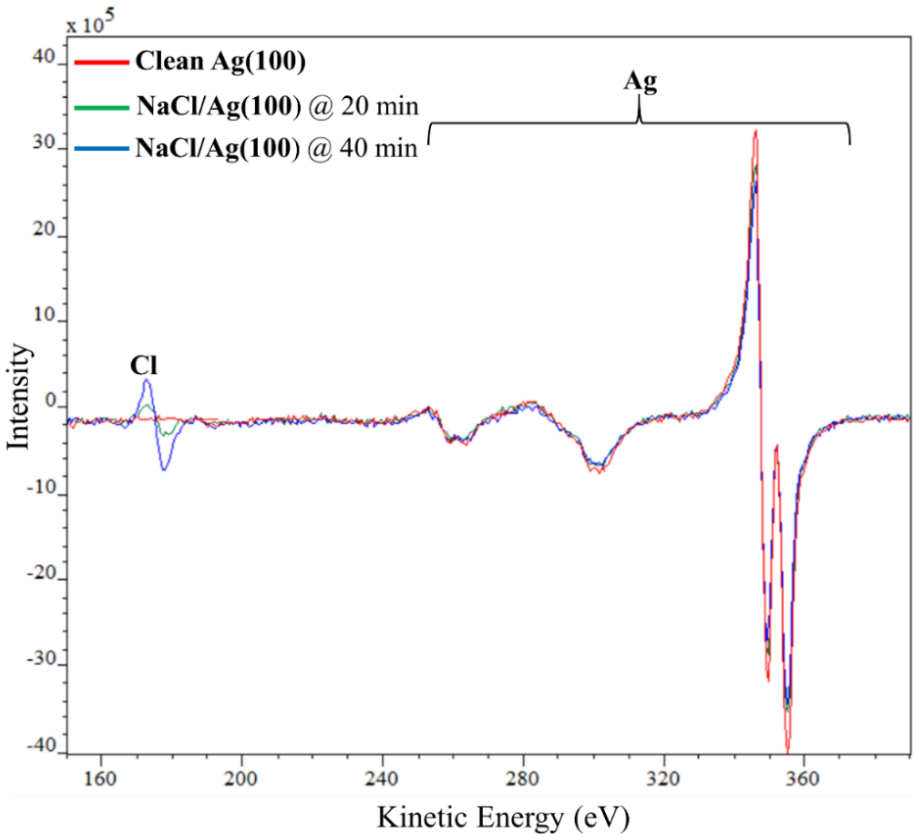

Figure 3.9: AES spectra before/after NaCl deposition. Red spectrum is a clean surface of Ag (001), green spectrum after deposition 20 min of NaCl on Ag(001) at 500 K, where Cl/Ag(t = 0) at 0.2. Blue spectrum after deposition 40 min of NaCl on Ag(001) at 500 K, where Cl/Ag(t = 0) at 0°.

Figure 3.9 shows the spectra of two ultra-thin NaCl films grown on Ag(001) at 500 K and the clean surface of Ag(001), the three peaks at 253, 282, and 346 eV correspond to the Ag signal and a peak at the energy of 173 eV corresponds to the Cl signal. The red spectrum is from the clean surface of Ag(001) before the deposition of NaCl, whereas the blue and the green spectra are taken after the deposition of NaCl at 500K, with two different deposition times, these spectra were taken the same growth condition as the films shown in Figs. 3.1 and 3.3, respectively. As can be seen, there is no carbon on the bare surface (the energy of the carbon peak lies at 271 eV), and the Cl peak from the 40 min deposition is clearly larger than that of the 20 min deposition. In other hand, the Na peak is absent because the energy of the peak is too high (between 930 to 990 eV which is

beyond the scale) and has a low intensity. We tried to measure this peak but there was no clear signal.

3.3 Thin insulating layer of Potassium Chloride (KCl)

In this section, the growth and characterization of KCl on Ag(001) will be discussed. The growth of KCl layer on Ag(001) has been previously reported by Kiguchi et al [8], and Müller et al [13]. The structure and the morphology of ultrathin films of KCl grown on Ag(001) have only been treated by Müller et al [13], whereas Kiguchi et al studied only the electronic properties of this film [8].

It is known that KCl has a high structural quality and an absence of rotational mosaicity during the growth, therefore, KCl layers are suitable for different experiments on dielectric films, e.g. to grow layers of organic molecules of high quality on these layers [13]. For this reason, we chose to study the growth of ultrathin KCl films on Ag(001). We investigated the structure and morphology of the KCl films with two different setups, RT-STM and LT-STM.

3.3.1 KCl deposition in RT-STM setup

KCl in the form of a solid powder is evaporated from a Knudsen effusion cell inside the preparation chamber of the RT-STM setup. In order to study the quality of the KCl film, the temperature of the KCl cell was about 750 K while the deposition time was varied between 5-10 min. The Ag (001) substrate temperature was held at 473 K in order to increase the diffusion of the molecular KCl on silver during the deposition to obtain larger KCl domains [1], [2].

3.3.1.1 Growth mode, atomic structure, and unit cell orientation

The initial geometry of the KCl film is characterized by Scanning Tunneling Microscopy (STM) at room temperature. Figure 3.10 shows an STM image of an ultrathin KCl film grown on Ag(001) at 473 K after a 10 min deposition of KCl. In (a), the STM image shows that the KCl forms a uniform and homogeneous layer and covers the Ag(001) steps without any discontinuities, which is in good agreement with the previous work by Müller et al [13]. It is important to remember that this is in contrast with NaCl growth which always forms islands on the surface of the metal and not a continuous layer [1]–[3], [5]. The continuity of the first layer across the Ag step edges

indicates a strong interstep diffusion and hence a very small Ehrlich–Schwoebel-barrier for the KCl [13]. The step edges of KCl are oriented at ≈ 45° to the [1$\bar{1}$0] and [110] axes of Ag(001).

The apparent height of a KCl step is about 130 pm, which is consistent with STM heights the KCl steps of 120 pm for KCl/Ag(001) reported by Müller et al [13]. In the RT-STM setup, the STM scan range is limited to 200 nm, which is the maximum size that can be scanned in a reasonable time with a reasonable resolution. Therefore, the bare areas of Ag were not observed because of 100% covering of KCl on Ag(001) on this scale. Measuring the height and determining the thickness of the KCl layer without observing the bare area of the silver substrate was not possible in this case, we estimated low thickness typically 2 to 5 ML because we were able to scan the topography of the KCl film with a very low bias voltage.

Figure 3.10(b) shows zoom on the center of the image in 3.10(a), which clearly reveals the atomic structure of the KCl layer covering the steps of the silver substrate. Further zooming in the center, we clearly see the atomic arrangement in 3.10 (c). The measured interatomic distance a = 0.46 ± 0.02 nm, which is consistent with the value expected for the unit cell of KCl, i.e., a = 0.445 nm. This value demonstrates that only one of the two ions is imaged, either K^+ or Cl^- ions [3], [4], [6], [13]. At positive bias, one would expect the atom with the highest Density of States to be the Cl^- ion. The study by Kiguchi et al [8] is particularly instructive. They studied the NEXAFS (near-edge-x-ray absorption fine structure) of MIGS (Metal-induced gap states) for the KCl/Cu(001) system. MIGS are electronic states formed at the semiconductor (or insulator)/metal interface when a free electron-like metal wave function penetrates into the semiconductor (or insulator) side. The unoccupied Cl-p and K-p electronic densities of states can be identified from the Cl-K-edge and K-K-edge NEXAFS, and the MIGS can be expected at the prepeak region. From their NEXAFS spectra, they observed a prepeak at the Cl edge originating from the MIGS but not at the K edge, indicating that the MIGS are formed only at the anion site [8].

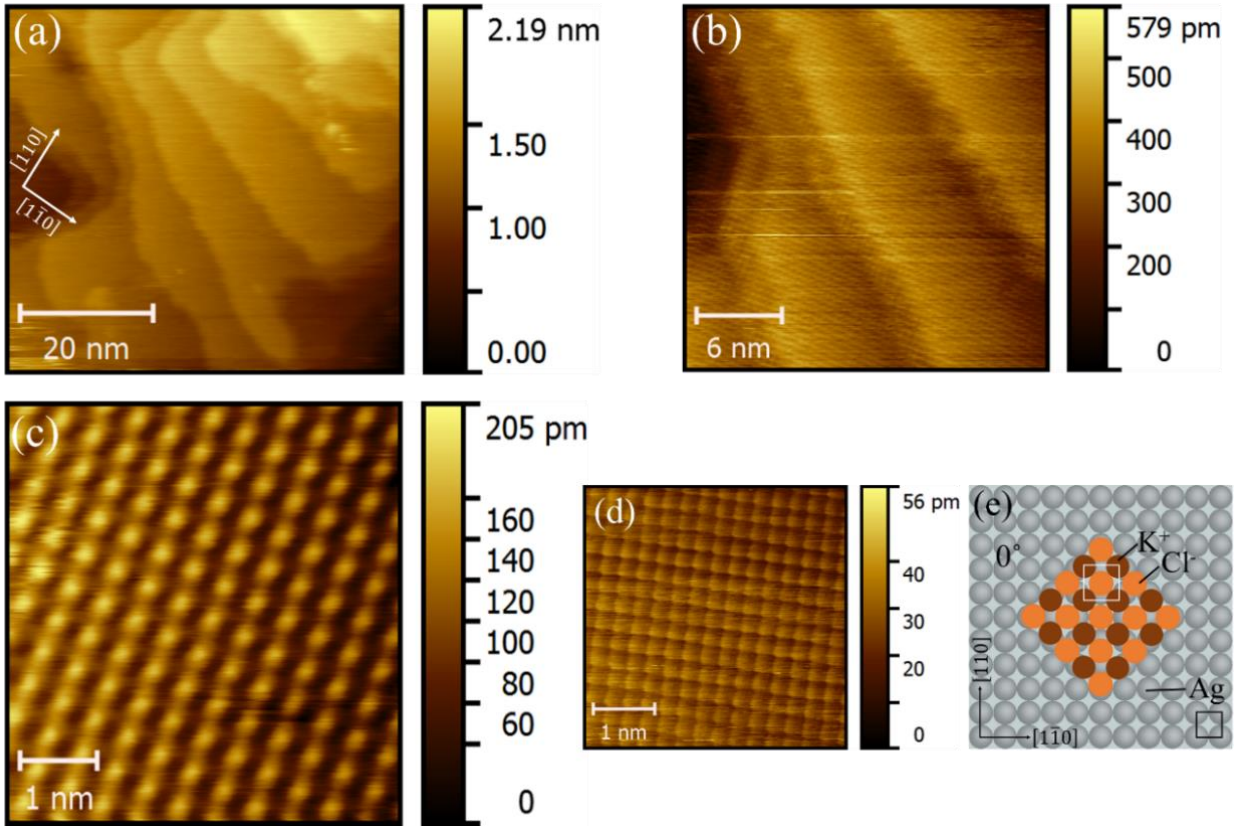

Figure 3. 10: STM topography of an ultrathin KCl film grown on Ag(001) at 473 K (a) 69.6 × 64.4 nm^2 (U_b = -1 V, I_t = 0.2 nA),(b) 30 × 30 nm^2 (U_b = -1 V, I_t = 0.2 nA) image on the center of the image (a), (c) 10 × 10 nm^2 (U_b = -0.5 V, I_t = 0.3 nA) an atomic resolved image of KCl, where KCl unit cell is parallel to the unit cell of Ag ($[001]_{Ag}$ // $[001]_{KCl}$) (0˚growth), (d) 5 × 5 nm^2 (U_b = -0.01 V, I_t = 2.8 nA) an atomic resolved image of Ag(001) substrate and schematic representation of Ag(001) and KCl domain. All the images were recorded at room temperature (300 K).

Fig. 3.10(d) is an atomically resolved image of the Ag(001) surface, with atomic distance a = 0.293 ± 0.004 nm. From the atomic structures of KCl and Ag(001), we can determine the KCl orientation along the $[1\bar{1}0]$ and [110] axes of Ag(001), where the unit cell of KCl is parallel to the unit cell of the Ag(001) surface. This is referred to as "0˚ growth" of KCl islands (KCl [011]//Ag[011] and KCl $[1\bar{1}0]$ //Ag$[1\bar{1}0]$). The 0˚ growth of KCl on Ag(001) was also observed by Müller et al [13].

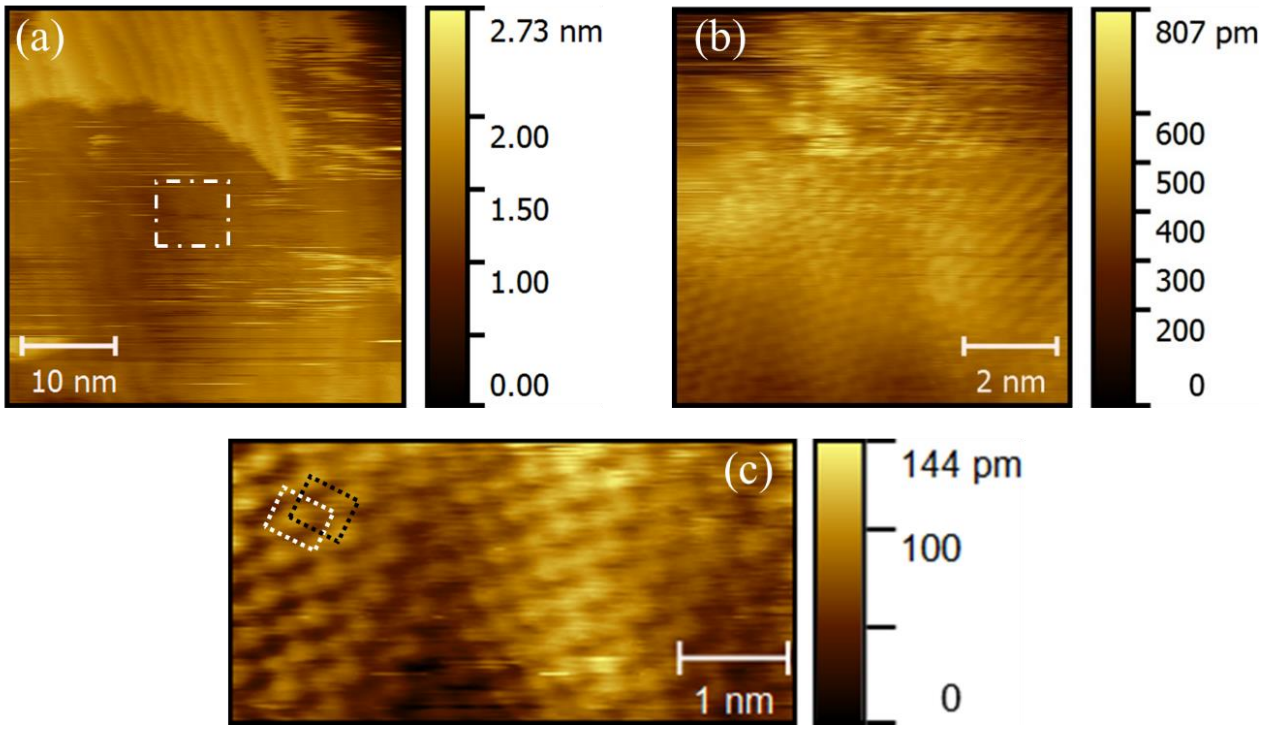

Figure 3. 11: STM topography of an ultrathin KCl film grown on Ag(001) at 473 K (a) 50 × 50 nm^2 (U_b = -0.8 V, I_t = 0.1 nA),(b) 10 × 10 nm^2 (U_b = -0.8 V, I_t = 0.1 nA) image on the center of the image (a), (c) 5.14 × 2.54 nm^2 (U_b = -0.8 V, I_t = 0.1 nA) an atomic resolved image of KCl, where KCl unit cell is parallel to the unit cell of Ag ([001]Ag // [001]KCl) (0˚growth). All the images were recorded at room temperature (300 K).

Figure 3.11 shows the STM images of another area of the same film as Fig. 3.10. In this figure, we scanned the 50 × 50 nm^2 area shown in (a). We zoomed image (a) in the center and obtained an image (10 × 10 nm^2) of KCl with the atomic structure shown in 3.11(b). Here the structure visible in the image suggests that both the K^+ and Cl^- ions are imaged. This was not observed previously in the growth of NaCl on Ag(001) [3], [4], [6], or KCl on Ag(001) [13], where only one of the two ions was imaged. To see both ions clearly, we show an 8.34 × 2.73 nm^2 zoom of image (b), which is shown in 3.11(c), the lattices of the K^+ and Cl^- ions now can be seen. The square white dotted line indicates the unit cell of one of these ions, with an atomic periodicity of about 0.46 ± 0.03 nm. The black dotted line corresponds to the lattice of the other species of ions, the atomic periodicity of this unit cell is about 0.47 ± 0.03 nm. In both cases, the value is

consistent with the value expected for the unit cell of KCl, i.e., a = 0.445 nm. Furthermore, the image here also shows that the unit cell of KCl is aligned with the unit cell of Ag(001) indicating a 0˚ growth mode of the KCl layer. However, the another possibility is perhaps due to a double tip effect when the tip has at least two atoms on its apex.

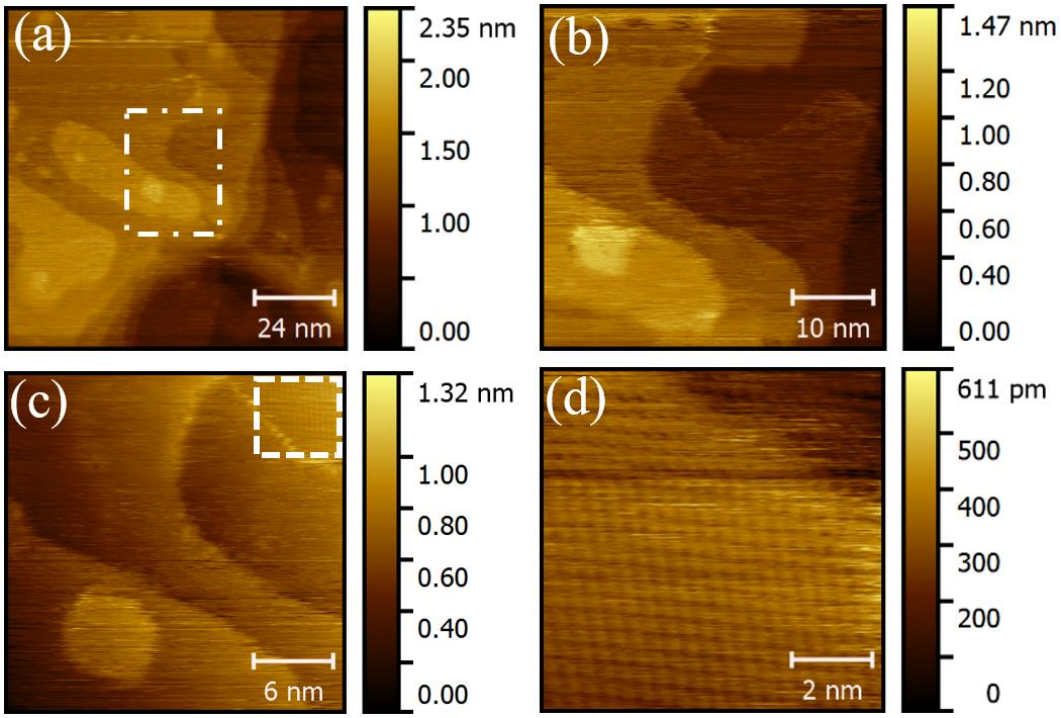

Figure 3. 12: STM topography of an ultrathin KCl film grown on Ag(001) at 398 K (a) 120 × 120 nm^2 (U_b = -0.8 V, I_t = 0.1 nA),(b) 50 × 50 nm^2 (U_b = -1.7 V, I_t = 0.3 nA) image on the center of the image (a), (c) 30 × 30 nm^2 (U_b = -1.7 V, It = 0.3 nA), (d) 10 × 10 nm^2 (U_b = -1.7 V, I_t = 0.4 nA) an atomic resolved image of KCl ,where KCl unit cell is oriented at 45◦ with the unit cell of Ag. All the images recorded at room temperature (300 K).

Figure 3.12 shows the STM images of an ultra-thin KCl film obtained after the same deposition time (10 min) as the film in Fig. 3.11 but grown at a different substrate temperature, i.e., at 398 K. This image shows the steps of silver uniformly covered with the first KCl layer and additional randomly distributed islands (second and third layer) with rounded corners when imaged at room temperature [13]. The mass centers of these islands are located at the terraces of the first uniform layer, in contrast to the report given in reference [13], where KCl islands are located at the step edges of the first wetting layer. In the upper right corner of the image (c) we can see the atomic

structure of KCl. We selected this area and we obtain a (10 ×10 nm^2) image (see Fig. 3.12(f)) which shows that only one of the two ions is imaged (K^+ or Cl^-) ions. Moreover, the KCl has a different orientation as compared with the image in the Figs. 3.10 and 3.11, the KCl unit cell is oriented at about 45° with respect to the Ag substrate (see the atomic structure of Ag substrate in Fig. 3.10). This means that the outer edges of these domains are oriented parallel to the $[1\bar{1}0]$ and [110] axes of Ag(001). The atomic distance between the next neighbor atoms is about 0.46 ± 0.01 nm, the value is consistent with the value expected for the KCl unit cell, i.e., a = 0.445 nm.

3.3.2 KCl deposition in LT-STM setup

KCl in the form of a solid powder is evaporated from a Knudsen effusion cell inside the analysis chamber of the LT-STM setup. The deposition time is varied in the 5-11 min range while the other parameters (sample temperature and the evaporation cell temperature) are kept constant. The Ag (001) substrate temperature during all the depositions is 435 K in order to increase KCl molecule diffusion on silver during the deposition to obtain larger KCl domains [1], [2].

3.3.2.1 Growth mode, atomic structure, and unit cell orientation

The initial geometry of the KCl film is characterized by Scanning Tunneling Microscopy (STM) at low temperature (78 K). Figures 3.13 - 3.20 show STM topography images of an ultrathin KCl film grown on Ag(001) at 435 K at evaporation cell temperature of 793 K and for three different deposition times (5, 7.5, and 11 min). On all samples, our STM images show large KCl domains, exceeding 1.5 μm^2 in area and surrounded by large bare Ag(001) areas. Within these domains, the KCl film is closed ("wetting layer") and has covered the Ag(001) steps without any discontinuities. The continuity of the first layer across the Ag step edges indicates a strong interstep diffusion [13]. The outer edges of these domains are straight and oriented at $\approx 45^\circ$ to the $[1\bar{1}0]$ and [110] axes of Ag(001). As previously reported, this is consistent with KCl(001) domains having their crystallographic directions parallel to those of Ag(001) on average; KCl [011]//Ag[011] and KCl $[1\bar{1}0]$ //Ag$[1\bar{1}0]$.

- **KCl films grown after 5 minutes deposition**

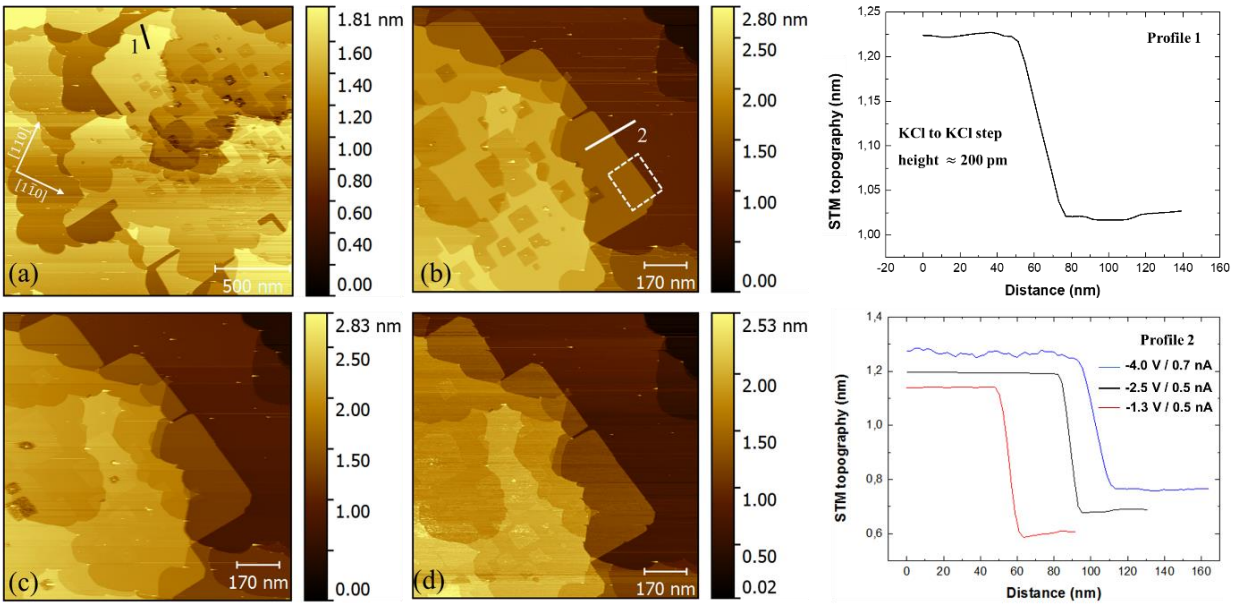

Figure 3.13: STM topography of an ultrathin KCl film grown on Ag(001) at 435 K. (a) 1410 × 1410 nm^2 (U_b = -2.5 V, I_t = 0.17 nA) , [(b) to (d)] 842 × 842 nm^2 images measured in the same area at different tip-sample biases and tunnel current setpoints: (b) U_b = -1.3 V, I_t = 0.5 nA; (c) U_b = -2.5 V, I_t = 0.5 nA; (d) U_b = -4 V, I_t = 0.7 nA. All STM images are recorded at low temperature (78 K).

Figure 3.13 shows four STM images of the ultrathin KCl film grown on Ag(001) at 435 K after 5 min deposition of KCl at evaporation cell temperature of 778 K. Image (a) is 1410 × 1410 nm^2 showing that the step of the silver is covered with an uniform layer of KCl. On the top of this layer we can see that the KCl islands have similar sizes and mainly square or rectangular shapes; these islands have side lengths in the 100 - 150 nm range.

Figure 3.13 (b)-(d) shows STM images in another area of the sample compared to the image (a). These were measured at a different lower bias voltage, U_b = -1.3 V in (b), U_b = -2.5 V in (c) and at a higher bias U_b = -4 V in (d). The KCl islands exhibit positive height contrast at U_b = -4 V, whereas this contrast is negative in image (c) and almost negligible in image (b).

We determined the local thickness of the KCl domains, i.e., the number of atomic monolayers (ML), from the apparent height measured by STM at different bias voltages [5], [6],

and we compared the measured values with previous STM [13] studies. Line profile 2 in image (b) is taken across the first wetting layer of KCl, we measured the apparent height of this wetting layer from the Ag to KCl step height. The measurement shows that this layer has the same STM height of about 0.55 nm at the three different bias voltages: -1.3 V at (b), -2.5 V at (c) and -4 V at (d), so we assign this thickness to 3 ML of KCl layer . In contrast with our previous observation for the growth of NaCl on Ag(001) taken at positive sample bias, where the apparent thickness of the NaCl islands varies as the bias voltage changes. We infer that the STM contrast and apparent height does not only depend on the bias voltage but also on the bias polarity (+/-), with some contrast inversion. Müller et al [13] have reported that the first wetting layer of KCl on Ag(001) exhibited STM height of about 250 pm at bias voltage 0.84 V and the apparent height of the KCl to KCl step (next layer) was about 120 pm. At this bias voltage, due to the noted exponential decay of the gap states, the height of the next layer (islands) is expected to be significantly smaller; roughly half that of the apparent height of the wetting layer [8], [13]. Since this was not the case, they assigned the height of the wetting layer to a single KCl layer and not to a double layer. However, we measured a KCl to KCl step height of about 200 pm (see line profile 1 in the image (a)), which is smaller than the half of the wetting layer (0.55 nm), we assign the height of the wetting layer to 3 ML. In the KCl bulk unit cell, the expected height for a single layer is 318 pm, and that of the double layer at 636 pm [13].

A selected area of the image shown in Fig. 3.13(b) is shown in Fig. 3.14(a) which shows the first wetting layer with 3ML thickness. Figure 3.14(b) is a zoomed image of (a) which showing clearly the atomic structure of KCl with high resolution, and upon further zooming in the center, we can clearly see the atomic arrangement of KCl shown in 3.14(c).

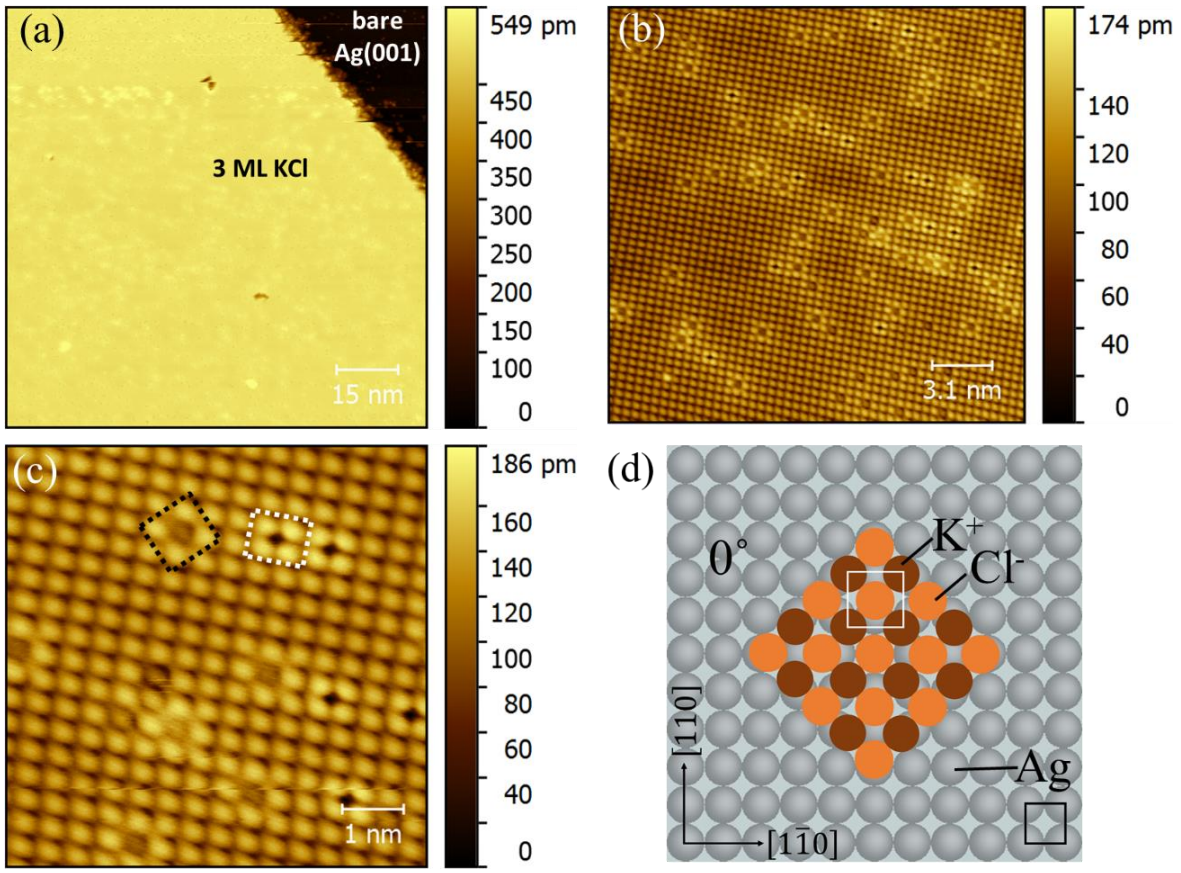

Figure 3.14: STM topography of an ultrathin KCl film grown on Ag(001) at 435 K (a) 74 × 74 nm^2 (U_b = -2.5 V, I_t = 0.2 nA),(b) 15.72 × 15.72 nm^2 (U_b = -1 V, I_t = 0.17 nA) image on the center of the image (a), (c) 5 × 5 nm^2 (U_b = -1 V, I_t = 0.17 nA) an atomic resolved image of KCl ,where KCl unit cell is parallel to the unit cell of Ag ($[0\ 0\ 1]_{Ag}$ // $[0\ 0\ 1]_{KCl}$) (0˚growth), (d) schematic representation of Ag(001) and KCl domain. All the STM images were recorded at low temperature (78 K).

The KCl unit cell is parallel to the Ag unit cell ([0 0 1] Ag // [0 0 1] KCl) corresponding to 0˚growth, with an atomic distance between the next neighbor atoms of about 0.44 ± 0.01 nm. This value is consistent with the value expected for the primitive unit cell of KCl, i.e., a = 0.445 nm. Because the surface grown here was exposed to the electron beam of the LEED for few seconds before STM measurement, the KCl atomic structure shows two different kinds of defects that are either composed of 4 bright atoms of the square lattice with a dark center or an atom of the lattice that has a lower DOS than its neighbors (in the form of a cross) (see Fig. 3.14 (b) and (c)). These

could be K and Cl vacancies (removed atoms), respectively or Cl vacancies in the second layers (dark centers) or in the top layer (cross).

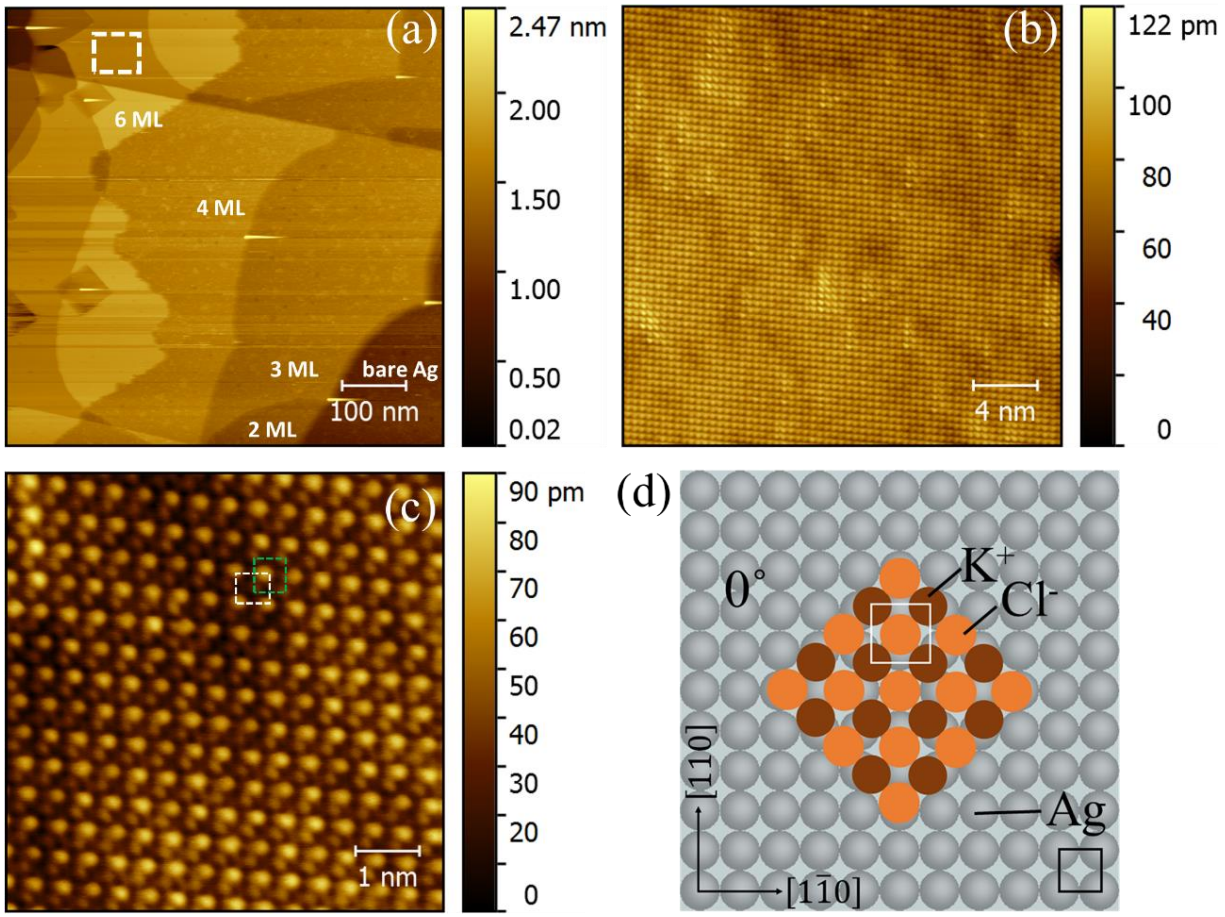

Figure 3.15: STM topography of an ultrathin KCl film grown on Ag(001) at 435 K (a) 500 × 500 nm^2 (U_b = -2.5 V, I_t = 0.7 nA), (b) 20 × 20 nm^2 (U_b = -1.79 V, I_t = 0. 7 nA) image of the selected area in the image (a) which shows the atomic resolution of KCl , (c) 5 × 5 nm^2 (U_b = -0.5 V, I_t = 0.2 nA) is a zoomed image of the image (b) ,where KCl unit cell is parallel to the unit cell of Ag ($[001]_{Ag}$ // $[001]_{KCl}$) (0˚growth), (d) schematic representation of Ag(001) and KCl domain. All the images recorded at low-temperature STM (78 K).

Figure 3.15 shows the STM images of another area with the same growth conditions as the previous images. The large-scale area in image (a) shows the silver steps covered with KCl. We selected an area on the top of the KCl layer in this image and we obtained the 20 × 20 nm^2 image shown in (b) that reveals the atomic structure of KCl. The image in (c) is a zoomed image of (b)

with a size of 5 × 5 nm^2. The image shows that the unit cell of KCl is aligned with the unit cell of Ag(001) (0˚ growth mode) as illustrated in (d). There are two possibilities to explain image (c). One of them is that we were able to image both of the K^+ and Cl^- ions, which is already observed in our previous experiment for the KCl growth on Ag(001) in the RT-STM setup (see Fig. 3.11). We measure the atomic distance for both ions, and we found that it is about 0.430 ± 0.007 nm for one species of ions (white dotted line) and for the other species of ions, it is about 0.437 ± 0.015 (green dotted line). In both cases, the value is consistent with the value expected for the unit cell of KCl, i.e., a = 0.445 nm. Another possibility is perhaps due to a double tip effect when the tip has at least two atoms on its apex. The smaller feature does not fall in the center of the lattice formed by the bigger feature; thus, it could be an artifact due to an additional atom on the tip.

- **KCl films grown after 7.5 minutes deposition**

Figures 3.16 and 3.17 show a series of STM images of an ultrathin KCl film grown on Ag(001) at 435 K after 7.5 min deposition of KCl at evaporation cell temperature of 778 K. In figure 3.16, the images are recorded on different areas of the sample and show that as the quantity of KCl increases the size and the density of the first wetting layer and the next layers increase in comparison with the previous deposition in Figs. 3.13 - 3.15. This is in agreement with the reported growth of a thin insulating layer of NaCl on Ag(001) by Cabailh et al [1]. One can observe from these images, that the growth of KCl on Ag(001) is Layer-plus-island (Stranski-Krastanov mode). In all images, the first wetting layer always appears to be composed of 3 ML, whereas subsequent layer has two growth modes, either island growth or layer growth (see Fig. 3.16 and Fig. 3.17), for the third layer always forms an island.

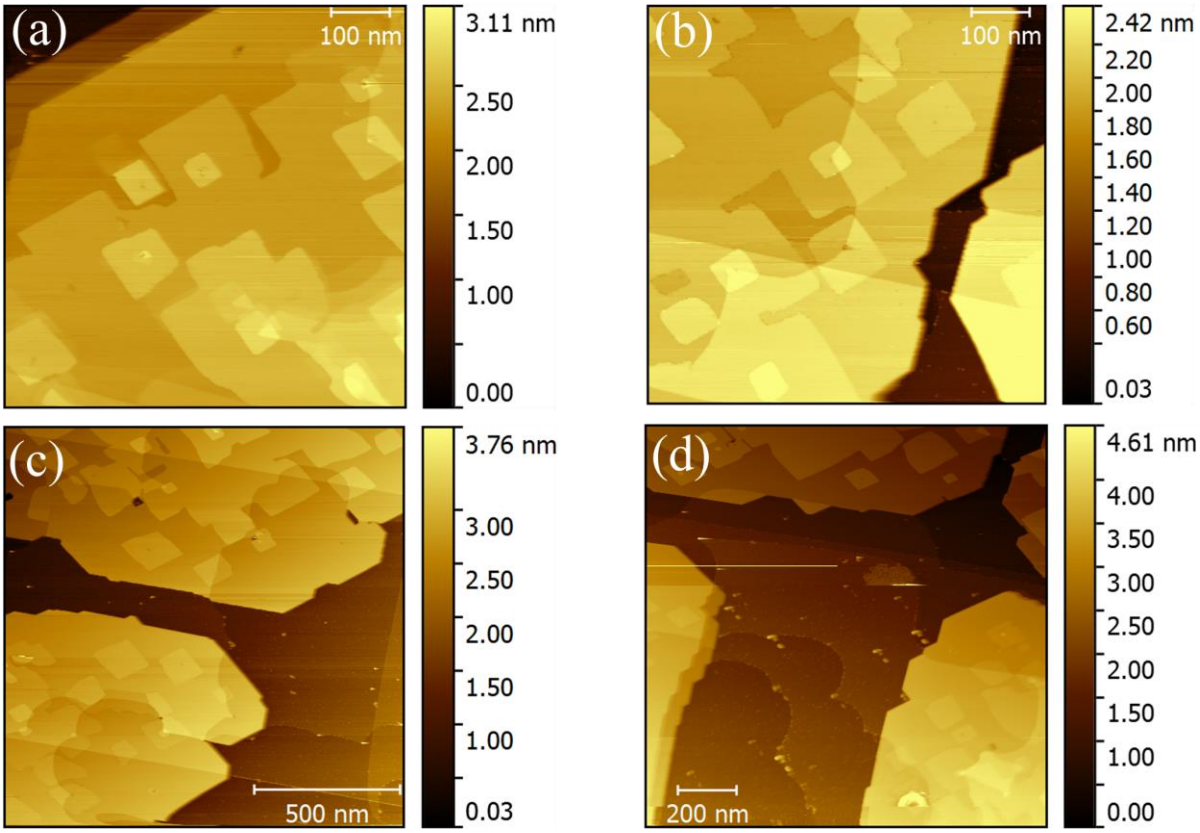

Figure 3.16: STM topography of an ultrathin KCl film grown on Ag(001) at 435 K at different areas of the sample. (a) and (b) 500 × 500 nm^2 (U_b = 4 V, I_t = 0.7 nA), (c) and (d) 1000 × 1000 nm^2 (U_b = 4 V, I_t = 0.7 nA). All STM images are recorded at low temperature (78 K).

Figures 3.17 shows STM images of the same area of the sample measured with the different bias voltages, a lower bias U_b = 2.5 V in (a), and a higher bias U_b = 4 V in (b). We determined the local thickness of the KCl domains, i.e., the number of atomic monolayers (ML), from the apparent height measured by STM at different bias voltages [5], [6], and we compared it with previous STM studies [13]. Profile 1 crosses a 3 monolayer (ML)-thick KCl wetting layer, and 4-ML, 5-ML, and 6-ML KCl domains of an island, which in addition features a defect or aggregate at the top. At low bias voltage (U_b = 2.5 V), in the area shown in Fig. 3.17(a) we measure STM heights of 0.68, 0.77, 0.89, and 0.97 nm, that we assign to thicknesses of 3, 4, 5, and 6 ML. At the higher bias voltage U_b = 4 V (see Fig. 3.17(b)) an STM height of the first wetting layer 3 ML KCl/Ag(001) is measured at 1.70 nm and the apparent thickness of the next KCl layers up to 6 ML is 0.30 ± 0.01 nm, which is close to their expected thickness (0.314 nm). These different values of the thickness under

different bias voltages has already been explained in our experiment for the growth of the NaCl on Ag(001) (see Fig. 3.2).

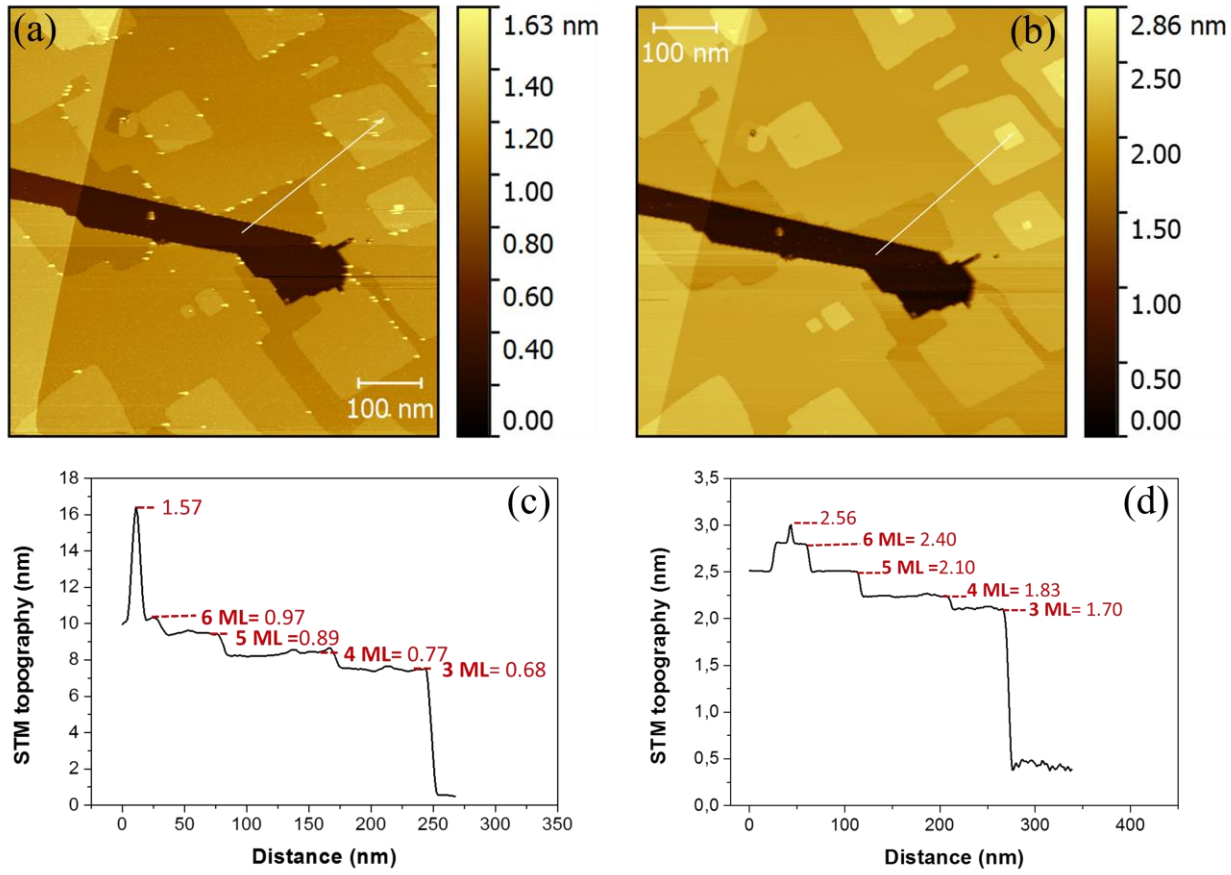

Figure 3.17: STM topography of an ultrathin KCl film grown on Ag(001) at 435 K at the same area and measured with two different bias voltage. 500 × 500 nm^2 image measured with and (U_b = 2.5 V, I_t = 0.3 nA) in (a) and with (U_b = 4 V, I_t = 0.7 nA) in (b), where (c) and (d) are apparent height profile along the line in the STM images (a) and (b) respectively. The correspondence between STM heights and numbers of KCl atomic layers (monolayer, ML) is given in inset. All STM images are recorded at low temperature (78 K).

- **KCl films grown after 11 minutes deposition**

Figures 3.18 and 3.19 show STM images of an ultrathin KCl film grown on Ag(001) at 435 K after 11 min deposition of KCl at evaporation cell temperature of 778 K. Figure 3.17 is recorded on different areas of the sample, and shows that by further increasing the quantity of KCl the size

of the KCl layer increases giving a high density of large islands. These islands have straight edges and are pinned at Ag steps and expand on both the upper and lower Ag terraces [1].

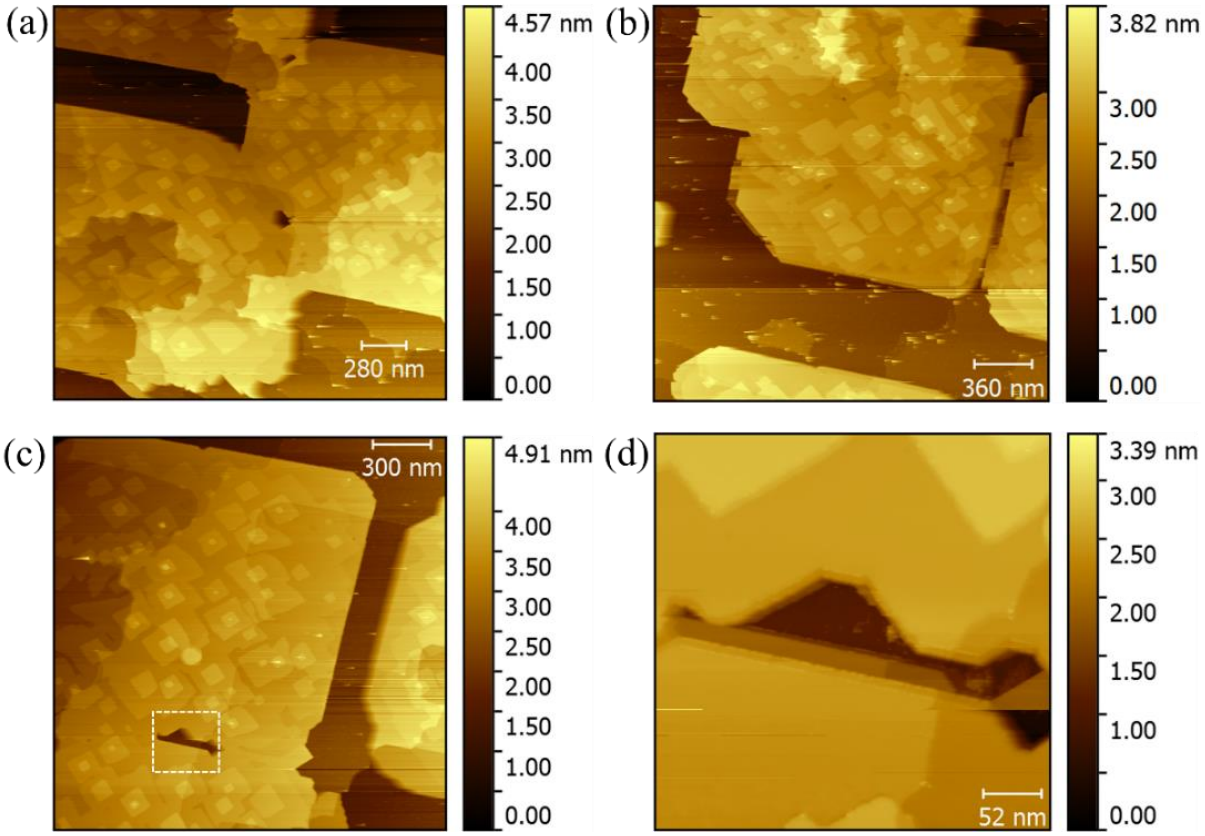

Figure 3.18: STM topography of an ultrathin KCl film grown on Ag(001) at 435 K at different areas of the sample. (a) and (b) 1800 × 1800 nm^2 (U_b = 4 V, I_t = 0.7 nA), (c) 1482 × 1482 nm^2 , and (d) 257.8 × 257.8 nm^2 all the image are scanned with (U_b = 4 V, I_t = 0.7). All STM images are recorded at low temperature (78 K).

Finally, the last figure is an area measured with two different bias voltages and with different polarity (+/-). Figure 3.19(a) shows an STM image scanned over a large area of 1800 × 1800 nm^2 and shows islands with large sizes. A selected area of the image, shown in image (a), was measured at U_b = 4 V. This area was scanned at different bias voltage in (b-d), with U_b = 4 V in (b), U_b = -2.5 V in (c) and U_b = 2.5 V in (d). Image (b) shows a double tip effect because we see copies of the layers overlaid on top of each other, displaced by a few nanometers. The first wetting

layer 3 ML KCl/Ag(001) exhibits an apparent STM height of 1.09 nm at U_b = 4 V, 0.69 nm at U_b = 2.5 V, and 0.493 nm at U_b = -2.5 V.

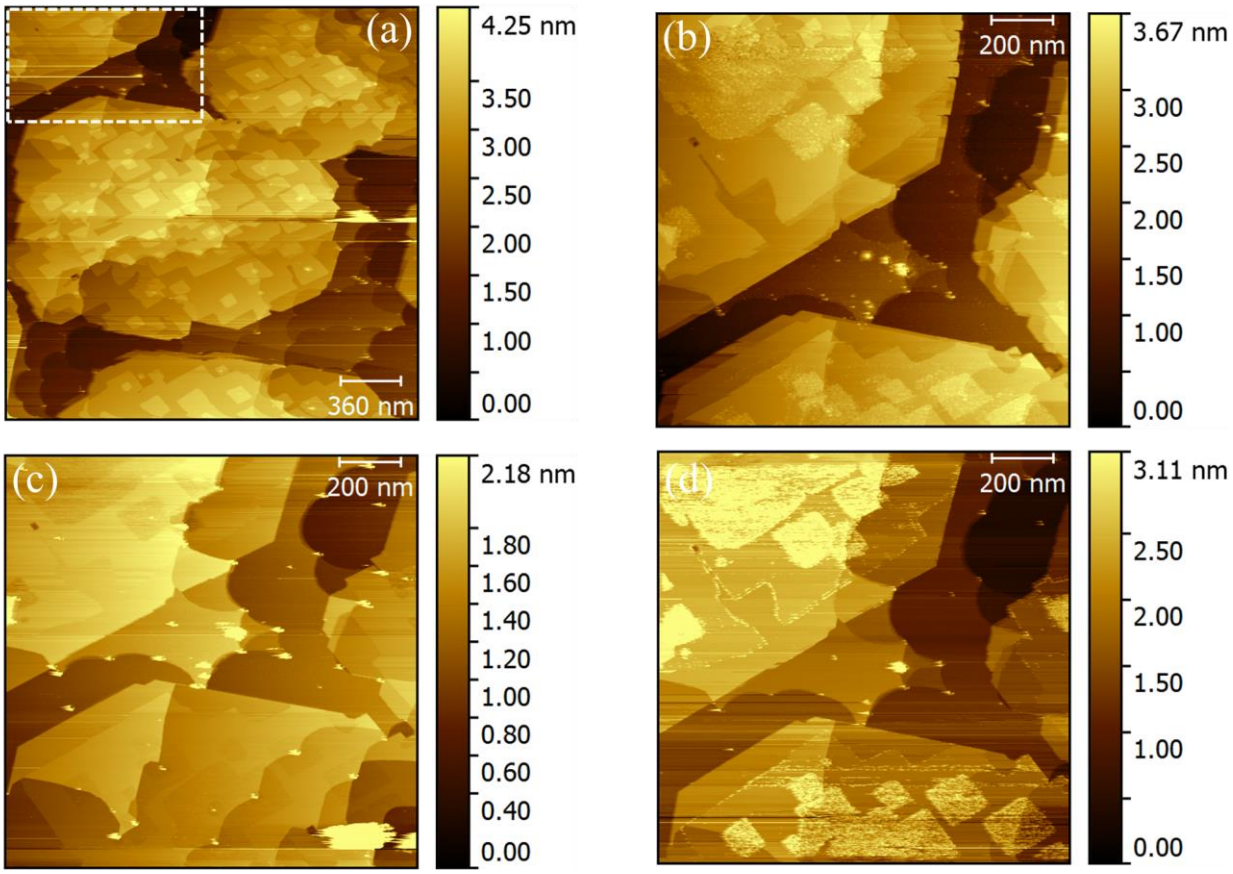

Figure 3.19: STM topography of an ultrathin KCl film grown on Ag(001) at 435 K. (a) 1800 × 1800 nm^2 (U_b = 4 V, I_t = 0.7 nA), (b-d) 979 × 979 nm^2 of the selected area in the image (a) scanned with different bias voltage , (U_b = 4 V, I_t = 0.7 nA) in (b), (U_b = -2.5 V, I_t = 0.5 nA) in (c) and (U_b = 2.5 V, I_t = 0.5 nA) in (d). All STM images are recorded at low temperature (78 K).

As we can see the apparent STM height at ± 2.5 V shows almost the same height as compared with the height at 4V, whereas their contrast is different, a positive height contrast in image (d) and a negative contrast in image (c). This observation was already seen in Fig. 3.13 for the growth of KCl on Ag(001) for 5 minutes. This indicates that the STM contrast and apparent height not only depend on the bias voltage but also on the bias polarity (+/-), with some contrast inversion. Finally, we infer for KCl films prepared in the LT-STM setup with different deposition times that the unit cells of KCl and Ag(001) are aligned. One particular orientation (0˚ orientation

with respect to the Ag substrate) is observed. For the KCl films prepared in the RT-STM setup, the KCl unit cell exhibit two particular orientations (0˚ and 45˚ orientations with respect to the Ag substrate). In both cases, no rotational mosaicity was observed contrary to the case of NaCl on Ag(001). This is in agreement with the growth the KCl on Ag(001) already reported by Müller et al [13].

3.4 Conclusions

In conclusion, The NaCl and KCl thin-film growth on Ag(001) as a function of temperature and quantity of these thin-films system are described and discussed in this chapter. The NaCl film is composed of large crystalline islands (Wolmer-Weber growth mode), whereas we observe that the growth of KCl on Ag(001) is Layer-plus-island (Stranski-Krastanov mode). The NaCl islands exhibit side lengths in the 100 - 200 nm range and mainly square or rectangular shapes, with rounded corners for the thinnest of them. By increasing the amount of NaCl for the same cell temperature, the NaCl films reveal similar features with larger side lengths, in the 200–500 nm range. As the substrate temperature or the amount of NaCl increases during deposition, the size and the density of the island and ad-islands also increase. These features were also observed for the KCl films. In addition, the NaCl island edges exhibit various orientations with respect to the substrate axes, in agreement with previously reported azimuthal mosaicity. The KCl domain exhibits two particular orientations (0˚ and 45˚ with respect to the Ag substrate), and no rotational mosaicity was observed contrary to the case of NaCl on Ag(001). Otherwise, we observe a pronounced Moiré pattern of NaCl with a periodicity of about 2.2 nm for the films grown at 413 K, which we assigned to the mismatch between the ad-layer and substrate.

On the other hand, the apparent layer thickness of the grown NaCl and KCl ultrathin layer measured by STM at different bias voltages show that these thicknesses are bias dependent. At low bias voltage (U_b = 1 V), the STM measurements show that the apparent thickness of the atomic NaCl layers is lower than their true thickness, because at this low bias the electrons tunnel from the tip to metal-induced gap states at the NaCl/Ag(001) interface as already demonstrated in the STM spectroscopy and the atomic-resolution STM images. In contrast, at a higher bias voltage U_b = 4 V, the apparent thickness of the atomic NaCl layers show that they are close to their true thickness, because in these conditions, electrons tunnel to an image potential state in front of the

Ag(001) surface, which is possible at U_b = 4 V because the first field emission resonance is shifted in energy from about 4.5 eV to 3.3 eV upon NaCl adsorption. Moreover, from the observed STM images of the KCl growth, we infer that the STM contrast and apparent height not only depends on the bias voltage but also on the bias polarity (+/-), with some contrast inversion.

3.5 Bibliography

[1] G. Cabailh, C. R. Henry, and C. Barth, "Thin NaCl films on silver (001): island growth and work function," *New J. Phys.*, vol. 14, no. 10, p. 103037, 2012.

[2] H.-C. Ploigt, C. Brun, M. Pivetta, F. Patthey, and W.-D. Schneider, "Local work function changes determined by field emission resonances: NaCl/Ag(100)," *Phys. Rev. B*, vol. 76, no. 19, p. 195404, Nov. 2007.

[3] M. Pivetta, F. Patthey, M. Stengel, A. Baldereschi, and W.-D. Schneider, "Local work function Moiré pattern on ultrathin ionic films: NaCl on Ag(100)," *Phys. Rev. B*, vol. 72, no. 11, p. 115404, Sep. 2005.

[4] E. Le Moal, M. Müller, O. Bauer, and M. Sokolowski, "Misfit driven azimuthal orientation of NaCl domains on Ag(100)," *Surf. Sci.*, vol. 603, no. 16, pp. 2434–2444, 2009.

[5] W. Hebenstreit, J. Redinger, Z. Horozova, M. Schmid, R. Podloucky, and P. Varga, "Atomic resolution by STM on ultra-thin films of alkali halides: experiment and local density calculations," *Surf. Sci.*, vol. 424, no. 2, pp. L321–L328, 1999.

[6] Q. Guo, Z. Qin, C. Liu, K. Zang, Y. Yu, and G. Cao, "Bias dependence of apparent layer thickness and Moiré pattern on NaCl/Cu(001)," *Surf. Sci.*, vol. 604, no. 19, pp. 1820–1824, 2010.

[7] R. Arita, Y. Tanida, K. Kuroki, and H. Aoki, "Electronic properties of metal-induced gap states at insulator/metal interfaces: Dependence on the alkali halide and the possibility of excitonic mechanism of superconductivity," *Phys. Rev. B*, vol. 69, no. 11, p. 115424, Mar. 2004.

[8] M. Kiguchi, G. Yoshikawa, S. Ikeda, and K. Saiki, "Electronic properties of metal-induced gap states formed at alkali-halide/metal interfaces," *Phys. Rev. B*, vol. 71, no. 15, p. 153401, Apr. 2005.

[9] X. Sun, M. P. Felicissimo, P. Rudolf, and F. Silly, "NaCl multi-layer islands grown on Au(111)-(22× √3) probed by scanning tunneling microscopy," *Nanotechnology*, vol. 19, no. 49, p. 495307, 2008.

[10] X. Sun and F. Silly, "NaCl islands decorated with 2D or 3D 3,4,9,10-perylene-tetracarboxylic-dianhydride nanostructures," *Appl. Surf. Sci.*, vol. 256, no. 7, pp. 2228–2231, 2010.

[11] J. Kramer, C. Tegenkamp, and H. Pfnür, "The growth of NaCl on flat and stepped silver surfaces," *J. Phys. Condens. Matter*, vol. 15, no. 38, p. 6473, 2003.

[12] K. Aït-Mansour, M. Bielmann, O. Gröning, P. Ruffieux, R. Fasel, and P. Gröning, "(2×1)-Na surface reconstruction induced by NaCl dissociation on Ag(110) during LEED analysis," *Appl. Surf. Sci.*, vol. 252, no. 18, pp. 6368–6374, 2006.

[13] M. Müller, J. Ikonomov, and M. Sokolowski, "Structure of Epitaxial Layers of KCl on Ag(100)," *Surf. Sci.*, vol. 605, no. 11, pp. 1090–1094, 2011.

Chapter 4

Reaction Kinetics of Ultrathin NaCl Films on Ag(001) upon Electron Irradiation

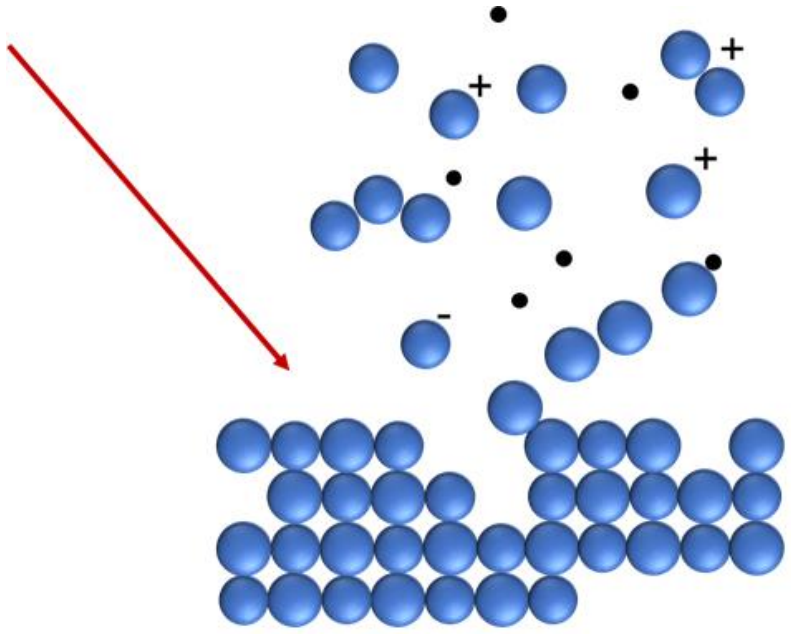

Table of Contents

4.1 Introduction:

In this chapter, we report on the reaction kinetics of ultrathin NaCl films grown on Ag(001) under irradiation with the electron beams of a LEED (primary electron energy 52–60 eV) and an AES (3 keV). Here, LEED and AES are used both to induce NaCl dissociation and to monitor the structural and chemical modifications of the sample surface. In addition, scanning tunneling microscopy (STM) is used to compare the topography of the as-grown and irradiated NaCl films. We observe that Cl depletion follows different reaction kinetics, as compared to previous studies on thick NaCl films and bulk crystals. Na atoms produced from NaCl dissociation diffuse to the bare areas of the Ag(001) surface, where they form Na-Ag superstructures that are known for the Na/Ag(001) system. Thus, we analyze the reaction kinetics and retrieve the rate constant of Cl depletion, and we propose models for the morphological evolution of the irradiated film and the formation of Na-Ag superstructures.

4.2 Cl Depletion Kinetics

The method employed to make semi-quantitative comparisons of the nominal thicknesses of the NaCl films is based on the intensity ratio of the chlorine and silver AES peaks. This is used to measure the changes in the Cl concentration.

The chemical modification of an ultrathin NaCl film upon electron irradiation is investigated using AES. We monitor the evolution of the Cl/Ag peak ratio as a function of the time that the sample is exposed to the 3 keV electron beam of the AES and we compare the results obtained for various film thicknesses. For the peak ratio, we use the peak-to-peak intensity of the Cl *LV V* and Ag M_4NN Auger lines, which lie at 181 eV and 358 eV, respectively. Fig. 4.1(a) shows one set of these data. We see in this graph that electron irradiation has induced Cl depletion. Moreover, the data can be fitted very well with a mono-exponential decay function with time $Cl/Ag(t) = \alpha+\beta \exp(-\gamma t)$, where α is a constant, β is the decay amplitude and γ is the decay rate coefficient. Analysing all the data sets in this way provides statistics on the reaction kinetics. Fig. 4.1(b) shows two spectra for the film in Fig. 4.1(a). In the first measurement at t=0, the ratio of Cl/Ag peak is 0.5. We can see clearly the high intensity of the chlorine peak at the very beginning of the irradiation (red spectrum). As the exposure time increases, the intensity of this peak

decreases and keeps decreasing gradually afterward. While after 8.5 min of exposure the Cl/Ag peak ratio is only 0.06 (blue spectrum).

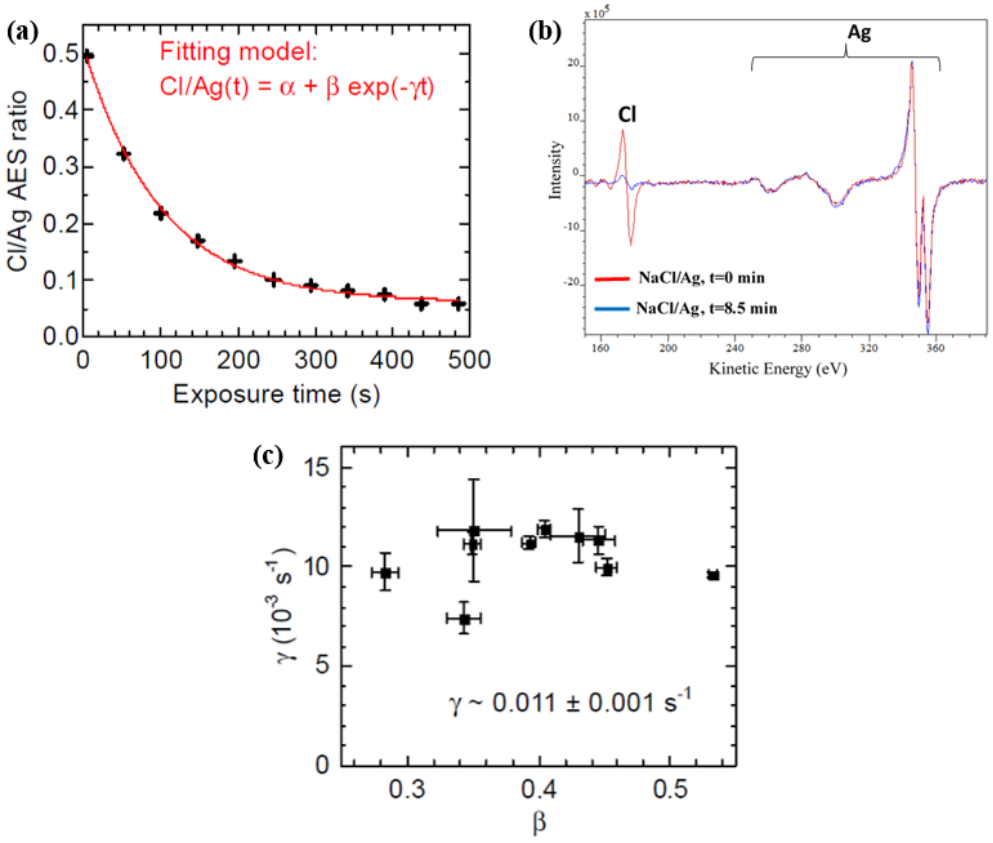

Figure 4.1: NaCl dissociation dynamics upon irradiation with the 3 keV electron beam of an AES. (a) Temporal evolution of the intensity ratio between the Cl and Ag AES peaks taken at Auger electron energies of 181 and 358 eV, respectively, versus irradiation time. Sample current is 0.5 ± 0.2 μA and beam spot area is about 1 mm^2. The experimental data are fitted using a mono-exponential decay model. (b) Statistics on the model parameters gives a mean decay rate coefficient $\langle\gamma\rangle = 0.011 \pm 0.001\ s^{-1}$ with no significant dependence of γ on the decay amplitude β. The data shown in this figure have been obtained for NaCl films grown on Ag(001) at 500 K.

Figure 4.1(c) shows the results obtained for the NaCl films grown on Ag(001) at 500 K. The decay rate coefficient γ is plotted versus the amplitude β of the decay, which is related (if neglecting the offset by α) to the NaCl film thickness. A mean decay rate coefficient $\langle\gamma\rangle = 0.011 \pm 0.001\ s^{-1}$ is found (i.e., a mean lifetime $\langle\tau\rangle = \langle \gamma^{-1} \rangle = 96 \pm 15\ s^{-1}$), with no significant

dependence on β. Thus, Cl depletion induced by electron irradiation in ultrathin NaCl films apparently follows first-order reaction kinetics during the first few hundreds of seconds. The offset $\alpha > 0$ in the fit, however, indicates that part of chlorine available at the surface remains at longer irradiation times or is not depleted with the same efficiency (e.g., due to the geometry of the irradiated film).

A pure first-order reaction would indeed proceed at a rate d[Cl]/dt that linearly depends on Cl concentration, as follows:

$$-\frac{d[Cl]}{dt} = k[Cl] \qquad (1)$$

$$[Cl](t) = [Cl](0)e^{-kt} \qquad (2)$$

Where the reaction rate coefficient *k* can be equated with γ. This is the ideal case of a surface reaction where the reaction rate coefficient *k* is independent of the surface coverage. There, no offset occurs and the concentration of reactants mono exponentially decays to zero at infinite time. Nevertheless, we can estimate the efficiency of the electron interaction with NaCl, for the part that behaves like a first-order reaction, using Fig. 4.1(c) and Eq. 1.

During AES measurements, the sample current is measured at 0.5 ± 0.2 μA and the electron beam spot has a diameter of about 1 mm^2, which corresponds to an incident electron flux φ_e of about 4×10^{12} electron mm^{-2} s^{-1}. This is compared with the surface density of Cl atoms ρ_{cl} in the NaCl(001) plane of about 6×10^{12} mm^{-2}. Thus, we obtain for a surface coverage of 1 ML, a depletion rate $k\rho_{cl}\varphi_e^{-1}$ of about one Cl atom per sixty incident electrons.

4.3 Surface reconstruction and Na atom ordering

Controlling the outcomes of the reaction, i.e., selecting the superstructures that result from the electron-induced dissociation of alkali-halide thin films, is key in the perspective of applications. Here, we show that this aspect is strongly related to the reaction kinetics since various superstructures occur during the course of the reaction.

Remarkably, we observe all the superstructures that have been reported in previous studies of Na deposition on Ag(001), each occurring at different steps of NaCl dissociation and with some dependence on the initial NaCl film thickness. Below, we show the results obtained from the NaCl films grown on Ag(001) at 500 K, which we then compare with the results obtained from those grown at 413 K (shown in Fig. 4.3).

Figure 4.2 shows experimental LEED images measured at different times during the reaction induced by the incident low-energy (52 eV) electrons. AES measurements carried out afterward on different (not previously irradiated) areas of the sample indicate Cl/Ag peak ratios of 0.2 and 0.5 for the NaCl films examined in Figs. 4.2 (a) and (d), respectively. In the first seconds of irradiation [see Fig. 4.2(a)], the LEED pattern exhibits nothing but the diffraction spots of the substrate and those of the NaCl film. The latter confirms our STM observations, i.e., the presence of (001)-terminated NaCl domains with parallel orientation
with respect to Ag(001) on average and low azimuthal mosaicity (elongated shape of the NaCl spots). Soon after, the first-order diffraction spots of a $p(2 \times 1)$ superstructure (and of its rotation-invariant) appear [see Fig. 4.2(b)]. Comparison with previous work on Na adsorption on Ag(001) [1] allows the $p(2 \times 1)$ super-structure to be assigned to a missing-row reconstruction of the Ag(001) surface.

As the sample is further irradiated, additional super structures are observed, which differ depending on the initial film thickness. In addition, the relative intensity of the background in the LEED images increases, which indicates an increasing disorder. The electron-induced disorder in the NaCl film is discussed further in Sec. 4.4.

In Fig. 4.2, the background is subtracted from the LEED images in order to improve the visibility of the diffraction spots of the ordered structures. In the LEED image shown in Fig. 4.2(c), which was recorded 218 s after that shown in Fig. 4.2(b), the NaCl spots have almost completely vanished and the pattern of an incommensurate structure is observed. The latter is characterized by weak and slightly elongated spots, as illustrated in the model. Such features have already been reported for the Na/Ag(001) system [2], and are interpreted as linear incommensurate chains of Na atoms ordered along the missing rows of the reconstructed silver surface. When a slightly thicker NaCl film is irradiated, we observe that the incommensurate structure mentioned above coexists with a commensurate $p(3 \times 3)$ [see Fig. 4.2(d)] or $p(4 \times 2)$ structure [see Fig. 4.4(b)].

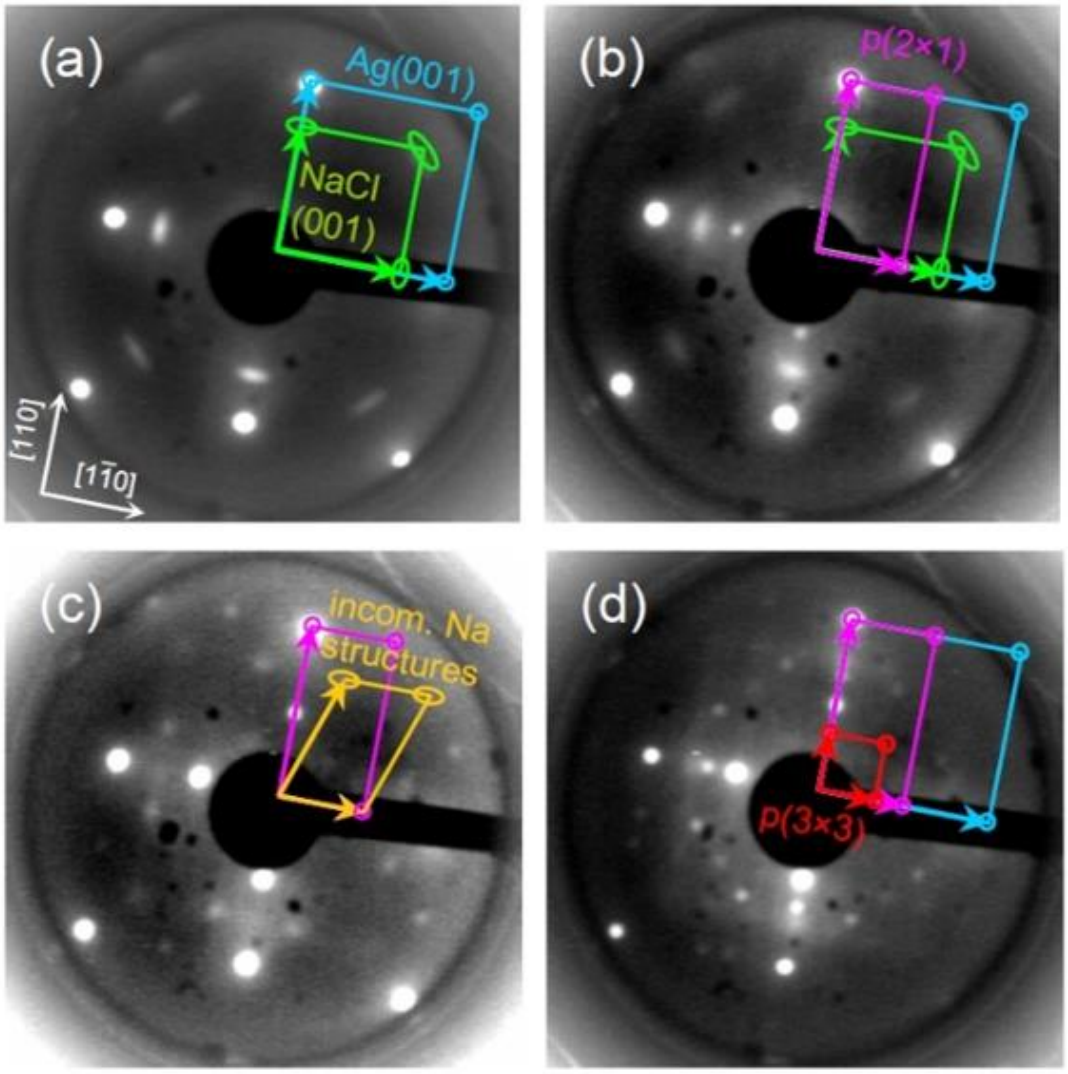

Figure 4. 2: Background-subtracted LEED images, obtained from ultrathin NaCl films grown on Ag(001) at 500 K. (a) NaCl on Ag(001) before dissociation. (b) Appearance of a *p*(2 × 1) structure in the early steps of NaCl dissociation, attributed to missing row reconstruction of the substrate surface. (c) Longer exposure to low-energy electrons (images b and c are separated in time by 218 s) yields an almost complete disappearance of the NaCl spots and an appearance of an incommensurate structure (weak elongated spots), attributed to 1D chains of Na atoms adsorbed on the reconstructed substrate. (d) Starting from a thicker NaCl film yields a *p*(3 × 3) structure, which is associated with the formation of an ordered Ag-Na surface alloy. All LEED images were measured at an electron energy 52 eV, except (d) recorded at 49 eV.

In a previous study of the Na/Ag(001) system, the (3 × 3) superstructure was identified as a 2D ordered Na-Ag surface alloy [1]. This results from a different type of missing-row reconstruction of Ag(001), where every third atomic row along the two orthogonal directions of the top substrate layer is substituted by Na atoms. The (4 × 2) superstructure has also been produced through Na deposition on Ag(001), but its precise nature has not yet been elucidated.

Conducting similar experiments on the NaCl films grown at 413 K yields similar results as those detailed above (see Fig. 4.3), excepted that the (4 × 2) superstructure and the incommensurate chains are not observed within the investigated irradiation time (500 s). In addition, the (3 × 3) superstructure is only visible for the thickest film (30 min deposition), which confirms the dependence on the film thickness and/or geometry.

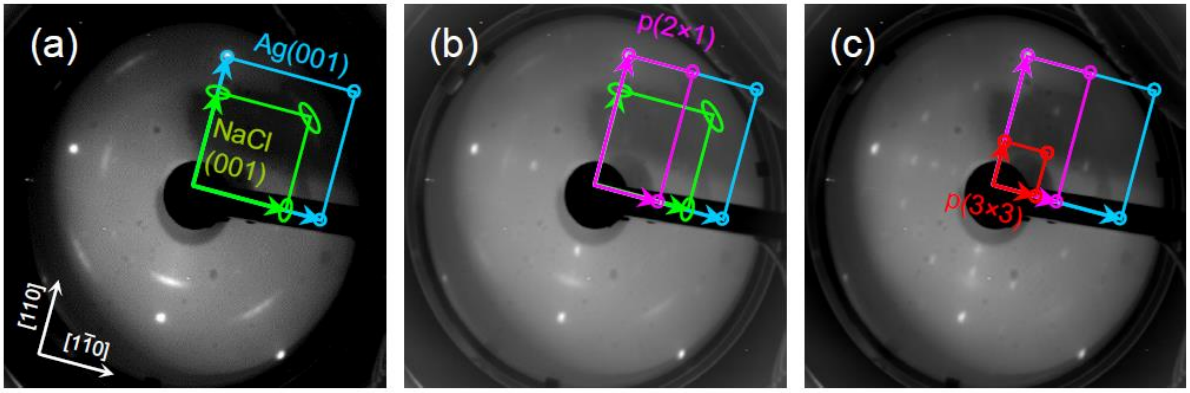

Figure 4. 3: LEED images, obtained from an ultrathin NaCl film grown on Ag(001) at 413 K. (a) NaCl on Ag(001) before dissociation. (b) Appearance of a *p*(2 × 1) structure after 100 s electron irradiation, attributed to the missing-row reconstruction of the substrate surface. (c) Longer exposure to low-energy electrons (from 330 s to 495 s) yields almost complete disappearance of the NaCl spots and appearance of a *p*(3 × 3) structure, which is associated with the formation of an ordered Ag-Na surface alloy. All LEED images measured at electron energy 52 eV.

Figure 4.3 shows experimental LEED images measured on an ultrathin NaCl films grown on Ag(001) at 413 K, at different times of the reaction induced by the incident low-energy (52 eV) electrons. These LEED data are obtained from the thicker of the two NaCl film samples grown at 413 K that we consider in this study (grown after 30 min deposition of NaCl at an evaporation

cell temperature of 793 K). In the first seconds of irradiation [see Fig. 4.3(a)], the LEED pattern exhibits nothing but the diffraction spots of the substrate and those of the NaCl film. The latter confirms our STM observations, i.e., the presence of (001)-terminated NaCl domains with comparatively high azimuthal mosaicity [3] (elongated shape of the NaCl spots), as compared to the NaCl films grown at 500 K [see Fig. 4.2(a)]. The image shown in Fig. 4.3(b) is measured after about 100 s irradiation with the electrons of the LEED. The first-order diffraction spots of a $p(2 \times 1)$ superstructure (and of its rotation-invariant) are visible, which is assigned to a missing-row reconstruction of the Ag(001) surface induced by Na adsorption on Ag(001) [1]. The image shown in Fig. 4.3(c) is obtained by averaging the LEED images over the irradiation time from 330 to 495 s. The NaCl spots have almost completely vanished and the spots of the (2×1) pattern remain. In addition, we observe a commensurate $p(3 \times 3)$ structure, which is ascribed to a 2D ordered Na-Ag surface alloy [1].

4.4 Kinetics of structural changes

Upon electron irradiation, both the chemical and the structural properties of the ultrathin NaCl films evolve, producing different LEED patterns in a time sequence. Interestingly, these diffraction patterns can be assigned to superstructures previously reported for the Na/Ag(001) system. We show below that they appear in a specific time order, with some of the superstructures occurring simultaneously and others sequentially. This is revealed by monitoring the diffraction spot intensity while irradiating the sample using the LEED.

Figure 4.4 shows the results obtained for two ultrathin NaCl films grown on Ag(001) at 500 K, which differ by a factor ≈ 4 in nominal thickness according to AES measurements, with a Cl/Ag(t = 0) ratio of 0.5 for the film shown in Figs. 4.4(a) to 4.4(c) and 0.12 for that in Fig. 4.4(d). At time t = 0 (before any irradiation), the LEED patterns exhibit the expected Ag(001) and NaCl(001) spots. On the thicker NaCl film, a rapid onset of the $p(2 \times 1)$ superstructure is observed almost from the beginning of the irradiation. On both NaCl films considered in Fig. 4.4, the intensity of the $p(2 \times 1)$ LEED pattern varies with time and its time derivative abruptly changes value (or even sign) during the first 400 s of irradiation before it seemingly reaches a plateau.

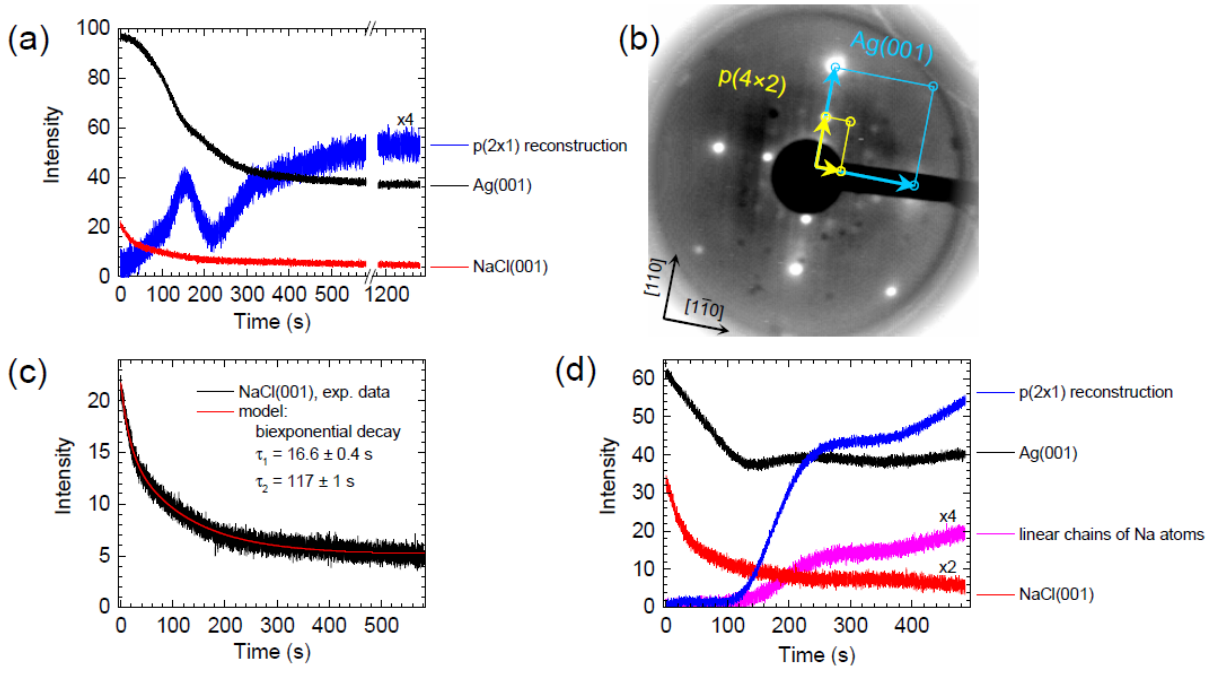

Figure 4. 4: LEED spot intensity versus time, measured on ultrathin NaCl films grown on Ag(001) at 500 K. [(a),(c),(d)] Temporal variations of the diffraction spots upon irradiation with the electron beam of the LEED. The intensity of the $(\bar{1},0)$ spots is monitored for the Ag(001) surface and its *p*(2 × 1) missing-row reconstruction and for the (001)-terminated NaCl film, whereas the intensity is averaged over several spots for the linear incommensurate chains of Na atoms. In (a), the time axis features a 600 s break during which the electron beam is blocked, before irradiation restarts at t ≈ 1180 s. (b) Background-subtracted LEED image recorded at electron energy 60 eV during the same experiment as in (a) at t ≈ 1250 s and revealing a *p*(4 × 2) superstructure. In (c), the temporal variation of the NaCl spot intensity [same data as in (a)] is fitted with a biexponential decay function with optimized short (τ_1) and long (τ_2) time constants. In order to improve visibility, some of the data are multiplied by 2 or 4 [when indicated in (a) and (d)]. As a relative thickness indication, AES measurements give Cl/Ag(t = 0) at 0.5 for the NaCl film considered in (a) to (c) and 0.12 for that used in (d). LEED measurements and irradiation were conducted at an electron energy of 60 eV for the thicker film and 53 eV for the thinner one.

In Fig. 4.4(a), the sample is irradiated for 580 s and then the electron beam is blocked for 600 s; after this period, the sample is exposed again to electrons and we measure the LEED image shown in Fig. 4.4(b). The intensity values before and after the break in Fig. 4.4(a) are comparable; at most, the curves continue to converge to their horizontal asymptotes while the sample is unexposed, presumably due to diffusion processes. In addition, the *p*(4 × 2) measured at t = 1250 s is already visible at t = 575 s (not shown), yet with a slightly lower contrast. Overall, electron irradiation seems not necessary to maintain the irradiation-induced superstructures, once a stationary state is reached.

We have reproduced these experiments on several ultrathin NaCl films grown at 500 K differing in nominal thickness and we have systematically observed the following features. Firstly, the LEED spots assigned to the *p*(2 × 1) surface reconstruction and the linear chains of Na atoms adsorbed in the missing rows of the reconstructed surface vary in intensity with irradiation time in the same way. As seen in Figs. 4.4(d), their respective curves change slope simultaneously. The intensity of the LEED spots related to the linear Na chains is much weaker than that of the (2 × 1) reconstruction, which hampers their observation on the investigated NaCl thicknesses, especially when the background level due to the disordering of the film is comparatively strong.

Secondly, the *p*(3 × 3) structure ascribed to surface alloying shows up later than the two above-mentioned superstructures. Finally, we observe that the intensity of the NaCl(001) spots decreases upon electron irradiation following a bi-exponential decay function over time. Attempts to fit the data with a mono-exponential model fail to correctly reproduce the first ≈ 50 s of the decay and tri- (or higher) exponential models lead to arbitrary results (i.e. totally dependent on the initial fit parametrization). The analysis of the data from Fig. 4.4(a) is shown in Fig. 4.4 (c), where the short (τ_1) and long (τ_2) time constants of the exponential decay retrieved from the fit are given. On average over nine sets of data, we obtain $<\tau_1> = (1.6 \pm 0.9) \times 10^1$ s and $<\tau_2> = (1.1 \pm 0.5) \times 10^2$ s, with a mean ratio $<\tau_1/\ \tau_2> \approx 0.10$. Expressed in terms of a fast γ_1 and a slow γ_2 rate coefficients, these read $<\gamma_1> = 0.09 \pm 0.06$ s^{-1} and $<\gamma_2> = 0.011 \pm 0.005$ s^{-1}, respectively. At the electron energy and emission current used for the LEED measurements shown in Fig. 4.4(c), the sample current is evaluated at 0.6 ± 0.2 μA and the electron beam spot has a diameter of about 1 mm^2. This corresponds to an incident electron flux φ_e of about 5×10^{12} electron mm^{-2} s^{-}

[1], which is similar to that used for AES operations described in Sec. 4.1. The electron mean free path in NaCl, however, is dependent on the incident electron energy and may thus be very different in LEED and AES experiments.

Figure 4.5 shows the results of similar experiments carried out on the NaCl films grown at 413 K. In Figs. 4.5(a) and 4.5(b), the NaCl films differ by their nominal thickness, the latter being the thicker. The same time sequence as for the films grown at 500 K is presented in Fig. 4.5(b), with a similar time evolution in the intensity variations of the LEED spots. We observe intensity variations in the LEED pattern of the $p(3 \times 3)$ structure during electron irradiation, which are temporally off-set with respect to those of the (2×1) surface reconstruction, possibly due to a competition in their respective development. The NaCl spot intensity in Fig. 4.5(b) exhibits a fast decay ($\gamma_1 \approx 0.02$ s^{-1}) during the first 120 s of irradiation, followed by a comparatively much slower decay (almost a plateau).

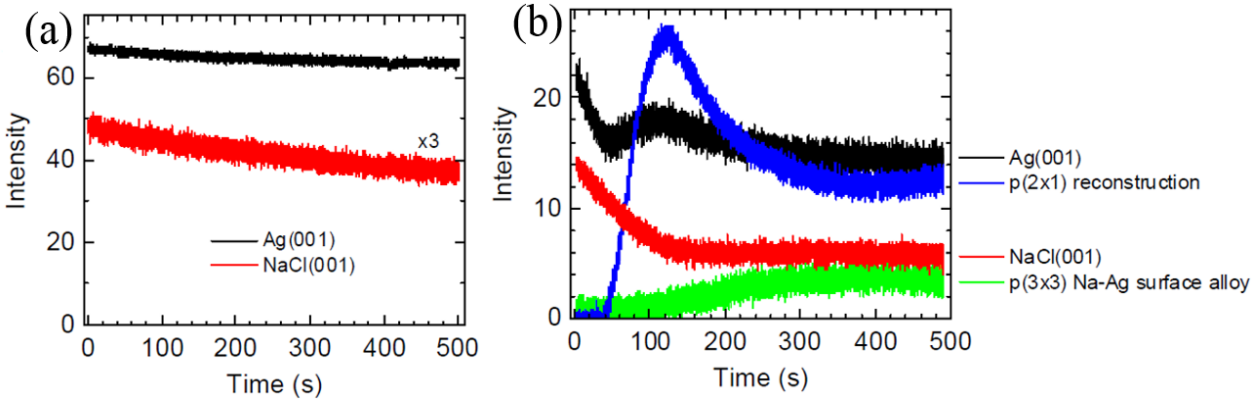

Figure 4.5: LEED spot intensity versus time, measured on ultrathin NaCl films grown on Ag(001) at 413 K. Temporal variations of the diffraction spots upon irradiation with the electron beam of the LEED. The intensity of the $(\bar{1},0)$ spots is monitored for the Ag(001) surface, $p(2 \times 1)$ missing-row reconstruction, and for the (001)-terminated NaCl film, whereas intensity is averaged over several spots for the $p(3 \times 3)$ Na-Ag surface alloy. In (b), the NaCl film is thicker than in (a), since the deposition time is 30 min, as compared to 10 min at the same cell temperature in (a).

In Fig. 4.5(a), where the NaCl film is thinner, slower kinetics are observed, compared to Fig. 4.5(b), with the NaCl spot intensity decaying at a rate $\gamma 1 \approx 0.002$ s-1. Several measurements were conducted on different areas of the sample with the thinnest NaCl film. In the area investigated in Fig. 4.5(a), no LEED spots other than those of Ag and NaCl were observed upon 500 s of electron irradiation. In some other areas, we could observe the onset of the (2 × 1) LEED pattern, but no other Na-Ag superstructures. The absence of the (3 × 3) structure after 500 s irradiation of the thinnest film may be ascribed either to the slower reaction kinetics or the limited amount of reactants.

4.5 Irradiation effects on NaCl film geometry

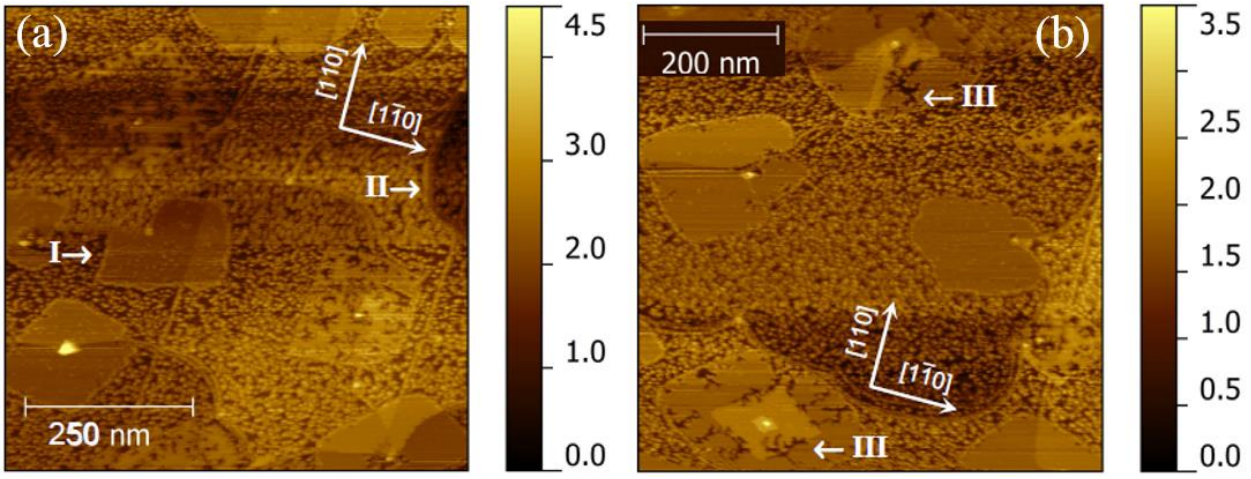

Figure 4.6: STM topography of NaCl films after electron irradiation. [(a), (b)] 680 × 680 nm^2 images (U_b = 4 V, I_t = 0.7 nA) of an ultrathin NaCl film grown on Ag(001) at 413 K (10 min deposition) after 600 s electron irradiation using the electron beam of the LEED (electron energy 52 eV) at sample current of 0.40 mA. All STM images are recorded at low temperature (78 K). The orientation of the [1 $\bar{1}$ 0] and [1 1 0] axes of Ag(001) is indicated in the images. **I**: NaCl island contour; **II**: substrate step edge; **III**: branch-shaped holes.

Looking at the geometry of the irradiated films in real space provides further information on the parameters that have an effect on the electron-induced modifications of the films. Figures 4.6 and 4.7 show post-irradiation STM topography images of two ultrathin NaCl films grown on

Ag(001) at 413 K, which differ in nominal thickness (the NaCl film is thicker in Fig. 4.7 as compared to Fig. 4.6). The electron beam, which is about 1 mm in diameter in the sample, is focused on selected areas on the sample (the top side of the silver crystal is 6 mm in diameter); thus, the effect of the electron dose can be investigated in STM by exploring the surface of the crystal. In Figs. 4.6 and 4.7, the irradiation time is 600 s. The modified geometry of the thinnest NaCl film, at the center of the irradiated area, where the electron dose is the highest, is shown in Figs. 4.6(a) and 4.6(b).

Despite the apparent disorder, one can distinguish the shape or the contour of the NaCl islands (see I in Fig. 4.6), as well as the step edges of the substrate (II). The NaCl islands exhibit nanometric holes (III), whose branch-like shape strongly differs from that of the holes seen in STM images of the as-grown NaCl films. We ascribe these holes to material removal due to the electron-induced dissociation of NaCl. Between the NaCl islands, the silver surface is decorated with tiny dots which, in most cases, exhibit no long-range order. The structure of these dots is not resolved at U_b = 4 V, due to the delocalization of the image potential states [4]. As shown in Fig. 4.7(d), higher lateral resolution is obtained at U_b = 1 V and we observe that the dots consist of single molecules or small aggregates. Most of the aggregates in Fig. 4.7(d) have the apparent height expected for a 1-ML NaCl layer (180 pm) [4] ; however, STM spectroscopy reveals the mixed nature of some of the disordered areas.

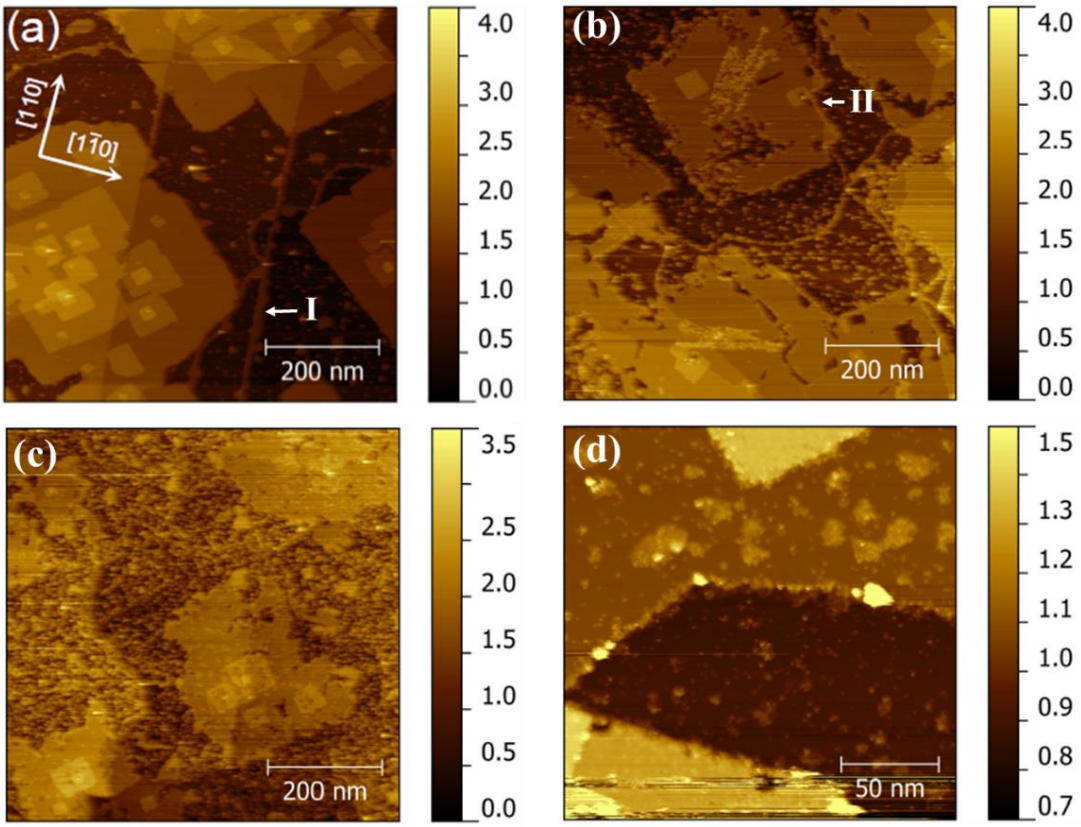

Figure 4.7: STM topography of NaCl films after irradiation at different electron doses. [(a)-(c)] 680 × 680 nm^2 images (U_b = 4 V, I_t = 0.7 nA) of an ultrathin NaCl film grown on Ag(001) at 413 K (30 min deposition) after 60 s electron irradiation using the electron beam of the LEED (electron energy 52 eV) at sample current of 0.40 mA. The three images are obtained on different areas of the sample, at the center and the periphery of the irradiated zone, which have thus received different electron doses (the electron beam is about 1 mm in diameter at the sample and the top side of the sample is 6 mm in diameter). The effective electron dose increases from (a) to (c) in this figure. (d) 197 × 197 nm^2 image (U_b = 1 V, I_t = 1 nA) of the same irradiated NaCl film, revealing the geometry of the disordered areas. All STM images are recorded at low temperature (78 K). The orientation of the [1 $\bar{1}$ 0] and [1 1 0] axes of Ag(001) is indicated in the image on the left. **I:** dots at the silver step edges; **II:** serrated island edges.

Figure 4.8 shows differential conductance (dI/dV) spectra, measured in open-loop conditions (the initial STM parameters are indicated in each panal), on ultrathin NaCl films grown at 413 K before and after electron irradiation. The dI/dV spectra of the as-grown NaCl domains exhibit a characteristic energy shift by ≈ 1.3 eV of the first field emission resonance of Ag(001) induced by NaCl adsorption [4]. On the irradiated samples, not all the STM spectra measured have similar spectroscopic signatures to the as-grown NaCl islands [see the spectra measured on the dots in Fig. 4.8(c)]. Larger energy shifts, up to ≈ 1.6 eV, are also observed, which is not expected for NaCl on Ag(001). Such large shifts are consistent with previous observations for Na adsorbed on Si(001) and Ge(001) surfaces [5], [6], where coverage dependent energy shifts of the work function by up to ≈ 2.5 eV were reported.

The dots preferentially adsorb at the step edges of the silver substrate. Interestingly, the edges of the NaCl islands have serrated aspects in the STM images, with higher STM height measured at U_b = 4 V compared to the island center. These observations reveal that electron irradiation induces a disordering process into the NaCl films, in addition to Cl depletion. We infer from Figure. 4.6 that this disordering is due to the removal of NaCl molecules from the island edges, which diffuse and adsorb on the substrate terraces and step edges. In addition, the adsorption of sodium atoms on the surface may contribute to hamper the growth of well-ordered NaCl domains.

In the image series shown in Fig. 4.7(a)-(c), the effective electron dose increases from (a) to (c). In Fig. 4.7(a), where the dose is the lowest, dots are visible between the islands, and preferentially at the step silver edges (see I in Fig 7); whereas, no holes are observed yet in the islands. In Fig. 4.7(b), where the dose is higher, the density of dots increases, and the islands have serrated edges (II). Holes are now visible in the islands. This supports the hypothesis of two distinct processes: disordering and Cl depletion.

Even though the post-irradiation STM measurements were done in the same areas as those studied using LEED, we could unfortunately not obtain within this study atomic resolution STM images showing in real space the ordered Na-Ag phases that we observe in LEED. Scanning the irradiated NaCl films at low bias without damaging the tip was extremely difficult, due to the presence of aggregates, and scanning at high voltage prevented atomic resolution, due to lateral delocalization of the image potential states. This hampered a statistical study on large areas of the

sample. Nevertheless, our observations indicate that disordered areas may largely dominate over the areas of ordered Na-Ag structures; which is consistent with the comparatively strong background observed in the LEED patterns of the irradiated samples.

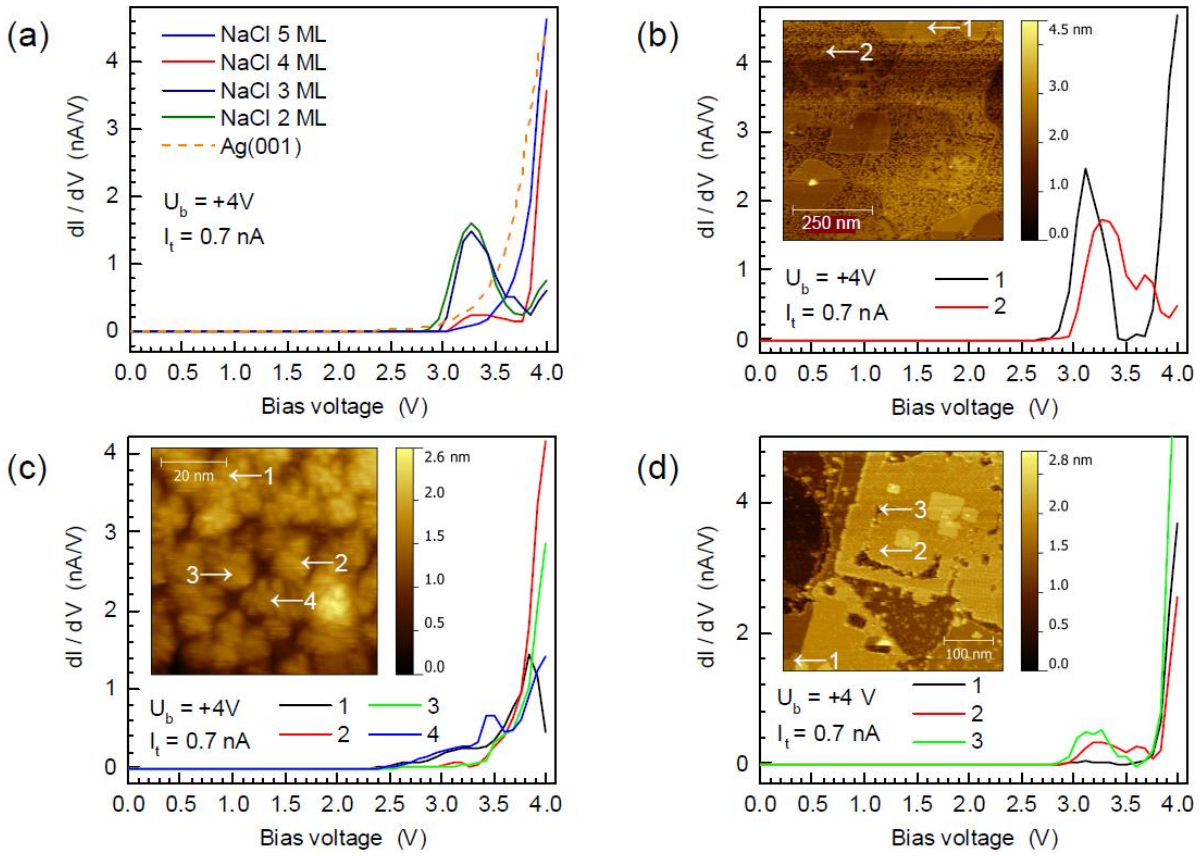

Figure 4.8: Differential conductance (dI/dV) spectra of ultrathin NaCl films grown on Ag(001) at 413 K (a) before and [(b)-(d)] after electron irradiation. (a) dI/dV spectra obtained on the as-grown NaCl domains shown in Fig. 1(b), whose thickness ranges from 2 to 5 NaCl atomic layers (monolayer, ML), and on the bare Ag(001) surface. (b, c) dI/dV spectra measured on the irradiated NaCl film shown in Fig. 4.6(a). (d) dI/dV spectra measured on the same NaCl film as shown in Fig. 4.7(b). All the dI/dV spectra are measured in open-loop conditions (the initial STM parameters are U_b = 4 V and I_t = 0.7 nA) by varying the bias voltage from 0 to 4 V by steps of 100 mV. The dI/dV spectra are measured at the position indicated by the apex of the arrows in the STM images (U_b = 4 V, I_t = 0.7 nA) shown in inset. All STM images are recorded at low temperature (78 K).

4.6 Discussion

In the bulk crystal and thick film cases, the irradiated material may be considered a virtually infinite reservoir of molecules to dissociate; in the ultrathin film case, however, the limited amount of reactants may have a strong effect on the reaction kinetics. Below, we discuss the results shown in this chapter with the aim of elucidating what is specific to ultrathin films in the kinetics of alkali halide dissociation induced by electron irradiation.

It is generally admitted that electron irradiation of alkali halides produces defects through the creation of electron-hole pairs, whose diffusion to the surface results in the desorption of particles; however, various mechanisms have been proposed, depending on the systems and the irradiation conditions (electron energy, sample temperature, surface geometry...) [7]–[9]. A review of the possible electronic processes leading to defect production, stimulated desorption and surface modification in irradiated alkali halides can be found in Ref. [9]. The elementary interactions of the system include the primary excitations, which produce free excitons and hot holes, the diffusion of hot electron-hole pairs, color centers and interstitial anions, and finally the emission of halogen and alkali atoms from the surface. For instance, no thermal desorption of halogen atoms can occur before the hot charge carriers are trapped and localized in the crystal lattice [10]. In contrast, the rearrangement of the lattice around the excitation products yields Frenkel defects, which diffuse and recombine at the surface; a process through which thermal desorption of both halogen and alkali atoms can occur [11].

The low-energy electron irradiation of cleaved KBr(001) and NaCl(001) crystal surfaces have motivated a number of studies in the past and a model has been proposed for the resulting desorption of halogen atoms. Within this model, incident electrons induce defects in the bulk (halogen vacancies and interstitial halogen atoms), which may diffuse to the surface where halogen atoms are ejected out of the plane and alkali metal atoms aggregate into metallic clusters [12]–[16]. Although this model suggests that electron induced desorption of alkali halide surfaces essentially leads to halogen atom removal, similar kinetics and desorption fluxes have been reported for halogen and alkali metal atoms [7], [8], [12], [16], [17]. This has been explained by surface diffusion of alkali metal atoms to the step edges of the alkali-halide surface, where electron-stimulated desorption of alkali metal atoms is more efficient [14]–[16]. As a result, the desorption kinetics are correlated with the surface density of step edges. In particular, alkali-

halide desorption from cleaved crystal surfaces has been shown to proceed layer by layer, which results in a periodic variation of the step density where each period corresponds to the removal of one atomic layer, and the same periodic oscillations were observed in both the desorption fluxes of halogens and alkali metals, [8], [14]–[17] In contrast, we do not observe such oscillations in the AES data measured from ultrathin NaCl films on Ag(001), where the Cl signal monotonously decays with increasing irradiation time. In addition, a significant amount of Na atoms must remain on the surface after NaCl dissociation that does not produce clusters, since our LEED measurements suggest the formation of ordered 1D chains of Na atoms and well-ordered Ag-Na surface alloys.

The periodic variation of the step density previously observed on cleaved alkali-halide crystal surfaces irradiated with electrons is well understood. It is known from real-space AFM measurements that randomly spread rectangular holes of monolayer depth are formed, whose edges are oriented along the main crystallographic directions of the (001) plane [14], [15], [17], [18]. It is the growth and coalescence of these holes that yield the oscillations in the step density [16].

On bulk crystals and thick films of alkali-halides, the opening of holes in the top layer reveals a surface that is of the same composition and structure. In contrast, if the film is thin enough for hole opening to reveal the bare surface of the underlying metal substrate (or even more if the film is not continuous), then alkali metal atoms may diffuse to the metallic surface. If energetically favored, the adsorption of these atoms onto (or their alloying with) the metallic surface is expected to dramatically change the kinetics of the electron stimulated desorption. This interpretation of the substrate effect is consistent with a previous study of electron-irradiated NaCl films grown on GaAs(001), where the authors reported the apparent vanishing of the Na desorption process for NaCl film thickness lower than about 10 ML [19].

The oscillations observed in the desorption rates of halide and alkali metal atoms from electron-irradiated bulk alkali-halides have been modeled using damped oscillator functions[18]. Different kinetics have been reported for thick NaCl(111) films grown on mica [12]; there, Friedenberg and Shapira found that the surface Cl concentration as measured by AES varies as a logarithmic function of the electron irradiation time. This behaviour was interpreted as an Elovitch-type mechanism (i.e., a standard model for chemisorption), where the activation energy for dissociation is concentration dependent. The argument for this interpretation is that the

increasing surface concentration of alkali metal atoms creates disorder, which slows down the dissociation of further alkali-halide molecules. In contrast, the AES measurements shown in Fig. 4.1 clearly show that Cl concentration decays exponentially upon increasing irradiation time and the data could not be fitted with either a logarithmic or a damped oscillator function of time. Presumably, the reaction rate constant is independent of the reactant and product concentration in the ultrathin film case because alkali metal atoms diffuse to bare substrate areas where they adsorb or react, thus not altering the environment of undissociated alkali-halide molecules as much as in the thick film case. The Cl concentration decay, however, does not drop to zero at long exposure times in Fig. 4.1; an offset, or slow decaying component, is observed. From the STM images of the irradiated films shown in Fig. 4.7, we infer that the bare substrate areas are increasingly occupied by disordered NaCl molecules removed from the NaCl islands as the irradiation proceeds. A change in the reaction kinetics is thus observed when the concentration of disordered NaCl molecules starts to hamper alkali metal atom diffusion to the bare substrate areas.

To summarize in a simplified way, the electron-induced modification of the ultrathin NaCl films proceeds in two stages. At the first reaction steps, Na diffusion on the bare substrate is not significantly affected by disorder and, thus, Cl depletion is not limited by Na accumulation on NaCl islands. After some irradiation time, however, Na diffusion is increasingly limited by disorder and this has a strong slowdown effect on the reaction kinetics. Depending on the initial film thickness, this effect occurs at a more or less early phase of the reaction and this is one of the factors that determine what Na-Ag superstructures finally form.

The comparison of the kinetics revealed by AES and LEED investigations is interesting. On the one hand, a mono-exponential decay is observed in the evolution of the Cl/Ag AES ratio shown in Fig. 4.1(a) with, however, an offset or slow decaying component, which indicates that part of the available chlorine is not desorbed with the same efficiency upon irradiation. On the other hand, the NaCl(001) LEED pattern shown in Fig. 4.4 decays in intensity following a bi-exponential law with fast γ_1 and slow γ_2 decay rates differing by about one order of magnitude. For the NaCl films grown at a lower temperature, as shown in Fig. 4.5, the time trace of the NaCl spots also exhibit a fast and a slow component (for the thickest film) or a mono-exponential decay with an apparent offset (for the thinnest film). Moreover, post-irradiation STM images

shown in Fig. 4.7 reveal that a fast disordering process coexists with a comparatively slower mechanism of hole formation, which is driven by Cl depletion from NaCl islands. Within this picture, our AES and LEED observations can be understood as follows. The fast intensity decay of the NaCl LEED pattern is due to the disordering process, where electron irradiation induces NaCl removal from the NaCl island edges; whereas its slow decay component is ascribed to the increasing density of Cl vacancies (and formation of holes) in the NaCl islands. The mono-exponential decay of the Cl/Ag AES ratio results from the Cl depletion from the NaCl islands and Na atom diffusion to bare silver areas, until the disordering process significantly reduces the available areas on bare Ag(001), which leads to a strong slowdown of the Cl depletion and yields almost a plateau in the AES data at long irradiation times.

Finally, the time sequence of the superstructures observed in LEED during the course of the dissociation reaction reveals crucial information on the mechanism through which these superstructures occur. Firstly, a missing-row $p(2 \times 1)$ surface reconstruction systematically shows up after some irradiation time, for all investigated initial nominal thickness of the NaCl film grown on Ag(001). The same surface reconstruction is known to occur upon adsorption of various alkali metals (Li, Na, K, Rb) on the (001) face of Cu, Ag, and Au crystals [2] at room temperature (RT) in a coverage range $\Theta \approx 0.2$ - 0.4. Here, Θ is defined as the ratio between the number of adsorbed alkali-metal atoms over the number of atoms in a (001) plane of the substrate; thus, the first alkali-metal monolayer may be completed at $\Theta < 1$. In all of these systems, the $p(2 \times 1)$ is the first superstructure to appear at RT upon increasing Θ. Alkali-metal atoms are known to form linear incommensurate chains in the missing rows of the reconstructed metal surface in the Na/Ag(001) and Li/Cu(001) systems [2], [20] at RT within a narrow coverage range, i.e., $\Theta = 0.37$ - 0.39 for Na/Ag(001) [2]. As well, (n x n) surface alloys (with n = 3, 4, 5) have been observed by LEED and STM measurements on several systems [2], including Li/Cu(001), Li/Ni(001) and Na/Ag(001), at RT and for $\Theta > 0.4$. Finally, the $p(4 \times 2)$ seems specific to the Na/Ag(001) system and has been obtained at RT for $\Theta > 0.55$ (Na monolayer is completed at $\Theta \approx 0.7$) [1].

Remarkably, we demonstrate that all the superstructures mentioned above may be obtained through electron-induced dissociation of ultrathin NaCl films grown on Ag(001). With the exception of the incommensurate chains, these superstructures occur within alkali metal surface

coverage ranges that do not overlap. Therefore, the fact that we see two or more [e.g., the (2 × 1) and (4 × 2) in Fig. 4.4(b) or the (3 × 3) and (2 × 1) at t ≈ 400 s in Fig. 4.5(b)] of these superstructures coexisting indicates that Na surface concentration must be highly heterogeneous. Furthermore, we see intensity oscillations in their LEED patterns (at constant sample current) as the reaction proceeds, which means that the Na surface concentration locally oscillates. The oscillations in the LEED patterns are only observed during the first 400 s on average and then the system seems to converge to an equilibrium state [as seen in Fig. 4.4(a)].

From the observations reported above, we conclude that, in electron-irradiated ultrathin NaCl films on Ag(001), areas where Na surface concentration can reach comparatively high values coexist with areas that are essentially covered with disordered NaCl molecules, together with the remaining parts of the initial NaCl, islands. This implies that Na atom diffusion occurs within limited areas, which can be ascribed to the accumulation of NaCl molecules at the step edges of the substrate. The slowdown in the reaction kinetics observed in LEED and AES after a few hundred seconds indicates that NaCl dissociation and Cl desorption from disordered NaCl molecules and aggregates is significantly lower than from well-ordered NaCl islands. As a result, the reaction kinetics are dependent on the surface coverage rate the ultrathin NaCl films, which will have an effect on the ratio between ordered and disordered NaCl areas. Moreover, the thickness of the NaCl islands has an effect on the electron-matter interaction efficiency, because the electron penetration depth is longer than the film thicknesses considered in this work.

4.7 Conclusion

In conclusion, the electron induced dissociation of ultrathin alkali-halide films grown on fcc metals differs, in terms of reaction kinetics and outcomes, from that of their thick film and bulk crystal counterparts. These differences mainly ensue from the limited amount of reactants and the product interactions with the substrate. At sufficiently low thickness (typically 2 to 5 ML), alkali halide films on metals may be discontinuous and/or exhibit holes, especially when their growth involves the coalescence of domains with mismatched orientations. Additional holes are expected to be formed upon electron irradiation, due to the creation of supplementary defects in the film. Therefore, the alkali metal atoms produced from alkali-halide dissociation do not only aggregate

in metallic clusters at the step edges, but also diffuse to bare areas of the metallic substrate, where they adsorb and can form superstructures or undergo alloying reactions.

All the superstructures that are known to be produced through deposition of Na atoms on Ag(001) were observed in LEED during the dissociation of ultrathin NaCl films grown on Ag(001). These superstructures, which include reconstructions of the Ag(001) surface and a 2D Na-Ag alloy, are found to occur in a reversible way, with their relative coverage varying in time during the first minutes of irradiation, due to local variations in the Na concentration. This indicates that the observed Na-Ag superstructures are metastable, meaning that the phase transitions between two of these Na-Ag superstructures, having different Na concentration ranges of existence, are not irreversible. This could not be demonstrated in the previous studies based on Na deposition on Ag(001), because the surface concentration in Na was monotonously increased.

In addition, the electron irradiation induces an increasing disorder in the ultrathin NaCl films, which slows down the reaction kinetics of both the dissociation of NaCl and the formation of Na superstructures on silver; as a result, the reaction kinetics and products depend on the NaCl film thickness. In the conditions used in this study, the disordered areas are found to strongly dominate the geometry of the electron irradiated films. Further investigations are necessary to control the ratio between the disordered and ordered areas, before electron irradiated alkali-halide ultrathin films can eventually be used as “templates” for anchoring single organic molecules or producing macro molecular structures on a surface [21]–[25].

4.8 Bibliography

[1] M. Imaki, S. Mizuno, and H. Tochihara, "Surface structure sequences formed on Ag(001) with increasing alkali-metal coverages at room temperature," *Surf. Sci.*, vol. 357, pp. 145–149, 1996.

[2] H. Tochihara and S. Mizuno, "Composite surface structures formed by restructuring-type adsorption of alkali-metals on fcc metals," *Prog. Surf. Sci.*, vol. 58, no. 1, pp. 1–74, 1998.

[3] E. Le Moal, M. Müller, O. Bauer, and M. Sokolowski, "Misfit driven azimuthal orientation of NaCl domains on Ag(100)," *Surf. Sci.*, vol. 603, no. 16, pp. 2434–2444, 2009.

[4] H.-C. Ploigt, C. Brun, M. Pivetta, F. Patthey, and W.-D. Schneider, "Local work function changes determined by field emission resonances: NaCl/Ag(100)," *Phys. Rev. B*, vol. 76, no. 19, p. 195404, Nov. 2007.

[5] B. Naydenov and L. Surnev, "Sodium adsorption on a Ge(100)-(2 × 1) surface," *Surf. Sci.*, vol. 370, no. 2, pp. 155–165, 1997.

[6] M. Tikhov, G. Boishin, and L. Surnev, "Sodium adsorption on a Si(001)-(2 × 1) surface," *Surf. Sci.*, vol. 241, no. 1, pp. 103–110, 1991.

[7] H. Tokutaka, M. Prutton, I. G. Higginbotham, and T. E. Gallon, "The (100) surfaces of alkali halides," *Surf. Sci.*, vol. 21, no. 2, pp. 233–240, 1970.

[8] M. Szymonski, J. Kolodziej, B. Such, P. Piatkowski, P. Struski, P. Czuba, and F. Krok, "Nano-scale modification of ionic surfaces induced by electronic transitions," *Prog. Surf. Sci.*, vol. 67, no. 1, pp. 123–138, 2001.

[9] C. Tegenkamp, H. Pfnür, W. Ernst, U. Malaske, J. Wollschläger, D. Peterka, K. M. Schröder, V. Zielasek, and M. Henzler, "Defects in epitaxial insulating thin films," *J. Phys. Condens. Matter*, vol. 11, no. 49, p. 9943, 1999.

[10] M. Szymoński, J. Kołodziej, Z. Postawa, P. Czuba, and P. Piatkowski, "Electron-stimulated desorption from ionic crystal surfaces," *Prog. Surf. Sci.*, vol. 48, no. 1, pp. 83–96, 1995.

[11] M. Szymoński, "On the model of the electron sputtering process of alkali halides," *Radiat. Eff.*, vol. 52, no. 1–2, pp. 9–13, Jan. 1980.

[12] A. Friedenberg and Y. Shapira, "Electron induced dissociation of the NaCl(111) surface," *Surf. Sci.*, vol. 87, no. 2, pp. 581–594, 1979.

[13] T. R. Pian, M. M. Traum, J. S. Kraus, N. H. Tolk, N. G. Stoffel, and G. Margaritondo, "Electron and photon stimulated desorption of positive ions from alkali halide surfaces," *Surf. Sci.*, vol. 128, no. 2, pp. 13–21, 1983.

[14] B. Such, P. Czuba, P. Piatkowski, and M. Szymonski, "AFM studies of electron-stimulated desorption process of KBr(001) surface," *Surf. Sci.*, vol. 451, no. 1, pp. 203–207, 2000.

[15] B. Such, J. Kolodziej, P. Czuba, P. Piatkowski, P. Struski, F. Krok, and M. Szymonski, "Surface Topography Dependent Desorption of Alkali Halides," *Phys. Rev. Lett.*, vol. 85, no. 12, pp. 2621–2624, Sep. 2000.

[16] J. J. Kolodziej, B. Such, P. Czuba, F. Krok, P. Piatkowski, P. Struski, M. Szymonski, R. Bennewitz, S. Schär, and E. Meyer, "Frenkel defect interactions at surfaces of irradiated alkali halides studied by non-contact atomic-force microscopy," *Surf. Sci.*, vol. 482, pp. 903–909, 2001.

[17] R. Bennewitz, S. Schär, V. Barwich, O. Pfeiffer, E. Meyer, F. Krok, B. Such, J. Kolodzej, and M. Szymonski, "Atomic-resolution images of radiation damage in KBr," *Surf. Sci.*, vol. 474, no. 1, pp. L197–L202, 2001.

[18] M. Goryl, B. Such, F. Krok, K. Meisel, J. J. Kolodziej, and M. Szymonski, "Atomic force microscopy studies of alkali halide surfaces nanostructured by DIET," *Surf. Sci.*, vol. 593, no. 1, pp. 147–154, 2005.

[19] M. Szymonski, J. Kolodziej, P. Czuba, P. Piatkowski, P. Korecki, Z. Postawa, and N. Itoh, "Thickness dependent electron stimulated desorption of thin epitaxial films of alkali halides," *Appl. Surf. Sci.*, vol. 100, pp. 102–106, 1996.

[20] Seigi Mizuno, Hiroshi Tochihara, and Takaaki Kawamura, "Missing-row-type restructuring of the Cu(001) surface induced by Li adsorption: a low-energy electron

diffraction analysis," *Surf. Sci.*, vol. 292, no. 3, pp. L811–L816, 1993.

[21] W. Ernst, M. Eichmann, H. Pfnür, K.-L. Jonas, V. von Oeynhausen, and K. H. Meiwes-Broer, "Adsorbate-induced one-dimensional long-range modulation of an epitaxial insulator film," *Appl. Phys. Lett.*, vol. 80, no. 14, pp. 2595–2597, Apr. 2002.

[22] Q. Guo, M. Huang, S. Lu, and G. Cao, "Ionic compound mediated rearrangement of 3, 4, 9, 10-perylene tetracarboxylic dianhydride molecules on Ag(100) surface," *Nanotechnology*, vol. 26, no. 27, p. 275603, 2015.

[23] J. Hieulle, D. Peyrot, Z. Jiang, and F. Silly, "Engineering two-dimensional hybrid NaCl-organic coordinated nanoarchitectures on metal surfaces," *Chem. Commun.*, vol. 51, no. 67, pp. 13162–13165, 2015.

[24] C. Zwick, A. Baby, M. Gruenewald, E. Verwüster, O. T. Hofmann, R. Forker, G. Fratesi, G. P. Brivio, E. Zojer, and T. Fritz, "Complex Stoichiometry-Dependent Reordering of 3,4,9,10-Perylenetetracarboxylic Dianhydride on Ag(111) upon K Intercalation," *ACS Nano*, vol. 10, no. 2, pp. 2365–2374, Feb. 2016.

[25] T. K. Shimizu, J. Jung, H. Imada, and Y. Kim, "Supramolecular Assembly through Interactions between Molecular Dipoles and Alkali Metal Ions," *Angew. Chemie*, vol. 126, no. 50, pp. 13949–13953, 2014.

Chapter 5

PTCDA Molecules on Ultrathin KCl Film

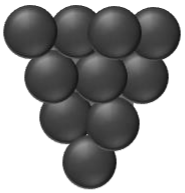

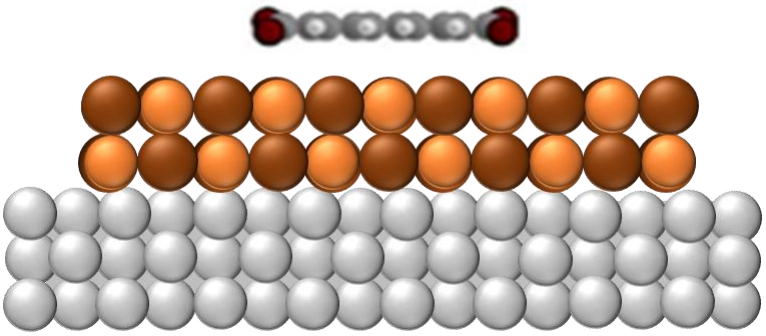

Table of Contents

5.1 Introduction

The current trend in the electronics industry to miniaturize devices makes molecular electronics a highly promising research field. Thin films of organic semiconductors, consisting of adsorbed molecules on surfaces, are crucial in this field because of their unique electrical and optoelectrical properties and their low fabrication cost. The interactions of organic molecules with different substrates influence their electronic and optical properties [1]. Therefore, understanding the behavior of organic molecules on surfaces is essential to efficiently develop and improve these devices.

On insulating surfaces, large molecules exhibit luminescence properties, unlike on metal surfaces where strong coupling of the molecular states to the metal and quenching of the excitations occur [2], [3]. When molecules on a metallic substrate are excited, charge transfer from the molecule to the metal surface occurs via hybridized molecule- substrate orbitals, which leads to the delocalization of the electron into the unoccupied metallic states [3]. Molecule-substrate interactions on insulating substrates are in general weaker compared to metallic ones, enabling intermolecular interactions and intrinsic molecular states to be observed. Thin alkali-halide films on metals are mostly used for this purpose [4]. The insulating layers allow decoupling of the molecular and metallic states from each other. This can be observed using scanning tunneling microscopy (STM), a surface-sensitive technique with high atomic and molecular resolution, and the ability to perform local spectroscopy (STS) on the surface [5].

Perylene-3,4,9,10-tetracarboxylic di-anhydride (PTCDA) is one of these organic molecules with promising applications in optical and semiconductor devices. In particular, it forms well-known structures called J-aggregates with very narrow luminescence spectra [4]. The structural formula of the PTCDA molecule is shown in Figure 5.1, the images in (a) and (b) show that the PTCDA molecules are planar. From the structure, we can observe a non-uniform charge distribution due to the negative partial charges at the oxygen atoms of the anhydride groups and the positive partial charges at the hydrogen atoms of the molecule. This is due to the difference in electronegatively between the C and the O in the anhydride group where O is more negative. The difference is in the opposite direction between the C and H.

The interaction between the PTCDA molecules are attributed the formation of Hydrogen bonds within the (102) crystal plane because the in-plane separation between neighboring molecular centers is (~ 12–15 A°), so this means that the separation between C-H and C-O is close. In contrast, for stacking in the out of the plane direction, the intermolecular interaction is attributed to π-bonds, because the molecular planes are separated by 3.4 A° [6]. On the other hand, the molecule-substrate interaction is substrate dependent. On the metal substrate this interaction corresponds to a van der Waals interaction whereas the interaction is electrostatic interaction when these molecules are deposited on the ionic substrate [7]. The charge distribution within the PTCDA molecules and the interplay between the intermolecular interactions and molecule–substrate interactions result in a variety of phases for the long-range ordered growth for PTCDA molecules on different substrates [5], [7].

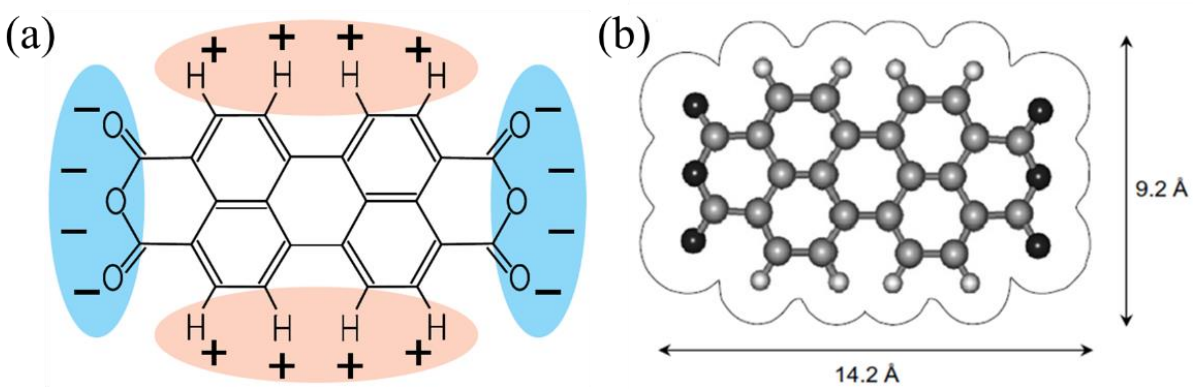

Figure 5.1: (a) Structure formula showing the partial negative charge on the Oxygen and the partial positive charge on the Hydrogen [5]. (b) Ball and stick model with hard sphere perimeter [8].

The conductivity of PTCDA films is also reported to be anisotropic. Understanding the growth of PTCDA films on insulating substrates is therefore key to controlling these direction-dependent properties so that the use of PTCDA in organic devices can be enhanced [9]. On different metal and salt surfaces, for example, different epitaxial adsorbate structures of PTCDA have been identified such as the so-called quadratic (Q), herringbone (HB), and brick wall (BW) structures. These structures are formed from different combinations of the non-equivalent sites of adjacent PTCDA molecules [10].

In this chapter we report on the formation of a thin film of PTCDA molecules on two different systems, on the silver substrate Ag(001) and on the KCl/Ag(001), using scanning tunneling microscopy (STM) in ultra-high vacuum. For deposition on the silver substrate we obtain a monolayer of PTCDA molecules that are arranged in a T-shape with a quadratic unit cell. On KCl/Ag(001), different arrangements for these molecules were found: on the bare silver, the molecules form islands with random shapes , and within these islands the molecules form a herringbone structure. On KCl films, both individual PTCDA molecules and a densely packed structure were found.

5.2 PTCDA molecules on Ag(001) substrate

In the first step, we studied the growth of the PTCDA molecules on the silver substrate, in order to optimise the growth parameters because PTCDA on the metal Ag(001) surface is stable at RT, unlike on the KCl and NaCl. The structure and the morphology of PTCDA molecules grown on Ag(001) have been reported by Ikonomov et al [8].

5.2.1 PTCDA molecules deposition in LT-STM

We have investigated the growth of the monolayer of PTCDA on Ag(001) in the LT-STM setup. PTCDA molecules are evaporated from a Knudsen effusion cell inside the analysis chamber at a base pressure of 8.9×10^{-10} mbar. The monolayer of PTCDA is obtained at a cell temperature of 522 K after a 50-minute deposition of these molecules. During deposition of PTCDA molecules, the sample temperature was 300 K.

Figure 5.2 shows STM images of PTCDA molecules grown on Ag(001) at 300 K. All the STM images in this figure show the step of the silver covered with PTCDA molecules with almost 100 % covering. The images also show simultaneously a continuous layer of PTCDA molecules with 1-2 ML thickness and a small domain of these molecules that are arranged randomly on the silver substrate. Ikonomov et al reported that at low coverage of less than 1 ML, the PTCDA molecules form islands on Ag(001) [8]. Since the coverage was between 1-2 ML in our experiment, the PTCDA islands were not observed. PTCDA molecules form a layer and almost covered all the Ag surface, while the rest of the surface is covered with a liquid-like phase of highly mobile molecules [8]. In addition, we use a longer deposition time (50 minutes deposition) to obtain the

monolayer structure of PTCDA, which gives time for the molecules to diffuse and form a uniform layer on Ag(001) surface, in contrast with the previous study by Ikonomov et al, where to grow a PTCDA monolayer on Ag(001), 2 minutes of deposition was used.

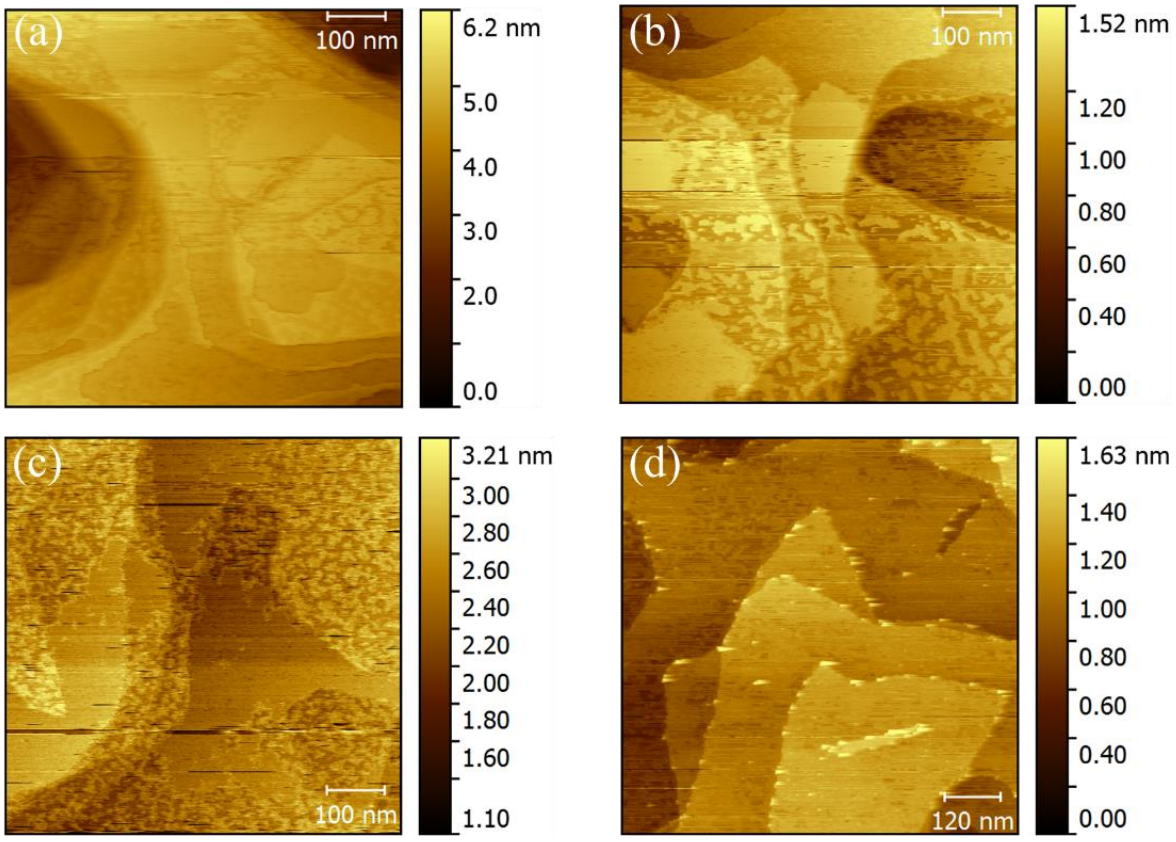

Figure 5.2: STM topography of PTCDA molecules on Ag(001) at 300 K , (a-c) 500 × 500 nm^2 measured with bias -2 V and tunneling setpoint 0.7 A in (a), 0.5 A in (b) and 0.75 A in (c). (d) 620 × 620 nm^2 (U_b = -0.8 V, I_t = 0.4 nA). All STM images are recorded at low temperature (78 K).

Figure 5.3 (a) and (b) present STM images of PTCDA molecules grown on Ag(001) at 300 K of the same area measured with slightly different tunneling conditions, as can be seen by the contrast in these images changing due to the variation of the tip-surface bias [9], [11]. Image 5.3(c), which is a selected area from image 5.3(b), shows the PTCDA monolayer on Ag(001). The structural order of these molecules is shown in the zoomed image 5.3(d). The image shows that the PTCDA monolayer forms a commensurate structure with a very high symmetry due to a strong

bonding to the silver surface [8]. The unit cell of this structure is quadratic and contains two molecules, which are perpendicular to each other and planar to the Ag(001) surface ,i.e. they, have T-shape arrangement. This is due to the molecular-molecular interaction, where H-bonds form between the anhydride and C-H edges of neighboring molecules. This observation is in agreement with previously reported studies of the PTCDA monolayer on Ag(001) [8]. Image (e) shows the hard sphere model of the PTCDA monolayer on Ag(100) drawn by Ikonomov et al [8].

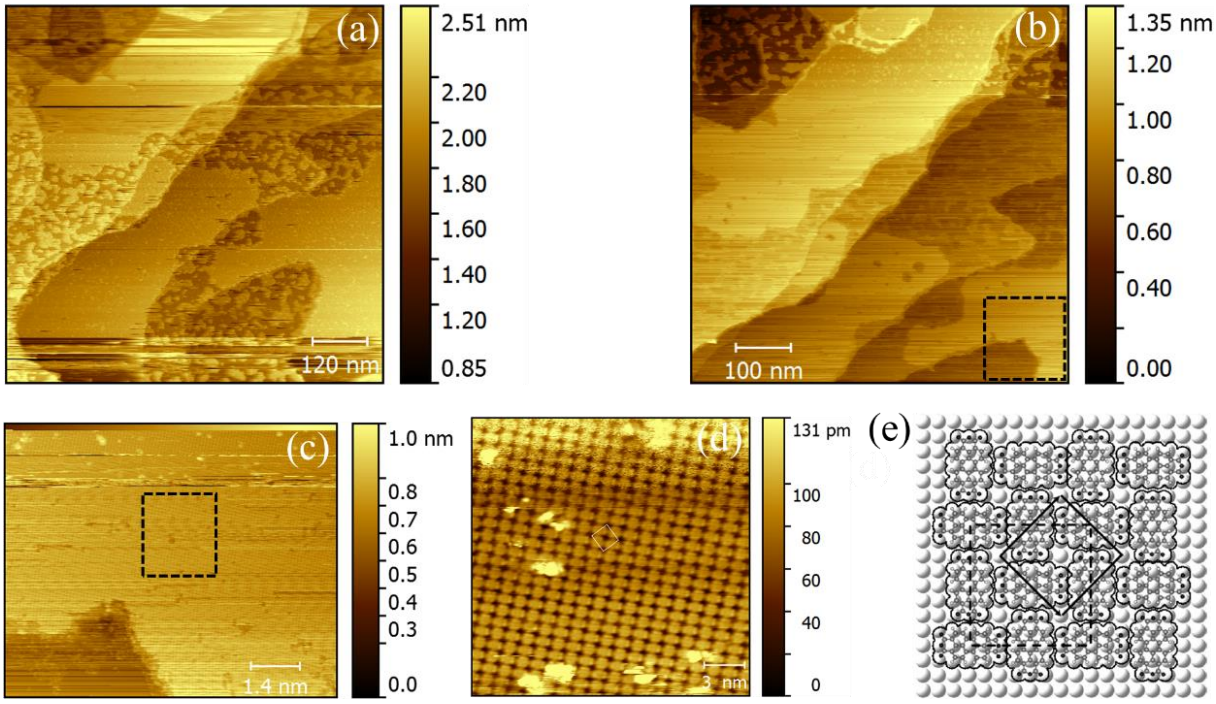

Figure 5.3: STM topography of PTCDA molecules on Ag(001) at 300 K in the same area , (a) 604 × 604 nm^2 (U_b = - 2 V, It = 0.4 nA) (b) 500 × 500 nm^2 (U_b = - 1.9 V, It = 0.7 nA), (c) 85 × 85 nm^2 (U_b = -1.9 V, I_t = 0.7 nA), (d) 15 × 15 nm^2 (U_b = - 2.63 V, It = 0.41 nA) shows the structure of monolayer PTCDA. (e) hard sphere model of the PTCDA monolayer on Ag(100). The full lines represent the primitive unit cell while the dashed lines represent the conventional c(8 × 8) unit cell [8]. All STM images are recorded at low temperature (78 K).

It has been reported that PTCDA monolayers normally form herringbone structures. The lattice constants of this structure are consistent with those of the (102) plane of the PTCDA bulk

structure deposited on close-packed noble metal surfaces. Depending on the deposition rate and the substrate temperature, this herringbone structure may vary to some extent [8], [12], [13]. In our case, the PTCDA monolayer exhibits a quadratic unit cell with the T-type arrangement instead of the herringbone structure due to the strong bonding of these molecules to the Ag surface [8]. This bonding influences the lateral interaction of the molecules so that the herringbone structure is unfavorable [8].

When the intermolecular interaction is attractive, the molecules form a T-type arrangement, as observed in the PTCDA monolayer on Ag(001), where there is an attractive interaction between the terminal anhydride groups and the hydrogen terminated perylene cores [8]. In contrast, for the growth of PTCDA on Ag(110), this interaction is repulsive, this indicates that the total adsorption energy of PTCDA/Ag(100) is larger than of PTCDA/Ag(110) [8].

Figure 5.4 shows STM images of PTCDA molecules grown on Ag(001) at 300 K on a different area of the sample, image (a) shows that the structure of PTCDA monolayer has a square unit cell and the silver atoms are observed simultaneously. Image (b) is a selected area of image (a). The unit cell of the PTCDA monolayer exhibits a =b=15.23 Å, which is close to the value observed by Ikonomov et al [8].This image shows that about one Ag atom of the surface is not covered by PTCDA molecule as previously reported in reference [8], (see the model in Fig. 5.4(d)).

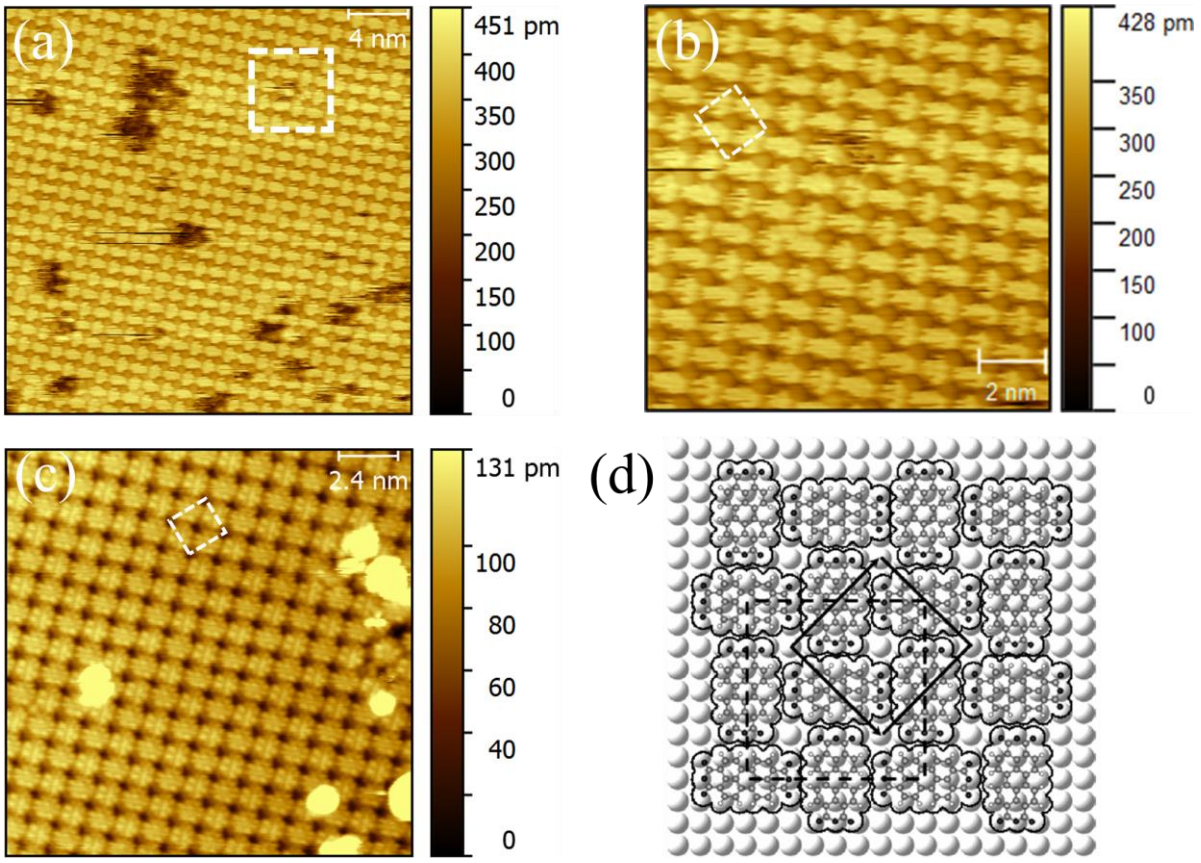

Figure 5.4: STM topography of PTCDA molecules on Ag(001) at 300 K, (a) 20 × 20 nm^2 (U_b = - 2.34 V, I_t = 0.2 nA) (b) zoomed image of (a), (c) 12.04 × 12.04 nm^2 (U_b = -2.83 V, I_t = 0.2 nA), (d) hard sphere model of the PTCDA monolayer on Ag(001) [8]. All STM images are recorded at low temperature (78 K).

Most of the time, in the STM images of the PTCDA monolayer, dark sites or holes appear between the molecules. These correspond to silver atoms not covered with PTCDA molecules [8] (see the image (c) in Fig. 5.4). In image (b), however, these dark sites appear as higher dark spheres which we could assume to be the exposed silver atoms. There are two possible explanations as to why we can now scan both the PTCDA and the silver atoms. First, a PTCDA molecule from the surface could become attached to the tip. In this case, the surface is now scanned with the density of states of the PTCDA molecule on the tip instead of the tungsten atoms on the tip. Second, because the silver surface is smooth, deposition of PTCDA molecules on this surface could induces

a restructuring of the silver atoms. Some of the atoms are not covered so they would be free to interact with the PTCDA molecules by rising in the pockets. These are visible in STM images.

The hard sphere model of the PTCDA monolayer on Ag(001) is shown in 5.4(d). In this model the central carbon ring in both molecules in the unit cell is centered on the top of an Ag atom [8], based on the model drawn for the PTCDA on Ag(111) [8], [14]. The carboxylic O atoms are also on top of Ag atoms, i.e., both of the molecules are adsorbed on high symmetry sites relative to the Ag atoms , therefore they are chemically and structurally equivalent [8]. On the contrary with PTCDA on Cu(100), where a monolayer of PTCDA forms a L-type arrangement instead of a T-type arrangement because the molecules in the unit cell do not have the same adsorption sites on Ag atoms (low symmetry sites) [15].

Figure 5.5(a) is another area of the sample which shows the silver steps covered with PTCDA molecules. The selected area of this image exhibits a PTCDA monolayer shown in the image (b). By changing slightly, the tunneling conditions, this structure becomes more clear as shown in image (c). The PTCDA monolayer exhibits a quadratic unit cell with the T-type arrangement (see structural model in (d)). This unit cell found to have the dimensions a=b=15.77 Å, which is consistent with the value of 16 Å reported by Ikonomov et al [8].

Finally, we did not manage to obtain the second layer of PTCDA molecules on our sample. However, Ikonomov et al have reported that for coverages above 1 ML, PTCDA forms a second layer on top of the monolayer [8]. From their LEED measurement they demonstrated that when the PTCDA second layer grows on the monolayer, the structure of the later does not change, where the diffraction spots of the underlying first layer and the second layer have been observed in the same LEED image [8]. The LEED pattern also showed that the structure of the second layer is an incommensurate structure and the unit cell vectors of the first and the second layer are parallel [8]. The difference between the two structures (PTCDA monolayer and second layer) is due to the bonding of these molecules to the Ag surface as mentioned above. This bonding is strong in the first layer which influences the lateral interaction of the molecules, whereas in the second layer, this influence is smaller [8]. In addition, the PTCDA monolayer exhibits one domain, whereas the second layer exhibits two symmetry equivalent domains [8].

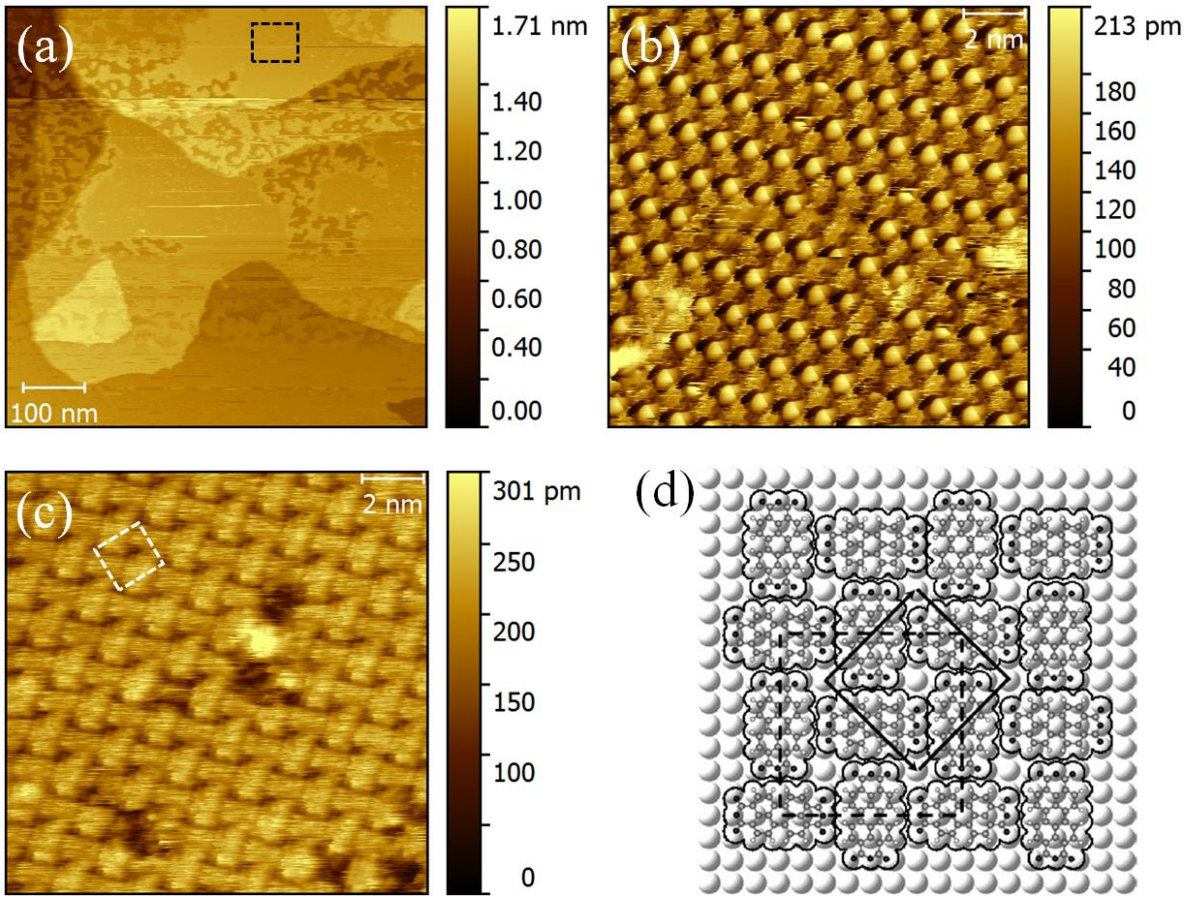

Figure 5.5: STM topography of PTCDA molecules on Ag(001) at 300 K, (a) 500 × 500 nm^2 (U_b = - 2V, I_t = 0.7 nA), (b) 10 × 10 nm^2 (U_b = - 2V, I_t = 0.7 nA) selected area of image (a) showing a monolayer of PTCDA molecules, (c) 12.04 × 12.04 nm^2 (U_b = -2.83 V, I_t = 0.2 nA),(d) hard sphere model of the PTCDA monolayer on Ag(001) [8]. All STM images are recorded at low temperature (78 K).

5.3 PTCDA molecules on KCl on Ag(001)

The second step in our experiment is to study the growth of PTCDA molecules on the KCl ultrathin film on Ag(001) substrate using STM measurement. The growth of PTCDA monolayer on 10 ML KCl epitaxially grown on Ag(001) has already been investigated by Müller et al [16] using spot-profile-analysis low energy electron diffraction (SPA-LEED). Guo et al also studied the

growth of PTCDA molecules on KCl on Ag(001) substrate using STM and LEED measurement [17].

5.3.1 State of the art

The morphology of PTCDA on bulk KCl was investigated by Dienel et al [1], using non-contact atomic force microscopy (nc-AFM). They found that PTCDA molecules at sub-monolayer coverage (coverage of 0.4 monolayers) form high islands that nucleate at the KCl steps. The resolved image of a PTCDA island shows a commensurate square-cell structure with lattice parameters of a = b = 12.6 ± 0.1 Å, forming the so-called BW structure. In this structure, the molecules adsorb flat and parallel to the surface and to each other with their long axis parallel [1$\bar{1}$0] or [11$\bar{0}$] (see Fig. 5.6 (a) and (b)). In thicker films (coverage of 1.4 monolayers) the PTCDA aggregated into crystallites and exhibited the herringbone structure in their resolved image. The structure is similar to a PTCDA bulk crystal.

The first principle calculation [10] and molecular force field calculation [1], [18] confirm the experimental finding for the BW-phase (most stable phase) for PTCDA on both the KCl and NaCl surfaces. Calculations by Aldahhak et al [10] showed that the PTCDA molecules in the BW-phase adsorb in square-cells with dimensions of a = b = 12.50 Å, $\gamma = 90°$ (associated with a 2 × 2 superstructure), and consistent with experimental observations. Moreover, the calculated adsorption energy (−2.75 eV) for this structure is higher than that of the other suggested structures (Herringbone (HB) and Q-phase). The BW-phase has one molecule in the unit cell while with respect the HB- and the Q-phase unit cells contain two molecules per unit cell rotated by 90° to each other.

On the other hand, compared to an isolated adsorbed molecule (E_{ads} = −2.49 eV), there is a slight gain in adsorption energy. This indicates the presence of stabilizing intermolecular interactions between PTCDA molecules. The adsorption energy of -2.75 eV is a combination of two terms: −0.38 eV (for molecule-molecule interactions) and −2.37 eV (for molecule-substrate interactions). The BW-phase, therefore, has a weaker molecule-substrate interaction compared to the isolated one, thereby inhibiting the distortion of the molecule [10].

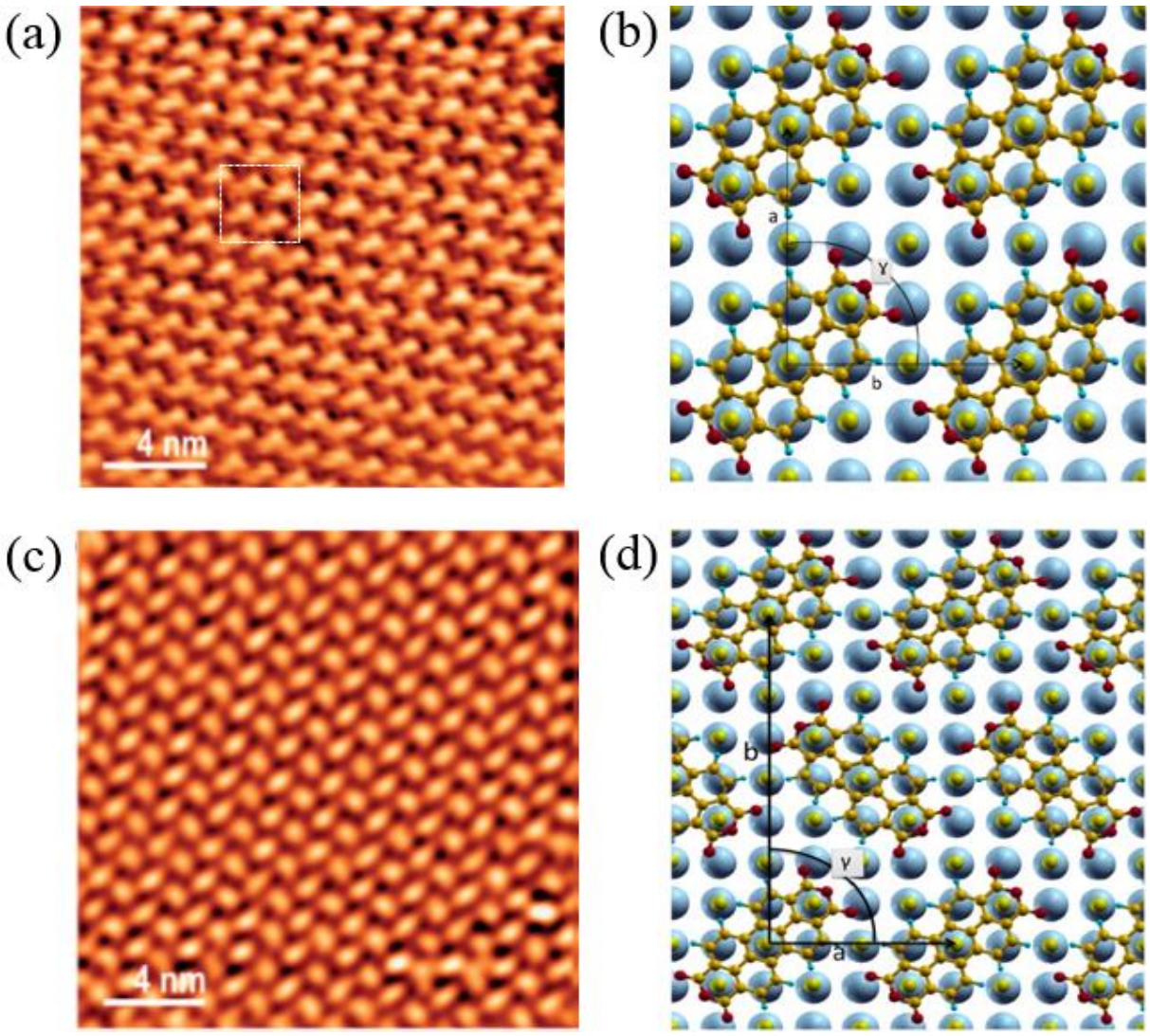

Figure 5.6: AFM image of PTCDA on bulk KCl(100). (a) PTCDA at sub-monolayer coverage (coverage of 0.4 monolayers) forms BW-structure. The supercell has the dimensions a = b = 12.6 ± 0.1 Å, γ = 90° [20]. (b) Structural model of the BW-phase [10]. (c) In the thicker films, thicker than one monolayer (coverage of 1.4 monolayers) PTCDA forms herringbone structure. (d) Structural model of the Herringbone phase (HB) of PTCDA on KCl(100) [10].

Sun et al studied the formation of PTCDA films on Au(111)-($22\times\sqrt{3}$) covered with NaCl islands [9]. They found that at low NaCl coverage, PTCDA molecules form 2D domains on the

Au(111) surface, and are preferentially nucleated at the step edges of the NaCl islands. However, at high NaCl coverage, PTCDA molecules form 3D clusters at the edges of the NaCl multilayers. Nevertheless, the adsorption sites of PTCDA molecules are PTCDA coverage dependent as explained in references [5] and [10]. Experimentally, the growth of PTCDA on Cu(111) covered with NaCl(100) islands was reported by Karacuban et al [5]. They demonstrated that the highest adsorption energy of the PTCDA molecules is found at the vacancies and steps of NaCl(100) islands. At a coverage of 0.1 ML, nucleation of the molecules begins at the polar step-edges, at defects, and at previously adsorbed molecules. At a coverage of 0.4 ML, step-edges are completely decorated with molecules, while the terraces of the substrate remain free of molecules [5].
The observation above was clarified by means of first principle calculations reported by Aldahhak et al [10]. The calculation showed that at low coverage, the PTCDA adsorbs at the vacant sites of the NaCl islands. After occupying all the vacancies, PTCDA molecules preferentially adsorb on other defect sites and the polar-terminated edges of the NaCl islands before finally resting on top of previously adsorbed molecules. The non-polar step-edges are decorated last, especially at higher coverages before extending to form flat surface terraces [10].

To end this, the PTCDA monolayer structures on a thin film of KCl [16] and NaCl [4] were obtained using SPA-LEED. Müller et al studied the growth of a PTCDA monolayer on 10 ML thick KCl on Ag(001) using LEED [16]. Their experiment showed identical structures to the PTCDA on bulk KCl(001), where their LEED pattern exhibited a quadratic unit cell with a fourfold symmetry. The observed PTCDA structure is a commensurate structure. In addition, they showed that the size of the PTCDA domains is not limited by the structural quality of the KCl layer since they found that the average domain size of the PTCDA layer is smaller than the domain size of the KCl films [16]. In addition, the growth of PTCDA monolayer on 10 ML of NaCl on Ag(001) was studied by Le Moal et al [4] using SPA-LEED. They obtained results identical to PTCDA on bulk NaCl. The LEED pattern showed that PTCDA molecules form a commensurate structure and are arranged in a square unit cell with dimensions of $a=b=17.0 \pm 0.1$ Å, which is in agreement with the calculated value of 16.92 Å.

5.3.2 PTCDA deposition

PTCDA molecules are evaporated from a Knudsen effusion cell inside the analysis chamber at a base pressure of 6.3×10^{-10} mbar and at a cell temperature of 553 K after a 30-minute deposition. During deposition of PTCDA molecules on the KCl film, the sample temperature was held at 300 K.

KCl ultrathin films were grown on Ag(001) at 435 K using an evaporation cell temperature of 793 K, and for two different deposition times of 7.5 and 11 min. The PTCDA molecules are investigated on two different KCl films mentioned above.

- **PTCDA deposited on the KCl film that grown on Ag(001) after 7.5 min**

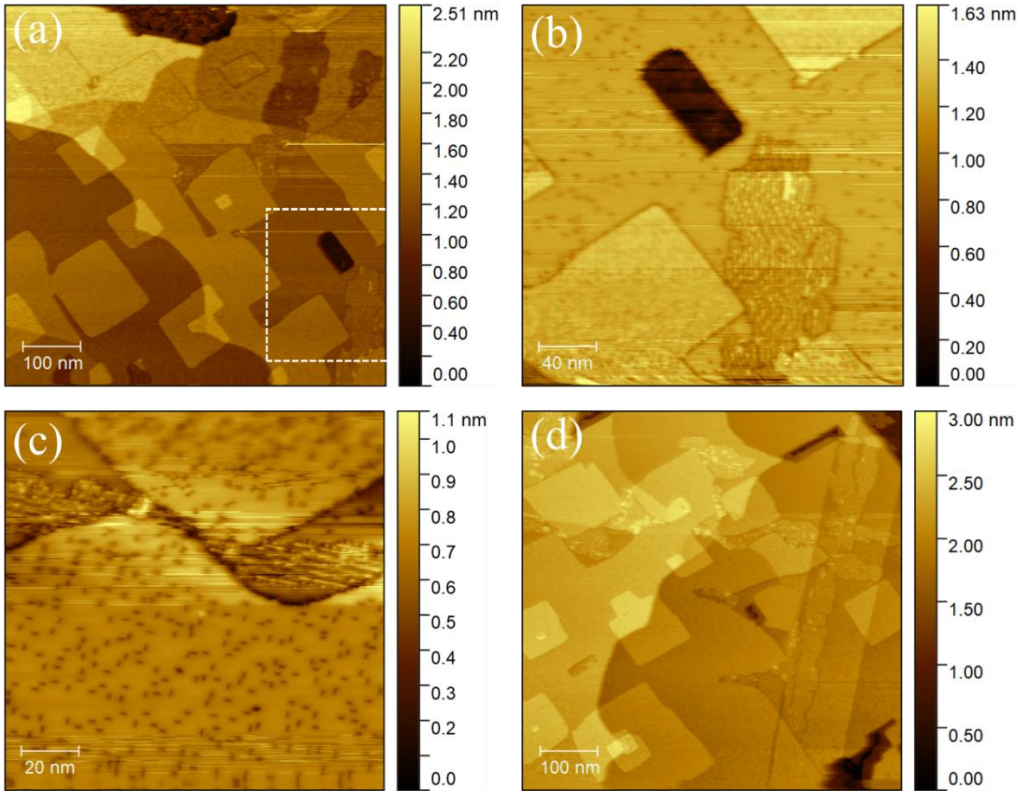

Figure 5.7: STM topography of PTCDA molecules on KCl on Ag(001) at 300 K, (a) 500 × 500 nm^2 (U_b = 4 V, I_t = 0.7 nA) (b) 200 × 200 nm^2 (U_b = 4 V, I_t = 0.7 nA) selected area of (a), (c) 100 × 100 nm^2 (U_b = 4 V, I_t = 0.5 nA), (d) 500 × 500 nm^2 (U_b = 4 V, I_t = 0.3 nA). All STM images are recorded at low temperature (78 K).

Figure 5.7 shows STM images of PTCDA molecules deposited on KCl on Ag(001) at 300 K. These images show that the silver surface and the KCl layers are covered with the PTCDA molecules with an occupation of almost 3.3 %, where the surface density of the PTCDA molecules is about 0.025 nm^{-2} within 400 nm^2 image. This is compared with the surface density of PTCDA molecules within the quadratic unit cell of about 0.75 nm^{-2} [8].

In the upper middle of the image (a), PTCDA molecules form islands with a random shape on the bare Ag(001) area. On the KCl film, 3D molecular aggregates are formed. Image (b) is a selected area of the image (a) showing an island of PTCDA molecules on top of the KCl layer. Within this island, the molecules are arranged in a particular structure (densely packed). In addition, the individual molecules are clearly resolved on the rest of the KCl surface. Image (c) shows clearly these individual molecules decorating the KCl layers. Two different adsorbed structures are expected depending on PTCDA coverage: the brick wall structure (BW) and the herringbone structure (HB), which have already been reported for the PTCDA on the bulk KCl(100) surface [10], [1] and on a 10 ML KCl film [16].

- **PTCDA deposited on the KCl film that grown on Ag(001) after 11 min**

Figure 5.8 shows the PTCDA molecules on the thicker KCl film compared to the previous KCl film shown in Fig. 5.7. Figure 5.8(a) is an area of the sample showing the large KCl domain with KCl islands on the top. PTCDA molecules covered the whole area (KCl layers and silver substrate) and form islands with random shapes on the bare area of the silver (see the upper left side of the image (a)). Image (b) is a selected area of the image (a), showing clearly the PTCDA molecules on the surface. We zoomed the upper area of this image to we obtain image (c) that shows apparently the PTCDA islands arranged on the silver steps (where the molecules are lying flat on the silver substrate), on the steps edges of the KCl layer, and on top of the KCl layers. Image(d) is the selected area with a black dotted line in panel (c). It can be clearly seen that the molecules have rearranged themselves into islands with a dense packing. They are found preferentially at step edges of the KCl layer. Since the substrate was kept at room temperature during the deposition of the PTCDA on the KCl film, the mobility of the molecules was relatively high. Therefore, they showed a tendency to dewet and to cluster (see the dark area in the image (d) with the high coverage of molecules), within this area no long-range order was found.

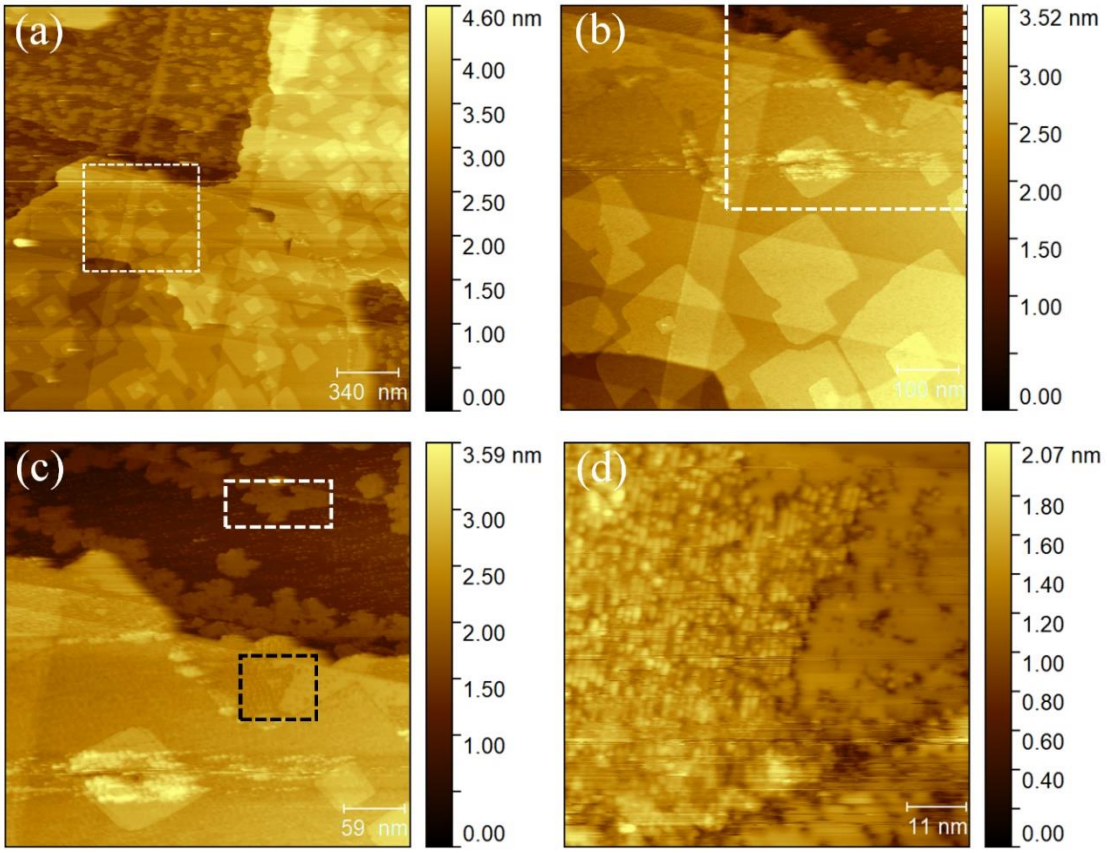

Figure 5.8: STM topography of PTCDA molecules on KCl on Ag(001) at 300 K, (a) 1700 × 1700 nm^2 (U_b = 4 V, I_t = 0.5 nA) (b) 500 × 500 nm^2 (U_b = 4 V, I_t = 0.2 nA) selected area of (a), (c) 279 × 279 nm^2 (U_b = 4 V, I_t = 0.5 nA), (d) 56.94 × 56.94 nm^2 (U_b = 4 V, I_t = 0.2 nA). All STM images are recorded at low temperature (78 K).

Figure 5.9(a) is a selected area on the silver substrate shown by the white dotted line the panel of Fig. 5.8(c). This image exhibits a structure of PTCDA molecules that are arranged in an L-shape instead of a T-shape or herringbone structure that is known for PTCDA molecules on Ag(001) surface [8], [19]. The observed L-phase structure has already been reported for PTCDA on Ag(001) substrate where a few percent of KCl molecules are present on the bare silver surface [17]. This may be due to the fact that the bare silver areas are covered by additional KCl molecules and it may be, however, that at the growth temperature, individual (disordered) KCl molecules between well-ordered KCl domains change the growth mode of the PTCDA domains on Ag. These may affect the arrangement of the PTCDA film, and thus, lead to the rotation of lattice from the T-

shape to L-shape. Note Guo et al have found in STM and LEED measurements that both the molecule and molecular superlattice would rotate after the dosing of KCl [17].

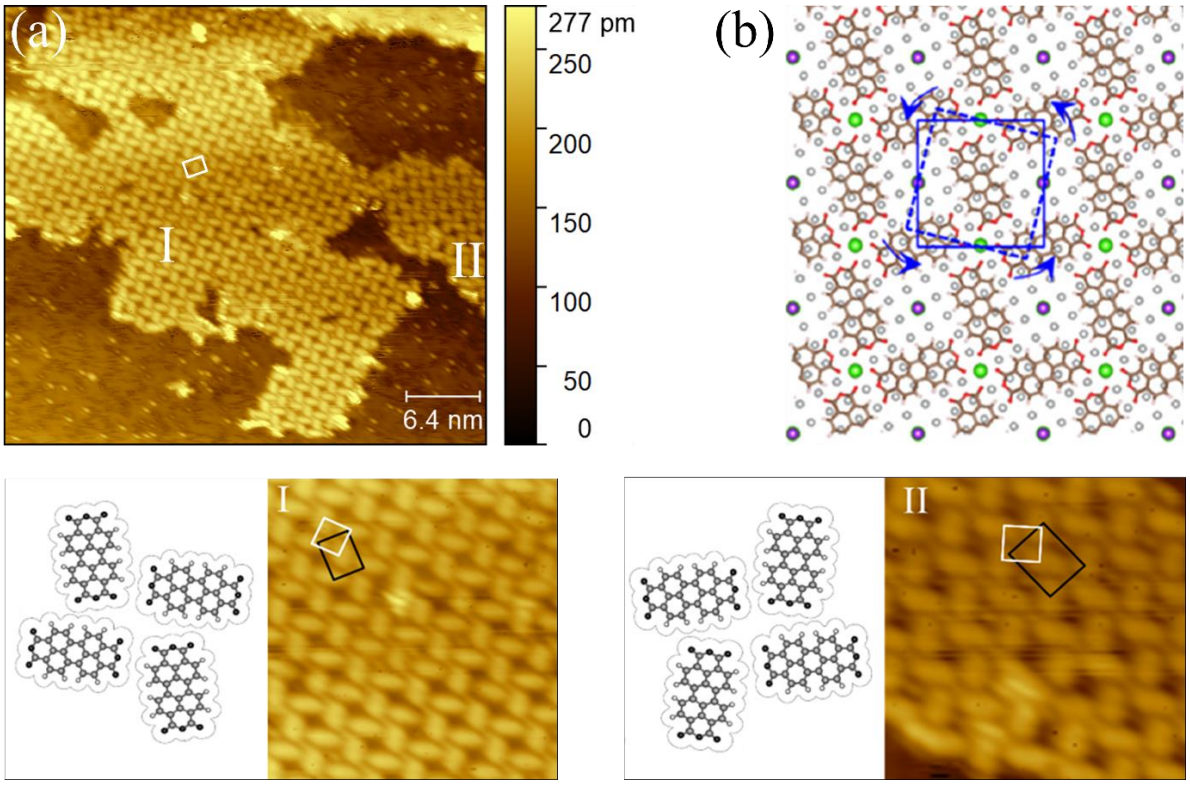

Figure 5.9: (a) is the selected areas with a white dotted line in panel of the Fig. 5.8(c) which shows the PTCDA structure on bare silver (31.91 × 22.23 nm^2, U_b = 2.5 V, I_t = 0.35 nA). The measured lattice parameters are: a=15.3 Å, b=14.8 Å and γ =81 ± 3.2°. (b) Structure model of PTCDA and KCl on Ag(001), where the green and the purple circles are the KCl molecules. The dashed/solid square indicates the PTCDA molecular lattice of the T-/L-structure, showing the rotation of the lattice from T-shape to L-shape [17]. The bottom images are the zoomed I and II areas of the image (a) showing PTCDA molecules on the bare silver area in more detail and arranged in L-shape structure in two different orientations (windmill-like structures [17]).

The measured lattice parameters of these molecules in Fig.5.9(a) are: a=15.3 Å, b=14.8 Å and γ =81 ± 3.2°, which is close to the value observed by Guo et al (a=b= 16.85 Å)[17]. We found in the L-structure that the molecules are tilted in two different ways (windmill-like structures [17])

as shown in the areas I and II of the image (a). In area I the centered molecule of the unit cell is perpendicular to the a and b axis, whereas it is parallel to these axes in area II. For both modifications the unit cell in both areas are aligned (see the bottom images of Fig. 5.9). This is in agreement with previously reported PTCDA molecules on Ag(001) substrate.

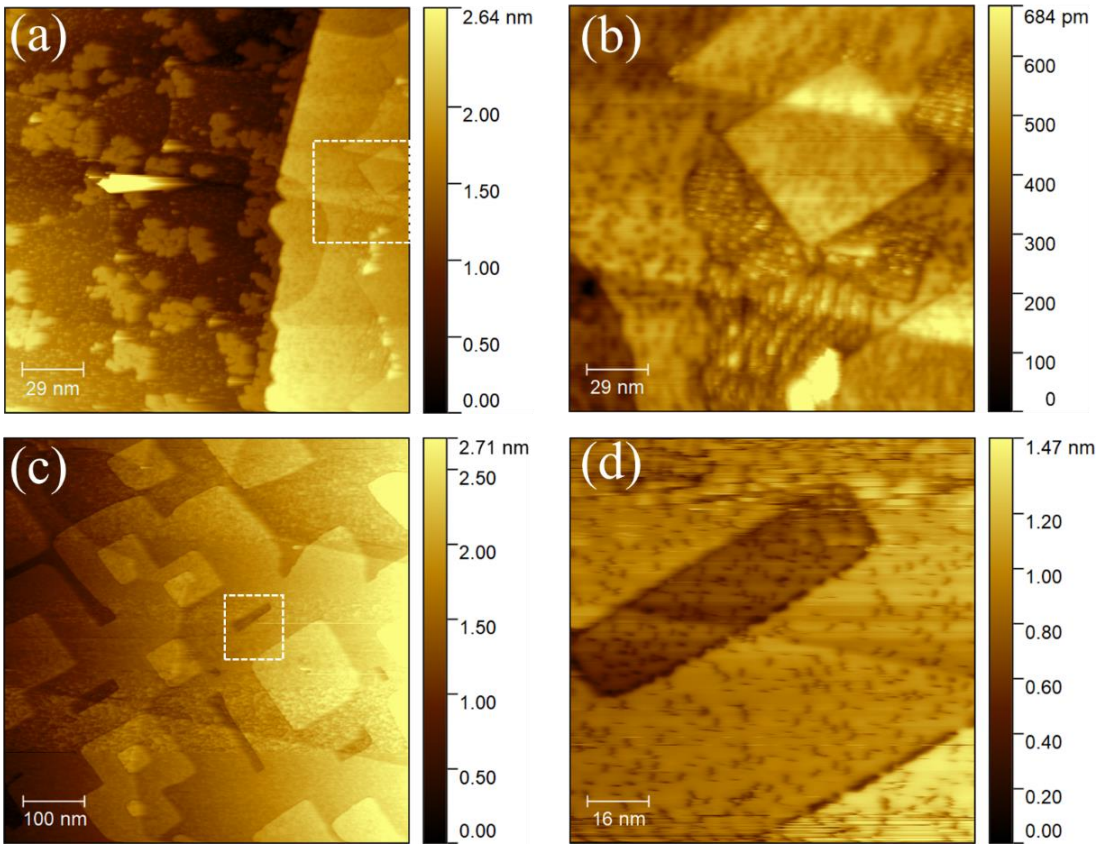

Figure 5.10: STM topography of PTCDA molecules on KCl on Ag(001) at 300 K, (a) 145 × 145 nm^2 (U_b = 4 V, I_t = 0.28 nA) (b) 145 × 145 nm^2 (U_b = 4 V, I_t = 0.28 nA) selected area of (a), (c) 500 × 500 nm^2 (U_b = 4 V, I_t = 0.25 nA), (d) 80 × 80 nm^2 (U_b = 4 V, I_t = 0.25 nA) selected area of (c). All STM images are recorded at low temperature (78 K).

Finally, the last figure 5.10 shows different areas of the same film as in Figs 5.8 and 5.9, which shows also that the islands have random shapes on the silver substrate, individual PTCDA molecules on the KCl layers, and a densely packed structure of these molecules on KCl layer. In addition, we were able to measure the PTCDA on a silver substrate with the bias voltage 2.5 V,

whereas it was not possible to measure these molecules on KCl layer with the bias lower than 4 V). The difficulties to image the structural arrangement of these molecules on the KCl film is perhaps due to several reasons. First, because PTCDA on the Ag(001) metal surface is stable at RT, unlike on the KCl and NaCl. Second, at the high coverage of thin insulting film, PTCDA molecules form 3D clusters on the surface [9].

5.4 Conclusions

In this chapter we have investigated the deposition of PTCDA molecules on the metallic substrate Ag(001) and on the KCl/Ag(001) systems using scanning tunnelling microscopy (STM). We observed that PTCDA forms monolayer films on the silver substrate with a coverage of almost 100 %. Within this monolayer, PTCDA molecules are arranged in T-shapes with a quadratic unit cell. On KCl/Ag(001), the STM images showed the formation of the individual PTCDA molecules (with a coverage of 3.3 %) and a densely packed structure on the KCl films. In addition, islands had random shapes on the bare silver area, where within these islands the molecules form a L-shaped lattice instead of a T-shape due to the presence of additional KCl molecules on bare silver left over from the growth of KCl and which affect the arrangement of the PTCDA molecules.

In order to avoid the formation of molecular aggregates and to obtain the structure of PTCDA on the KCl film, further experiments are necessary and many growth parameters need to be improved, especially the method of cooling the system during the growth of PTCDA on KCl.

5.5 Bibliography

[1] T. Dienel, C. Loppacher, S. C. B. Mannsfeld, R. Forker, and T. Fritz, "Growth-Mode-Induced Narrowing of Optical Spectra of an Organic Adlayer," *Adv. Mater.*, vol. 20, no. 5, pp. 959–963, 2008.

[2] M. Müller, E. Le Moal, R. Scholz, and M. Sokolowski, "Exciton and polarization contributions to optical transition energies in an epitaxial organic monolayer on a dielectric substrate," *Phys. Rev. B*, vol. 83, no. 24, p. 241203, 2011.

[3] W. Gebauer, A. Langner, M. Schneider, M. Sokolowski, and E. Umbach, "Luminescence quenching of ordered π-conjugated molecules near a metal surface: Quaterthiophene and PTCDA on Ag(111)," *Phys. Rev. B*, vol. 69, no. 15, p. 155431, 2004.

[4] E. Le Moal, M. Müller, O. Bauer, and M. Sokolowski, "Stable and metastable phases of PTCDA on epitaxial NaCl films on Ag(100)," *Phys. Rev. B*, vol. 82, no. 4, p. 45301, 2010.

[5] H. Karacuban, S. Koch, M. Fendrich, T. Wagner, and R. Möller, "PTCDA on Cu(111) partially covered with NaCl," *Nanotechnology*, vol. 22, no. 29, p. 295305, 2011.

[6] H. Proehl, T. Dienel, R. Nitsche, and T. Fritz, "Formation of Solid-State Excitons in Ultrathin Crystalline Films of PTCDA: From Single Molecules to Molecular Stacks," *Phys. Rev. Lett.*, vol. 93, no. 9, p. 97403, 2004.

[7] F. S. Tautz, "Structure and bonding of large aromatic molecules on noble metal surfaces: The example of PTCDA," *Prog. Surf. Sci.*, vol. 82, no. 9, pp. 479–520, 2007.

[8] J. Ikonomov, O. Bauer, and M. Sokolowski, "Highly ordered thin films of perylene-3,4,9,10-tetracarboxylic acid dianhydride (PTCDA) on Ag(100)," *Surf. Sci.*, vol. 602, no. 12, pp. 2061–2068, 2008.

[9] X. Sun and F. Silly, "NaCl islands decorated with 2D or 3D 3,4,9,10-perylene-tetracarboxylic-dianhydride nanostructures," *Appl. Surf. Sci.*, vol. 256, no. 7, pp. 2228–2231, 2010.

[10] H. Aldahhak, W. G. Schmidt, and E. Rauls, "Adsorption of PTCDA on NaCl(100) and KCl(100)," *Surf. Sci.*, vol. 617, no. Supplement C, pp. 242–248, 2013.

[11] X. Sun, M. P. Felicissimo, P. Rudolf, and F. Silly, "NaCl multi-layer islands grown on Au(111)-(22× √3) probed by scanning tunneling microscopy," *Nanotechnology*, vol. 19, no. 49, p. 495307, 2008.

[12] A. J. Lovinger, S. R. Forrest, M. L. Kaplan, P. H. Schmidt, and T. Venkatesan, "Structural and morphological investigation of the development of electrical conductivity in ion-irradiated thin films of an organic material," *J. Appl. Phys.*, vol. 55, no. 2, pp. 476–482, Jan. 1984.

[13] M. Möbus, N. Karl, and T. Kobayashi, "Structure of perylene-tetracarboxylic-dianhydride thin films on alkali halide crystal substrates," *J. Cryst. Growth*, vol. 116, no. 3, pp. 495–504, 1992.

[14] A. Kraft, R. Temirov, S. K. M. Henze, S. Soubatch, M. Rohlfing, and F. S. Tautz, "Lateral adsorption geometry and site-specific electronic structure of a large organic chemisorbate on a metal surface," *Phys. Rev. B*, vol. 74, no. 4, p. 41402, 2006.

[15] A. Schmidt, T. J. Schuerlein, G. E. Collins, and N. R. Armstrong, "Ordered Ultrathin Films of Perylenetetracarboxylic Dianhydride (PTCDA) and Dimethylperylenebis(dicarboximide) (Me-PTCDI) on Cu(100): Characterization of Structure and Surface Stoichiometry by LEED, TDMS, and XPS," *J. Phys. Chem.*, vol. 99, no. 30, pp. 11770–11779, Jul. 1995.

[16] M. Müller, J. Ikonomov, and M. Sokolowski, "Structure of Epitaxial Layers of KCl on Ag(100)," *Surf. Sci.*, vol. 605, no. 11, pp. 1090–1094, 2011.

[17] Q. Guo, M. Huang, S. Lu, and G. Cao, "Ionic compound mediated rearrangement of 3, 4, 9, 10-perylene tetracarboxylic dianhydride molecules on Ag(100) surface," *Nanotechnology*, vol. 26, no. 27, p. 275603, 2015.

[18] S. A. Burke, W. Ji, J. M. Mativetsky, J. M. Topple, S. Fostner, H.-J. Gao, H. Guo, and P. Grütter, "Strain Induced Dewetting of a Molecular System: Bimodal Growth of PTCDA on NaCl," *Phys. Rev. Lett.*, vol. 100, no. 18, p. 186104, May 2008.

[19] A. J. Lovinger, S. R. Forrest, M. L. Kaplan, P. H. Schmidt, and T. Venkatesan, "Structural and morphological investigation of the development of electrical conductivity in ion-

irradiated thin films of an organic material," *J. Appl. Phys.*, vol. 55, no. 2, pp. 476–482, Jan. 1984.

Conclusions & Perspectives

We have shown through our STM measurements that thin insulating films on a metal substrate have different growth modes; island growth for the NaCl film and Layer-plus-island growth for the KCl film. The quality of these films depend on the growth conditions in particular such as the sample temperature, the deposition time, and the cell temperature, to the extent that various epitaxial relationships with the substrate are found. In addition, at a sufficiently low thickness (typically 2 to 5 ML), we have shown that alkali halide films on metals may be discontinuous and/or exhibit holes, especially when their growth involves the coalescence of domains with mismatched orientations. The apparent thickness measurements of the as grown NaCl and KCl ultrathin layers provided by STM shows that the apparent thickness and the STM contrast of these two insulating films vary as a function of the bias voltage, as well as the bias polarity (+/-).

The most important results presented in this thesis concern the effects of electron irradiation on thin alkali-halide films using LEED and AES. Until now, this has rarely been considered; in particular, the case of ultra-thin alkali-halide films composed of one or two monolayers, grown on fcc metals had not been addressed. We have confirmed that the electron-induced dissociation of ultrathin alkali-halide films grown on fcc metals differs, in terms of reaction kinetics and outcomes, from that of their thick film and bulk crystal counterparts. These differences issue mainly from the limited amount of reactants and the product interactions with the substrate. We have observed that Cl depletion follows different reaction kinetics, as compared to previous studies on thick NaCl films and bulk crystals. Na atoms produced from NaCl dissociation diffuse to bare areas of the Ag(001) surface, where they form Na-Ag superstructures that are known for the Na/Ag(001) system. STM was used to examine the film geometry and thickness of the irradiated ultrathin films which showed that the dissociation of the ultrathin NaCl films follows two processes; (i) the electron irradiation increases the NaCl disorder through the removal of NaCl from the island edges, which slows down the reaction kinetics of NaCl dissociation, and (ii) the formation of Na superstructures on silver. Further investigations are necessary to control the ratio between the

disordered and ordered areas since such alkali-halide films are increasingly used as spacers to electronically decouple organic molecules from metallic substrates in atomically controlled systems for single molecule spectroscopy measurements.

The second objective of this thesis was to study thin organic films of the PTCDA molecule by using the ultrathin KCl film as spacer to decouple PTCDA molecules from the metal Ag(001) substrate. To avoid the dissociation of KCl films only STM has used. The arrangement of PTCDA molecules within islands on bare silver substrate was observed, where both individual molecules and densely packed structures on KCl films were found. However, disordered adsorbates of PTCDA and KCl molecules are also found. These form during the growth of the PTCDA and KCl films. The presence of additional KCl molecules may affect the arrangement of the PTCDA film and the apparent thickness measurements for both films. In order to avoid this, a controlled cooling procedure will be necessary during the growth. This system can be used to study the electrical excitation of the luminescence with electrons using STM tip, which only occurs when the molecules are deposited on an insulating substrate, otherwise it is quenched due to charge transfer from the molecules to the substrate.

Finally we have studied thin film of KCl grown on Ag(001) using GIFAD, in order to obtain more detailed information on the growth mode (Appendix). The experiment was performed with the He beam aligned along two directions of the sample; [110] and [001]. In both directions we found that, contrary to NaCl, KCl thin films adopt a unique orientation with respect to the substrate. In addition, no relaxation of the KCl film was found in both 0˚ and 45˚ orientations with respect to the silver surface. Furthermore, we found no azimuthal mosaicity since no additional diffraction spots were observed on KCl when changing from the 0˚ to the 45˚ orientation. However, our results show high apparent corrugation compared to the bulk KCl. Two reasons could explain this increase in corrugation; the rumpling process where the potassium atom is much closer to the metal substrate, or the charge transfer from the silver to the chlorine atoms.

Appendix

Grazing incidence fast atom diffraction: KCl on Ag(001)

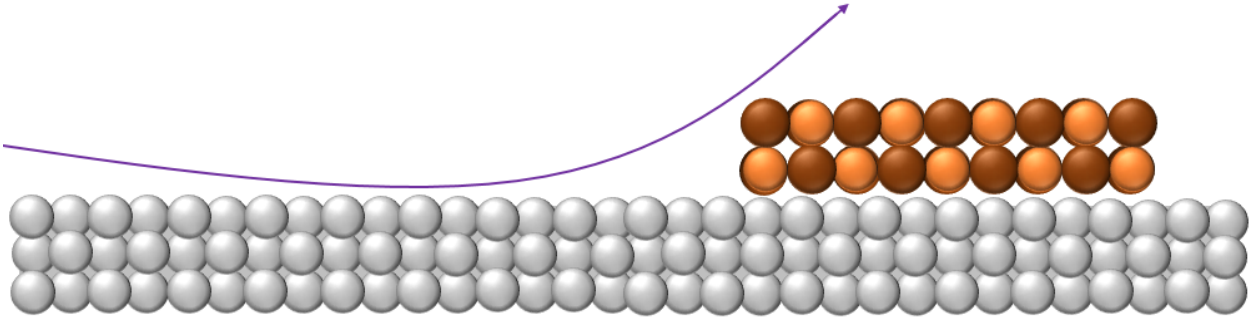

Table of Contents

1. Introduction

Grazing Incidence Fast Atom Diffraction (GIFAD) is a new technique developed at ISMO and used for the determination of the structural properties of crystalline surfaces or thin films. It is based on the diffraction of He atoms at energies around 1 keV and incidence angles typically lower than 1.5° with respect to the surface plane. Although the associated de Broglie wavelength is very small compared to the lattice parameters of crystals, a clear and well resolved diffraction pattern can be observed, even at surface temperatures exceeding 500°C. GIFAD has proved to be an effective technique on insulators [1], [2], semiconductors [3] and metals [4]. Its ability to provide valuable information in real time during film growth has also been demonstrated, first on the layer-by-layer homoepitaxial growth of GaAs(100) [5] more recently on the growth of an ultra-thin organic layer [6].

In the following sections, we describe the principle of GIFAD, the experimental apparatus, and method and the experimental results.

2. Principle of GIFAD

2.1 Typical de Broglie wavelength

In 1924 the French scientist Louis de Broglie postulated the wave matter hypothesis to explain quantum mechanics [7]–[9]. He proposed that matter behaves like a wave and suggested that the electrons also have wave-like properties similar to light. Later this hypothesis was called Broglie-particle theory waves and matter waves are referred to as de Broglie waves. Equation (1) gives the de Broglie wavelength λ, which associated with a particle with mass and is related to its momentum p, through the Planck constant h.

$$\lambda = \frac{h}{p} \qquad (1)$$

Using the relation:

$$\vec{p} = m\vec{v} \qquad (2)$$

The de Broglie wavelength λ can be re-written as follows:

$$\lambda = \frac{h}{p} = \frac{h}{mv} \qquad (3)$$

Where v and m are the velocity and the mass of the particle. This wave matter hypothesis has been confirmed experimentally for electrons, neutral atoms, molecules, and neutrons.

2.2 Scattering geometry and derivation of lattice parameter

The Von Laue formalism [10] can be used to interpret the distribution of the diffraction peaks:

$$\begin{aligned} a \cdot \Delta k &= 2\pi h \\ b \cdot \Delta k &= 2\pi k \\ c \cdot \Delta k &= 2\pi l \end{aligned} \qquad (4)$$

Where a, b, c are the primitive vectors of the crystal lattice, and h, k, l are the reflection's reciprocal lattice indices. As with Bragg's formalism $n\lambda = 2d\sin\theta$, Von Laue's formalism provides a way to explain X-ray diffraction at crystal surfaces by considering the interferences of a wave and connecting the observed pattern of interference to the crystal lattice.

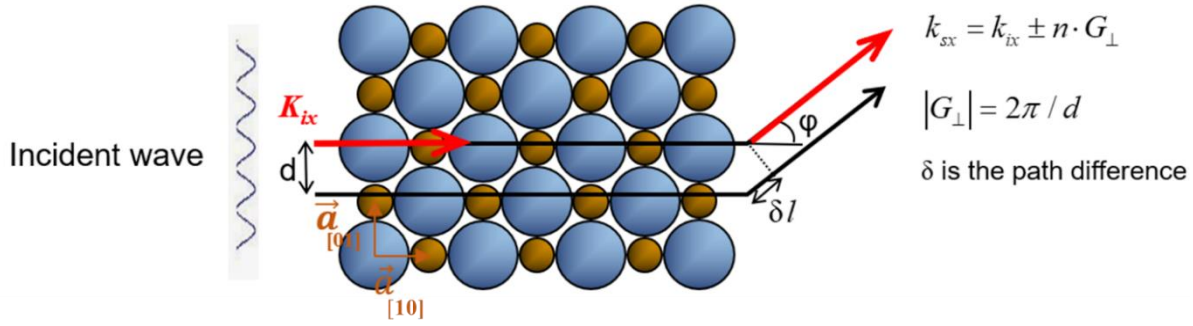

Figure 1: Top view of a NaCl type surface (001). The basis vectors a_{01} and a_{10} form the elementary mesh of the surface for the reciprocal lattice. The beam is oriented along the direction [10], which corresponds to the direction <100> with respect to the Miller indices of the crystal volume. The surface has rows of perfectly aligned atoms along the directions parallel and transverse to the direction of propagation as well as along the directions [11]. Only the diffraction from the rows parallel to the direction of propagation is observed in grazing incidence.

In our case, the beam consists of atoms with kinetic energy E_0 in the keV range where the wavelength is given by the de Broglie formula (3). The atoms of the beam arrive one by one on

the crystal and diffract individually on the crystal lattice. The observed diffraction pattern is therefore the statistical accumulation of a large number of atomic diffraction events by the same periodic lattice.

A simple approach to understand the diffraction pattern is to use a semi-classical approach where the wave associated to the projectile is represented by a plane wave to which we can attribute an incident wave vector $\overrightarrow{K_i} = \overrightarrow{K_{ix}} + \overrightarrow{K_{iy}} + \overrightarrow{K_{iz}}$ and an outgoing wave vector $\overrightarrow{K_s} = \overrightarrow{K_{sx}} + \overrightarrow{K_{sy}} + \overrightarrow{K_{sz}}$ corresponding to the incident beam. In the case where the beam is perfectly aligned along the crystallographic direction: $\varphi_i = 0$ (where φ is the azimuthal angle) and therefore, the component of the wave vector along the "y" axis is zero $K_{iy}=0$.

In the grazing incidence adopted here, the energy associated to the atom motion normal to the surface, given by $E_\perp = E_0 \sin^2 \theta_i$, is typically lower than 1 eV. Thus atoms do not penetrate the crystal volume, they diffract on the crystalline surface: that is a planar crystal. The latter is related to a two-dimensional network of atoms that can be described as a periodic network of rows of atoms aligned with the beam (direction x), and each row is formed by a periodic arrangement of atoms (direction y). Constructive interference occurs between successive rows at a given exit angle if the path difference travelled by the incident wave over two successive rows corresponds to an integer multiple of the wavelength. The diffracting element is therefore the row of atoms. By adopting the formalism of Von Laue, the preceding considerations allow us to formulate constructive interferences for the waves according to:

$$\overrightarrow{K_s} - \overrightarrow{K_i} = \overrightarrow{G}$$

This is the condition for the Bragg diffraction in the reciprocal space. Where $\overrightarrow{G}$ is a linear combination of the reciprocal lattice vectors $\overrightarrow{G_1}$ and $\overrightarrow{G_2}$ associated respectively with the periodicities along the propagation direction (x) and along the transverse direction (y) such that, where $a_i = d$ is the inter-row distance along the considered direction.

$$\overrightarrow{G} = n_1 \overrightarrow{G_1} + n_2 \overrightarrow{G_2} \qquad n_1, n_2 \in Z$$

In grazing incidence, $n_1 = 0$ for energetic considerations, so that the fast atoms are only sensitive to the periodicity of the average corrugation of the rows of atoms. This periodicity does not necessarily correspond to the periodicity of the crystal network. As an illustration, take the

case of the surface of NaCl(001): the periodicity of the rows perceived by the beam in the <11> direction is $a_{<11>} = \frac{a_{NaCl}}{2\sqrt{2}}$. On the other hand, along the <01> direction, two rows of successive atoms present identical mean corrugations although the atomic arrangements are shifted by one atom, the periodicity to be considered is, therefore: $a_{<01>} = \frac{a_{NaCl}}{2}$.

In space (θ, φ), the position of the diffraction orders is parameterized by the K_{sy} component which can only take multiple discrete values of $2\pi / a_{raws}$. For a given order n [11] we have:

$$\varphi s_n = \arctan\left(\frac{K_{sy}}{K_{ix}}\right) = \arctan\left(\frac{n \cdot \lambda_{atom}}{a_{rows} \cos(\theta_i)}\right)$$

Because of the grazing incidence, the previous expression can be simplified and a simple expression of the angular difference between the orders of diffractions is obtained:

$$\Delta\Phi \approx \frac{\lambda_{atom}}{a_{raws}}$$

2.3 Averaging property

Atom scattering from surfaces is described by the atom-surface potential V(x, y, z). In the simplest approximation, the actual surface that is probed by the beam can be obtained by drawing the equipotential surface for which $V(x,y,z) = E_{\perp}$. Neglecting the weak attractive forces, this equipotential is equivalent to an isodensity surface. A corrugated surface resembles an egg-box as illustrated in the left panel of Fig.2. Such a shape is typically observed in AFM and STM measurements. The 2D corrugated surface (egg-box) is transformed by averaging to a corrugated iron-plate.

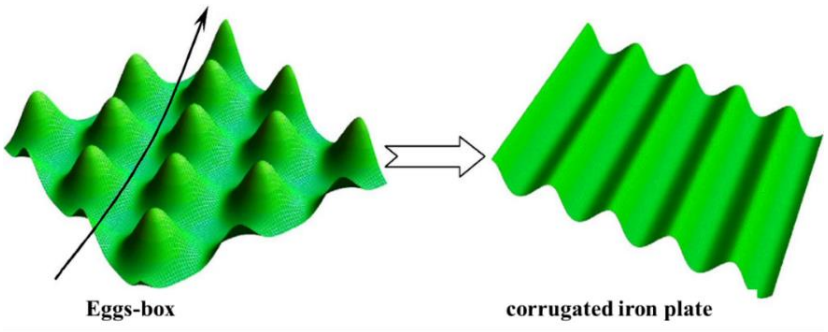

Figure 2: Equipotential planes of a surface. Left: eggs-box (not averaged), right: averaged along the beam direction.

If the shape of the iron-plate is sinusoidal, meaning that it can be described by the following expression:

$$\xi(y) = h_c a_{raws} \cos(2\pi \frac{y}{a_{raws}})$$

where h_c a_{raws} is the amplitude of the corrugation function (difference of altitude between crest and trough), then the amplitude of scattering of the order n is a Bessel function of order $m, m \in \mathbb{N}$ such as $m = |n|$:

$$A(G_y) = J_m(x) \quad \text{with: } x = 2\pi \frac{h_{c.arrows}}{\lambda_\perp} \quad \text{and} \quad m = |n|$$

where $\lambda_\perp$ is the wavelength associated to the motion normal to the surface [12]. The intensity of the n^{th} diffraction order is, therefore:

$$P_n = J_m^2(x) \text{ with } \sum P_n = 1$$

3. Experimental apparatus

3.1 Experimental setup

The GIFAD experiments were performed under Ultra-High Vacuum (UHV) conditions. The setup consists of an ion gun, input deflectors (beam correction), a set of collimating diaphragms, a neutralization chamber, output deflectors (ion deviation), preparation chamber, and detector. Figure 1 shows the view of the whole experimental device.

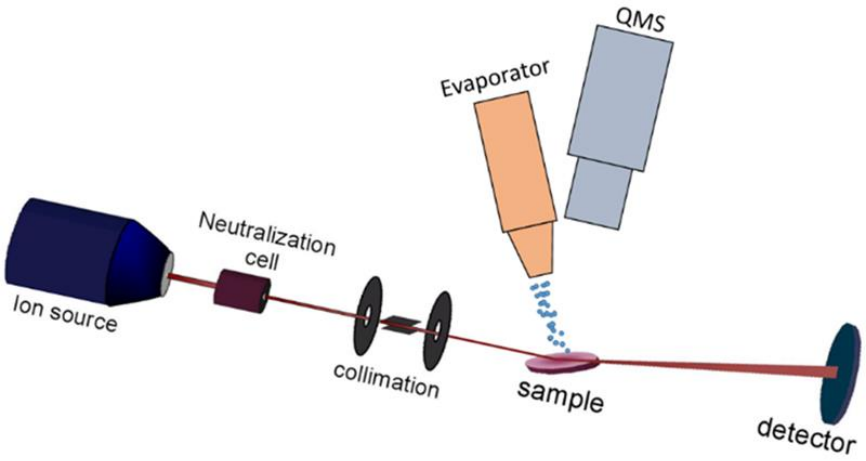

Figure 3: Schematic view of the experimental setup.

3.2 Beam line

The beam line is composed of an ion gun, a neutralization chamber and a series of diaphragms. The beam line does not require a very high vacuum, but on the other hand, it is necessary that the atmosphere therein contains only trace amounts of reactive chemical elements such as oxygen or water that could strongly damage the filaments of the ion source and pollute the beam. The overall scheme of the beam line is shown in Fig.3.

3.2.1 Ion Gun

The gas is injected into the ion gun and is ionized by electron bombardment. This ion gun can produce currents in order of μA of singly-charged ions of noble gases (He^+, $Ne^{+,}$ and Ar^+). These ions are then extracted from the source and accelerated to energies ranging from a few hundreds of eV up to a few keV, with an energy dispersion in order of 1 eV. The ion gun is equipped with a set of lenses, and four deviating plates that allow the ion beam to be shaped and control the focus. For the current study, we used a primary He+ beam at 1 keV energy.

3.2.2 Neutralization Chamber

The beam extracted from the ion gun enters into the neutralization chamber and is neutralized by resonant charge transfer from a He gas. To avoid multiple collisions that would increase the beam divergence, the pressure in the neutralization cell is tuned so that the obtained

neutralization beam remains below 20 %. The surviving ions are deflected away using electrostatic deflectors located upstream from the neutralization cell.

3.2.3 Beam collimation

The diffraction process is only possible if the wave packet associated with the He atoms is larger than the period d of the crystal. This condition, which translates into a minimum coherence length $L_c = \frac{\lambda}{\alpha} > d$ implies a minimum value for the beam divergence angle α. The only way to reduce the bean divergence is to use a set of apertures; thus we use typically two diaphragms of 100μm diameter separated by 30 cm.

3.3 The detector

Finally, after the interaction between the beam and the sample, the diffraction pattern was observed using a position-sensitive particle detector. This detector consists of a phosphor screen behind a chevron assembly of two micro-channel plates. The intensity distribution of the scattered particles is then collected by a CCD camera located on the air side behind the phosphor screen.

3.4 Main Chamber (Interaction chamber)

Interaction of the beam with the crystalline surface takes phase in this chamber, where the sample is located in the center of the interaction chamber. The sample is mounted on a molybdenum support on a mechanical manipulator arm which is equipped with a motor that controls the two rotation angles of the sample (azimuthal and polar). The beam incidence angle θ_I can be adjusted between 0.2 and 1.5°, thus providing a large variation of the normal energy defined as $E_\perp = E_0 \sin^2 \theta_i$ where E_0 is the total beam energy.

It is necessary to work in an ultra-high vacuum in this chamber, in order to maintain a very clean surface of our samples and to avoid that they are covered too quickly by adsorbed molecules. Therefore, the experiment is performed in the pressure range between 10^{-10}-10^{-11} mbar which is achieved using an ion-pump and a turbo-molecular pump.

This chamber is equipped with an electron bombardment evaporator and a Quadrupole Mass Spectrometer (QMS). Both can be operated simultaneously during the GIFAD measurements. The sputtering and annealing operations also were performed in this chamber, for

several purposes; to clean the surface, to prepare the surface, and to perform measurements at different temperatures.

In our experiment, we used silver Ag(001) as a substrate, and we prepared it using several cycles of sputtering and annealing, where we sputtered with Ar^+ ions using the following parameters (Ar^+ ions energy =0.5 keV, the pressure of ions gas ~ 5 $\times 10^{-6}$ mbar, sample current ~ 5μA during 40 minutes), while the sample is held at room temperature. For the thin film growth (KCl/Ag(001)), we use potassium chloride (KCl) powder of 99.999% purity (trace metals basis) purchased from Sigma Aldrich (Saint Louis, MO, USA). KCl molecules were evaporated from a molybdenum crucible at a temperature around 800 K. During evaporation, the crucible was biased at 300 V to ensure sufficient heating by electrons emitted from a hot filament. Since the crucible temperature could not be directly measured, it was only evaluated from the value given by a thermocouple located away from the crucible. The QMS was used to measure the chemical composition of the residual gas, to detect the minimum temperature for evaporating KCl and evaluate the actual amount deposited on the sample through a basic temperature programmed desorption.

4. Experimental results: KCl growth on Ag(001)

During the growth of KCl on Ag(001), we recorded the intensity distribution of the scattered particles as a sequence of 3500 images, each with 1 s exposure. The most basic treatment of the data consists in observing the time evolution of the total intensity within the specular zone; this parameter measures the reflectivity change induced by the film growth. The reflectivity is extremely sensitive to topographic defects (step edges, ad-atoms or ad-molecules). The results are shown in Figure 4. The blue curve is the corrected reflectivity curve obtained by subtracting the noise signal (red curve) from the raw signal (black curve). The red curve is obtained by integrating the intensity inside an area with equal size but located well outside the specular zone where no scattered intensity is expected; this intensity is proportional to the background noise in the specular zone. The noise comes from the electron bombardment evaporator and is due to charged particles escaping when the shutter is open.

Before opening the shutter, the reflectivity is high but decreases slightly (by 4%) due to possible adsorption KCl molecules finding their way around the shutter. The diffraction pattern is characterized by intense spots corresponding to the Ag(001) substrate (see insert in figure 4).

After 500 s, we open the shutter and the reflectivity drops sharply before reading a minimum at about 1190 s. Then the reflectivity recovers slightly and the shutter is closed at 1810 s while still recording the reflectivity to observe any spontaneous evolution of the film.

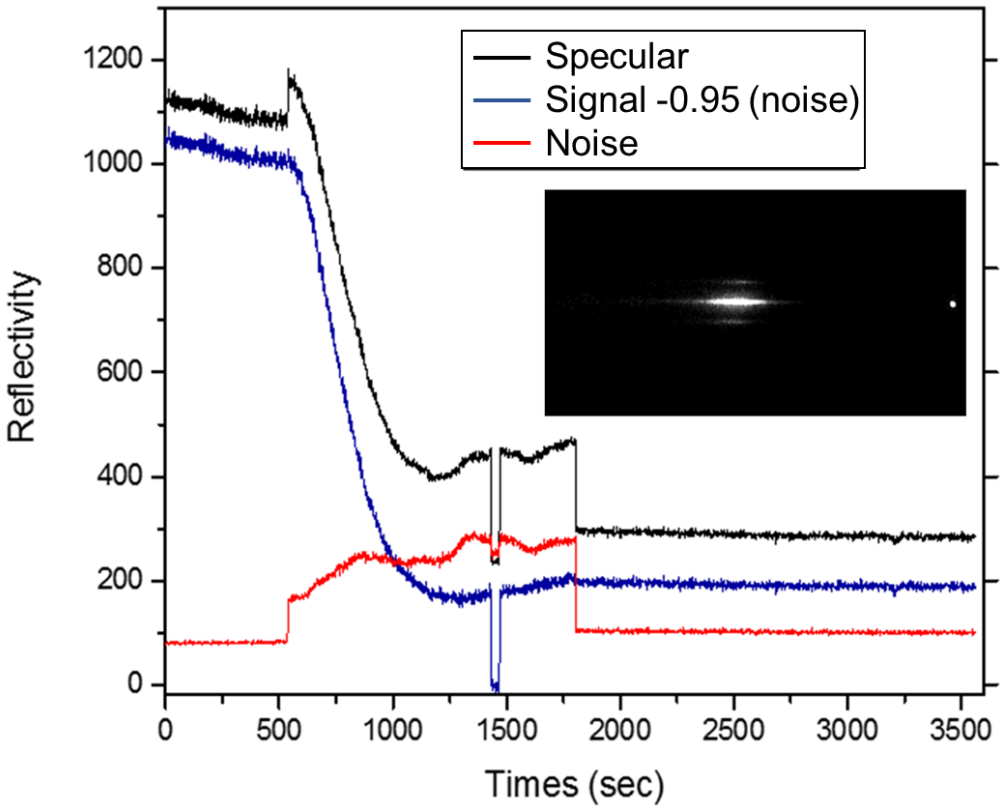

Figure 4: Surface reflectivity as a function of deposition time of KCl on Ag(001). The intensity is integrated inside a rectangular area centered on the specular zone (see figure 5). The red curve is obtained by integrating the intensity inside an area with equal size but located well outside the specular zone where no scattered intensity is expected, this intensity is proportional to the background noise in the specular zone. Finally, the net signal (black curve) is calculated from the difference corrected by a factor describing the inhomogeneity of the background signal.

- **The Intensity of the diffraction pattern of KCl Film grown on Ag(001)**

At any time in the deposition sequence, we can identify the diffraction pattern characteristic of a long-range order on the surface. The intensity profile of the diffraction patterns within the specular rectangle can then be traced during deposition. Figure 5 (right) shows an example of

extracting an intensity profile from a diffraction pattern averaged between 3320-3500 s. The average intensity of the diffraction patterns is shown in the left-hand side of Figure 5, plotted as a function of pixels of the traced rectangle at different time intervals during KCl deposition (which correspond to different intervals along the black curve in Fig.4). One can notice a continuous improvement of the diffraction pattern (intensity and resolution of the diffraction peaks) with time. The diffraction orders are more intense and well-defined after closing the shutter and become most evident between 3320-3500 s (purple curve). This perhaps indicates that at this point, we have either a complete layer or large islands of KCl on the surface. The signal to noise ratio is then improved at this interval (3320-3500 s) by recording the image acquisition over 1 second for each image (Figure 5, right). From their left/right symmetry with respect to the central 0^{th} order, these profiles indicate that the Ag(100) substrate and the KCl film share a common crystallographic direction. It is important to note that although the reflectivity remains fairly constant after closing the shutter (figure 4), figure 5 (left) shows that the film evolves towards a better organization; the Bragg peaks of the pink curve are better resolved that in the blue curve.

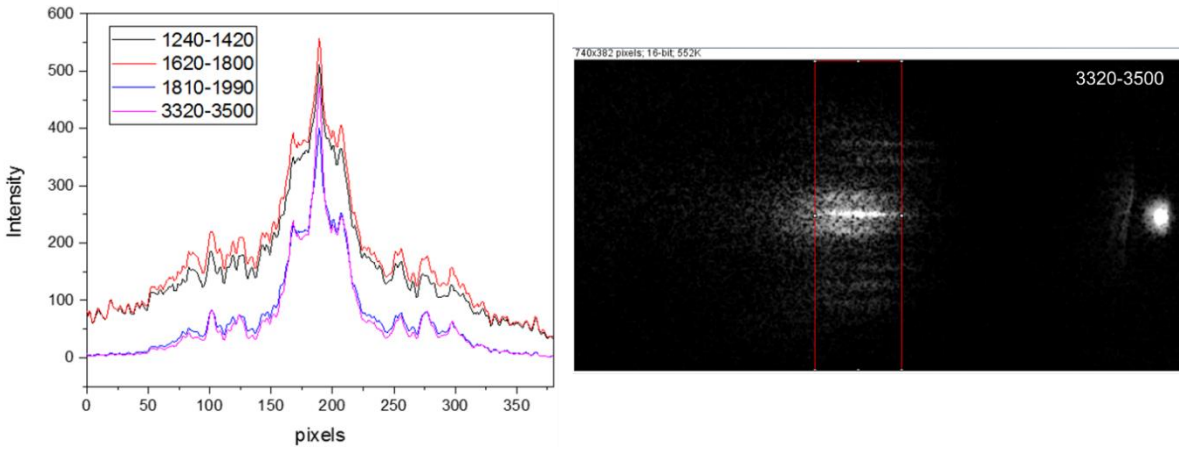

Figure 5: Left: Intensity profiles averaged across different time intervals during the deposition of KCl on Ag(001) as traced from the diffraction patterns. Right: Diffraction patterns (averaged from images recorded between 3320-3500 s) of 0.6 keV He atoms scattered from KCl film surface grown on Ag(001) under Φ_{in}=0.7°. The narrow spot on the right of the image is the direct beam.

Rather than observing selected diffraction patterns at specific times during the deposition sequence, the dynamics of the film growth and organization are better revealed by observing the continuous evolution of the diffraction pattern. The intensity of the diffraction pattern is defined by three variables: the polar angle (θ), the azimuthal angle (φ), and the deposition time: $I=f(\theta,\varphi,t)$. We integrated the intensity of the diffraction pattern along the selected zone of the θ axis (the same as that shown in figure 5):

$$I' = \int_{\theta_1}^{\theta_2} f(\theta,\varphi,t)\, d\theta = f'(\varphi,t)$$

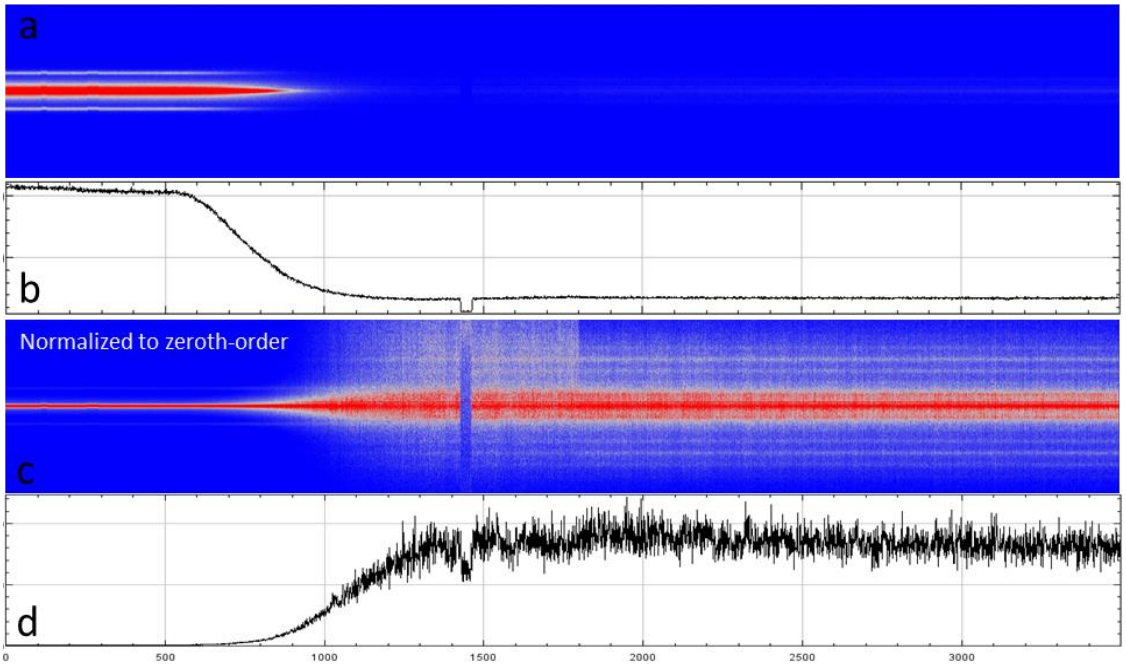

Figure 6: Diffraction pattern intensity of (a) Ag(001) and KCl as a function of the deposition time, integrated along the θ axis. The middle panel (c) shows the same pattern as in (a) but normalized to the zeroth-order. The diffraction patterns of both Ag and KCl are overlapping between 750 to 1500 s of the deposition but only the diffraction pattern of KCl dominates after 1500 s. The reflectivity curves as a function of deposition time are shown in b and d which directly correspond to the intensity profiles in (a) and (c) respectively.

Figure 6(a) shows the time evolution of the intensity associated with the diffraction pattern of both Ag(001) and KCl during the sequence. Figure 6(b) shows the reflectivity curve

(same as that of figure 4). Because of the intensity drop, the Bragg peaks from Ag(001) slowly disappear. To better visualize the appearance of the diffraction pattern from the KCl film, the 2D graph of figure 6a is normalized relative to the intensity of the zeroth-order. The result is shown in figure 6c. We now clearly see how the crystalline KCl builds up. In figure 6d, we plot the intensity of the higher order diffraction peaks that necessarily are due to the KCl film. From this graph, it is noticeable that the diffraction patterns of the KCl and Ag(001) are overlapping between the 750 to 1200 s of deposition. Beyond 1200 s, only the diffraction pattern of KCl is visible.

- **Directions and lattice parameter of KCl**

At the end of the sequence, additional GIFAD measurements were performed to look for additional diffraction pattern as the crystal azimuthal angle is varied. The previous growth sequence had been performed with the GIFAD beam along the [110] direction of Ag(001). The azimuthal scan only shows a diffraction pattern after rotation by 45°. We conclude that, contrary to NaCl, KCl thin films adopt a unique orientation with respect to the substrate, there is no mosaicity.

Figure 7 shows the intensity of the diffraction orders of KCl on Ag(001) in two directions; [110] in the top row and [100] in the bottom row. We measured the periodic distance of KCl unit cell from the intensity profiles shown in Figure 7, and the parameter that we obtained is presented in table1. The period seen on the bare substrate is used as a reference for calibration.

	Period seen by GIFAD	**Direction**	**Lattice parameter**
Bare Ag(100)	2.89 Å (reference)	[011]	4.09 Å (reference)
KCl/Ag(100)	4.43 ± 0.02 Å	[011] of KCl(100)	6.27 ± 0.02 Å
The bulk lattice parameter of KCl=6.29 Å			

Table 1: Table shows the parameter of the Ag and KCl that seen in GIFAD.

We observed that no relaxation was found in the growth of KCl in both 0˚ and 45˚ orientations with respect to the silver surface and also no azimuthal mosaicity was found since no additional diffraction spots were observed on KCl when changing from the 0˚ to the 45˚

orientation. However, our results show high apparent corrugation compared to the bulk KCl. Two reasons could explain this increase in corrugation; the rumpling process where the potassium atom is much closer to the metal substrate, or the charge transfer from the silver to the chlorine atoms.

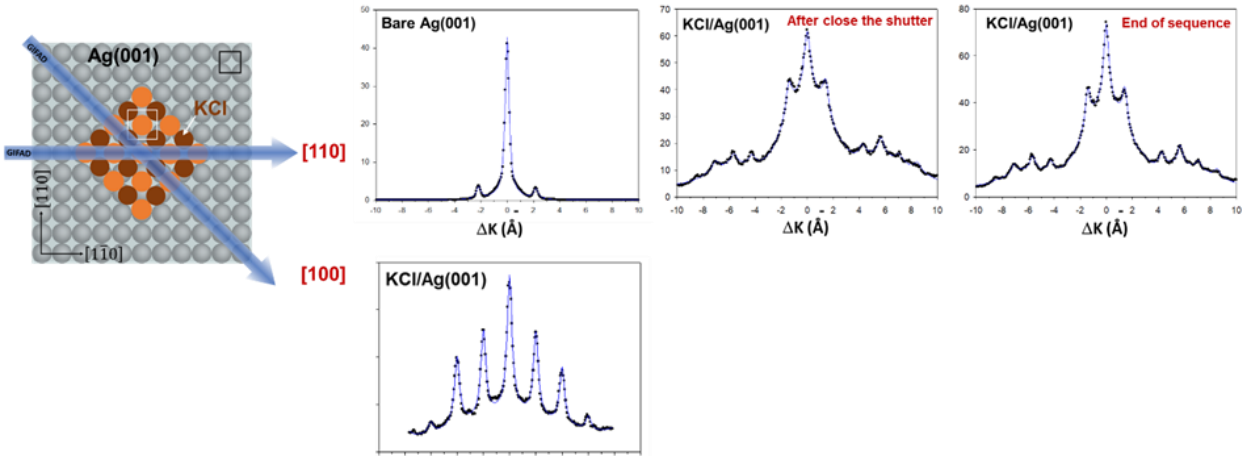

Figure 7: Intensity profiles of the diffraction pattern of Ag(001) surface and KCl film in two directions [110] in the top row and [100] in the bottom row.

5. Bibliography

[1] A. Schüller, S. Wethekam, and H. Winter, "Diffraction of Fast Atomic Projectiles during Grazing Scattering from a LiF(001) Surface," *Phys. Rev. Lett.*, vol. 98, no. 1, p. 16103, Jan. 2007.

[2] P. Rousseau, H. Khemliche, A. G. Borisov, and P. Roncin, "Quantum Scattering of Fast Atoms and Molecules on Surfaces," *Phys. Rev. Lett.*, vol. 98, no. 1, p. 16104, Jan. 2007.

[3] H. Khemliche, P. Rousseau, P. Roncin, V. H. Etgens, and F. Finocchi, "Grazing incidence fast atom diffraction: An innovative approach to surface structure analysis," *Appl. Phys. Lett.*, vol. 95, no. 15, p. 151901, Oct. 2009.

[4] N. Bundaleski, H. Khemliche, P. Soulisse, and P. Roncin, "Grazing Incidence Diffraction of keV Helium Atoms on a Ag(110) Surface," *Phys. Rev. Lett.*, vol. 101, no. 17, p. 177601, Oct. 2008.

[5] P. Atkinson, M. Eddrief, V. H. Etgens, H. Khemliche, M. Debiossac, A. Momeni, M. Mulier, B. Lalmi, and P. Roncin, "Dynamic grazing incidence fast atom diffraction during molecular beam epitaxial growth of GaAs," *Appl. Phys. Lett.*, vol. 105, no. 2, p. 21602, Jul. 2014.

[6] A. Momeni, E. M. Staicu Casagrande, A. Dechaux, and H. Khemliche, "Ultrafast Crystallization Dynamics at an Organic–Inorganic Interface Revealed in Real Time by Grazing Incidence Fast Atom Diffraction," *J. Phys. Chem. Lett.*, vol. 9, no. 4, pp. 908–913, Feb. 2018.

[7] L. de Broglie, "La mécanique ondulatoire et la structure atomique de la matière et du rayonnement," *J. Phys. Radium*, vol. 8, no. 5, pp. 225–241, 1927.

[8] L. de Broglie, "The reinterpretation of wave mechanics," *Found. Phys.*, vol. 1, no. 1, pp. 5–15, Mar. 1970.

[9] L. de Broglie, "On the Theory of Quanta," *Quantum*, vol. 10, no. III, p. 81, 1987.

[10] C. Kittel, "Introduction to Solid State Physics," p. 616, 1976.

[11] P. Soulisse, "Développement d'un dispositif expérimental pour la diffraction d'atomes rapides et étude de surfaces d'isolants ioniques," *PhD thesis*, 2011.

[12] J. R. Manson, H. Khemliche, and P. Roncin, "Theory of grazing incidence diffraction of fast atoms and molecules from surfaces," *Phys. Rev. B*, vol. 78, no. 15, p. 155408, Oct. 2008.

Résumé

En conclusion, dans ma thèse, nous avons montré grâce à des mesures STM que des films isolants minces d'halogénures alcalins déposés sur un substrat métallique ont des modes de croissance différents; la croissance par l'îlot pour le film de NaCl et la croissance en couche et îlot pour le film de KCl. La qualité de ces films dépend en particulier des conditions de croissance telles que la température de l'échantillon, le temps de dépôt et la température de la cellule, en fonction notamment des différentes relations épitaxiques avec le substrat. De plus, pour des épaisseurs suffisamment faible (typiquement 2 à 5 ML), nous avons montré que les films d'halogénures alcalins sur des métaux peuvent être discontinus et / ou présenter des trous, spécialement quand leur croissance implique la coalescence de domaines avec des orientations désappariées. Les mesures d'épaisseur apparente des couches ultraminces NaCl et KCl obtenues par STM montrent que l'épaisseur apparente et le contraste STM de ces deux films isolants varient en fonction de la tension de polarisation, ainsi que de la polarité (+/-).

Les résultats les plus importants présentés dans cette thèse concernent les effets de l'irradiation par des électrons de films minces d'halogénures alcalins en utilisant les diagnostiques LEED et AES. Jusqu'à présent, cela n'a que rarement été considéré; en particulier, le cas des films d'halogénures alcalins ultra-minces mono- ou bi- couches, déposes sur des métaux fcc, face-centrered cubic, cubique à faces centrées, n'a pas été abordé. Nous avons confirmé que la dissociation induite par électrons de films d'halogénures alcalins ultraminces déposes sur des métaux fcc diffère, en termes de cinétiques de réaction et de résultats finaux, observée pour des films épais et des cristaux massifs. Ces différences proviennent principalement de la quantité limitée des réactifs utilises et des interactions du produit avec le substrat. Nous avons observé que la déplétion en Cl suit une cinétique de réaction différente, de celle observée des études antérieures sur des films de NaCl épais et des cristaux massifs. Les atomes de Na produits par la dissociation de NaCl diffusent vers des zones vides de la surface Ag (001), où ils forment des superstructures de Na-Ag qui sont commues dans les cas du pour le système Na / Ag (001). La STM a été utilisé pour caractériser la géométrie et l'épaisseur des films ultraminces irradiés ; il a montré que la dissociation des films ultra-minces de NaCl relève de deux processus ; (i) l'irradiation par les électrons augmente le désordre de NaCl en déplacement le NaCl des bords de l'îlot, ce qui ralentit la cinétique de réaction de la dissociation

du NaCl et (ii) la formation de superstructures de Na sur l'argent. Des études complémentaires sont nécessaires pour contrôler le rapport entre les nombres de zones désordonnées et ordonnées ; en effet, ces films d'halogénures alcalins sont de plus en plus utilisés comme séparateurs pour découpler électroniquement des molécules organiques de leurs substrats métalliques dans des systèmes contrôlés au niveau atomique pour réaliser des mesures de spectroscopie à une seule molécule.

Le second objectif de cette thèse était d'étudier des films organiques minces de la molécule PTCDA en utilisant le film de KCl ultramince comme un séparateur pour découpler ces molécules du substrat de métal Ag(001). Pour éviter la dissociation des films de KCl, seule la STM a été utilisée. L'arrangement des molécules de PTCDA sur les îlots de KCl formés sur un substrat d'argent a été observé où trouve des molécules individuelles et des structures denses et tassées sur des films de KCl ont été trouvées. Cependant, on trouve également des molécules de PTCDA et KCl adsorbées de manière désordonnée. Elles se sont formées pendant la croissance des films PTCDA et KCl et elles peuvent affecter l'arrangement du film PTCDA ainsi que les mesures d'épaisseur apparente de chacun des deux films. Afin d'éviter cet effet, une procédure standard de refroidissement sera nécessaire pendant la croissance. Ce système peut être utilisé pour étudier l'excitation électronique de la luminescence produite par la pointe de la STM ; cela se produit uniquement lorsque les molécules sont déposées sur un substrat isolant, sinon la luminescence n'apparait pas raison du transfert de charge des molécules vers le substrat.

Enfin, nous avons étudié le film mince de film de KCl dépose sur Ag (001) par mesure GIFAD, afin d'obtenir des informations plus détaillées sur le mode de croissance. L'expérience a été effectuée avec le faisceau aligné avec dans deux directions de l'échantillon; [110] et [001]. Dans les deux directions, nous avons trouvé que, contrairement au NaCl, les couches minces de KCl adoptent une orientation unique par rapport au substrat, où aucune relaxation n'a été observée dans la croissance de KCl dans les orientations 0˚ et 45˚ par rapport à la surface argentée. De même, aucune dispersion azimutale des orientations cristallines n'a été trouvée, puis que des points de diffraction supplémentaires de KCl n'ont pas été vus lors du changement d'orientation de 0˚ à 45˚. Cependant, nos résultats montrent une forte ondulation apparente par rapport au KCl massif qui présente une faible ondulation. L'augmentation de l'ondulation apparente a deux explications possibles, (i) le processus de froissement qui entraîne que l'atome

de potassium est beaucoup plus proche du substrat métallique, et (ii) le transfert de charge de l'argent vers les atomes de chlore.

université PARIS-SACLAY | ÉCOLE DOCTORALE Ondes et Matière (EDOM)

Titre : Couches Minces d'Halogénures de Métaux Alcalins : Structure et Réactivité sous Irradiation Electronique

Mots clés : Science des Surfaces, Couches Minces d'Halogénures de Métaux Alcalins, Microscope à Effet Tunnel, Désorption Induite par Electrons

Résumé : NaCl et KCl sont des matériaux à large bande interdite d'énergie, qui sont de plus en plus utilisés sous forme de couches minces en sciences des surfaces et dans des études de spectroscopie de molécules individuelles, pour découpler électroniquement des molécules organiques d'un substrat métallique. De plus, la réactivité de NaCl et KCl, sous forme de cristaux massifs, sous irradiation électronique ou photonique, a été beaucoup étudiée depuis les années 1970s.

Dans ce mémoire de thèse, nous présentons les résultats d'une étude détaillée de couches minces de NaCl et de KCl sur Ag(001) par microscopie et spectroscopie à effet tunnel (STM/STS), diffraction des électrons lents (LEED) et spectroscopie d'électrons Auger (AES) sous ultravide. Afin d'obtenir des couches minces de haute qualité sur une surface métallique et de contrôler les propriétés de ces couches (épaisseur, taille et orientation des domaines, etc.), nous étudions en détails la formation de la couche en fonction des paramètres de croissance. De plus, les mesures de topographie STM montrent que l'épaisseur apparente et le contraste STM des couches isolantes dépendent de la différence de potentiel pointe-surface.

Nous décrivons les modifications induites par irradiation électronique d'halogénures Les cinétiques et produits de réaction sont examinés dans le cas de couches de NaCl sur Ag(001). Les modifications structurales et chimiques sous faisceau d'électrons d'énergie 52-60 eV et 3 keV sont étudiées en utilisant respectivement le LEED et l'AES. Les effets de l'irradiation sur la géométrie et l'épaisseur des couches (allant de 2 à 5 couches atomiques) sont mesurés en STM. Nous observons que la déplétion en chlore induite par l'irradiation suit une cinétique différente de celles précédemment décrites pour les couches épaisses et cristaux massifs de NaCl. Les atomes de sodium produits par la dissociation de NaCl diffusent vers les zones nues de la surface Ag(001), où ceux-ci forment des superstructures Na-Ag connues pour le système Na/Ag(001). La modification des couches est le résultat de deux processus, pouvant être interprétés comme une désorganisation rapide de la couche avec l'arrachement de molécules de NaCl des bords d'îlots, et une perte lente de l'ordre structural à l'intérieur des îlots de NaCl due à la formation de trous par déplétion du chlore. La cinétique de la croissance des superstructures Na-Ag est expliquée par la diffusion limitée sur la surface irradiée, en raison de l'agrégation de molécules de NaCl désordonnées aux bords de marches du substrat.

Nous avons également entrepris l'étude par STM de molécules de PTCDA déposées sur le substrat métallique Ag(001) et sur le système KCl/Ag(001). Nous obtenons une monocouche de PTCDA sur Ag(001) qui présente un arrangement avec une maille carrée. Sur les films de KCl, des molécules de PTCDA isolées ainsi que des structures empilées compactes ont été trouvées.

Université Paris-Saclay
Espace Technologique / Immeuble Discovery
Route de l'Orme aux Merisiers RD 128 / 91190 Saint-Aubin, France

université PARIS-SACLAY | ÉCOLE DOCTORALE Ondes et Matière (EDOM)

Title : Alkali-Halide Thin Films: Growth, Structure and Reactivity upon Electron Irradiation

Keywords : Surface Science, Thin Alkali-Halide Films, Scanning Tunneling Microscope, Electron-Induced Desorption

Abstract : NaCl and KCl are wide band gap materials that are increasingly used as thin films in surface science and single-molecule spectroscopy studies to electronically decouple organic molecules from a metal substrate. In addition, the reactivity of bulk NaCl and KCl crystals under electron irradiation has been widley studied since the year 1970 s.

In this dissertation, we report a detailed investigation on the structures of two different thin films of NaCl and KCl grown on the Ag(001) substrate by scanning tunneling microscopy (STM), scanning tunneling spectroscopy (STS), low energy electron diffraction (LEED), and Auger electron spectroscopy (AES) in ultrathin vacuum condition. In order to obtain high-quality thin films and to control the properties of these films on the metal surface (film thickness, domain size, domain orientation, etc), we study in detail the film growth, especially as a function of the growth parameters. In addition, the apparent height measurements by STM show that the apparent thickness and the STM contrast of these two insulating films are bias dependent.

We report on an electron-induced modification of alkali halides in the ultrathin film regime. The reaction kinetics and products of the modifications are investigated in the case of NaCl films grown on Ag(001). Their structural and chemical modification upon irradiation with electrons of energy 52–60 eV and 3 keV is studied using LEED and AES, respectively. The irradiation effects on the film geometry and thickness (ranging from between two and five atomic layers) are examined using STM. We observe that Cl depletion follows different reaction kinetics, as compared to previous studies on thick NaCl films and bulk crystals. Na atoms produced from NaCl dissociation diffuse to bare areas of the Ag(001) surface, where they form Na-Ag superstructures that are known for the Na/Ag(001) system. The modification of the film is shown to proceed through two processes, which are interpreted as a fast disordering of the film with removal of NaCl from the island edges and a slow decrease of the structural order in the NaCl with formation of holes due to Cl depletion. The kinetics of the Na-Ag superstructure growth is explained by the limited diffusion on the irradiated surface, due to aggregation of disordered NaCl molecules at the substrate step edges.

We have also investigated the deposition of PTCDA molecules on the metallic substrate Ag(001) and on the KCl/Ag(001) system using STM. We obtain a monolayer of PTCDA molecules on Ag(001) that is arranged in a square unit cell. On KCl films, both individual PTCDA molecules and a densely packed structure are found.

Université Paris-Saclay
Espace Technologique / Immeuble Discovery
Route de l'Orme aux Merisiers RD 128 / 91190 Saint-Aubin, France